Aerosol remote sensing in polar regions

by

Claudio Tomasi [(1)], Alexander A. Kokhanovsky [(2, 3)], Angelo Lupi [(1)], Christoph Ritter [(4)], Alexander Smirnov [(5, 6)], Norman T. O'Neill [(7)], Robert S. Stone [(8, 9)], Brent N. Holben [(6)], Stephan Nyeki [(10)], Christoph Wehrli [(10)], Andreas Stohl [(11)], Mauro Mazzola [(1)], Christian Lanconelli [(1)], Vito Vitale [(1)], Kerstin Stebel [(11)], Veijo Aaltonen [(12)], Gerrit de Leeuw [(12, 13)], Edith Rodriguez [(12)], Andreas B. Herber [(14)], Vladimir F. Radionov [(15)], Tymon Zielinski [(16)], Tomasz Petelski [(16)], Sergey M. Sakerin [(17)], Dmitry M. Kabanov [(17)], Yong Xue [(18, 19)], Linlu Mei [(19)], Larysa Istomina [(2)], Richard Wagener [(20)], Bruce McArthur [(21)], Piotr S. Sobolewski [(22)], Rigel Kivi [(23)], Yann Courcoux [(24)], Pierre Larouche [(25)], Stephen Broccardo [(26)] and Stuart J. Piketh [(27)]

[(1)] Climate Change Division, Institute of Atmospheric Sciences and Climate (ISAC), Italian National Research Council (CNR), Bologna, Italy.

[(2)] Institute of Environmental Physics (IUP), University of Bremen, Bremen, Germany.

[(3)] EUMETSAT, Eumetsat Allee 1, D-64295 Darmstadt, Germany.

[(4)] Climate System Division, Alfred Wegener Institute for Polar and Marine Research, Potsdam, Germany.

[(5)] Sigma Space Corporation, Lantham, Maryland, USA.

[(6)] Biospheric Sciences Branch, NASA/Goddard Space Flight Center (GSFC), Greenbelt, Maryland, USA.

[(7)] Canadian Network for the Detection of Atmospheric Change (CANDAC) and CARTEL, Dept. of Applied Geomatics, University of Sherbrooke, Sherbrooke, Québec, Canada.

[(8)] Global Monitoring Division (GMD), National Oceanic and Atmospheric Administration (NOAA), Boulder, Colorado, USA.

[9] Cooperative Institute for Research in Environmental Sciences (CIRES), University of Colorado, Boulder, Colorado, USA.
[10] Physikalisch-Meteorologisches Observatorium (PMOD)/World Radiation Centre (WRC), Davos, Switzerland.
[11] Norwegian Institute for Air Research (NILU), Kjeller, Norway.
[12] Climate and Global Change Division, Finnish Meteorological Institute (FMI), Helsinki, Finland.
[13] Department of Physics, University of Helsinki, Finland.
[14] Climate System Division, Alfred Wegener Institute for Polar and Marine Research, Bremerhaven, Germany.
[15] Arctic and Antarctic Research Institute (AARI), St. Petersburg, Russia.
[16] Institute of Oceanology (IO), Polish Academy of Sciences (PAS), Sopot, Poland.
[17] V. E. Zuev Institute of Atmospheric Optics (IAO), Siberian Branch (SB), Russian Academy of Sciences (RAS), Tomsk, Russia.
[18] Faculty of Life Sciences and Computing, London Metropolitan University, London, United Kingdom.
[19] Key Laboratory of Digital Earth Science, Institute of Remote Sensing and Digital Earth, Chinese Academy of Sciences, Beijing, 100094, China
[20] Brookhaven National Laboratory, Environmental and Climate Sciences Dept., Upton, NY, USA.
[21] Environment Canada, Downsview, North York, Ontario, Canada; now with Agriculture and Agri-food Canada.
[22] Institute of Geophysics, Polish Academy of Sciences (PAS), Warsaw, Poland.
[23] Arctic Research Center, Finnish Meteorological Institute (FMI), Sodankylä, Finland.
[24] Institute de l'Atmosphère de la Réunion (OPAR), Univ. de la Réunion - CNRS, Saint Denis de la Réunion, France.
[25] Institut Maurice-Lamontagne, Mont-Joli, Quebec, Canada.
[26] Geography, Archeology and Environmental Science, University of the Witwatersrand, Johannesburg, South Africa.
[27] Climatology Research Group, Unit for Environmental Sciences and Management, North-West University, Potchefstroom, South Africa.

Corresponding author: Claudio Tomasi
Phone: + 39 051 639 9594
Fax: + 39 051 639 9652
E-mail:c.tomasi@isac.cnr.it

64

65 **Abstract**

66 Multi-year sets of ground-based sun-photometer measurements conducted at 12 Arctic sites and 9
67 Antarctic sites were examined to determine daily mean values of aerosol optical thickness $\tau(\lambda)$ at
68 visible and near-infrared wavelengths, from which best-fit values of Ångström's exponent α were
69 calculated. Analysing these data, the monthly mean values of $\tau(0.50\ \mu m)$ and α and the relative
70 frequency histograms of the daily mean values of both parameters were determined for winter-
71 spring and summer-autumn in the Arctic and for austral summer in Antarctica. The Arctic and
72 Antarctic covariance plots of the seasonal median values of α versus $\tau(0.50\ \mu m)$ showed: (i) a
73 considerable increase in $\tau(0.50\ \mu m)$ for the Arctic aerosol from summer to winter-spring, without
74 marked changes in α; and (ii) a marked increase in $\tau(0.50\ \mu m)$ passing from the Antarctic Plateau to
75 coastal sites, whereas α decreased considerably due to the larger fraction of sea-salt aerosol. Good
76 agreement was found when comparing ground-based sun-photometer measurements of $\tau(\lambda)$ and α
77 at Arctic and Antarctic coastal sites with Microtops measurements conducted during numerous
78 AERONET/MAN cruises from 2006 to 2013 in three Arctic Ocean sectors and in coastal and off-
79 shore regions of the Southern Atlantic, Pacific, and Indian Oceans, and the Antarctic Peninsula.
80 Lidar measurements were also examined to characterise vertical profiles of the aerosol
81 backscattering coefficient measured throughout the year at Ny-Ålesund. Satellite-based MODIS,
82 MISR, and AATSR retrievals of $\tau(\lambda)$ over large parts of the oceanic polar regions during spring and
83 summer were in close agreement with ship-borne and coastal ground-based sun-photometer
84 measurements. An overview of the chemical composition of fine and accumulation/coarse mode
85 particles is also presented, based on *in-situ* measurements at Arctic and Antarctic sites. Fourteen
86 log-normal aerosol number size-distributions were defined to represent the average features of fine
87 and accumulation/coarse mode particles for Arctic haze, summer background aerosol, Asian dust
88 and boreal forest fire smoke, and for various background austral summer aerosol types at coastal

and high-altitude Antarctic sites. The main columnar aerosol optical characteristics were determined for all 14 particle modes, based on *in-situ* measurements of the scattering and absorption coefficients. Diurnally averaged direct aerosol-induced radiative forcing and efficiency were calculated for a set of multimodal aerosol extinction models, using various Bidirectional Reflectance Distribution Function models over vegetation-covered, oceanic and snow-covered surfaces. These gave a reliable measure of the pronounced effects of aerosols on the radiation balance of the surface-atmosphere system over polar regions.

Key words:

Sun-photometer measurements

Aerosol optical thickness

Polar aerosol optical characteristics

Lidar backscattering coefficient profiles

Satellite aerosol remote sensing

Multimodal aerosol extinction models

1. Introduction.

Aerosols are one of the greatest sources of uncertainty in climate modeling, as their microphysical, chemical and optical characteristics as well as their concentration vary in time and in space, inducing significant direct radiative forcing effects on the surface-atmosphere system. In addition, they can alter cloud optical features and indirectly impact climate. The aim of this paper is to present an overview of the optical characteristics of atmospheric aerosol observed in polar regions during the past two decades, including recent measurements conducted with ground-based and ship-borne sun-photometers, or retrieved from remote sensing data recorded with visible and infrared sensors mounted onboard various satellite platforms. Optical instruments (e.g., lidars, sun-photometers) measure the characteristics of the atmospheric light field (internal, reflected, or transmitted). Specific procedures therefore need to be applied to convert optical signals to aerosol characteristics, such as particle size and shape distributions, or chemical composition. Similar procedures are also needed to derive the vertical concentration distribution from columnar measurements. They are based on the solution of the inverse problem of radiative transfer theory accounting for multiple light scattering, molecular and aerosol scattering and absorption, and surface reflectance effects.

The presence of a visibility-reducing haze in the Arctic was already noted by early explorers in the 19th century (see Garrett and Verzella, 2008, for a historical overview). The explorers also documented that haze particles were deposited on snow in remote parts of the Arctic (e.g., Nordenskiöld, 1883) and haze layers were also observed later by pilots in the 1950s (Mitchell, 1957). The source of the haze was debated for almost a century but poorly understood until the 1970s when it was suggested that this “Arctic Haze” originated from emissions in northern mid-latitudes and was transported into the Arctic over thousands of kilometers (Rahn et al., 1977, Barrie et al., 1981). The seasonality of the haze, which peaks in winter and early spring, was explained by the fact that removal processes are inefficient in the Arctic during that time of the year (Shaw, 1995).

Polar aerosols originate from both natural and anthropogenic sources (Shaw, 1988, 1995). In the Arctic regions, natural aerosols have been found to contain an oceanic sea-salt mass fraction that frequently exceeds 50% on summer days, and a mass fraction of 30-35% due to mineral dust, with lower percentages of non-sea-salt (nss) sulphate, methane sulphonic acid (MSA), and biomass burning combustion products. In contrast, anthropogenic particles have higher concentrations of sulphates, organic matter (OM) and black carbon (BC) with respect to natural aerosol (Quinn et al., 2002, 2007; Sharma et al., 2006). In fact, boreal forest fire (hereinafter referred to as BFF) smoke transported from North America and Siberia often contributes to enhance soot concentration in summer (Damoah et al., 2004; Stohl et al., 2006). Rather high aerosol mass concentrations of anthropogenic origin are frequently transported from North America and especially Eurasia in the winter and spring months, leading to intense Arctic haze episodes (Shaw, 1995). For instance, Polissar et al. (2001) conducted studies on the BC source regions in Alaska from 1991 to 1999 finding that predominant contributions have been given by large-scale mining and industrial activities in South and Eastern Siberia. In the North-European sector of the Arctic, the dominant sources of sulphates and nitrates (and to a lesser extent of water-soluble OM and BC) are located in Europe and Siberia, due to both urban pollution and industrial activities (Hirdman et al., 2010). Episodes of Asian dust transport have also been observed over the past years in the North-American sector of the Arctic, especially in spring (Stone et al., 2007), together with local transport of soil particles mobilized by strong winds, which provisionally enhance the mass concentrations of elemental components, such as Al, Si, Mg and Ca (Polissar et al., 1998). The Arctic atmosphere's stratification is highly stable, with frequent and strong inversions near the surface, which limit turbulence and reduce the dry deposition of aerosols to the surface (Strunin et al., 1997). They also decouple the sea ice inversion layer from the Arctic free troposphere, leading to very different chemical and physical properties of aerosols in the sea ice inversion layer where aerosols are depleted, and higher up where a sulphate-rich background aerosol typically of anthropogenic origin is often found (Brock et al., 2011). In addition, organic-rich biomass burning layers occur in the free

troposphere but rarely reach the surface (Brock et al., 2011; Warneke et al., 2010). The low-altitude high-latitude atmosphere in the southern hemisphere is similarly stably stratified as the Arctic's but also influenced strongly by katabatic winds bringing down air from the high altitudes of interior Antarctica (Stohl and Sodemann, 2010).

On larger scales, the stable Arctic stratification leads to the so-called polar dome, where isentropes form shells above the Arctic. As atmospheric transport tends to follow the isentropes, direct transport of air masses from mid-latitude pollution source regions into the Arctic lower troposphere is very inefficient. According to Stohl (2006), polluted air masses from lower latitudes typically follow one of five major transport pathways (see Fig. 1): (1) lifting at the Arctic front, where wet scavenging is efficient; (2) lifting at lower latitudes (at the polar front or convection), where wet scavenging is even more efficient; (3) most importantly for Arctic surface aerosol concentrations, low-level transport over land in winter where strong radiative cooling allows air masses to enter the polar dome; (4) slow descent by radiative cooling of upper-tropospheric air masses into the polar dome; (5) slow mixing across the lateral boundaries of the dome. Forest or agricultural fires are important, as they produce strong aerosol plumes in the mid- to high-latitude free troposphere, which can subsequently enter the Arctic by one of the previously mentioned processes.

In addition to long-range pollution transport, local emission sources can be important. For instance, emissions from cruise ships can lead to measurable enhancements of BC and other aerosols in the Svalbard archipelago (Eckhardt et al., 2013). Diesel generators can also locally pollute the environment (Hagler et al., 2008). Aircraft emissions north of the Arctic circle are primarily injected into the stratosphere where removal is inefficient and these emissions can slowly descend (Whitt et al., 2011). All these local sources can also enhance the Arctic aerosol background; however, quantification of their contribution relative to long-range transport of pollution from sources outside the Arctic remains uncertain. In addition, sulphate and volcanic ash from high-latitude eruptions can occasionally influence the Arctic troposphere (e.g., Hoffmann et al., 2010). The stratospheric background aerosol in the Arctic as elsewhere can be perturbed by explosive

183 volcanic eruptions (especially in the tropics) for several years. Some volcanic aerosol emission
184 episodes have been observed by Bourassa et al. (2010) and O'Neill et al. (2012) over last few years,
185 involving the low stratosphere over short periods of a few months.
186 Transport processes in the high-latitude southern hemisphere are similar to those sketched for the
187 Arctic in Fig. 1. As in the northern hemisphere, polluted air masses from the lower-latitude
188 continents are quasi-isentropically lifted to higher altitudes and, furthermore, there is no low-
189 altitude transport pathway over land in winter (i.e., the analogue to transport pathway number 3 in
190 Fig. 1 is missing in the southern hemisphere). Consequently, as in the Arctic, the lowermost
191 troposphere in the Antarctic is very isolated and, thus, contains little anthropogenic pollution
192 transported from lower-latitude continents (Stohl and Sodemann, 2010). A major difference to the
193 Arctic, however, is the high topography of the Antarctic continent. This means that the most
194 isolated air masses (as measured by the time since last exposure to pollution sources at lower-
195 latitude continents) are not found close to the pole, as in the Arctic, but in the coastal areas
196 surrounding Antarctica (Stohl and Sodemann, 2010). Descent over the Antarctic continent is
197 stronger than over the Arctic and can also bring down air from the stratosphere, and air from the
198 Antarctic interior is transported down to coastal areas by strong katabatic winds.
199 In Antarctica, aerosols sampled at coastal sites originate almost totally from natural processes, with
200 a prevailing oceanic sea-salt mass content of 55-60%, and lower percentages of nss sulphate (20-
201 30%) and mineral dust (10-20%) (Tomasi et al., 2012). Only very low mass fractions of nitrates,
202 water-soluble OM and BC have been monitored in Antarctica, mainly associated with transport
203 from remote anthropogenic sources (Wolff and Cachier, 1998) or biomass burning (Fiebig et al.,
204 2009) in mid-latitude areas. More than 60-80% of particulate matter suspended over the Antarctic
205 Plateau has been estimated to consist of nss sulphates formed from biogenic sulphur compounds
206 and/or MSA, due to long-range transport in the free troposphere and subsequent subsidence
207 processes. Therefore, aerosols sampled at these high-altitude sites contain only moderate mass

208 fractions of nitrates, and minor or totally negligible mass percentages of mineral dust, water-soluble
209 OM and BC (Tomasi et al., 2007, 2012).
210 The paper is organized as follows. In the next section the ground-based remote sensing
211 measurements of atmospheric aerosol are reviewed (sun-photometers, lidars). Section 3 gives a
212 description of ship-borne aerosol remote sensing instruments. Section 4 discusses aerosol
213 backscattering coefficient profiles from lidar measurements, while Section 5 is dedicated to
214 airborne and satellite observations of polar aerosols. The last section presents the most important
215 optical characteristics and size-distribution features of polar aerosols, which are appropriate for
216 calculations of direct radiative forcing effects induced by aerosols on the climate system.
217
218 **2. Ground-based remote sensing measurements**
219 *2.1. Spectral measurements of aerosol optical thickness*
220 Ground-based remote sensing of the optical characteristics of aerosols in the atmospheric column is
221 usually conducted with multi-wavelength sun-photometers. A sun-photometer is oriented towards
222 the Sun to detect the solar radiation attenuated along the slant path from the top-of-atmosphere
223 (TOA) to the ground. The atmospheric aerosol load leads to a decrease in the solar radiation
224 transmitted through the atmosphere. This decrease depends on the aerosol optical thickness
225 (hereinafter referred to as AOT and/or using symbol $\tau(\lambda)$), which is given by the integral of the
226 volume aerosol extinction coefficient along the vertical path of the atmosphere.
227 The networks, sites and sun-photometers whose data were employed in this paper are defined and
228 characterized in Tables 1 and 2 for the Arctic and Antarctic regions, respectively. The largest
229 networks of sun-photometers in the world are AERONET and SKYNET. Spectral measurements of
230 $\tau(\lambda)$ are performed with AERONET sun-photometers (Holben et al., 1998) at 8 wavelengths
231 ranging from 0.340 to 1.600 μm, and with SKYNET instruments (Nakajima et al., 2007) at 10
232 wavelengths from 0.315 to 2.200 μm. The Cimel CE-318 sun-photometers of the AERONET
233 network are currently used at several Arctic sites: Barrow (since March 2002), Thule (since March

2007), Hornsund (since April 2005), Sodankylä (since February 2007), Tiksi (since June 2010), Resolute Bay (since July 2004), Eureka-0PAL (since April 2007) and Eureka-PEARL (since May 2007). The last three sites, located in the Nunavut region of Canada, are part of the AEROCAN/AERONET network. In addition, an AERONET sun-photometer has been intermittently used since 2002 by the Atmospheric Optics Group (GOA) (University of Valladolid, Spain) at the Arctic Lidar Observatory for Middle Atmosphere Research (ALOMAR), located on the Andøya Rocket Range, near Andenes (Northern Norway) (Toledano et al., 2012). AERONET sun-photometers have been used to obtain Level 2.0 $\tau(\lambda)$ measurements at the South Pole (since November 2007), and occasionally at Dome Concordia (in January and December 2003) in Antarctica. AERONET Level 1.5 measurements of $\tau(\lambda)$ are available for McMurdo on the Ross Sea (from February to December 1997, in the austral summer 2001/2002, and in January-February 2011), at Marambio (Antarctic Peninsula) since October 2007, at Vechernaya Hill (Thala Hills, Enderby Land) since December 2008, and at Utsteinen (Dronning Maud Land) since February 2009. However, because these data were not promoted to Level 2.0, they were not considered in the present study. A PREDE POM-01L sun/sky radiometer was used in Antarctica during the 2001-2002 austral summer by Di Carmine et al., (2005) at the Mario Zucchelli station. PREDE instruments have been used since 2001 in Antarctica at Syowa (East Ongul Island, Lützow-Holm Bay) by the National Institute of Polar Research (NIPR, Tokyo, Japan) since 2001, at Rothera by the British Antarctic Survey (BAS) since January 2008, and at Halley by BAS since February 2009. In addition, Precision Filter Radiometer (PFR) sun-photometers (Wehrli, 2000; Nyeki et al., 2012) from the Global Atmosphere Watch (GAW) PFR network are currently used in the Arctic at Summit by PMOD/WRC (Switzerland), at Ny-Ålesund by NILU (Norway), and at Sodankylä by FMI (Finland), and in Antarctica at Marambio by FMI and at Troll by NILU. The instrumental and geometrical characteristics of the PFR sun-photometer are described by Wehrli (2000).

The monochromatic total optical thickness $\tau_{TOT}(\lambda)$ of the atmosphere is commonly calculated in terms of the well known Lambert-Beer law for a certain sun-photometer output voltage $J(\lambda)$ taken

within a spectral channel centred at wavelength λ and for a certain apparent solar zenith angle θ_0. The monochromatic value of $\tau_{TOT}(\lambda)$ is given by (Shaw, 1976):

$$\tau_{TOT}(\lambda) = (1/m) \ln [R\, J_0(\lambda)/J(\lambda)] \quad , \tag{1}$$

where:

(i) m is the relative optical air mass calculated as a function of θ_0 using a realistic model of the atmosphere, in which wet-air refraction and Earth/atmosphere curvature effects on the direct solar radiation passing through the atmosphere are properly taken into account (Thomason et al., 1983; Tomasi and Petkov, 2014); (ii) $J(\lambda)$ is the output signal (proportional to solar irradiance) measured by the ground-based solar pointing sun-photometer; (iii) $J_0(\lambda)$ is the output signal that would be measured by the sun-photometer outside the terrestrial atmosphere, at the mean Earth-Sun distance; and (iv) R accounts for $J_0(\lambda)$ variations as a function of the daily Earth-Sun distance (Iqbal, 1983).

The solar radiation reaching the surface for cloud-free sky conditions is attenuated not only by aerosol extinction but also by Rayleigh outscattering as well as absorption by minor gases (mainly water vapour (H_2O), ozone (O_3), nitrogen dioxide (NO_2) and its dimer (N_2O_4), and oxygen dimer (O_4)). The spectral values of $\tau(\lambda)$ within the main windows of the atmospheric transmission spectrum are accordingly calculated by subtracting the Rayleigh scattering and absorption optical thicknesses from $\tau_{TOT}(\lambda)$.

AOT is usually a smooth function of wavelength λ (measured in μm), which can be approximated by the following simple formula:

$$\tau(\lambda) = \tau(\lambda_0)(\lambda/\lambda_0)^{-\alpha}, \tag{2}$$

where α is the so-called Ångström (1964) wavelength exponent, and λ_0 is usually assumed to be equal to 1 μm. In reality, the analytical form defined in Eq. (2) can be convex or concave depending on the relative contents of fine and coarse particles in the atmospheric column. O'Neill et al. (2001a) demonstrated that the variation in $\tau(\lambda)$ and its first and second spectral derivatives (named

here α and α', respectively) can be realistically described in terms of the spectral interaction between the individual optical components of a bimodal size-distribution. O'Neill et al. (2001a) then showed that one can exploit the spectral curvature information in the measured $\tau(\lambda)$ to permit a direct estimate of a fine-mode Ångström exponent (α_f) as well as the optical fraction of fine-mode particles. However, an analysis of α and α' determined in real cases and taking into account that both $\alpha(0.44\text{-}0.87\ \mu m)$ and α' are closely related to the spectral features of $\tau(\lambda)$ showed that propagation of errors leads to an error $\Delta\alpha/\alpha \sim 2\ \Delta\tau(\lambda)/\tau(\lambda)$ and an error $\Delta\alpha'/\alpha' \sim 5\ \Delta\tau(\lambda)/\tau(\lambda)$, respectively (Gobbi et al., 2007). These estimates yield values of $\Delta\alpha/\alpha$ and $\Delta\alpha'/\alpha'$ that are > ~ 20% and > ~ 50%, respectively, for $\tau(\lambda) \leq 0.10$ and a typical sunphotometry error equal to ~ 0.01. To avoid relative errors > ~ 30% in $\Delta\alpha'/\alpha'$, Gobbi et al. (2007) suggested using only observations of $\tau(\lambda) > 0.15$. We applied the same criterion as a threshold for accepting outputs from the Spectral Deconvolution Algorithm (SDA) of O'Neill et al. (2003) (notably the fine-mode Ångström exponent, which offers an alternative refinement to the calculation of α): our logic being that α and α' are input parameters to SDA and we did not want to introduce unacceptable processing errors to the extraction of a spectral exponent indicator. These limitations to the use of spectral values of α and α' were also applied by Yoon et al. (2012), who only considered observations with $\tau(0.44\ \mu m) > 0.15$ in order to avoid relative errors > 30% in α'. Tomasi et al. (2007) showed that for the period 1977-2006, $\tau(0.50\ \mu m)$ did not exceed 0.15 for background summer aerosol conditions at Barrow, Alert, Summit, Ny-Ålesund, Hornsund, Sodankylä and Andenes/ALOMAR in the Arctic, and was greater than 0.15 only during very strong episodes of Arctic haze in late winter and spring, and BFF smoke transport in summer. Similarly, Tomasi et al. (2012) found that (i) the measurements of $\tau(0.50\ \mu m)$ recorded from 2000 to 2012 at Ny-Ålesund were estimated to exceed 0.15 in summer (June to September) in only a few cases of strong transport of BFF smoke from lower latitudes; even in winter (December to March), they were higher than 0.15 only for 10% of the cases, typically associated with Arctic haze transport episodes; (ii) measurements of $\tau(0.50\ \mu m) > 0.15$

309 recorded at Barrow over the same period were observed only in a few percent of cases, as a result of
310 Arctic haze; and (iii) daily mean background summer values of $\tau(0.50\ \mu m)$ measured at Tiksi in
311 Siberia were always lower than 0.08 during the summer 2010. With regard to Antarctic aerosol,
312 Tomasi et al. (2007) estimated that the daily mean values of $\tau(0.50\ \mu m)$ were lower than 0.10 during
313 the austral summer months at Marambio, Neumayer, Aboa, Mirny, Molodezhnaya, Syowa, Mario
314 Zucchelli, Kohnen, Dome Concordia and South Pole. In particular, examining the sun-photometer
315 measurements carried out from 2005 to 2010, Tomasi et al. (2012) reported that the austral summer
316 values of $\tau(0.50\ \mu m)$ measured at Neumayer and Mirny were < 0.10 during the whole season, while
317 those measured at South Pole never exceeded 0.06.
318 Therefore, since the values of $\tau(0.44\ \mu m)$ determined from the sun-photometer measurements
319 conducted in polar regions are mostly lower than 0.15 and thus below the value recommended by
320 Gobbi et al. (2007), we have decided not to determine the exponent α_f using the O'Neill et al.
321 (2001b) algorithm, but to calculate the best-fit value of the Ångström exponent α over the spectral
322 range $0.40 \leq \lambda \leq 0.87$ μm using Eq. (2). In real cases, the exponent α provides by itself a first rough
323 estimate of the optical influence of the fine particle component on $\tau(\lambda)$, since it gradually decreases
324 on average from cases where fine particle extinction predominates to cases where coarse particles
325 are optically predominant.
326 In all cases with relatively high values of $\tau(0.50\ \mu m)$, the AERONET and SKYNET sun/sky
327 radiometers can also be used to provide regular measurements of sky-brightness along the solar
328 almucantar (an azimuthal circle around the local normal whose zenith angle equals the solar zenith
329 angle θ_0) and also in the principal plane containing the direction to the Sun and the local normal.
330 The analysis of these measurements enables better constraints for solving the inverse problem
331 (while accounting for multiple scattering and surface reflectance effects) and allowing the following
332 parameters to be derived: (i) the aerosol single scattering albedo $\omega(\lambda)$, (ii) the phase function $P(\Theta)$,

(iii) the particle number density size distribution $N(r) = dN(r)/d(\ln r)$) given as a function of particle radius r, and (iv) the complex refractive index $n(\lambda)$ - i $k(\lambda)$ (King and Dubovik, 2013).

The data analysis performed in this paper was subject to certain data processing constraints across networks of instruments. In the first instance, all network protocols differ in many (typically) minor details such as the means of estimating molecular optical thicknesses and solar air masses, the nominal time interval between measurements and calibration protocols. In general, all data sets were cloud-screened using temporal-based criteria that were developed and rigorously tested by each network group. Only Level 2.0 AERONET data were used: this corresponds to temporal-based cloud-screened data (Smirnov et al., 2000) that has undergone a final quality assurance step. The GMD/NOAA data acquired at Barrow and Alert were further cloud-screened using a spectral criterion wherein $\tau(\lambda)$ spectra were eliminated for $\alpha < 0.38$. This added cloud-screening feature was found to be necessary in order to eliminate the influence of homogeneous, thin cirrus clouds that has escaped the temporal cloud-screening step. Finally we note that the specific spectral ranges of the α computations, while being nominally limited to $0.40 \leq \lambda \leq 0.87$ μm are given in Tables 1 and 2 for each type of instrument (the α regression was carried out for all wavelength channels between and including the wavelength extremes given in the "Spectral interval" column).

Before presenting the evaluations of the seasonal variations in parameters $\tau(0.50\ \mu m)$ and α measured at the various Arctic and Antarctic sites, it seems useful for the reader to give a measure of the experimental errors and variability features associated with the aerosol optical characteristics varying as a function of aerosol origin and their chemical composition evolutionary patterns:

(i) the mean experimental error of AOT measured with the most sophisticated sun-photometers leads to an uncertainty of ~0.01 in the visible and near-IR, mainly due to calibration errors (Eck et al., 1999);

356 (ii) the relative errors of exponent α determined in terms of Ångström's (1964) formula is about
357 twice the relative error of AOT (Gobbi et al., 2007), therefore leading to obtain at polar sites
358 relative errors close to 30% and, hence, absolute errors of ~0.50 (Mazzola et al., 2012); and
359 (iii) the spread of α arising from the natural variability of Arctic and Antarctic aerosol types has
360 been estimated by Stone (2002), Tomasi et al. (2007) and Treffeisen et al. (2007) to yield average
361 uncertainties of ± 0.4 for Arctic summer background aerosols, ± 0.6 for Arctic aerosols including
362 particular cases (like Asian dust and boreal smoke particles), and ± 0.5 for austral summer
363 background aerosol observed at Antarctic sites.
364
365 *2.1.1. Measurements in the Arctic*
366 In order to define the seasonal variations in polar aerosol optical characteristics, sun-photometer
367 measurements of $\tau(\lambda)$ conducted at various visible and near-infrared wavelengths can be
368 conveniently examined to evaluate the exponent α in terms of Eq. (2). Such measurements have
369 been carried out at various Arctic and Antarctic sites during the past decades, providing useful
370 information on polar aerosol optical and microphysical features. In fact, $\tau(\lambda)$ gives a measure of the
371 overall aerosol extinction along the vertical atmospheric path, while α depends on the combination
372 of the different extinction effects produced by fine and accumulation/coarse mode particles. Values
373 of α higher than 1.3 are usually observed in air masses where Aitken nuclei and very fine particles
374 (having radii r < ~0.12 μm) optically predominate, while relatively low values of α < 1.0 are
375 observed when accumulation (over the $0.12 \leq r \leq 1.25$ μm range) and coarse (over the $r > 1.25$ μm
376 range) mode particles produce stronger extinction effects. The vertical profile of the aerosol volume
377 backscattering coefficient can be determined by means of lidar measurements, allowing the
378 classification of aerosol layers in the troposphere and lower stratosphere.
379 Direct solar radiation measurements have been regularly conducted for cloud-free sky conditions at
380 numerous polar sites over the past decades, using multi-spectral sun-photometers of different

381 design. Tables 1 and 2 list the 12 Arctic sites and 9 Antarctic sites, whose data were employed in
382 this study together with their geographical coordinates, measurement periods, the peak-wavelengths
383 of the spectral channels used to measure AOT and determine the best-fit value of α, and the main
384 references where the technical characteristics of the instruments are detailed. The geographical
385 location of these sites are separately indicated in Fig. 2 for Arctic and Antarctic regions.
386 The individual measurements of the spectral values of $\tau(\lambda)$ and of the exponent α obtained from the
387 analysis of the field data recorded for cloud-free sky conditions were then averaged to yield daily
388 means. Since the present analysis is devoted to tropospheric aerosols, the sun-photometer
389 measurements conducted in the presence of stratospheric layers of volcanic particles were removed
390 for the following sites and intervals at: (a) the Arctic sites, in May 2006 (Soufrière Hills eruption),
391 October 2006 (Tavurvur eruption) (Stone et al., 2014), from mid-August to late September 2008
392 (Kasatochi eruption) (Hoffmann et al., 2010), from early July to early October 2009 (Sarychev
393 eruption) (O'Neill et al., 2012), and in April 2010 (Eyjafjallajokull eruption), as well as the sun-
394 photometer data collected at Barrow during the periods that followed both the Okmok eruption in
395 July 2008, and the Mt. Redoubt eruption in March 2009 (Tomasi et al., 2012); and (b) the Antarctic
396 sites, for all data affected by volcanic features comparable to those of Mt. Pinatubo observed from
397 late spring 1992 to late autumn 1994 (Stone et al., 1993; Stone, 2002). Actually, the Stratospheric
398 Aerosol and Gas Experiment (SAGE II) observations made since 2000 over Antarctica did not
399 provide evidence of appreciable extinction features produced by volcanic particle layers at
400 stratospheric altitudes (Thomason and Peter, 2006; Thomason et al., 2008), as also confirmed by the
401 analysis of sun-photometer measurements conducted at Mirny, Neumayer, Mario Zucchelli and
402 South Pole from 2000 to 2010 (Tomasi et al., 2012).
403 The remaining daily mean "tropospheric" data collected at each site were then subdivided into
404 monthly sub-sets consisting of data measured in different years, for which the multi-year monthly
405 mean values of $\tau(0.50\ \mu m)$ and α were determined. Relative frequency histograms (hereinafter
406 referred to as RFHs) were defined separately using the daily mean values of $\tau(0.50\ \mu m)$ and α

407 collected at Arctic sites during the following seasons: (i) winter-spring, from December to May,
408 when Arctic haze events were most frequent, and (ii) the summer-autumn, from June to October, to
409 characterize background aerosols in summer. For the Antarctic sites, RFHs were determined for
410 austral summer (from late November to February), to define the mean optical characteristics of
411 background aerosols.
412
413 *2.1.1.1. Measurements in Northern Alaska*
414 Two multi-year sets of sun-photometer measurements from Barrow, located on the Arctic Ocean
415 coast, were analysed in the present study: (a) the first series, acquired with the Carter Scott sun-
416 photometer, was conducted from March 2000 to September 2012 by GMD/NOAA (see Table 1)
417 and consisted of spectral $\tau(\lambda)$ measurements, taken every minute on apparently cloud-free days and
418 then cloud-screened by applying the GMD/NOAA selection procedure (for $\alpha(0.412\ \mu m/0.675\ \mu m)$
419 < 0.38); and (b) the second series was AERONET data collected from March 2002 to September
420 2013 (see Table 1). The results are shown in Fig. 3 for the GMD/NOAA and AERONET
421 measurements, where the data coverage is 94% and 78% of the overall 14-year period (March 2000
422 to September 2013), respectively. The GMD/NOAA monthly mean values of $\tau(0.50\ \mu m)$ increase
423 from about 0.07 in February to more than 0.12 in April and May, and then gradually decrease to
424 less than 0.10 in June and July, and to around 0.05 in October, with (grey toned) standard deviations
425 σ_τ > 0.05 from April to July, and < ~ 0.03 in the other months. Similar results were obtained for the
426 AERONET measurements, which exhibited monthly mean values of $\tau(0.50\ \mu m)$ that increased from
427 about 0.12 in March to more than 0.16 in April, and then decreased to 0.10 in June and August and
428 0.05 in September and October, with σ_τ > 0.05 from April to August, and < ~ 0.03 for the other
429 months. The monthly mean values of α determined from the GMD/NOAA and AERONET
430 measurements were rather stable from February to April, varying from 1.10 to 1.20, with a standard
431 deviation σ_α = 0.3 on average, followed by a convex cap from April to August, with values close to

1.50 from May to July, and increasing values from 1.30 to ~ 1.50 in August-October. Figure 3 also shows the RFHs of the daily mean values of $\tau(0.50\ \mu m)$ and α measured during the winter-spring and summer-autumn seasonal periods. The analytical curves drawn to represent the RFHs are normal curves and are normalized to yield unit (100%) integration over the measured sampling intervals of $\tau(0.50\ \mu m)$ and α shown in Fig. 3. The RFHs for both instruments were very similar, although showing appreciable discrepancies between the means and percentiles, which are in general lower than the corresponding standard deviations. The seasonal mean values of $\tau(0.50\ \mu m)$ were equal to 0.12 and 0.13 in winter-spring, for the GMD/NOAA and AERONET data, respectively, and close to 0.08 in summer-autumn for both data-sets. The RFHs also have long-tails towards high values for winter-spring data, and larger kurtosis in summer-autumn. The long-tail features could in part be ascribed to larger $\tau(0.50\ \mu m)$ values in April and May (ranging from 0.12 to 0.16) attributable to the frequent Arctic haze cases observed in spring but would also be, in part, due to the (asymmetrical) log-normal distribution that is arguably a better fit to the AOT RFHs in general (c.f. O'Neill et al., 2000).

The small discrepancies found between the time-patterns of the monthly mean values of $\tau(0.50\ \mu m)$ and α defined for both data-sets as well as those between the RFHs of both parameters might well be attributable to slight differences in the total observation periods of both sun-photometers and/or differences in GMD/NOAA and AERONET cloud-screening. The different seasonal features of $\tau(0.50\ \mu m)$ and α shown in Fig. 3 arise mainly from the origins of the aerosol load, associated with the transport of continental polluted air masses mainly from North America and Asia, in winter-spring (Hirdman et al., 2010). It can also be seen in Fig. 3 that the left-hand wings of the RFHs for α contain some values < 0.75: these are probably due to an optical predominance of coarse mode sea-salt aerosols and/or local blown dust. Similarly, a fraction of values with α < 1.20 are presumably related to Asian dust transport episodes (Di Pierro et al., 2011) that are most frequently

observed in March and April, and which are generally characterised by persistent extinction features typical of coarse mineral dust particles (Stone et al., 2007).

2.1.1.2. Measurements in Northern Canada (Nunavut)

The results derived from the AERONET/AEROCAN measurements conducted at Resolute Bay and Eureka-0PAL, and those carried out by GMD/NOAA at Alert (Canada) (see Table 1) over the past decade are shown in Fig. 4, as obtained for air masses containing aerosols mainly transported from the North American and Arctic Ocean areas (Hirdman et al., 2010) over these three Canadian sites. The monthly mean values of $\tau(0.50\ \mu m)$ exhibit: (i) rather high values related to Arctic haze in March-April, varying between 0.10 and 0.15, and (ii) relatively low values in the subsequent months, decreasing to around 0.05 in September at all the three sites. The month-to-month differences, varying on average from 0.05 at Resolute Bay and Alert in March-June to 0.01 at Alert in September, are similar to or smaller than the monthly mean values of σ_τ. The winter-spring RFHs exhibit higher mean values of $\tau(0.50\ \mu m)$, ranging from 0.09 to 0.12, and broader right-hand wings compared to the summer-autumn period, where the RFHs are narrower, giving seasonal mean values varying from 0.06 to no more than 0.08.

Relatively small differences were found between the monthly mean values of α in winter-spring and summer-autumn, with: (i) stable values close to 1.50 in March-June at Resolute Bay, gradually decreasing to 1.0 in July-September; and (ii) values increasing from 1.0 to 1.5 in March-June at Eureka and Alert, and remaining close to 1.50 from July to September (with $\sigma_\alpha < \sim 0.3$). The monthly mean values of α determined at Resolute Bay and Eureka-0PAL are appreciably higher than those measured at Barrow, presumably as a result of the weaker extinction produced by coarse sea-salt particles and/or local dust, and weaker contributions of Asian dust in the spring months. Figure 4 shows that the seasonal RFHs of daily mean α values do not exhibit symmetrical shapes: (i) the winter-spring RFHs are rather wide, showing long-tailed left-hand wings and mean values

481 varying from 1.29 (at Alert) to 1.52 (at Resolute Bay), and (ii) the summer-autumn RFHs are
482 characterised by mean values varying from 1.46 (Alert) to 1.64 (Eureka). Only moderate, relative
483 increases in the coarse particle content occurred at Resolute Bay from winter-spring to summer,
484 while greater winter-spring to summer-autumn variations were measured at Eureka and Alert
485 presumably due to fine particle smoke transported from North American boreal forest fires (Stohl et
486 al., 2006). Finally, it is worth noting that a few cases were found with $\alpha < 0.40$ at Alert, despite the
487 $\alpha < 0.38$ cloud-screening rejection criterion. They were presumably associated with prevailing
488 extinction by coarse mode sea-salt aerosols transported from the Arctic Ocean, especially in the
489 spring months.
490
491 *2.1.1.3. Measurements in Greenland*
492 Figure 5 shows the results derived from the multi-year sets of sun-photometer measurements
493 conducted at: (i) the Thule AERONET site, in the north-western corner of Greenland; (ii) the
494 Summit PMOD/WRC site, located in the middle of the Central Greenland ice sheet; and (iii)
495 Ittoqqortoormiit AERONET site, on the eastern coast of Greenland (see Table 1 for details on these
496 sites).
497 The monthly mean $\tau(0.50\ \mu m)$ values at Thule decreased slowly from about 0.10 in April-May to
498 around 0.05 in June-September, with $\sigma_\tau \sim 0.03$, while α was rather stable with monthly mean values
499 ranging from 1.40 to 1.50 from March to September, with $\sigma_\alpha \sim 0.3$. The winter-spring $\tau(0.50\ \mu m)$
500 RFH is characterized by a mean value of 0.093 and an asymmetric shape whose long-tailed, right-
501 hand wing is influenced by the frequent occurrences of Arctic haze episodes. The summer-autumn
502 RFH for $\tau(0.50\ \mu m)$ was more symmetric, with mean and median values equal to 0.058 and 0.049,
503 respectively, and values of the 25th and 75th percentiles relatively close to the median value, as can
504 be seen in Fig. 5. Very similar shapes of both seasonal RFHs for α were obtained, with mean values
505 of 1.38 in winter-spring and 1.41 in summer-autumn, and similar values of the main percentiles

506 from winter-spring to summer-autumn, indicating no relevant seasonal changes in the aerosol size-
507 distribution.
508 Rather stable monthly mean values of $\tau(0.50\ \mu m)$ were obtained at the high-altitude Summit station,
509 equal to 0.05 ± 0.03 from March to August, and about 0.03 ± 0.01 in September and October. Both
510 seasonal RFHs of the daily mean $\tau(0.50\ \mu m)$ values assumed very similar shapes, with mean values
511 close to 0.05, and values of the main percentiles differing by no more than 0.01 from season to the
512 other. Greater differences were determined between the two seasonal RFHs of α, with mean values
513 equal to 1.27 in winter-spring and 1.52 in summer-autumn, and the main percentiles differing by no
514 more than 0.3. These aerosol optical characteristics indicate that Summit is representative of the
515 Arctic free troposphere, influenced mainly by particulate transport from North America and Europe,
516 and only weakly by Siberian aerosols (Hirdman et al., 2010).
517 The monthly mean values of $\tau(0.50\ \mu m)$ at Ittoqqortoormiit showed similar seasonal variations to
518 those at Thule, gradually decreasing from ~ 0.08 in March to less than 0.04 in September-October,
519 with $\sigma_\tau = 0.05$ in spring, gradually decreasing in summer until reaching values of ~ 0.01 in autumn.
520 The monthly mean α values increase from ~ 1.00 in March to ~ 1.50 in summer, and slowly
521 decrease in September and October, varying around 1.40, with $\sigma_\alpha = 0.2$ in March and close to 0.3 in
522 the other months. The RFHs for $\tau(0.50\ \mu m)$ did not vary largely from winter-spring to summer-
523 autumn. The seasonal mean values were equal to 0.068 in winter-spring and 0.052 in summer-
524 autumn, which were not considerably different from the median values in both seasons. They give a
525 measure of the appreciable decrease in $\tau(0.50\ \mu m)$ observed from winter-spring to summer-autumn.
526 The seasonal RFHs for α are more similar to those obtained at Summit than those of Thule. In fact,
527 the winter-spring mean value of α was equal to 1.28, and the summer-autumn value equal to 1.45.
528 These results suggest that the atmospheric content of fine mode particles increases considerably
529 from winter to summer at Ittoqqortoormiit. Such variations are probably associated with the marked
530 extinction effects produced by maritime accumulation/coarse mode particles in winter-spring and

531 the predominant aerosol extinction effects produced by background continental particles mainly
532 transported in summer-autumn from Europe and North America and containing in general
533 significant loads of both anthropogenic and BFF particles.
534 The seasonal changes shown in Fig. 5 at the three Greenland sites can be mainly attributed to the
535 variations in aerosol transport processes from anthropogenic/polluted regions or remote oceanic
536 mid-latitude areas, and only rarely to Asian dust. Actually, the transport processes of anthropogenic
537 soot aerosols are known to appreciably enhance $\tau(\lambda)$, yielding rather high values of α in general
538 (Tomasi et al., 2007; Stone et al., 2008). This may also occur in free-tropospheric layers, as
539 observed during airborne measurements conducted at mid-altitudes over the Arctic Ocean (Stone et
540 al., 2010).
541
542 *2.1.1.4. Measurements in Spitsbergen (Svalbard)*
543 The results obtained at Ny-Ålesund, Barentsburg and Hornsund (Svalbard, Norway) from four
544 different series of measurements are shown in Fig. 6, as conducted by AWI (Bremerhaven,
545 Germany) and NILU (Kjeller, Norway) at Ny-Ålesund, IAO-SB-RAS (Tomsk, Russia) at
546 Barentsburg, and the Institute of Geophysics (Warsaw University, PAS, Poland) in cooperation with
547 NASA/GSFC (USA) at Hornsund (see Table 1).
548 The AWI monthly mean values of $\tau(0.50\ \mu m)$ varied from 0.07 to 0.09 in winter-spring, and
549 considerably decreased in summer-autumn from about 0.05 in June to 0.02 in October, with σ_τ =
550 0.03 on average. The NILU monthly mean values of $\tau(0.50\ \mu m)$ were equal to ~ 0.10 from March to
551 May, and varied from 0.06 in June-July to less than 0.05 in August-September, with σ_τ equal to
552 0.04 in spring and 0.03 in summer and autumn. The comparison between the AWI and NILU results
553 shows good agreement, although the NILU values were occasionally higher than those for AWI by
554 no more than 10% on average in spring, such discrepancies probably arising from the slightly
555 dissimilar measurement periods of 14 and 8 years, respectively. The AWI monthly mean values of
556 α increased from less than 1.30 in March to 1.50 in May, and slowly decreased in summer-autumn

until reaching a value < 1.20 in September and becoming nearly equal to 1.50 in October, with σ_α = 0.30 on average, while the NILU values increased slowly from 1.20 in March to 1.50 in June, and slowly decreased to ~ 1.30 in September, with σ_α = 0.20 in all months. These discrepancies of no more than 15% are in general smaller than the monthly values of σ_α. Therefore, it is not surprising that the RFHs found for the daily mean $\tau(0.50\ \mu m)$ values derived from the AWI and NILU data-sets differ considerably from one season to another: (i) the AWI and NILU winter-spring mean values were equal to 0.082 and 0.089, respectively, with the main percentiles differing by no more than 0.007; and (ii) the AWI and NILU summer-autumn mean values of $\tau(0.50\ \mu m)$ were equal to 0.052 and 0.059, respectively, with σ_τ = 0.04 on average, and having differences between the main percentiles no greater than 0.02. The AWI seasonal RFHs of α yielded mean values of 1.32 in winter-spring and 1.28 in summer-autumn, while NILU RFHs gave mean values of 1.35 in winter-spring and 1.38 in summer-autumn. Comparable values of the three main percentiles of the AWI and NILU RFHs were also obtained, differing by less than 0.1 in winter-spring and less than 0.2 in summer-autumn. Therefore, the analysis of the AWI and NILU RFHs of α showed: (i) more dispersed features of α in winter-spring, presumably due to the larger variability of fine and coarse particle concentrations during the frequent Arctic haze episodes, and (ii) values of α mainly varying from 1.00 to 1.60 in summer-autumn, due to the large variability of the fine particle mode atmospheric content (mainly related to BFFs smoke particle transport) with respect to that of accumulation/coarse mode particles (mainly of oceanic origin).

The data-sets of $\tau(0.50\ \mu m)$ and α derived from the Barentsburg IAO measurements consisted of a number of daily measurements smaller than 10% of that given by the AWI and NILU Ny-Ålesund measurements. The monthly mean $\tau(0.50\ \mu m)$ values varied from 0.07 to 0.10, with σ_τ = 0.02 on average, and those of α increased from ~ 0.90 to 1.40 during summer, with σ_α = 0.2. Therefore, these measurements differ only slightly from those measured at Ny-Ålesund over longer multi-year periods. The RFHs of the daily mean values of $\tau(0.50\ \mu m)$ and α were prepared only for the

582 summer-autumn period, and were found to have a seasonal mean value of $\tau(0.50\ \mu m)$ = 0.078, with
583 the main percentiles differing by less than 0.02 from the mean. These values are appreciably higher
584 than those determined at Ny-Ålesund from the AWI and NILU data-sets. A summer-autumn mean
585 value of α = 1.29 was obtained, with only slightly differing values of the main percentiles, and a
586 considerably narrower RFH curve than those from the AWI and NILU data-sets measured at Ny-
587 Ålesund.
588 The Ny-Ålesund results can also be compared in Fig. 6 with the AERONET measurements
589 recorded at Hornsund. The Hornsund results are in close agreement with those of Ny-Ålesund, since
590 the Hornsund monthly mean values of $\tau(0.50\ \mu m)$ varied from 0.10 to no more than 0.12 in winter-
591 spring, with σ_τ = 0.04 on average, and from 0.06 to 0.08 in summer autumn, with σ_τ < 0.03. The
592 monthly mean values of α were rather stable at Hornsund, mainly ranging from 1.20 to 1.50, and
593 showing small differences with respect to the AWI and NILU results. The Hornsund RFHs of
594 $\tau(0.50\ \mu m)$ show that the winter-spring daily mean values were on average higher than those
595 obtained in summer-autumn, by more than 0.03, with differences between the main seasonal
596 percentiles no higher than 0.04. Small variations in α < 0.07 were observed from one season to the
597 other between the seasonal mean values and the main percentiles. The long-tailed left-hand wings
598 of the RFHs of α determined during both seasons suggest that important extinction effects were
599 presumably produced by the sea-salt accumulation/coarse mode particles during both seasons.
600 The seasonal variations in $\tau(0.50\ \mu m)$ shown in Fig. 6 are mainly due to the different aerosol
601 extinction features produced over the Svalbard region by Arctic haze, especially in spring, and by
602 background aerosol in summer. They are in part associated with the significant seasonal mean
603 decrease in the mean concentration of sulphate particles measured within the atmospheric ground-
604 layer. For instance, on the basis of long-range routine measurements of particulate chemical
605 composition conducted at the Zeppelin station (78° 58' N, 11° 53' E, 474 m a.m.s.l.), near Ny-
606 Ålesund (Svalbard), Ström et al. (2003) estimated that the mean mass concentration of nss sulphate

607 ions decreases on average with season, changing from about 3×10^{-1} μg m^{-3} in March-April (for
608 frequent Arctic haze episodes) to around 5×10^{-2} μg m^{-3} in late summer (for background aerosol
609 conditions). These features arise from the fact that the frequent Arctic haze episodes observed in
610 winter and spring over the Svalbard region are mainly due to aerosol transport from the Eurasian
611 area, rather than from North America or East Asia (Hirdman et al., 2010). The region north of 70
612 °N is isolated in summer from the mid-latitude aerosol sources, as demonstrated by Stohl et al.
613 (2006), who analysed aerosol transport patterns into the Arctic. BFF smoke particles are
614 episodically transported over the Svalbard region in summer, from the Siberian region and
615 sometimes from North America (Tomasi et al., 2007; Stone et al., 2008). For instance, huge
616 emissions from BFFs in North America reached Svalbard (Stohl et al., 2006) in July 2004, while
617 agricultural fires in Eastern Europe caused very strong pollution levels in the Arctic during spring
618 2006 (Stohl et al., 2007; Lund Myhre et al., 2007).
619
620 *2.1.1.5. Measurements in Scandinavian and Siberian regions*
621 Figure 7 shows the time-patterns of the monthly mean values of $\tau(0.50\ \mu m)$ and α and the winter-
622 spring and summer-autumn RFHs of both parameters, derived from the sets of FMI/PFR and
623 AERONET sun-photometer measurements carried out at Sodankylä (Northern Finland), and the set
624 of AERONET measurements conducted at Tiksi in Northern-Central Siberia (Russia) (see Table 1).
625 The FMI/PFR monthly mean values of $\tau(0.50\ \mu m)$ slowly increased from ~ 0.05 in February to 0.08
626 in May, remained quite stable from June to August, then slowly decreased to 0.05 in September-
627 October, with comparable values of σ_τ ranging mainly from 0.04 to ± 0.06, without showing clear
628 variations from winter-spring to summer-autumn. The monthly mean values of α increased from
629 about 1.10 in February to over 1.50 in July, and then gradually decreased to 0.75 in November.
630 Different time-patterns of the monthly mean values of $\tau(0.50\ \mu m)$ and α were obtained from the
631 AERONET measurements conducted at Sodankylä over a shorter 7-year period, including only

about a third of the daily PFR observations, and giving monthly mean values of $\tau(0.50\ \mu m)$ varying from 0.05 to 0.09 in winter-spring, and from 0.06 to 0.11 in summer, which then decreased to less than 0.04 in September-October. The monthly mean values of α varied from 1.20 to 1.40 in winter-spring, increasing to more than 1.70 in July and decreasing to nearly 1.00 in October.

To provide a more complete picture of the atmospheric turbidity features over Northern Scandinavia, the time-patterns of the PFR and AERONET monthly mean values of $\tau(0.50\ \mu m)$ and α obtained at Sodankylä are compared in Fig. 7 with those determined by Toledano et al. (2012) analysing the $\tau(0.50\ \mu m)$ and α data-sets collected at: (i) Kiruna (67° 51' N, 20° 13' E, 580 m a.m.s.l.) in Northern Sweden (270 km WNW from Sodankylä) using the GAW-PFR sun-photometer of the Swedish Meteorological and Hydrological Institute (SMHI) from 2007 to 2010 by, and (ii) Andenes/ALOMAR (69° 18' N, 16° 01' E, 380 m a.m.s.l.) in Northern Norway, using the AERONET/RIMA Cimel CE-318 sun-photometer from 2002 to 2007. The Kiruna PFR results are compared in Fig. 7 with those recorded at Sodankylä. The Kiruna monthly mean values of $\tau(0.50\ \mu m)$ were rather stable over the whole measurement period, with σ_τ varying from 0.01 to 0.04, while the monthly mean values of α increased from 1.10 in February to nearly 1.60 in July, and then decreased gradually to ~ 1.00 in August and 1.20 in October, with values of σ_α varying from 0.10 to 0.25. Thus, the Kiruna monthly mean values of $\tau(0.50\ \mu m)$ closely agree with those measured at Sodankylä and only exhibit small differences between the August-October monthly mean values of α.

A similar comparison is also made in Fig. 7 between the AERONET/FMI results obtained at Sodankylä and the ALOMAR results derived from the AERONET/RIMA Cimel CE-318 sun-photometer measurements at Andenes, from 2002 to 2007. The ALOMAR monthly mean values of $\tau(0.50\ \mu m)$ increased from about 0.04 in February to 0.13 in May, and then slowly decreased to around 0.11 in September-October, having values of σ_τ mainly varying from 0.04 to 0.06. Therefore, the ALOMAR evaluations of $\tau(0.50\ \mu m)$ were in general considerably higher than those

657 measured at Sodankylä, with differences comparable to the standard deviations. The ALOMAR
658 monthly mean values of α varied at Andenes from about 0.85 to 1.05 in February-May, increased in
659 the following months to ~ 1.30, and subsequently decreased in late summer and autumn to reach a
660 value close to 1.00 in October, with σ_α varying mainly from 0.20 in winter-spring to 0.40 in
661 summer-autumn. These findings indicate that the ALOMAR monthly mean values of α were
662 considerably higher than the AERONET evaluations obtained at Sodankylä, by about 15% on
663 average, presumably because of the more pronounced extinction effects by maritime particles.
664 The time-patterns of the monthly mean values of $\tau(0.50\ \mu m)$ and α shown in Fig. 7, as obtained by
665 us at Sodankylä, and at Kiruna and Andenes by Toledano et al. (2012) differ appreciably from those
666 typically observed at the other Arctic sites located at higher latitudes and shown in Figs. 3-6. The
667 reason for such differences is that the air masses reaching Northern Scandinavia during the year
668 originate from the Eurasian continent and mid-latitude Atlantic Ocean in 56% of cases, and from
669 the Arctic Basin and Northern Atlantic Ocean in the remaining 44% (Aaltonen et al., 2006). Due to
670 the alternation of polluted air masses from Eurasia with sea-salt particles from ocean areas, the
671 monthly mean values of $\tau(\lambda)$ were rather stable over the entire year, while the monthly mean values
672 of α were higher in early summer, when the Arctic Basin was the principal aerosol source. Because
673 of the efficient transport processes taking place during the year from continental polluted or ocean
674 areas, the FMI/PFR and AERONET Sodankylä RFHs of $\tau(0.50\ \mu m)$ did not exhibit significant
675 differences between the seasonal mean values and the main percentiles defined in winter-spring and
676 summer-autumn. These had monthly mean values of around 0.08 and 0.07 in winter-spring,
677 respectively, with the main percentiles differing by no more than 0.01, and summer-autumn
678 monthly mean values close to 0.07 on average, with differences of about 0.01 between the main
679 percentiles. The FMI/PFR and AERONET Sodankylä monthly mean values of α decreased by 0.10-
680 0.20 on average, from winter-spring to summer-autumn. Clearer discrepancies over both seasonal
681 periods were found, with FMI mean values of about 1.32 and 1.52 in winter-spring and summer-

682 autumn, respectively, and AERONET mean values equal to 1.23 and 1.44 in the same two seasons,
683 providing similar values of the main seasonal percentiles.
684 A comparison between the winter-spring and summer-autumn estimates of $\tau(0.50\ \mu m)$ and α was
685 not made at Tiksi, since AERONET sun-photometer measurements have been routinely conducted
686 at this remote Siberian site only over the May-October period. The monthly mean values of $\tau(0.50$
687 $\mu m)$ exhibit a clear increase from ~ 0.13 in May to 0.16 in July, with large average values of $\sigma_\tau =$
688 0.14, followed by a marked decrease in the subsequent months to about 0.05 ± 0.03 in October.
689 Such large variations in $\tau(0.50\ \mu m)$ were associated with a slow decrease in the monthly mean
690 values of α from 1.9 in May to ~ 1.5 in September, for which $\sigma_\alpha \leq 0.2$. The rather high values of
691 $\tau(0.50\ \mu m)$ and α determined in summer were probably due to the frequent BFF smoke transport
692 episodes from the inner regions of Siberia. In fact, the summer-autumn RFH of $\tau(0.50\ \mu m)$ exhibits
693 a mean value close to 0.09 and a value of the 75th percentile equal to 0.12, which are both
694 appreciably higher than those measured at Sodankylä in summer. The RFH of α yields a mean
695 value of 1.57, and shows a long-tailed left-hand wing with 25th percentile of 1.39, and a long-tailed
696 right-hand wing with 75th percentile of 1.74. This rather high value is probably associated with
697 small fine particles generated by combustion processes, which dominate extinction effects.
698 In summary, the Arctic results provide evidence of the seasonality of $\tau(0.50\ \mu m)$ and α. A scatter
699 plot of the median values of α versus those of $\tau(0.50\ \mu m)$ is shown in Fig. 8a, separately for the
700 winter-spring and summer-autumn seasonal periods. Figure 8a shows that the median values of α
701 vary from 1.10 to 1.70 over the whole year, with: (i) winter-spring median values of $\tau(0.50\ \mu m)$
702 ranging from 1.20 to 1.50 over the 0.04-0.12 range, and (ii) summer-autumn median $\tau(0.50\ \mu m)$
703 values all smaller than 0.08 and mainly ranging from 1.30 to 1.70. These features suggest that
704 appreciable differences characterize aerosol extinction in: (a) winter-spring, when the median
705 values of $\tau(0.50\ \mu m)$ vary greatly from one Arctic site to another. This results from their
706 dependency on the importance of particulate transport from the most densely populated mid-latitude

707 regions toward the Arctic, which is particularly strong in late winter and early spring; and (b)
708 summer, when the background aerosol composition varies from one site to another, as a result of
709 different extinction characteristics of fine and coarse mode particles transported from remote
710 regions.
711
712 *2.1.2. Measurements in Antarctica*
713 Ground-based sun-photometer measurements of aerosol optical parameters have been conducted in
714 Antarctica during the short austral summer period. In the present study, nine multi-year sets of
715 measurements made since 2000 have been analysed (see Table 2), collected at six coastal sites
716 (Marambio, Neumayer, Novolazarevskaya, Mirny, Syowa, and Mario Zucchelli), a mid-altitude
717 station (Troll) and two high-altitude sites (Dome Concordia and South Pole).
718
719 *2.1.2.1. Measurements at coastal and mid-altitude sites*
720 The results obtained from the sun-photometer measurements carried out at Marambio, Neumayer
721 and Troll are presented in Fig. 9. The Marambio measurements were conducted from September to
722 April, and provided monthly mean values of $\tau(0.50\ \mu m)$ varying from ~ 0.03 in January to 0.06 in
723 March (with σ_τ varying from 0.02 to 0.04) and α ranging from 0.50 in March to 1.50 in November-
724 January (with σ_α = 0.50 on average). The austral summer RFHs exhibit regular features with mean
725 values of $\tau(0.50\ \mu m)$ = 0.038 and α = 1.20, probably due to sea-salt particles, which dominate
726 extinction. The Neumayer measurements were conducted over the September-April period, showing
727 rather stable time-patterns of the monthly mean values of $\tau(0.50\ \mu m)$, ranging from 0.04 to 0.06
728 (with σ_τ = 0.03 on average) and associated with very stable values of α varying from 0.50 to 1.00
729 (with σ_α = 0.3 on average), which indicate that aerosols are mostly of oceanic origin. The RFHs of
730 both optical parameters are similar to those determined at Marambio, showing mean values of
731 $\tau(0.50\ \mu m)$ = 0.041 and α = 0.82, confirming that these stable extinction features are mainly

732 produced by sea-salt particles. The time-patterns of the monthly mean values of $\tau(0.50\ \mu m)$ and α
733 measured at Troll, about 235 km from the Atlantic Ocean coast in the Queen Maud Land, were also
734 quite stable from September to April, yielding values of $\tau(0.50\ \mu m)$ varying from ~ 0.02 to 0.03
735 (with $\sigma_\tau < 0.005$), and values of α slowly increasing from 1.25 in September to ~ 1.50 in January,
736 and then decreasing to 1.00 in April. The RFH of $\tau(0.50\ \mu m)$ exhibits nearly symmetrical features
737 with little dispersion, with a mean value of 0.023, and 25th and 75th percentiles equal to 0.019 and
738 0.026, respectively, while the RFH of α was also quite symmetrical over the 0.60-2.10 range, with a
739 mean value of 1.42 and 25th and 75th percentiles differing by less than 0.4 one from the other. These
740 estimates of $\tau(0.50\ \mu m)$ and α differ appreciably from those obtained at Marambio and Neumayer,
741 showing that the aerosol extinction features are only in part produced by maritime aerosols at this
742 mid-altitude site, and in part by fine mode particles, such as nss sulphate aerosols.
743 Figure 10 shows the results obtained from the measurements conducted at Novolazarevskaya
744 (Queen Maud Land) and Mirny (on the Davis Sea coast), using various sun-photometer models
745 during different years, as reported in Table 2. The monthly mean values of $\tau(0.50\ \mu m)$ obtained at
746 Novolazarevskaya were very close to 0.02 ± 0.01 over the whole period, while α varied from about
747 0.80 in November to 1.10 in January, with σ_α equal to 0.10 in the first two months and 0.50 in
748 January and February. The RFH of $\tau(0.50\ \mu m)$ exhibited a leptokurtic curve, with mean value close
749 to 0.02, while a more dispersed distribution curve was shown by the RFH of α, with the mean value
750 close to unity, and 25th and 75th percentiles differing by less than 0.20 from it. The monthly mean
751 values of $\tau(0.50\ \mu m)$ determined at Mirny varied from 0.02 to 0.03 (with $\sigma_\tau = 0.01$), and those of α
752 from 1.50 to 2.00 in September-January, which then slowly decreased to ~ 1.20 in April. The RFH
753 of $\tau(0.50\ \mu m)$ exhibited features which had a nearly symmetrical peak, with a mean value of 0.025,
754 only slightly differing from that obtained at Novolazarevskaya, while the RFH of α was found to be
755 dispersed and platykurtic, having a mean value of 1.60, and 25th and 75th percentiles differing by
756 more than 0.40 from the mean value. Therefore, it can be concluded that the aerosol extinction

757 features shown in Fig. 10 are predominantly produced by sea-salt particles generated by winds over
758 the ocean, yielding values of α mainly ranging from 0.50 to 1.30.
759 The results derived from the measurements conducted at Syowa and Mario Zucchelli are shown in
760 Fig. 11, as obtained using various sun-photometer models over the different periods reported in
761 Table 2. The monthly mean values of $\tau(0.50\ \mu m)$ varied from less than 0.02 to ~ 0.04 over the
762 September-April period (with $\sigma_\tau < 0.03$), while the monthly mean values of α were also very stable,
763 and described a large maximum of around 1.30 in December, with minima of ~ 1.00 in September
764 and ~ 0.90 in April. The RFH of $\tau(0.50\ \mu m)$ assumed a mesokurtic shape, skewed to the right, with
765 the mean value close to 0.02, while the RFH of α exhibited mesokurtic and symmetrical features,
766 arising from sea-salt particles, which caused the predominant extinction. The ISAC-CNR
767 measurements conducted at Mario Zucchelli provided the time-patterns of the monthly mean values
768 of $\tau(0.50\ \mu m)$ shown in Fig. 11, which were close to 0.02 in November and December (with $\sigma_\tau =$
769 0.01) and then increased to ~ 0.04 in January and February (with $\sigma_\tau = 0.02$), while the monthly
770 mean values of α were stable and very close to 1.00 from November to January, and equal to ~ 0.80
771 in February (with σ_α not exceeding 0.30). The RFHs of $\tau(0.50\ \mu m)$ and α were found to exhibit
772 more dispersed features than those determined at Syowa and both Russian stations, giving mean
773 values equal to 0.04 and 0.96, respectively. However, they clearly indicate that aerosol extinction is
774 mainly due to sea-salt particles at this coastal site, yielding values of α ranging in general from 0.50
775 to 1.30.
776
777 *2.1.2.2. Measurements at the high-altitude sites on the Antarctic Plateau*
778 The results obtained analysing the sun-photometer measurements conducted since 2000 at the
779 Dome Concordia and South Pole high-altitude sites are shown in Fig. 12. The measurements were
780 conducted by five groups using different instruments over distinct periods, as reported in Table 2.
781 Due to the background transport of aerosols from very remote sources and the predominant role of

782 subsidence processes on the aerosol load, the time-patterns of the monthly mean values of $\tau(0.50\ \mu m)$
783 determined at Dome Concordia with different sun-photometers were found to be very stable,
784 mainly ranging from 0.02 to 0.04 (with σ_τ evaluated to be $\leq$ 0.01) in September-April. The
785 corresponding monthly mean values of α mainly varied from 1.00 to 2.00, with σ_α = 0.20 on
786 average. The RFH of $\tau(0.50\ \mu m)$ exhibited a well-marked leptokurtic shape, with a mean value
787 close to 0.02, while the RFH of α showed dispersed features over the 0.5-2.2 range, with a mean
788 value close to 1.40, and 25th and 75th percentiles equal to about 1.0 and 1.80, respectively.
789 The South Pole multi-year measurements conducted by GMD/NOAA at the Amundsen-Scott base
790 were found to provide very stable time-patterns of the monthly mean values of $\tau(0.50\ \mu m)$, mainly
791 ranging from September to March from ~ 0.02 and 0.04 (with σ_τ = 0.01 on average), and monthly
792 mean values of α varying from 1.00 to 2.00, with the highest values in October and November
793 (with σ_α = 0.10 on average). The AERONET monthly mean values of $\tau(0.50\ \mu m)$ were found to
794 increase from about 0.01 to 0.02 over the November-February period, with σ_τ = 0.01 on average,
795 the uncertainty of these measurements being primarily due to both calibration (estimated by Eck et
796 al. (1999) to be of ~ 0.01 in the visible), and forward scattered light entering the instrument (Sinyuk
797 et al., 2012). Very stable monthly mean values of α ~ 1.00 were correspondingly found, with σ_α =
798 0.50 on average. Both RFHs of $\tau(0.50\ \mu m)$ derived from the GMD/NOAA and AERONET
799 measurements assumed very narrow and "peaked" curves, with mean values of around 0.02, which
800 appeared to be slightly skewed to the right. The corresponding RFHs of α presented dispersed
801 features over the 0.50-2.00 range, with mean values of 1.54 and 1.06. Although such clearly
802 dispersed results suggest the presence of an important fraction of large-size particles, it is important
803 to take into account that a predominant particulate mass fraction of around 66% was estimated to
804 consist of nss sulphates at South Pole, with lower concentrations of nitrates and sea-salt particles
805 (Arimoto et al., 2004; Tomasi et al.2012), mainly associated with the background transport of
806 aerosols from very remote sources and the strong effects exerted by subsidence processes. A few

807 cases showing values of $\alpha < 0.50$ were probably caused by consistent loads of diamond dust ice-
808 crystals within the lower planetary boundary layer (hereinafter referred to as PBL), due to wind
809 mobilization.
810 The covariance of the median values of $\tau(0.50\ \mu m)$ and α obtained at the nine Antarctic sun-
811 photometer stations is shown in Fig. 13a. There are two clusters: (i) the first at coastal sites, where
812 the median values of $\tau(0.50\ \mu m)$ were in general considerably higher (at least by a factor two) than
813 those found at the high-altitude Antarctic sites, and the median values of α are in general smaller
814 than 1.20, and (ii) the second cluster, with lower median values of $\tau(0.50\ \mu m)$ and median values of
815 $\alpha > 1.40$, for which aerosol extinction is predominantly due to sea-salt coarse particles. It is
816 interesting to note that lower median values of $\tau(0.50\ \mu m)$ associated with higher values of α were
817 observed at the coastal sites of Mirny and Marambio, probably because of aeolian fine particles,
818 which dominated extinction effects when compared to sea-salt particles. The median values of
819 $\tau(0.50\ \mu m)$ and α determined at the Troll mid-altitude station indicate that the extinction effects
820 exhibit intermediate features at this non-coastal site. This can probably be attributed in part to sea-
821 salt aerosol and in part to background nss sulphate aerosol transported over large distances, which
822 themselves contribute toward an appreciable enhancement in α. As can be seen in Fig. 13a, the
823 weak median values of $\tau(0.50\ \mu m)$ and relatively strong median values of α at Dome Concordia and
824 South Pole (the latter being partially obscured by the DMC-OPAR symbol) show that atmospheric
825 aerosol extinction is rather weak above the Antarctic Plateau and mainly produced by fine particles
826 consisting of nss sulphates. The lower extremes of the α error bars and the low α value of the
827 AERONET South Pole point are likely due to near-surface diamond dust layers that are observed on
828 windy, cloud-free days at these sites.
829
830 **3. Ship-borne measurements.**

831 A large number of ship-borne measurements of the main columnar aerosol radiative parameters $\tau(\lambda)$
832 and α were made over the Arctic and Antarctic oceanic regions during the past 10 years. The
833 cruises were conducted by research groups and institutions from different countries, using hand-
834 held Microtops II sun-photometers calibrated at the NASA/GSFC calibration facility. As can be
835 seen in Fig. 2, large areas of the polar oceans were studied during these cruises, yielding an
836 exhaustive picture of aerosol optical characteristics in these high-latitude remote regions. These
837 ship-borne sun-photometer measurements were conducted as a part of the activities promoted and
838 developed in the framework of the Maritime Aerosol Network (MAN), which is a component of the
839 AERONET network (see http://aeronet.gsfc.nasa.gov/new_web/maritime_aerosol_network.html).
840 The measurements of $\tau(\lambda)$ were carried out at visible and near-infrared wavelengths. Arctic Ocean
841 cruises are listed in Table 3, while those taken in the oceanic regions around Antarctica are listed in
842 Table 4. The hand-held Microtops II sun-photometers are equipped with five narrow-band
843 interference filters with peak-wavelengths of 0.340 (or 0.380), 0.440, 0.675, 0.870 and 0.936 μm for
844 most cruises, or 0.440, 0.500, 0.675, 0.870 and 0.936 μm in other cruises, as reported in Tables 3
845 and 4. The first four filters of each spectral set were used to measure the spectral values of $\tau(\lambda)$ and
846 determine the best-fit value of exponent α over the wavelength range from 0.440 to 0.870 μm,
847 while the measurements taken at 0.936 μm were combined with those made within the nearby
848 channel centred at 0.870 μm to evaluate precipitable water (Smirnov et al., 2009). Among the data-
849 sets available at the MAN website, we only selected measurements conducted since 2006 at
850 latitudes higher than 67° N in the Arctic and within ocean areas far by no more than 1000 km from
851 the Antarctic coasts. In addition, the measurement sets obtained by Tomasi et al. (2007) during the
852 RV Oceania cruises made in the summer months of 2003 and 2006 were included in the present
853 analysis.
854
855 *3.1. Aerosol measurements in the Arctic Ocean.*

856 Fourteen Arctic Ocean cruises were selected for this study, as summarized in Table 3. The data-set
857 collected during the cruise of RV Polarstern (Alfred Wegener Institute (AWI), Bremerhaven,
858 Germany) in August-September 2009 was not examined to evaluate the background tropospheric
859 aerosol extinction features, because these measurements were found to be strongly affected by the
860 extinction of stratospheric volcanic aerosols generated by the Sarychev eruption in July-October
861 2009. No evidence of Sarychev volcanic particle extinction at stratospheric levels was found in
862 CALIPSO (Cloud-Aerosol Lidar and Infrared Pathfinder Satellite Observations) data recorded over
863 the Beaufort Sea (O'Neill et al., 2012) during the CCGS Amundsen cruise of August 2009.
864 Therefore, this set of measurements was used to calculate the extinction effects associated in
865 August 2009 with the BFF smoke particles transported from the North-American forests over the
866 Arctic Ocean. In order to study the aerosol extinction features of the Arctic Ocean, the 14 Microtops
867 sun-photometer data-sets collected during the above-selected MAN cruises were subdivided into
868 three sub-sets pertaining to the following large-scale oceanic sectors: (a) Northern Greenland Sea
869 and Norwegian Sea (hereinafter referred to as GNS sector), between 20° W and 30° E longitudes;
870 (b) Barents Sea and West Siberian Sea (BWS sector), between 30° E and 130° E longitudes; and (c)
871 the North American Arctic Ocean (NAA sector), including the East Chukchi Sea, the Bering Strait,
872 the Beaufort Sea and the Amundsen Gulf, between 170° W and 110° W longitudes. No MAN
873 cruises were carried out in the East Siberian Sea and West Chukchi Sea sectors, at latitudes higher
874 than 67 °N and longitudes ranging from 130° E to 170 °W, as well as in the Canadian sector from
875 110 °W to 20° W longitudes, including the Baffin Bay, the Davis Straits and the Northern Atlantic
876 Ocean.
877 The same criteria as used for the ground-based stationary sun-photometer measurements taken at
878 the various Arctic sites were also adopted to examine the ship-borne measurements, including the
879 selection of data made to reject all the measurements affected by stratospheric volcanic particle
880 extinction. The daily mean values of $\tau(0.50\ \mu m)$ and α obtained from the data-sets collected within
881 each of the three oceanic sectors were subdivided into monthly sub-sets to determine the monthly

882 mean values of both parameters, and define their RFHs separately for the winter-spring (Arctic
883 haze) and summer-autumn (background aerosol) periods. The main purpose of the analysis was to
884 provide evidence of the seasonal characteristics of aerosol optical parameters in the Arctic Ocean
885 areas far from anthropogenic aerosol sources.
886
887 *3.1.1. Northern Greenland Sea and Norwegian Sea.*
888 Monthly mean values of $\tau(0.50\ \mu m)$ and α derived from the Microtops measurements performed
889 during nine cruises made in the Norwegian Sea, west of Spitsbergen, and one cruise in the northern
890 Greenland Sea and Norwegian Sea are shown in Fig. 14a. Values of $\tau(0.50\ \mu m)$ gradually decreased
891 from less than 0.10 in April to nearly 0.05 in August, with values of $\sigma_\tau < 0.03$ over the entire
892 period. The monthly mean values of α were rather stable from April to August, ranging from 1.20
893 to 1.30, with values of σ_α equal to 0.10 in spring and 0.40 in summer. These features suggest that
894 the columnar aerosol content was mixed in spring, consisting of anthropogenic (Arctic haze) and
895 natural sea-salt aerosols, and contained sea-salt aerosol mixed with BFF smoke particles in summer.
896 In fact, the aerosol extinction parameters measured in spring and summer with the Microtops sun-
897 photometers turn out to be very similar to those determined at Ittoqqortoormiit and Hornsund from
898 the AERONET sun-photometer measurements, during spring (when polluted air masses are mainly
899 transported from Europe) and summer (when polar air masses are transported from the Arctic land
900 and oceanic regions toward the Svalbard Archipelago) (Rozwadowska et al., 2010; Rozwadowska
901 and Sobolewski, 2010). These variable features can be more clearly seen by considering the
902 seasonal RFHs of $\tau(0.50\ \mu m)$ and α shown in Fig. 14b, derived from the measurements taken on 77
903 measurement days in the Greenland Sea and Norwegian Sea (GNS) sector. The RFH of $\tau(0.50\ \mu m)$
904 exhibits a large peak over the 0.02-0.20 range, with a mean value equal to 0.075, and 25^{th} and 75^{th}
905 percentiles equal to 0.054 and 0.094, respectively, indicating significant variations even in the
906 remote Arctic Ocean. The corresponding RFH of α is also rather wide, showing a mean value of

907 1.23, and 25th and 75th percentiles equal to 1.02 and 1.47, respectively, as a result of the
908 combination of natural maritime and anthropogenic/continental aerosol loads. It is worth noticing
909 that the GNS average values of $\tau(0.50\ \mu m)$ and α agree fairly well with those determined at
910 Ittoqqortoormiit (Fig. 5) and Hornsund (Fig. 6) and exhibit similar relationships between α and
911 $\tau(0.50\ \mu m)$ to those of the above-mentioned AERONET stations (compare Fig. 8a with those of Fig.
912 8b).
913
914 *3.1.2. Barents Sea and West Siberian Sea*
915 Only the RV Polarstern 2012 cruise crossed the Barents Sea and West Siberian Sea (BWS) sector,
916 in August 2012, at latitudes varying from 80° N to 84° N and longitudes ranging from 28° E to 120°
917 E (see Fig. 2). Thus, the monthly mean values of $\tau(0.50\ \mu m)$ and α were only calculated for three
918 measurement days, giving statistically poor values of $\tau(0.50\ \mu m) = 0.054 \pm 0.010$ and $\alpha = 1.42 \pm$
919 0.33. As noted in Fig. 14a, the above value of $\tau(0.50\ \mu m)$ closely agrees with that measured within
920 the GNS sector on the same month, and α is slightly higher than that measured in August within the
921 same sector. Such results are typical of an oceanic area during relatively calm wind periods.
922
923 *3.1.3. North American Arctic Ocean*
924 Within the North American Arctic (NAA) oceanic sector, including the East Chukchi Sea, Bering
925 Strait, Beaufort Sea and Amundsen Gulf, only four cruises were considered among those reported in
926 Table 3. The time-patterns of the monthly mean values of $\tau(0.50\ \mu m)$ and α calculated over the
927 March-September period are shown in Fig. 14a. Monthly mean value of $\tau(0.50\ \mu m)$ were about 0.10
928 in March, peaked in April and May at 0.17 and 0.20, respectively, and decreased in the summer
929 months to 0.10 in June and 0.05 in September. No pronounced variations in α were obtained, with
930 values from 0.90 to 1.20 from March to September, and σ_α varying from 0.20 (in April) to 0.50 (in
931 July). An overall number of 58 measurement days was collected in this oceanic sector over the 7-

month period from March to September, for which calculations of the RFHs were made, illustrating a statistically robust data-set. The RFH of $\tau(0.50\ \mu m)$ showed a more dispersed distribution curve over the 0.02-0.25 range than that determined for the GNS sector, with a mean value of 0.16, which was considerably higher than that measured in the GNS sector, and also had wider right-hand wings. The RFH of α exhibits a similar shape to that determined in the GNS sector, with a mean value close to 1.10.

The median values and the 25th and 75th percentiles of parameters $\tau(0.50\ \mu m)$ and α were calculated for the sets of daily mean values derived from the Microtops sun-photometer measurements conducted over the GNS, BWS and NAA sectors. The results are shown in Fig. 8b for an easier comparison with those derived from the ground-based sun-photometer measurements conducted at Arctic sites. The ship-borne measurements provided median values of $\tau(0.50\ \mu m)$ ranging from 0.04 to about 0.13, which are therefore comparable with the mean background extinction parameter measured in summer at the ground-based stations. The ship-borne median values of α varied mainly from 1.10 to 1.50, and were appreciably lower than those measured in summer-autumn at the land stations: the scatter plot shown in Fig. 8b provides clear evidence of the prevailing oceanic origins of these aerosol loads.

3.2. Aerosol measurements in the Antarctic Ocean.

Eighteen AERONET/MAN cruises were conducted from 2006 to early 2013 over the Antarctic Oceans. They are listed in Table 4, together with the geographical areas covered by the various cruises, the number of measurements days (see also Fig. 2), the measurement periods and the spectral characteristics of the portable Microtops sun-photometers onboard the vessels. To analyze the aerosol optical parameters more homogeneously, the sun-photometer data-sets recorded during the 18 cruises were subdivided into the following four sub-sets: (1) the Southern Indian Ocean (IND) sector, between 20° E and 150° E longitudes; (2) the Southern Pacific Ocean (PAC) sector, between 150° E and 75° W longitudes; (3) the Southern Atlantic Ocean (ATL) sector, between 50°

958 W and 20° E longitudes; and (4) the oceanic region around the Antarctic Peninsula (APE), between
959 75° and 50° W longitudes. The daily mean values of $\tau(0.50\ \mu m)$ and α measured with the portable
960 Microtops sun-photometers calibrated at NASA/GSFC facility (Smirnov et al., 2009, 2011) were
961 analysed separately for coastal data (for distances smaller than 300 km from the Antarctic coast)
962 and off-shore data (for distances of 300 to 1000 km from the coast), according to the criteria used
963 by Wilson et al. (2010) to distinguish the data related to a significant landmass from those of pure
964 oceanic origin (i.e., given for the large part by maritime aerosols generated by wind-related
965 sources). The overall set of Microtops data was then examined following the same criteria adopted
966 to analyse the Arctic ship-borne measurements, separately for the above-mentioned four oceanic
967 sectors.
968
969 *3.2.1. Southern Indian Ocean*
970 As can be seen in Table 4, eleven cruises were conducted in the Southern Indian Ocean, during
971 periods from December to March in the years from 2005/2006 to 2011/2012, collecting an overall
972 set of 226 coastal measurement days, and only nine off-shore measurement days (see Fig. 2). The
973 time-patterns of the monthly mean values of $\tau(0.50\ \mu m)$ and α are shown in Fig. 15a for coastal and
974 off-shore data. AOT values of $\tau(0.50\ \mu m)$ were rather stable from December to April over the
975 coastal areas, varying from 0.010 to 0.025, with $\sigma_\tau = \pm\ 0.01$ on average, and were appreciably
976 greater over the off-shore area, being close to ~ 0.06 in January, 0.04 in November and December,
977 and 0.02 in February. The coastal values of α varied from 1.20 to 1.40 in the December-April
978 period, while the off-shore values decreased from 1.20 to less than 0.60 from November to
979 December, and then slowly increased to around 0.90 in February. These findings give a measure of
980 the increase in $\tau(\lambda)$ and the variations in α, which are observed passing from coastal to off-shore
981 areas as a result of the stronger production of sea-salt coarse particles. The daily mean values of
982 $\tau(0.50\ \mu m)$ and α were derived over the Southern Indian Ocean on 226 measurement days near the

983 Antarctic coasts, and on only nine days in off-shore areas. Therefore, only the RFHs of the coastal
984 daily mean values of $\tau(0.50\ \mu m)$ and α have been analysed: the RFH of $\tau(0.50\ \mu m)$ shown in Fig.
985 15b presents a very narrow curve, with a mean value of 0.024, and 25th and 75th percentiles very
986 close to the mean, while the RFH of α exhibits a broad curve, with a mean value of 1.20 and 25th
987 and 75th percentiles equal to 0.84 and 1.51. These findings clearly indicate that a large variability
988 characterizes the sea-salt accumulation and coarse mode particle concentrations in coastal areas.
989
990 *3.2.2. Southern Pacific Ocean*
991 As reported in Table 4, only three AERONET/MAN cruises were conducted in the Southern Pacific
992 Ocean over the December-January periods of 2007/2008 to 2009/2010, over the area defined in Fig.
993 2, giving an overall number of 20 coastal and 5 off-shore measurement days. The monthly mean
994 values of $\tau(0.50\ \mu m)$ and α varied from 0.03 to 0.04 near the coasts, and from 0.04 to 0.05 in the
995 off-shore areas, while the coastal monthly mean values of α decreased from ~ 1.45 in December to
996 ~ 1.00 in January, and the off-shore values from 1.40 to 0.70. The values of $\tau(0.50\ \mu m)$ and α result
997 to closely agree with those measured at Neumayer, Novolazarevskaya, Mirny, Syowa, and Mario
998 Zucchelli, shown in Figs. 9-12. A coastal median value of $\tau(0.50\ \mu m)$ equal to ~ 0.04 was obtained,
999 with the main percentiles differing by less than 0.02, while the median value of α was equal to 1.20,
1000 with the main percentiles differing by about 0.50. The off-shore data-set provided a similar value of
1001 $\tau(0.50\ \mu m)$ and more distant main percentiles, with a median value of α = 1.15, and main
1002 percentiles differing by more than 0.40.
1003
1004 *3.2.3. Southern Atlantic Ocean*
1005 A large set of AERONET/MAN sun-photometer measurements was collected in the Southern
1006 Atlantic Ocean during five cruises conducted in 2007/2008, 2011/2012 and 2012/2013, as reported
1007 in Table 4, giving 63 coastal and only 8 off-shore measurement days. The monthly mean values of

1008 $\tau(0.50\ \mu m)$ varied from 0.03 in December to less than 0.02 in April, with σ_τ = 0.01 on average,
1009 while those of α increased from ~ 1.10 in December to 1.50 in February, and then decreased to 1.30
1010 in April. The RFH of the coastal $\tau(0.50\ \mu m)$ values was found to exhibit similar features to those
1011 determined in the coastal area of the Antarctic Indian Ocean, with a leptokurtic shape having a
1012 mean value of 0.025 and the 25th and 75th percentiles differing by less than 0.01, while the RFH of
1013 α showed a rather broad shape over the 0.5-2.4 range, with a mean value of 1.39 and the 25th and
1014 75th percentiles differing by about 0.30, thus being similar to that determined for the Pacific Ocean
1015 coastal data-set.
1016
1017 *3.2.4. Around the Antarctic Peninsula*
1018 Numerous aerosol optical data were collected in coastal areas surrounding the Antarctic Peninsula
1019 during the seven AERONET/MAN cruises conducted from 2007/2008 to 2012/2013, as reported in
1020 Table 4, collecting an overall number of 49 measurement days, not far from the coasts. The time-
1021 patterns of monthly mean values of $\tau(0.50\ \mu m)$ and α obtained from these measurements are shown
1022 in Fig. 15b. A very high value of $\tau(0.50\ \mu m)$ close to 0.12 was obtained in October, followed by
1023 decreasing monthly mean values equal to 0.08 in November and lower than 0.06 in December, and
1024 then varying from 0.04 to 0.06 over the January-March period, with σ_τ = 0.02 on average. The
1025 monthly mean values of α were all rather low, varying from 0.50 to 1.00 over the October-February
1026 period, with σ_α = 0.20 on average. The exceptionally high monthly mean values of $\tau(0.50\ \mu m)$ were
1027 determined in October and November for measurement days giving values of α varying from 0.24
1028 to 0.69, and presenting prevailing transport of air masses from the off-shore areas of the Drake
1029 Passage. Similar aerosol optical characteristics were observed by Posyniak and Markowicz (2009)
1030 for flows from the North-Eastern quadrant, accompanied by low visibility conditions because of the
1031 transport of large amounts of sea-salt particles from the Drake Passage, with wind speed > 10 m/s.
1032 Relatively low daily mean values of α were measured on these days, ranging from 0.43 to 0.73, due

1033 to maritime aerosols generated by the strong winds, which dominated extinction. For southerly
1034 wind circulation, considerably lower values of $\tau(0.50\ \mu m)$ were measured in this coastal area.
1035 Therefore, because of the large variability of wind directions, the RFH of $\tau(0.50\ \mu m)$ determined
1036 over the October-March period exhibited rather dispersed features, with a mean value of ~ 0.05 and
1037 the 25th and 75th percentiles differing by less than 0.02. These evaluations are higher by about a
1038 factor 2 than those obtained over the coastal areas of the Indian and Atlantic Oceans, because of the
1039 more significant contribution of sea-salt accumulation and coarse mode particles generated by
1040 stronger winds. The RFH of α shows a rather broad shape over the range $\alpha < 1.5$, with a mean
1041 value close to 0.70, which is about half of that measured over the Indian and Atlantic Ocean coastal
1042 areas, and the 25th and 75th percentiles differing by no more than 0.30, due to the predominant
1043 extinction by maritime particles.
1044 The above results obtained from the coastal and off-shore data recorded over the four sectors of the
1045 Southern Antarctic Ocean are characterized by features of $\tau(0.50\ \mu m)$ and α typical of sea-salt
1046 maritime particles, as can be clearly seen in Fig. 13b, in which the median values of α are plotted
1047 versus the median values of $\tau(0.50\ \mu m)$, separately for the coastal and off-shore data. The
1048 comparison between these results and the scatter plot shown in Fig. 13a shows that they are very
1049 similar to those derived from the sun-photometer measurements conducted at the coastal Antarctic
1050 stations, since the cluster derived from the AERONET/MAN measurements of α and $\tau(0.50\ \mu m)$
1051 essentially covers the same domain of the ground-based measurements recorded at Marambio,
1052 Novolazarevskaya, Syowa, Neumayer, and Mario Zucchelli, although exhibiting slightly lower
1053 values of α.
1054
1055 **4. Aerosol backscattering coefficient profiles from lidar measurements**
1056 Lidar sends a light pulse through the atmosphere and the telescope collects the backscattered lidar
1057 return signal. As the speed of light is known, one can easily calculate the exact atmospheric

1058 position, from which the lidar signal has originated. Therefore, the determination of aerosol vertical
1059 structure is possible, at least over the altitude range in which the image of the laser is completely
1060 within the field-of-view of the recording telescope. Lidar pulses can be generated at several
1061 wavelengths and polarization elements can also be used at the point of light entrance to the
1062 telescope. This enables a determination of the shape of scatterers because spherical particles do not
1063 depolarize light, while non-spherical particles normally do.
1064 Overcoming the considerable operational and logistic difficulties, various lidar systems have been
1065 deployed in the polar regions to measure: (i) the vertical profiles of backscatter and extinction
1066 coefficients of the various aerosols, cloud droplets and ice crystals, as well as their microphysical
1067 and radiative characteristics; (ii) the vertical distribution of temperature and water vapour mixing
1068 ratio; and (iii) the ozone concentration at stratospheric levels, to more thoroughly investigate the
1069 role of Polar Stratospheric Clouds in destroying ozone molecules at polar latitudes. Actually, most
1070 of these measurements were conducted to study the dynamic features of the ozone hole in
1071 Antarctica and ozone depletion in the Arctic region associated with the polar vortex occurrences,
1072 and the physical characteristics of tropospheric clouds, while relatively few measurement
1073 campaigns were specifically conducted with lidar techniques to investigate the optical
1074 characteristics of tropospheric aerosols at polar latitudes. An exhaustive description of the lidar
1075 measurements conducted in polar regions over the past few decades was recently made (Nott and
1076 Duck, 2011). Lidar activities were conducted in the Arctic at the following sites:
1077 (i) Barrow (Northern Alaska), where long-term lidar measurements were recorded and a micropulse
1078 lidar is currently used to carry out cloud climatology studies that have evaluated average seasonal
1079 cloud occurrences of 65% in winter, 68% in spring, 83% in summer, and 89% in autumn, with an
1080 annual mean decrease of -4.8% per year over the past 10 years (Dong et al., 2010).
1081 (ii) Eureka (Nunavut, Canada)), where an elastic lidar was used from 1993 to 1997 to carry out
1082 winter-time aerosol measurements for studying the occurrences of clouds and Arctic haze.
1083 Backscatter peaks due to haze particle layers were frequently observed at altitudes lower than 3 km,

and more occasionally at altitudes of 3-5 km, for relative humidity < 60% over ice, while clouds dominate at > 80% over ice. Spectral measurements of the aerosol backscatter coefficient $\beta_{bs}(\lambda)$ and depolarization ratio $\delta_V(\lambda)$ were regularly conducted from 2005 to 2010, over the height range from 70 m up to approximately 15 km, using a High Spectral Resolution Lidar (HSRL) of the University of Wisconsin (USA), at the wavelengths 0.532 and 1.064 μm, for the aerosol backscatter coefficient $\beta_{bs}(\lambda)$, and 0.532 μm only for $\delta_V(\lambda)$ and $\beta_{ext}(\lambda)$. This lidar system was used together with a millimeter cloud radar to classify the various cloud particle types. Since 2008, a troposphere ozone-DIAL (Differential Absorption Lidar) and a Raman lidar have been operated simultaneously, equipped with aerosol channels in the visible and ultraviolet light and water vapour and rotational Raman temperature channels.

(iii) Alert (Nunavut, Canada), where an elastic lidar was operated in 1984-1986 to measure the vertical profiles of aerosol backscatter coefficient.

(iv) Summit (Central Greenland), where a depolarization lidar and a micropulse lidar were used since 2010, to characterize the aerosol types suspended over the Greenland ice-sheet.

(v) Ny-Ålesund (Spitsbergen, Svalbard), where various lidar models were used, such as: (a) a stratospheric lidar since 1988; (b) the KARL (Koldewey-Aerosol-Raman-Lidar) since 1999, this system being equipped with aerosol channels, depolarization and ultraviolet and visible water vapour channels, and subsequently rebuilt in 2008 with enhanced multi-wavelength aerosol channels to cover the 0.45-30 km altitude range; and (c) an automated micropulse lidar (Hoffmann et al., 2009) since 2003, as a part of the MPLNET and NDACC networks, which provided cloud and aerosol measurements in March and April 2007, useful to characterise air masses as a function of depolarization and backscatter ratios.

(vi) Hornsund (Spitsbergen, Svalbard), where an automated lidar has been operated since 2009, to measure the vertical profiles of volume extinction coefficient $\beta_{ext}(0.532\ \mu m)$ produced by aerosols

1108 during transport episodes of unpolluted air masses from the Greenland Sea and Norwegian Sea
1109 areas; and
1110 (vi) Andøya Rocket Range (Arctic Lidar Observatory for Middle Atmosphere Research,
1111 ALOMAR), near Andenes (Northern Norway), where a tropospheric lidar was installed in 2005 and
1112 a polarization-sensitive bistatic lidar system has been used since 2006 to study the vertical
1113 distribution features of polar aerosols and their optical characteristics.
1114 The above-mentioned field measurements provided vertical profiles of the most significant aerosol
1115 scattering parameters, illustrating that the Arctic haze particles are in general present below the 3
1116 km level during severe haze events, and occasionally at 3-5 km altitudes, as shown by the
1117 measurements conducted at Eureka (Nott and Duck, 2011). During the dense haze episode observed
1118 with the KARL lidar at Ny-Ålesund on May 2, 2006, strong extinction features were recorded from
1119 the ground up to 2.5 km altitude, which showed multi-layered profiles of the aerosol backscattering
1120 coefficient $\beta_{bs}(0.532\ \mu m)$ decreasing on average from 3.5 km^{-1} near the ground to below 0.5 km^{-1} at
1121 2.5 km altitude. Conversely, for unpolluted air conditions, the scale height of $\beta_{bs}(0.532\ \mu m)$ was
1122 often found to vary from 1.0 to 1.3 km at Ny-Ålesund, as estimated for instance by Hoffmann et al.
1123 (2012) who examined the backscatter ratio measurements conducted with the KARL lidar over the
1124 whole of 2007.
1125 However, so far our knowledge of Arctic haze from a lidar point of view is still incomplete, because
1126 the majority of published results are based on case studies. Therefore, the yearly cycle of aerosols
1127 has been studied in this paper on the basis of the lidar measurements conducted at Ny-Ålesund over
1128 the period from 1 November, 2012, to 31 October, 2013, examining the overall set of KARL lidar
1129 measurements taken without cloud interferences and with resolutions of 60 m in height and 10
1130 minutes in time, according to Ansmann (1992). To guarantee a homogeneous data set, only lidar
1131 profiles with identical technical settings have been considered. Moreover, cloud screening was
1132 conducted and the lowest 800 m were removed from the analysis due to overlap (Weitkamp, 2005).
1133 Finally, the data derived from the Vaisala RS-92 radiosonde data collected at the site have been

used to subtract the Rayleigh backscatter coefficient from the lidar data. The fact that the time of the lidar observation does not coincide with the launch of the radiosonde should cause errors no higher than 5% in evaluating the aerosol backscatter coefficient. This is probably even an upper bound, since Rogers et al. (2011) only estimated a 3% bias for the CALIOP (Cloud-Aerosol Lidar with Orthogonal Polarization) lidar on board the CALIPSO satellite. Figure 16 shows the monthly averaged profiles of the aerosol volumetric backscatter coefficient $\beta_{bs}(0.532\ \mu m)$ from January to May and the three bi-monthly averaged profiles from June to December, providing evidence of significant variations in this optical parameter throughout the year. A clear annual cycle of the aerosol backscatter coefficient can be seen, which increased in February mainly in the low troposphere and reached its maximum values during March and April in the whole troposphere, subsequently decreasing appreciably in May. The months June to January were relatively clear, always showing appreciably lower values at all altitudes. Another view of the same data is shown in Fig. 17, where the monthly averaged values of $\beta_{bs}(0.532\ \mu m)$ were integrated over five partial height-intervals and the total range from 0.8 to 7.0 km. The results show that the Arctic haze layer starts to form at low altitudes early in the season and lasts until May not only in the low troposphere but also at high altitudes. In fact, the maximum values below 2.5 km altitude have been found in March, while the largest values of $\beta_{bs}(0.532\ \mu m)$ occur in April at 1.5-2.5 km altitudes. It can be also noted in Fig. 17 that the haze season starts more rapidly than it disappears, since the increase in backscatter observed between January and March is steeper, whereas the decline lasts from April till August.

The annual cycle of the lidar ratio $S_a(0.532\ \mu m)$ between the aerosol extinction coefficient $\beta_{ext}(0.532\ \mu m)$ and the aerosol backscatter coefficient $\beta_{bs}(0.532\ \mu m)$ is presented in Fig. 18, separately calculated over the altitude sub-ranges $z < 3.5$ km and $z > 3.5$ km and over the whole altitude range, for the KARL lidar measurements conducted from early November 2012 to late October 2013. It shows that $S_a(0.532\ \mu m)$ takes the highest values in June-July and generally

1159 increases with altitude. However, its annual cycle is not very pronounced below 3.5 km altitude,
1160 where most of the aerosol is located, presenting values varying from 30 to 35 sr. This is typical of
1161 clean continental aerosol (Winker et al., 2009). Conversely, the monthly mean values of $S_a(0.532\ \mu m)$
1162 calculated above 3.5 km were estimated to vary from 30 to 40 sr in winter, i.e. assuming values
1163 typical of clean continental aerosol and dust, and to increase until reaching surprisingly high values
1164 of 60 - 70 sr in summer, which are normally typical of BFF smoke and polluted continental aerosol.
1165 However, one has to keep in mind that the lidar ratio depends not only on the chemical composition
1166 but also on the shape and size-distribution of aerosols. It also agrees well with the evaluations of
1167 $S_a(0.532\ \mu m)$ made by Ackermann (1998) for different aerosol types suspended in air for relative
1168 humidity conditions ranging from 40% to 50%, estimated to be of 27 sr for maritime aerosols and
1169 around 55 sr for continental aerosol suspended in relatively dry air masses, like those frequently
1170 observed in the polar atmosphere over land (which probably indicate a decrease in the influence of
1171 marine air masses with altitude). Due to the contributions of both low and high tropospheric
1172 regions, the overall values of $S_a(0.532\ \mu m)$ were estimated to range mainly from 30 to 50 sr.
1173 To quantify the direct radiative forcing of Arctic haze, it is very important to know the
1174 morphological and optical features of atmospheric aerosols, as well as the multimodal size-
1175 distribution, the refractive index and the particle shape. The ratio of the perpendicular to parallel
1176 polarized backscatter returns from aerosols at a certain wavelength λ gives the volume
1177 depolarization ratio $\delta_V(\lambda)$, which provides an effective range-resolved method of determining
1178 whether the laser pulse has been backscattered by spherical or non-spherical aerosols (Winker et al.,
1179 2009). Bearing in mind that spherical particles do not depolarize the incoming solar radiation, the
1180 scatter plot of the monthly (from January to May) and bi-monthly (from June to December)
1181 averaged values of depolarisation ratio percentage are shown in Fig. 19 versus the aerosol
1182 backscatter coefficient $\beta_{bs}(0.532\ \mu m)$, as obtained from the KARL lidar measurements conducted
1183 from early November 2012 to late October 2013. Generally quite low values of aerosol
1184 depolarization ratio $\delta_V(0.532\ \mu m)$ have been found (appreciably lower for instance than those of

1185 desert dust), with the lowest values in January, and values ranging from 2.0% to 2.6% in October-
1186 December, over the range of $\beta_{bs}(0.532\ \mu m) < 4.5 \times 10^{-4}$ km^{-1} sr^{-1}. Remarkably higher depolarisation
1187 values, greater than 2.6%, have been found during the maximum of the haze season, in March and
1188 April, for values of $\beta_{bs}(0.532\ \mu m)$ ranging from 4.0×10^{-4} to 5.5×10^{-4} km^{-1} sr^{-1}. This means that
1189 Mie theory, while being a fair assumption to model the forcing of Arctic aerosol during most of the
1190 year, is less accurate during spring time.
1191 Lidar measurements were taken at the coastal Antarctic stations of Syowa, Mario Zucchelli,
1192 McMurdo and Dumont d'Urville (66° 40' S, 140° 01' E), and at the Antarctic Plateau sites of Dome
1193 Concordia and South Pole over the past decades (see the Antarctic map in Fig. 2), to monitor the
1194 microphysical parameters of clouds at various altitudes (for cloud climatology studies), and only
1195 occasionally to measure the vertical profile of the tropospheric aerosol scattering coefficient
1196 $\beta_{ext}(0.532\ \mu m)$. It was found in general that the cloud-free vertical profile of aerosol scattering does
1197 not exhibit particularly dense layers near the surface, but shows that $\beta_{ext}(0.532\ \mu m)$ decreases
1198 rapidly with height, to reach the free troposphere "background aerosol" conditions immediately
1199 above the marine PBL. The first lidar measurements were conducted during the 1974/1975 austral
1200 summer at South Pole, where regular measurements have also been carried out with a micro-pulse
1201 system since 1999, mainly to study the microphysical characteristics of diamond dust and blowing
1202 snow events. Ground-based lidar measurements have also been regularly conducted at Dome
1203 Concordia since 2007, by using the elastic-backscatter and depolarization lidar system of the IFAC-
1204 CNR Institute (Florence, Italy). Analysis of these data revealed that "diamond dust" ice-crystals are
1205 often present during windy conditions at this remote site, within the boundary-layer of 100-200 m
1206 depth, while aerosols contribute to yield slowly decreasing values of $\beta_{sca}(0.532\ \mu m)$ with height,
1207 until rapidly reaching the background conditions of the free troposphere.
1208 Diamond dust episodes were also frequently observed over the Arctic Ocean. Ground-based lidar
1209 and radar were used for this purpose during the Surface Heat Budget of the Arctic Ocean (SHEBA)
1210 programme, determining the physical characteristics of diamond dust ice-crystals and assessing the

surface radiative effects induced by such particles under cloud-free sky conditions. Examining a set of 188 diamond dust or ice crystals episodes over the western Arctic Ocean between November 1997 and May 1998, Intrieri and Shupe (2004) found that diamond dust episodes covered about 13% of the time between November and mid-May over the Arctic Ocean and were never observed from mid-May to October. Lidar measurements highlighted that the diamond dust vertical depth varied from 100 m to 1000 m on the various cloud-free sky days, although it was most frequently observed to involve the lower 250 m of the troposphere on average, thus contributing to induce only small radiative effects on the sea ice surface.

Airborne lidar measurements of vertical profiles of aerosol extinction and backscatter coefficients were conducted in the Arctic, over the Svalbard area in spring 2000, 2004 and 2007, during the ASTAR (Arctic Study of Aerosol Clouds and Radiation) campaigns, together with complementary ground-based lidar measurements at Ny-Ålesund (Spitsbergen). The ASTAR 2000 campaign ran from 12 March until 25 April 2000 with extensive flight operations over the Svalbard region using the AWI aircraft POLAR 4. Simultaneous ground-based measurements were conducted at Ny-Ålesund (at both German Koldewey and Japanese Rabben stations as well as at the Zeppelin station). Vertical profiles of various aerosol parameters were measured during the campaign and provided evidence of the strong temporal variability of the Arctic spring aerosol with height. A strong haze event occurred between 21 and 25 March, in which AOT measured from ground-based observation was 0.18, i.e. largely greater than the aerosol background value measured in summer. The airborne measurements made on 23 March showed a high aerosol layer with an extinction coefficient of 0.03 km^{-1} or more up to 3 km. The chemical analyses of airborne measurements showed that such an aerosol transported from anthropogenic sources mainly consisted of sulphate, soot and sea-salt particles (Yamanouchi et al., 2005). Lidar measurements of 532/355 nm colour ratio were obtained by Lampert et al. (2009) during the ASTAR 2007 experiment, indicating the presence of particles with an effective diameter < 5 μm. However, Lampert et al. (2010) found rather low Arctic haze levels in spring 2007, examining lidar measurements of cloud and aerosol

1237 layers. As pointed out by Hoffmann et al. (2009), the Arctic haze optical thickness $\tau(0.50\ \mu m)$
1238 measured during such a seasonal period was evaluated to vary mainly from 0.05 to 0.08, compared
1239 to a 14-year average value of 0.10. The PBL extended up to 2.5 km altitude and predominantly
1240 contained well-hydrated particles, such as local sea-spray derived sulphates.
1241 Various airborne lidar measurements were conducted as part of the POLARCAT programme during
1242 the 2007-2008 International Polar Year, to define the aerosol radiative characteristics. In particular,
1243 analysing the backscatter measurements provided by the LEANDRE multi-channel lidar mounted
1244 on the ATR-42 aircraft, cases of aerosol transport from Europe and Eastern Asia were monitored in
1245 April 2008 by de Villiers et al. (2010). These studies showed that anthropogenic aerosols
1246 originating in Europe exhibited in general smaller sizes than Asian particles within the PBL below a
1247 height of 0.8 km and within layers at heights ranging from 2.8 to 4.5 km, consisting mainly of
1248 biomass burning substances and urban/industrial particulate matter, with aerosol backscatter
1249 coefficient $\beta_{bs}(0.532\ \mu m)$ ranging from 1.2×10^{-3} to 2.2×10^{-3} km^{-1} sr^{-1}, and depolarization ratio
1250 varying from 1.6% to 2.1% (with standard deviations of 0.3% on average). Conversely, the Asian
1251 dust plume observed in April 2008 was estimated to contain larger particles, presenting some well-
1252 defined aerosol layers at altitudes from 1.7 to 5.6 km, with $\beta_{bs}(0.532\ \mu m)$ varying from 1.6×10^{-3} to
1253 3.9×10^{-3} km^{-1} sr^{-1}, and depolarization ratio values equal to 2.0% (smoke particles), 3.0 - 5.0%
1254 (clean continental aerosol), 8.0% (dust), and 4.0 - 10.0% (polluted dust).
1255 The above results were obtained using also the Level 2.0 products given by the CALIOP lidar
1256 mounted on the CALIPSO satellite, which was launched in April 2006 (Winker et al., 2009, 2010)
1257 as a part of the A-train constellation of satellites, and has an orbit inclination of 98.2°, thus
1258 providing coverage to 82° latitude. This wide coverage has proven immensely important in polar
1259 regions, where ground-based installations are few and far between. The CALIOP lidar operates at
1260 wavelengths of 0.532 and 1.064 μm, with a depolarization ratio measured at 0.532 μm, and was
1261 used to characterize the various aerosol types by assuming in such an approach a set of values of
1262 lidar ratios $S_a(0.532\ \mu m)$ and $S_a(1.064\ \mu m)$ equal to 20 and 45 sr for clean marine aerosol, 35 and 30

1263 sr for clean continental aerosol, 40 and 30 sr for dust, 65 and 30 sr for polluted dust, 70 and 30 sr
1264 for polluted continental aerosol, and 70 and 40 sr for combustion smoke particles, respectively
1265 (Winker et al., 2009).
1266 A first airborne campaign referred to as the Polar Airborne Measurements and Arctic Regional
1267 Climate Model Simulation Project (PAMARCMiP) took place during April 2009 in the Arctic,
1268 using a pair of downward-looking lidars, a depolarization aerosol lidar and a tropospheric ozone
1269 DIAL mounted onboard the Polar 5 research aircraft of the Alfred Wegener Institute (AWI) for
1270 Polar and Marine Research (Germany). On the basis of the evaluations made by Rogers et al.
1271 (2011), it can be assumed that a relative 3% bias of aerosol backscatter coefficient $\beta_{bs}(0.532\ \mu m)$
1272 was made on average, due to a wrong assumption of the Rayleigh backscatter coefficient used to
1273 correct the overall lidar backscatter coefficient. A series of flights was conducted from
1274 Longyearbyen (Svalbard) across the western Arctic to Barrow (Alaska), reaching Station Nord
1275 (Greenland), Alert, NP-36 (at 88° 40' N latitude), Eureka, Resolute Bay, Sachs Harbor, Inuvik, and
1276 Fairbanks, while complementary ground-based lidar measurements were regularly conducted at Ny-
1277 Ålesund, Eureka and Barrow (Stone et al., 2010). Significant aerosol backscatter and extinction
1278 effects were measured over the entire region, mainly caused by haze particles with diameters
1279 ranging from 0.13 to 0.20 μm. The PAMARCMiP lidar measurements showed that the aerosol
1280 extinction coefficient decreased in general with height from the surface to the top-level of the
1281 thermal inversion layer, found to be on average equal to 4 km, and often presented a secondary peak
1282 above. A second PAMARCMiP airborne campaign was conducted with the Polar 5 aircraft during
1283 April 2011, following the route from Longyearbyen to Barrow, flying over Station Nord, Alert,
1284 Eureka, Resolute Bay and Inuvik (Herber et al., 2012). During both campaigns, black carbon was
1285 observed at all altitudes sampled but at relatively low concentrations compared with historical
1286 values.
1287 A climatological study of Arctic aerosols was made by Devasthale et al. (2011) examining the
1288 CALIOP measurements recorded from June 2006 to May 2010. The study showed that the bulk of

1289 the aerosol particles are confined within the first 1000 m of the troposphere, from about 65% of
1290 cases in winter to 45% in summer, while the rest is mainly suspended within the middle
1291 troposphere, at altitudes ranging from 3 to 5 km, especially in spring. The relative occurrences of
1292 aerosol types in the vertical profiles show that clean continental aerosol is the largest contributor in
1293 all seasons except in summer, while polluted continental aerosols are the second largest contributor
1294 to the total number of observed aerosol layers in winter and spring, and clean marine aerosol is the
1295 second largest contributor in summer and autumn. The average vertical profile of aerosol extinction
1296 coefficient was found to exhibit a pronounced peak at heights of about 0.4-0.7 km. Associated with
1297 the intrusions from mid-latitudes, polluted continental and smoke aerosols presented much broader
1298 distributions of optical and geometrical thicknesses, appearing to be more often optically thicker
1299 and higher up in the troposphere.
1300
1301 **5. Airborne and satellite measurements**
1302 *5.1. Basic remarks*
1303 Airborne sun-photometry employs ground-based techniques adapted to the special requirements
1304 (notably solar tracking) of an aircraft environment. Relatively frequent measurements can be made
1305 during ascending or descending profiles to achieve vertically stratified AOT measurements, which
1306 are sensitive to the aerosol vertical structure and can be converted to volume extinction coefficient
1307 profiles, which are analogous to the aerosol backscatter coefficient profiles derived from lidar
1308 measurements and shown in Fig. 16 (see Section 4). It is also possible to carry out measurements
1309 onboard airplanes flying above and below pollution plumes. These aircraft measurements offer the
1310 possibility of surveying large areas in relatively short time-periods, which is not possible, e.g., for
1311 ship-borne measurements. In particular, airborne measurements of this kind were made during the
1312 PAMARCMiP airborne campaign of April 2009 (Stone et al., 2010), in which various airborne lidar
1313 systems and a multi-wavelength sun-photometer were mounted onboard the AWI Polar 5 research
1314 aircraft to perform numerous measurements of volume aerosol scattering and extinction coefficients

1315 were conducted over the wide area from Svalbard across the western Arctic to Barrow, from the
1316 European to the Alaskan Arctic, and from sub-Arctic latitudes to near the Pole. The sun-photometer
1317 measurements were performed using a 8-channel sun-photometer system manufactured by
1318 NOAA/GMD (Boulder, Colorado, USA) in cooperation with ISAC-CNR (Bologna, Italy), and
1319 equipped with narrow-band visible and near-IR channels centred at wavelengths ranging from 0.355
1320 to 1.064 μm, while the lidar measurements were conducted using a pair of downward-looking
1321 lidars, a depolarization aerosol lidar and a tropospheric ozone DIAL. Additional independent *in-situ*
1322 measurements of particle size-distribution were also made onboard the AWI Polar 5 aircraft, and
1323 light extinction data were derived from the airborne lidar measurements to investigate the spectral
1324 effects produced by haze particles.
1325 The measurements revealed that the spatial variations in $\tau(\lambda)$ observed during the most turbid
1326 period of the 2009 haze season were closely related to the atmospheric circulation patterns regulated
1327 by a dominant airflow from Eurasian anthropogenic sources. In addition, lidar observations showed
1328 the presence of elevated aerosol layers, as shown at Ny-Ålesund by Treffeisen et al. (2007) in early
1329 May 2006 during a transport event of biomass burning aerosols from agricultural fires in eastern
1330 Europe, and by Stock et al. (2012) in March 2008 during a BFF smoke pollution event over the
1331 European Arctic region.
1332 Background values of $\tau(0.50\ \mu m)$ not exceeding 0.06 were determined in the most remote areas,
1333 while haze values of $\tau(0.50\ \mu m)$ varying from 0.12 to around 0.35 were measured, with the highest
1334 values found in the Beaufort Sea region toward the end of April. Such values of $\tau(\lambda)$ were
1335 anomalously high compared with those measured in the previous three years, because of the
1336 transport of haze particles from the industrial regions in Europe and Northern Asia. Arctic haze
1337 particles were frequently found to be concentrated within and just above the surface-based
1338 temperature inversion layer, showing in general bimodal size-distribution features, consisting of an
1339 accumulation mode of moderately small (water-soluble) particles and an additional mode mainly
1340 composed of insoluble coarse particles. In addition, the *in-situ* sampling and optical measurements

1341 revealed a marked decrease in the mean particle size with increasing altitude from the surface to 4
1342 km, yielding values of the Ångström exponent $\alpha(0.412\text{-}0.675\ \mu m)$ varying from 1.40 to 1.70. The
1343 airborne measurements showed that black carbon (BC) was highest near the North Pole, suggesting
1344 long-range transport from combustion sources. However, the BC concentration measurements
1345 performed near the surface were nearly an order of magnitude lower than those reported from
1346 similar campaigns in the 1980s. Enhanced opacity at higher altitudes during the campaign was
1347 attributed to an accumulation of industrial pollutants in the upper troposphere, consisting of residual
1348 aged aerosol and soot particles originating from coal burning in China, in combination with
1349 volcanic aerosol resulting from the March-April 2009 eruptions of Mount Redoubt in Alaska and
1350 perhaps minor contributions from aircraft emissions. The Arctic haze particles observed during
1351 April 2009 were estimated to have reduced the net short-wave irradiance by -2 to -5 W m^{-2},
1352 resulting in a slight cooling of the surface. Examining the data recorded during the second
1353 PAMARCMiP airborne campaign in April 2011, and some aerosol measurements coordinated with
1354 satellite flyovers of NASA's CALIPSO mission, Herber et al. (2012) found that such satellite-borne
1355 data can be useful to validate aerosol retrievals from the lidar and sun-photometer measurements
1356 made onboard the Polar 5 aircraft.
1357 Even larger areas than those covered by airborne sun-photometer campaigns can be monitored by
1358 means of satellite observations. The retrieval of aerosol properties from satellite-based
1359 measurements is an ill-posed problem. The satellite retrieved aerosol optical thickness over bright
1360 surfaces such as snow and ice is often biased and leads to errors when estimating aerosol-radiation
1361 interactions (IPCC, 2013). Polar-orbit satellite-mounted sensors like MODIS (Moderate Resolution
1362 Imaging Spectroradiometer) and MERIS (Medium Resolution Imaging Spectrometer) utilize multi-
1363 spectral information to characterize surface properties. The NASA/MODIS "dark-target" (DT)
1364 approach developed for the retrieval of aerosol properties uses the 2.1 µm band to estimate the
1365 reflectance in visible bands (Kaufman et al., 1997). The empirical relationships between the surface
1366 reflectance of visible channels and 2.1 µm channel were improved by considering the effect of

geometry and surface types (Levy et al., 2007), while information on global aerosol properties was determined as a function of location and season by performing cluster analysis of *in-situ* measurements (Levy et al., 2010). The major limitation of the MODIS DT algorithm is that no retrievals are performed when the surface reflectance of the 2.1 μm channel is higher than 0.25 (Levy et al., 2007). For the retrieval over bright surfaces, such as desert and urban regions, Hsu et al (2004) developed the Deep Blue (DB) algorithm utilizing the fact that the surface is much darker in the short blue spectral channels compared with longer wavelengths. The second generation of DB algorithm, the so-called Enhanced Deep Blue algorithm, improved estimates of the surface reflectance, aerosol model selection and cloud screening schemes (Sayer et al., 2012; Hsu et al., 2013). The current MODIS Collection 6.0 AOT product is created from three separate retrieval algorithms for different surface types (Levy et al., 2013): they are two DT algorithms for dark ocean surface as well as the vegetated/dark-soiled land and a DB algorithm over desert/arid land. MODIS Collection 6 also provides a 3 km AOT product compared to Collection 5 (Remer et al., 2013). The Bremen AErosol Retrieval (BAER) algorithm for MERIS (von Hoyningen-Huene et al., 2003, 2011) utilizes the Normalized Difference Vegetation Index (NDVI). Polar-orbit satellites with multi-view observations such as AATSR (Advanced Along Track Scanning Radiometer) (Curier et al., 2009) and MISR (Multi-angle Imaging Spectroradiometer) (Diner et al., 2005a) make use of the Bidirectional Reflectance Distribution Function (hereinafter referred to as BRDF) surface properties to constrain the ill-posed inverse problem. A time series method is the most popular aerosol retrieval method for geostationary satellite based on the assumption that the surface reflectance does not change significantly during a short period of time (Knapp et al. 2002; Govaerts et al., 2010; Mei et al., 2012). The retrievals based on POLDER (Polarization and Directionality of the Earth's Reflectances) (Deuze, et al., 2001; Dubovik et al., 2011) intensity and degree of polarization measurements provide more accurate AOT products with the advantage that the contribution of land surfaces to the degree of polarization at the TOA is generally smaller in the visible as compared to the contribution of the underlying surface to the light intensity as measured on a satellite.

1393 Among the various satellite-based observations, those provided by MODIS (Justice et al., 1998)
1394 mounted on the Terra and Aqua platforms are particularly useful for evaluating the AOT features in
1395 the polar regions, over the ocean and ice-free land surfaces, and studying aerosol climatology
1396 associated with the sources, transport and sinks of specific aerosol types (e.g., sulphates and
1397 biomass-burning smoke particles). The twin MODIS sensors have been flying on the Terra platform
1398 since 2000 and on the Aqua platform since 2002, giving a large data-set of aerosol products using a
1399 number of algorithms over the past decades to retrieve columnar aerosol parameters over sea and
1400 land (Tanré et al., 1997; Kaufman et al., 1997; Hsu et al., 2004; Remer et al., 2005; Levy et al.,
1401 2013; Xue et al., 2014). To define the average seasonal maps of $\tau(0.55\ \mu m)$, we downloaded data-
1402 sets of MODIS/Terra and MODIS/Aqua monthly Level-3 data (Atmosphere Monthly Global 1 × 1
1403 Degrees Products MOD08_M3.051 and MYD08_M3.051, for the Terra and Aqua platforms,
1404 respectively) from the Giovanni website (http://disc.sci.gsfc.nasa.gov/giovanni). These had been
1405 collected for cloud-free atmospheric conditions over the eight years from January 2005 to
1406 December 2012, at Arctic latitudes ≥ 67 °N and Antarctic latitudes ≥ 62 °S. The cloud-screened
1407 Arctic AOT data-set was divided into seasonal sub-sets of $\tau(0.55\ \mu m)$ for spring (March to May)
1408 and summer (June to August), separately for Terra and Aqua observations. The seasonal average
1409 maps of Level-3 AOT $\tau(0.55\ \mu m)$ derived from MODIS/Aqua and MODIS/Terra are separately
1410 shown in Fig. 20, for 1° × 1° pixels over oceans and land areas not covered by snow and ice. The
1411 values of $\tau(0.55\ \mu m)$ in the summer months are mainly lower than 0.15, with some areas
1412 characterized by average values ranging from 0.15 to 0.30 over the Central and Western Siberian
1413 Sea, and the Chukchi Sea, as well as over the Beaufort Sea, presumably due to the transport of BFF
1414 aerosol from Siberia and North America, respectively. The spring average values of $\tau(0.55\ \mu m)$
1415 range mainly from 0.10 to 0.25, with peaks of more than 0.30 in the Siberian, North American and
1416 North European sectors, associated with dense Arctic haze transported from the anthropogenic mid-
1417 latitude sources. These findings closely agree with the results obtained from the ground-based sun-

1418 photometer measurements conducted at coastal sites (Fig. 8a) and from the ship-borne
1419 AERONET/MAN measurements (Fig. 8b). Figure 20 also shows that AOT cannot be retrieved from
1420 the MODIS data using the operational MODIS algorithm over Greenland and the North Pole in both
1421 spring and summer, and over large regions of Northern America and Siberia in spring, because of
1422 the high reflectance of the surfaces covered by sea ice and snow and also because of generally small
1423 values of AOT in these areas.
1424 Reliable maps of exponent α cannot be retrieved from MODIS data over both land and ocean
1425 surfaces because of the low values of AOT in the polar regions and the relevant uncertainties
1426 affecting the MODIS aerosol products (Mishchenko et al., 2010; Kahn et al., 2011). In particular,
1427 Levy et al. (2013) determined the Collection 6 MODIS aerosol products to retrieve AOT and
1428 aerosol size-parameters from MODIS-observed spectral reflectance data and found that the
1429 Ångström exponent product over land cannot be reliably used. These findings were confirmed by
1430 Mielonen at al. (2011) who stated that MODIS data do not provide quantitative information about
1431 aerosol size and parameter α over land. Similarly, as a result of a validation study of Collection 5
1432 MODIS Level-2 Aqua and Terra AOT and α products over ocean, Schutgens et al. (2013) found
1433 that these products exhibit significant biases due to wind speed and cloudiness of the observed
1434 scene, being significantly affected by AOT and α random errors due to cloud fraction contributions.
1435 On the basis of these results, we have decided to examine here only the MODIS AOT data and
1436 exclude from the present analysis the MODIS α products obtained over snow- and ice-free land and
1437 ocean regions, since they were presumably affected by considerable uncertainties arising from: (i)
1438 the presence of cloud-fractions within the $1° \times 1°$ pixels that cannot be correctly evaluated, and (ii)
1439 the variability of AOT at visible and near-infrared wavelengths, due to cloud extinction effects,
1440 which may efficiently contribute to lower exponent α. On the basis of the AERONET/MAN
1441 measurements, this parameter was evaluated to range from less than 1.00 to around 1.75 over the

1442 Arctic Ocean sectors in spring and summer, and from less than 0.50 to about 2.00 in Antarctica,
1443 with in general lower values over the off-shore areas far from the Antarctic coasts.
1444 The Antarctic aerosol data-set downloaded from the Giovanni website over the latitude range ≥ 62°
1445 S covers not only the land region of the Antarctic continent but also the off-shore ocean areas no
1446 further than 1000 km from the coasts. Only the MODIS/Aqua and MODIS/Terra data collected
1447 from December to February were separately examined to determine the maps of average $\tau(0.55$
1448 $\mu m)$, limited in practice to the oceanic areas only (Fig. 21). The results indicate that such seasonal
1449 average values of $\tau(0.55\ \mu m)$ are lower than 0.10 over all ocean areas close to the Antarctic coasts
1450 and sometimes can exceed 0.10 over the off-shore areas, in close agreement with the values derived
1451 from ground-based sun-photometer measurements at coastal Antarctic sites (Fig. 13a) and from
1452 AERONET/MAN measurements (Fig. 13b).
1453 Figure 21 also shows that no useful information is available from MODIS observations over the
1454 interior of Antarctica when using the traditional retrieval procedures. The retrieval of $\tau(\lambda)$ over a
1455 bright surface is indeed a very difficult task, because it is hard to separate the radiance contributions
1456 by the reflecting surface and atmospheric aerosol back-scattering to the overall radiance observed
1457 by a satellite-borne sensor at the TOA-level, especially for the very large solar zenith angles typical
1458 of polar latitudes. Mei et al. (2013a) overcame the above difficulties by following a synergetic
1459 approach based on the use of both MODIS/Terra and MODIS/Aqua data, together with: (i) the *a-*
1460 *priori* assumption of aerosol optical parameters retrieved over snow made with the Aerosol
1461 Properties Retrieval over Snow (APRS) algorithm, and (ii) an appropriate model of the BRDF
1462 reflectance representing snow-covered surfaces. The APRS algorithm was based on the operational
1463 bi-angle approach proposed by Xue and Cracknell (1995) to retrieve non-absorbing aerosol
1464 extinction parameters over land surfaces (Tang et al., 2005; Wang et al., 2012), in which particulate
1465 absorption was considered, and a two-stream approximation was adopted. This new algorithm was
1466 found reliable by Mei et al. (2013a) by means of an extended comparison between the values of
1467 $\tau(0.55\ \mu m)$ retrieved from MODIS data and simultaneous AERONET measurements made at six

high-latitude Arctic stations (Andenes, Barrow, Ittoqqortoormiit, 0PAL, Thule, and PEARL) in April 2010 and April 2011 (i.e., during periods in which Arctic haze frequently occurs). A regression line with slope coefficient equal to +0.764 was found by applying the least squares method to a set of 70 MODIS retrieved values of $\tau(0.55\ \mu m)$ obtained with a 10 km × 10 km resolution plotted versus the corresponding AERONET measurements, with a regression coefficient equal to +0.81 and a root mean square error RMSE = 0.079. In particular, comparing the MODIS retrieved values of $\tau(0.55\ \mu m)$ with the AERONET measured values at the above stations, Mei et al. (2013a) found relative discrepancies between them ranging from a few percent to more than 30% in cases with $\tau(0.55\ \mu m) > 0.20$, presumably associated with strong Arctic haze extinction.

These results demonstrate the considerable potential of the APRS algorithm to retrieve $\tau(\lambda)$ at visible wavelengths over the Arctic, for highly reflective snow/ice surfaces and large solar zenith angles, as can be seen in the maps of $\tau(0.55\ \mu m)$ derived from the MODIS/Aqua observations made on 29 March and 3 May in 2006 (Fig. 22), using the method of Mei et al. (2013a).

5.2. Aerosol optical thickness retrievals over snow and ice using backscattered solar light

Of particular relevance for remote sensing applications in polar regions, are the multiple-view (MISR) and double-view (AATSR) sensors. The measurements made with these instruments allow the contribution from underlying bright surfaces (e.g., snow and ice) to be removed, assuming that the atmosphere is the same for observations made at different angles, in all cases where the atmosphere is not filled with broken clouds. MISR is a sensor built by the Jet Propulsion Laboratory (JPL) and hosted on the NASA Terra platform, which was launched on 18 December 1999, and became operational in February 2000. It was designed to measure the intensity of solar radiation reflected by the surface-atmosphere system in various directions and spectral bands, with the main mission of measuring the intensity of solar radiation reflected and absorbed by the Earth. The device is composed of nine separate digital cameras, each with four spectral bands (blue, green, red, and near-infrared), that view the Earth at nine different angles (Diner et al., 1998). The algorithms

1494 for AOT retrieval from the MISR observations are discussed in Martonchik et al. (1998a, 1998b)
1495 and Diner et al. (2005a), and further assessed by Martonchik et al. (2002) and Kahn et al. (2005,
1496 2010). Examining the MISR monthly Level-3 data (Monthly Global 0.5° x 0.5° Aerosol Product,
1497 MIL3MAE.004) recorded during the 2005-2012 period, the regional maps of monthly average AOT
1498 were determined in the present study, over the Arctic region for latitudes ≥ 67 °N, and the Antarctic
1499 region for latitudes ≥ 62 °S. The monthly average values of $\tau(0.55\ \mu m)$ collected over the Arctic
1500 region under cloudless sky conditions were separated into a pair of seasonal sub-sets for spring
1501 (March-April-May) and summer (June-July-August), from which the seasonal average maps of
1502 $\tau(0.55\ \mu m)$ shown in Fig. 23 were obtained. It can be seen that these results are very similar to those
1503 retrieved from the MODIS data in Fig. 20, with spring average values of $\tau(0.55\ \mu m)$ varying mainly
1504 from 0.10 to 0.25, and being higher than 0.20 (and sometimes exceeding 0.30) over large areas of
1505 Central and Eastern Siberia as in the North American sector, presumably associated with dense
1506 Arctic haze transport episodes. The average summer values of $\tau(0.55\ \mu m)$ were found to mainly
1507 range from 0.05 to 0.15, showing similar features to those detected by MODIS observations. With
1508 regard to this, it is worth mentioning that Campbell et al (2012) examined (i) MODIS and MISR
1509 observations made over the Arctic regions in 2007, obtaining estimates of $\tau(0.55\ \mu m)$ all lower than
1510 0.10, and (ii) a CALIOP data-set collected in 2007, determining mean day-time and night-time
1511 values of $\tau(0.532\ \mu m)$ all lower than 0.15. In addition, examining the CALIOP data recorded over
1512 the Arctic in 2008, Winker et al. (2013) obtained mean cloud-free day-time values of $\tau(0.532\ \mu m)$
1513 mainly lower than 0.05 and mean cloud-free night-time values of $\tau(0.532\ \mu m)$ not exceeding 0.10 in
1514 March-May and September-February. In particular, they determined average values of $\tau(0.532\ \mu m)$
1515 from the CALIOP observations made from 2007 to 2011 that were lower than: (i) 0.02 over inner
1516 Greenland, (ii) 0.08 over the GNS sector surrounding the Svalbard region, (iii) 0.12 over the
1517 Scandinavian area, (iv) 0.12 over the Western Siberian Sea sector, (v) 0.05 over the Eastern
1518 Siberian Sea sector, and (vi) 0.06 over the North-American sector of the Arctic Ocean. These data

1519 are in good agreement with ground-based sun-photometer measurements (Figs. 3-8) and
1520 AERONET/MAN ship-borne measurements (Figs. 8b and 14), which showed that $\tau(0.50\ \mu m)$
1521 mainly varies from 0.08 to 0.16 in spring and from 0.04 to 0.10 in summer.
1522 The same procedure was also followed in the analysis of MISR data recorded over Antarctica
1523 during the austral summer from 2005 to 2012 (Fig. 23), which indicates that the seasonal average
1524 values of $\tau(0.55\ \mu m)$ are lower than 0.10 over the greater part of the coastal ocean areas around
1525 Antarctica and vary mainly from 0.10 to 0.25 over the off-shore areas very far from the coasts, due
1526 to effective sea-salt production by strong winds. These features are very similar to those obtained
1527 from MODIS observations (Fig. 21) and those derived from the AERONET/MAN measurements
1528 carried out in the coastal and off-shore ocean areas surrounding the Antarctic continent (Fig. 13b).
1529 The AATSR sensor is a dual-view (nadir and 55^o forward) radiometer on board the European Space
1530 Agency (ESA) Environmental Satellite (ENVISAT), which was launched in March 2002 and is one
1531 of the satellite instruments designed for providing a well-calibrated long-term global data-set of
1532 satellite data for climate research (Grey and North, 2009). ENVISAT was on a sun-synchronous
1533 orbit with an equator passing time of about 10 am. AATSR has a ground pixel resolution which is
1534 equal to 1 x 1 km^2 at nadir and a swath width of 500 km, thus taking about six days to achieve full
1535 global coverage (three days at mid-latitudes). Observations in both views are made at seven
1536 wavelengths: 0.55 µm, 0.66 µm, 0.87 µm, 1.6 µm, 3.7 µm, 11 µm and 12 µm, the spectral
1537 resolution of visible channels is approximately 20 nm, which avoids atmospheric water vapour
1538 absorption regions in the electromagnetic spectrum. Contact was lost with ENVISAT on April 2012
1539 after 10 years of service. The follow-up SLSTR mission as currently foreseen on Sentinel-3 will
1540 ensure the continuity of the multi-view-angle method into the future.
1541 The reflectance at the TOA-level can be described as the sum of the atmospheric path reflectance
1542 (black surface reflectance) and the atmosphere-surface interaction (Kaufman et al., 1997). With the
1543 use of AATSR dual-view observations, the ratio between observations in the forward and nadir
1544 directions can be determined by calculating the difference between TOA reflectance and

1545 atmospheric path reflectance in both directions and taking features of the total atmospheric
1546 transmission into account (Istomina et al., 2010; Mei et al., 2013b). It is worth mentioning that the
1547 ratio of both AATSR directional observations is not sensitive to the snow albedo, which reduces the
1548 high snow albedo effect on AOT retrieval over the Arctic region. For pure snow, Istomina et al.
1549 (2009) used an analytical snow BRDF model to estimate the ratio of both directional observations
1550 with a correction for TOA reflectance, where this approach was affected by the shape of the BRDF
1551 and not by its magnitude (Vermote et al., 1997a). Mei and Xue (2013) used an equivalent snow and
1552 ice mixture pixel for the spectral surface reflectance: it is constructed using a linear mixing model
1553 of snow and ice spectra tuned by the Normalized Difference Snow Index (NDSI) as an indicator of
1554 snow cover. Before calculating NDSI, cloud and free water were masked and a Look-Up-Table
1555 method was used to retrieve AOT.
1556 Current operational AOT retrieval algorithms, such as MODIS DT (Levy et al., 2013), MISR
1557 algorithm (Diner et al.2005b; Kahn et al. 2010) and AATSR (Holzer-Popp et al., 2013), can
1558 determine AOT over the Arctic Ocean (Glantz et al., 2014). Evaluation of the MODIS/Aqua AOT
1559 product over Svalbard using a 9-year set of AERONET observations gives an accuracy of ±0.03 ±
1560 0.05 AOT (Glantz et al., 2014). The AOT maps defined by Holzer-Popp et al. (2013) in September
1561 2008 qualitatively show an overestimation over the Arctic Ocean compared with the 9-year mean
1562 values from the MODIS Aqua product, AERONET and Alfred Wegener Institute (AWI)
1563 observations, which have been separately estimated, giving values of AOT equal to ±0.031 ± 0.021,
1564 ± 0.031 ± 0.022, and ± 0.024 ± 0.052, respectively (Glantz et al., 2014). However, due to the high
1565 reflectance of surface encountered for large solar zenith angles in the Arctic (Mei et al., 2013a,
1566 Macdonald et al., 2014), it is very difficult to quantitatively retrieve AOT over snow and ice.
1567 Stamnes et al (2004) pointed out that the TOA reflectance is sensitive to AOT over both very bright
1568 and dark surfaces, demonstrating the possibility of retrieving AOT over Arctic regions. Recent
1569 publications (Istomina et al., 2011; Mei et al., 2013a; Mei et al., 2013b) show promising AOT
1570 results over snow/ice covered regions, as described below.

1571 Preliminary attempts based on the above concepts were tried by Istomina et al. (2010) to
1572 individualise cloud-free snow-covered areas using AATSR measurements, and to discriminate clear
1573 snow fields for the retrieval of AOT. In addition to the aerosol retrieval method at the above-
1574 mentioned visible and near-infrared wavelengths (Istomina et al., 2009), the AATSR measurements
1575 in the 3.7 μm channel were also utilized to retrieve AOT (Istomina et al., 2011). Radiative transfer
1576 simulations for the accumulation and coarse particle modes of four main aerosol components were
1577 conducted in order to represent the retrieved $\tau(\lambda)$ in the visible region of the spectrum. The
1578 advantage of this algorithm is that it can be used over any blackbody-like surface (open ocean, sea
1579 ice, snow-covered land). An example of its usage is shown in Fig. 24.
1580 Improved results were obtained by Mei et al. (2013b) using the Dual-View Multi-Spectral (DVMS)
1581 approach, in which the dual view is used to separately evaluate the contributions made by
1582 atmospheric aerosols and underlying surfaces to the reflectance measured by this satellite sensor at
1583 the TOA-level. The algorithm uses an analytical snow BRDF model to estimate the ratio of snow
1584 reflectances in the nadir and forward views, and the atmospheric contribution to the TOA-level
1585 reflectance, obtained using the dark pixel method over the adjacent ocean surface, by assuming that
1586 this value applies over nearby land surfaces in the absence of significant sources across the
1587 coastline. An iteration involving all four AATSR spectral channels in the visible and near-infrared
1588 is used to retrieve the most relevant $\tau(0.55\ \mu m)$ information. The method was illustrated for AATSR
1589 overpasses over Greenland in April 2009, during cloud-free sky periods.
1590 Some examples of the results achieved by Mei et al. (2013b) in Fig. 25 show the daily maps of
1591 $\tau(0.55\ \mu m)$ retrieved from AATSR data recorded on four days in April 2009 with 1 km × 1 km
1592 resolution over the western part of Greenland, under cloud-free sky conditions. It can be seen that
1593 $\tau(0.55\ \mu m)$ had very low values smaller than 0.10, with little spatial variation for moderate
1594 contributions of sea spray aerosol associated with the very low wind speeds at the surface, as
1595 observed on the chosen days.

A comparison test between the values of $\tau(0.55\ \mu m)$ retrieved using the DVMS approach for high-quality AATSR observations and the corresponding AERONET values measured at Thule (North-western Greenland) during April 2009 exhibited a good correlation, with a regression coefficient equal to + 0.76 (Mei et al., 2013b). However, it should be mentioned that such good results were obtained for a selected set of measurements, containing a high number of cases with $\tau(0.55\ \mu m) >$ 0.12, due to the frequent occurrence of Arctic haze episodes in April. A synergetic approach to retrieve aerosol optical characteristics over the Arctic, using data from the MODIS sensor mounted onboard the Terra and Aqua platforms and prior knowledge of aerosol optical parameters retrieved over snow (as assumed in the APRS procedure), was presented by Mei et al. (2013a). Bearing in mind that cloud contamination can cause abnormally high retrieved values of AOT, the analysis of MODIS data was limited to only clear-sky pixels selected through MODIS cloud products and visual inspection. In applying the APRS procedure, it was realistically assumed that the aerosol optical parameters do not change during the time between the overpasses of Terra and Aqua platforms. A comparison was also made between the values of $\tau(0.55\ \mu m)$ retrieved over Greenland from MODIS observations following the APRS procedure and those derived from AATSR data with the DVMS method. This comparison showed that the APRS values of $\tau(0.55\ \mu m)$ ranged from 0.07 to 0.09 over the monitored areas, while the DVMS ones were mainly ~0.09, and exhibited a maximum value just 0.6% lower than that derived from MODIS data.

It has to be mentioned that the global application of the above-cited AOT retrieval algorithms for both MODIS and AATSR is still very much limited due to several challenges which are listed below. For instance, one of the major issues is the cloud masking over snow and ice. Cloud screening for AOT retrieval in the Arctic is a challenge due to the similarity of snow/ice and cloud reflective properties in the visible region of the spectrum. The sensitivity of AOT retrievals over snow to atmospheric particulate matter implies a potentially high contamination of the aerosol product with eventually unscreened clouds. It is for these two reasons that many cloud masking algorithms developed for a general case of multiple surface types, such as open water, vegetation

and various soils, are of questionable quality over snow and ice. An example of this is the operational AATSR cloud mask provided with the level 1b AATSR product (Istomina et al., 2010). The main approach to distinguishing clouds from the underlying surface is that clouds are generally brighter and colder than the underlying surface. However, this is not always the case over snow/ice covered regions such as the Arctic. A prominent spectral signature of snow and ice makes it possible to discriminate clouds using NIR and TIR channels. At the same time, not all sensors have such channels. Therefore, cloud screening algorithms over snow differ from sensor to sensor in order to most effectively utilize the available features (which are not only the spectral and spatial resolution, but also different observation directions and polarization measurements). The resulting cloud mask over snow and ice obtained from different sensors also differs in quality. Employing absolute or relative thresholds (e.g. NDSI or NDVI) in the available VIS, NIR and IR channels to separate clouds from snow and ice is a commonly used approach which gives a robust cloud mask over snow for common applications (MERIS, AATSR, SCIAMACHY) (Allen et al., 1990; Istomina et al., 2010; Schlundt et al., 2011). However, as the thresholds are often empirically derived and based on a limited data set, this approach might have drawbacks when it comes to particular surface or cloud types, e.g. ice clouds over snow. Possible mis-classification here could be: (1) mistaking heavy aerosol loads for clouds, as e.g. might be the case of MODIS test BT11 - BT3.9 (Ackerman et al., 2010), or (2) mistaking snow surfaces for clouds as in MODIS test BT11 - BT12, which is used to detect cirrus over many surface types also covered by snow and ice (Ackerman et al., 2010). Mis-classification may occur due to snow emissivity being sensitive to grain size at these wavelengths, and creating a difference between the brightness temperatures BTs recorded in the 11 and 12 μm channels (Hori et al., 2006).

A snow BRDF model can also be used to derive the threshold value for the NIR spectral channel, as shown by Spangenberg et al. (2001) and Trepte et al. (2001). This approach might have difficulties in distinguishing cloudy conditions from cloud-free but aerosol-polluted scenarios. The best results can be obtained by combining the various approaches such as thresholding, image clustering,

supervised and unsupervised classification, usage of oxygen and water vapour absorption bands if available (e.g. MERIS) (Gomez-Chova et al., 2007) together with usage of external topography data, land/water masks, ecosystem maps and daily operational snow/ice products (MODIS, MISR) (Ackerman et al., 1998; Liu et al., 2004; Shi et al., 2002, 2007). The MODIS cloud mask product with confidence cloudy flag generally works well for thick warm clouds over the Arctic by using 19 channels and auxiliary inputs such as the topography, but will have difficulties with optically thin cold clouds such as cirrus due to the similarity of both cloud types. A comprehensive combined cloud mask is also available for AVHRR (Saunders and Kriebel, 1988; Gesell, 1989; Key and Barry, 1989; Han et al., 1999). However, the challenge of applying a cloud mask over snow is still current even for radiometers equipped with IR and NIR bands.

Another challenge of any AOT retrieval over snow is the variability of snow and sea ice types in the field, the effect of surface melt or ageing, pollution, and regarding sea ice the effect of varying sea ice concentrations. All these effects make it difficult to reliably account for the surface signal contribution to AOT for retrievals over snow surfaces even when double-viewing observational techniques (e.g. AATSR or simultaneous MODIS Terra and Aqua usage) are used. At the same time, as the AOT in the Arctic is rather low (background values ~ 0.05, up to 0.1-0.3 during haze events with occasionally higher peaks), the surface signal is responsible for the greatest part of the TOA signal measured by satellites. Multispectral AOT retrievals are in addition challenged by a high variability in ice and snow surface types, depending on grain size, pollution, density, etc (Warren and Wiscombe, 1980; Negi et al., 2010). The variability of the aerosol types, which includes a varying scattering phase function shape, spectral behaviour and particle size distribution, makes it even more challenging to reliably retrieve the AOT, especially when spectral information on both the surface and atmosphere is used simultaneously. The sensitivity to complex polar atmospheric conditions and temperature inversions (especially for IR channels used for the retrieval or the cloud mask) are currently not taken into account and also need to be investigated. The satellite-retrieval algorithms proposed by Istomina et al. (2011), Mei et al. (2013a) and Mei et al.

(2013b) can only be used for an initial qualitative evaluation of the atmospheric aerosol load and only for selected apparently cloud-free scenes. They are able to give a correct impression of spatial and temporal AOT distributions on a regional scale under the assumption that the surface and aerosol properties do not change, but need to be further improved with more flexibility regarding surface types, their extensive validation and specifically developed cloud masking being the first priorities. Due to the above listed issues and challenges, application on a global basis is currently not possible.

6. Optical characteristics of Arctic and Antarctic aerosols

To obtain a realistic representation of the optical properties of atmospheric aerosol derived from ground-based and ship-borne sun-photometer measurements, a set of aerosol extinction models has been defined here by taking into account the evaluations of aerosol radiative parameters determined from sun-photometric and *in-situ* optical measurements made at various Arctic and Antarctic sites. The main results obtained for the fine, accumulation and coarse mode particles are presented in the following two sub-sections for four Arctic and four Antarctic aerosol types.

6.1 Arctic aerosol particle size-distributions and optical characteristics

Multi-year measurements of aerosol chemical composition and light scattering and absorption coefficients were conducted at Barrow by Quinn et al. (2002), separately for the sub-micron and super-micron particle modes, showing that: (i) extinction effects are dominated by sulphate fine particles during the spring-time Arctic haze episodes, and by sea-salt accumulation mode particles formed from wind-driven sea spray in winter, and (ii) sub-micron sulphate and sea-salt particles efficiently contribute during summer to attenuate the incoming solar radiation. Both sulphate and sea-salt particle concentrations followed well-defined annual cycles at Barrow, Alert and Arctic EMEP sites (Quinn et al., 2007). Bimodal features of the aerosol size-distribution were reported at Barrow by Delene and Ogren (2002), who found that the overall visible light scattering and

absorption at the ground-level is given over the entire year by two particle modes: (i) an accumulation mode (with mode diameter D_c < 1 μm) yielding annual mean values of volume scattering coefficient β_{sca} = 6.17 ± 3.61 Mm^{-1}, volume absorption coefficient β_{abs} = 0.36 ± 0.38 Mm^{-1}, ground-level Ångström exponent α_o = 1.67 ± 0.36, and ground-level single-scattering albedo ω_o = 0.954 ± 0.028; and (ii) a coarse mode (with D_c < 10 μm), giving annual mean values of β_{sca} = 9.76 ± 5.20 Mm^{-1}, β_{abs} = 0.39 ± 0.41 Mm^{-1}, α_o = 1.11 ± 0.39, and ω_o = 0.965 ± 0.023.

Multimodal features of the fine particle size-distribution were also reported by Ström et al. (2003) on examining particulate matter sampled at the Zeppelin station (near Ny-Ålesund) with a Differential Mobility Particle Sizer (DMPS) over the D < 1 μm diameter range. For such multimodal characteristics of the sub-micron aerosols and considering that α varies throughout the year from more than 1.8 (for prevailing extinction by fine particles) to less than 1 (for predominant attenuation by coarse particles), a set of particulate extinction models is proposed here, each given by a linear combination of a fine particle mode with an accumulation or coarse particle mode, to represent the optical properties of airborne aerosols. In this approach, the overall size distribution can be defined for a certain value of α by varying the percentage number density concentrations of both modes until the measured value of α is fitted.

Each aerosol unimodal size-distribution curve was represented by a log-normal curve having the analytical form,

$$N(r) = dN(r)/d(Log\, r) = \frac{N_o}{\sqrt{2\pi}\ (\ln 10)\ (Log\, \sigma)} \exp\left[-\frac{1}{2}\left(\frac{Log\, r - Log\, r_c}{Log\ \sigma}\right)^2\right], \qquad (3)$$

where N_o is the total particle number concentration (measured in cm^{-3}), ln 10 is a constant approximately equal to 2.3026, *Log* is the decadal logarithm (with base = 10), σ is the geometric standard deviation, and r_c is the mode radius (measured in μm). Thus, the following size-distribution curves were defined to represent four different Arctic aerosol types:

1723 (1) The size-distribution curve of winter-spring Arctic haze particles, consisting of: (i) a fine
1724 particle mode of dry-air Arctic water-soluble aerosol, and (ii) an accumulation particle mode of sea-
1725 salt particles, according to the Hess et al. (1998) OPAC models.
1726 (2) The average size distribution of summer background aerosols, consisting of: (i) a fine particle
1727 mode predominantly composed of mineral dust nuclei and water-soluble substances, and (ii) a
1728 coarse particle mode of sea-salt particles, as defined by Hess et al. (1998).
1729 (3) The average size distribution curve of Asian dust, consisting of: (i) a mineral dust nuclei mode,
1730 and (ii) a mineral coarse particle mode, having features similar to those represented by Hess et al.
1731 (1998) in the mineral dust OPAC models, and chosen to simulate an episode of Asian dust transport
1732 over a ground-layer of unpolluted aerosol observed by Stone et al. (2007) at Barrow.
1733 (4) The overall size-distribution curve of a summer background aerosol model containing BFF
1734 smoke, assumed to consist of: (i) a fine combustion particle mode, and (ii) an accumulation particle
1735 mode. Both modes were assumed to consist of a mixture of combustion dust and soot particles
1736 giving a ratio of 12.86 between the scattering and absorption coefficients, leading to a single-
1737 scattering albedo value $\omega = 0.928$, as indicated by the *in-situ* measurements conducted by Mielonen
1738 et al. (2013) for Russian wildfire particles.
1739 Each of the above eight modes was represented in terms of Eq. (3) for the values of shape-
1740 parameters r_c and σ given in Table 5, while the unimodal optical/chemical characteristics were
1741 represented assuming the mass percentages of the 6S dry-air components defined by Vermote et al.
1742 (1997a) and provided in Table 5 for each pair of modes, according to the chemical composition
1743 estimates made by Quinn et al. (2007) and Tomasi et al. (2012).
1744 The spectral values of the real $n(\lambda)$ and imaginary $k(\lambda)$ parts of the particle refractive index obtained
1745 for the Arctic aerosol models given in Table 5 were found to decrease very slowly with wavelength
1746 over the 0.40-1.0 μm spectral range. They are reported in Table 5 for λ = 0.55 μm, together with
1747 values of the single-scattering albedo $\omega(0.55\ \mu m)$, asymmetry factor $g(0.55\ \mu m)$, volume extinction
1748 coefficient $\beta_{ext}(0.55\ \mu m)$, and exponent α. It can be seen in Table 5 that the single-scattering albedo

1749 $\omega(0.55\ \mu m)$ of the fine Arctic haze particle mode is equal to 0.86 and that of the accumulation mode
1750 is equal to 0.937. Therefore, using the present bimodal model, $\omega(0.55\ \mu m)$ is made to vary over the
1751 0.86-0.94 range as a function of the mass fractions of the fine and accumulation particles. The
1752 assumptions made for this optical parameter agree very well with ground-level measurements of
1753 $\omega_o(0.55\ \mu m)$ obtained from *in-situ* nephelometer and aethalometer [(*)] measurements carried out by:
1754 (i) Bodhaine (1995), who estimated a monthly mean value of 0.928 in March at Barrow, (ii) Sharma
1755 et al. (2006), who determined an average value of 0.94 from February to May at Barrow, and (iii)
1756 Ström et al. (2003), who estimated a monthly mean value $\omega_o(0.55\ \mu m) = 0.94$ in spring at Zeppelin,
1757 and monthly mean values varying from 0.84 to 0.91 in late autumn and winter.
1758 The calculations presented in Table 5 provide a single-scattering albedo value $\omega(0.55\ \mu m) = 0.93$
1759 for the Arctic summer background fine particle mode, and 0.81 for the corresponding coarse
1760 particle mode, suggesting that $\omega(0.55\ \mu m)$ varies mainly over the 0.81-0.93 range during the Arctic
1761 summer. The results do not differ considerably from those of: (i) Ström et al. (2003), who found
1762 that $\omega_o(0.55\ \mu m)$ assumes values varying mainly from 0.94 to 0.98 in spring and summer at
1763 Zeppelin, and (ii) Tomasi et al. (2012), who obtained monthly mean values of $\omega_o(0.55\ \mu m)$ equal to
1764 0.93 ± 0.04 in June, 0.86 ± 0.09 in July, 0.91 ± 0.08 in August, and 0.89 ± 0.09 in September,
1765 yielding a seasonal average value of 0.90 ± 0.07 at Ny-Ålesund during summer 2010. The values of
1766 $\omega(0.55\ \mu m)$ assumed in Table 5 for the Asian dust are close to 0.96 for the fine particle mode and
1767 0.67 for the coarse particle mode, indicating that this parameter is presumably subject to decrease
1768 gradually as α assumes lower values as a result of the increase in the relative super-micron dust
1769 content. The fine and coarse particle components of the BFF smoke were both found to yield values
1770 of $\omega(0.55\ \mu m)$ close to 0.90, according to Mielonen et al. (2013).

[(*)] for detailed technical characteristics of the two instruments, see Bodhaine (1995), and Anderson and Ogren (1998).

1771 The angular distribution curves of phase function $P(\Theta)$ determined for the eight unimodal size-
1772 distribution curves defined in Table 5 to represent the four Arctic aerosol types are shown on the
1773 left-hand side of Fig. 26. The calculations clearly show that the most pronounced forward scattering
1774 lobe is produced by the Asian dust coarse mode and, to a lesser extent, by the coarse mode of Arctic
1775 summer background aerosol, which yields the lowest lateral scattering (at Θ = 90°) and the
1776 strongest backward scattering (at Θ = 180°).
1777 The linear combinations of fine and accumulation/coarse particle modes considered in Table 5 for
1778 the four Arctic aerosol types were made to vary until best-fit values of α were obtained from field
1779 sun-photometer measurements, which provide the unimodal column particle number concentrations
1780 for each field-measured value of $\tau(0.50\ \mu m)$. The following four cases were examined: (a) the
1781 winter-spring aerosol case recorded at Eureka during the Arctic haze periods of 2007 and 2008,
1782 with average values of $\tau(0.50\ \mu m)$ = 0.12 and α = 1.48, (b) the summer background aerosol case
1783 determined at Tiksi, giving mean values of $\tau(0.50\ \mu m)$ = 0.08 and α = 1.60, (c) the Asian dust
1784 transport episode observed at Barrow on 16 April, 2002, yielding average daily values of $\tau(0.50$
1785 $\mu m)$ = 0.22 and α = 0.26, and (d) the BFF smoke case observed by Stock et al. (2012) at Ny-
1786 Ålesund on 23 March, 2008, giving average daily values of $\tau(0.50\ \mu m)$ = 0.22 and α = 1.50. The
1787 best-fit bimodal size-distribution curves determined for the four cases are presented on the left-hand
1788 side of Fig. 27, together with the corresponding column particle number concentration of the fine
1789 mode (N_f) and accumulation/coarse mode ($N_{a/c}$). The bimodal size-distribution curves obtained for
1790 the winter-spring case (a) and the BFF smoke case (d) exhibit in practice a nearly unimodal shape,
1791 since $N_{a/c}$ is lower than N_f by about 7 orders of magnitude in case (a) and by more than 4 orders of
1792 magnitude in case (d). Conversely, the bimodal size-distribution curves obtained in cases (b) and
1793 (c), each using one of the coarse particle modes defined in Table 5, exhibit rapidly decreasing right-
1794 hand wings of the columnar number content over the whole super-micron radius range, associated
1795 with sea-salt and dust particle loads.

1796

1797 *6.2. Antarctic aerosol particle size-distributions and optical properties*

1798 Multimodal characteristics of the aerosol size-distribution curves were also reported at Antarctic
1799 coastal and high-altitude sites. Analyzing a set of size-segregated particle samples collected at
1800 Mario Zucchelli (Terra Nova Bay) in austral summer 1995, over the 0.035-16 μm aerodynamic
1801 diameter range, Hillamo et al. (1998) found that the particle size distribution usually consists of four
1802 modes: (i) a mode of Aitken nuclei and fine particles, with mode diameter D_c = 0.07 μm, which
1803 contributes ~ 1% to the total particulate mass content, (ii) an accumulation particle mode with $D_c \approx$
1804 0.30 μm, contributing 14%, (iii) a large particle mode with $D_c \sim 2$ μm (22%), and (iv) a coarse
1805 particle mode with $D_c \approx 6.5$ μm (63%). Similar results were obtained by Weller and Lampert (2008)
1806 at Neumayer, revealing a seasonal cycle characterized by nss sulphate particles in austral summer,
1807 which dominated optical effects, and prevailing extinction by sea-salt aerosol in the other seasons.
1808 They found an average aerosol mass concentration at ground-level close to 1.1 μg m^{-3} in austral
1809 winter and 1.3 μg m^{-3} in austral summer. The average chemical composition of particulate mass
1810 consisted of: (i) 48% sea-salt, 33% nss sulphate, 12% MSA, and ~ 7% nitrates mixed with mineral
1811 dust and ammonium during the austral summer, and (ii) 93% sea-salt particles, with a few percent
1812 of nss sulphate, nitrate, MSA, ammonium and mineral dust in the austral winter. Minikin et al.
1813 (1998) found that the nss sulphate and MSA concentrations measured in the austral summer at the
1814 coastal stations of Neumayer, Halley and Dumont d'Urville are closely correlated, showing a
1815 regular sequence of pronounced peaks of both such biogenic sulphur aerosol components, mainly
1816 formed from dimethyl sulfide (DMS).

1817 The aerosol chemical composition was investigated at the Finnish station of Aboa, about 150 km
1818 from the Atlantic Ocean coast in Queen Maud Land, by Kerminen et al. (2000), Teinilä et al. (2000)
1819 and Koponen et al. (2003), who analysed sets of regular aerosol sampling measurements conducted
1820 from December 1997 to February 1998. The sea-salt particle concentration was estimated to be

1821 considerably lower than those measured at Mario Zucchelli and Neumayer. Multimodal features of
1822 the particle size distribution curve were detected in most cases over the $0.045 \leq D \leq 15$ μm range,
1823 with five principal modes: (i) a first mode of fine particles, over the 0.03-0.10 μm range, consisting
1824 of 63% nss sulphate, 29% ammonium, and 8% MSA mass percentages, (ii) two accumulation
1825 particle modes, with average values of D_c close to 0.30 and 0.65 μm, both consisting on average of
1826 61% nss sulphate, 22% MSA, and ~ 14% ammonium, besides a few percents of sea-salt particles,
1827 (iii) a large particle mode, with D_c varying from 1.4 to 1.9 μm, and consisting of 52% sea-salt, 27%
1828 nss sulphate, 12% MSA, and minor percentages of nitrates and ammonium ions, and (iv) a coarse
1829 particle mode, with daily mean values of D_c varying from 2 to 5 μm, and containing on average
1830 63% sea-salt, 16% nitrate, 14% nss sulphate, 5% MSA and 2% ammonium. These compositional
1831 characteristics indicate that biogenic sulphur compounds constitute on average more than 90% of
1832 the aerosol mass concentration of sub-micron particles, ~ 50% of the accumulation mode particle
1833 mass, and ~ 30% of the coarse mode particle mass. Correspondingly, sea-salt particles were found
1834 to mainly contribute to the super-micron aerosol mode by more than 60% on average. The above
1835 results were substantively confirmed by Virkkula et al. (2006), who analysed a large set of
1836 particulate samples collected in January 2000 using a 12-stage low-pressure impactor, and observed
1837 a pair of sea-salt particle modes centred at $D_c \approx 0.8$ μm and $D_c \approx 3$ μm, respectively, and a pair of
1838 nitrate particle modes centred at diameters D_c of ~ 1.2 μm and ~ 3 μm.
1839 The Antarctic Plateau aerosol size-distribution were found to consist of a fine particle mode mainly
1840 composed of nss sulphate and MSA substances at South Pole during the austral summer (Hara et
1841 al., 2004), when aerosols are predominantly due to strong subsidence effects from the free
1842 troposphere. However, sea-salt accumulation and coarse particles can be often transported over the
1843 Antarctic Plateau in air masses with relatively high mass concentrations on days characterised by
1844 intense advection of oceanic air masses over the interior of Antarctic continent, associated with
1845 large storm systems (Shaw, 1988). Therefore, in the particular cases yielding values of α

1846 appreciably lower than 1.8, the overall particle size-distribution was represented using a bimodal
1847 size-distribution model consisting of a fine particle mode mainly containing nss sulphates and a sea-
1848 salt coarse particle mode.
1849 On the basis of the above measurements, the following size-distribution curves were considered:
1850 (a) The average size distribution of Antarctic austral summer coastal aerosol was assumed to be
1851 bimodal, since the extinction effects produced by the Aitken nuclei and very fine particle modes
1852 reported by Hillamo et al. (1998) were neglected. It was represented by the linear combination of:
1853 (i) a first particle mode consisting of fine nss sulphate and sea-salt accumulation mode aerosols,
1854 with low contents of mineral nuclei and soot particles, and (ii) a coarse mode mainly composed of
1855 sea-salt particles. The composition of both modes was defined using the 6S (Vermote et al., 1997b)
1856 mass percentages reported in Table 5, according to the composition data calculated by Tomasi et al.
1857 (2012) at Mario Zucchelli and Neumayer. In both particle modes, the soot mass concentration was
1858 assumed taking into account the low values of BC mass concentration measured by Wolff and
1859 Cachier (1998) at Halley during the austral summer, ranging in general from 1.0 to 2.0 ng m^{-3}.
1860 (b) The average size distribution of austral summer background aerosol over the Antarctic Plateau
1861 was represented by: (i) a fine particle mode mainly containing nss sulphates and minor percentages
1862 of sea-salt and dust particles, with a soot content equal to 40% of that estimated by Wolff and
1863 Cachier (1998) at a coastal site. and (ii) a coarse particle mode composed mainly of sea-salt
1864 particles, and containing lower mass percentages of water-soluble and dust-like 6S (Vermote et al.,
1865 1997b) components, as given in Table 5.
1866 (c) The average size-distribution of Antarctic austral winter aerosol at coastal sites was not based on
1867 sun-photometer measurements, as such measurements have neither been conducted during the
1868 austral winter at coastal sites (for 66° - 75° S latitudes) nor at Antarctic Plateau stations. In order to
1869 achieve reliable evaluations of complex refractive index $n(\lambda) - i\ k(\lambda)$ and the other radiative
1870 parameters during the austral winter, the chemical composition data determined by Minikin et al.
1871 (1998) at Neumayer and other Antarctic coastal sites over the 14-year period from 1983 to 1996

were taken into account. These *in-situ* measurements showed a regular sequence of pronounced mass concentration minima of biogenic sulphur aerosol components originating from DMS in austral winter and some marked peaks in summer. In particular, they found that: (i) the nss sulphate mass concentration decreased on average from 50 to 4 ng m^{-3} (i.e. by 92%) from austral summer to winter, and (ii) MSA mass concentration decreased from 17 to 2 ng m^{-3} (i.e. by more than 88%), because of a strong reduction in biogenic sources of both chemical species during the local winter. Conversely, the sea-salt particle mass concentration was estimated by Weller and Lampert (2008) to increase at Neumayer by more than 40%, passing from an average summer value of 597 ± 830 ng m^{-3} to an average winter value of 844 ± 1100 ng m^{-3}. Despite the plausible strong decrease in sea-salt particle concentration caused by the ice coverage of the ocean areas near the Antarctic continent, the observed austral winter increase in the sea-salt concentration was probably due to the more intense transport of maritime particles from the lower latitude oceanic ice-free areas characterised by higher wind speed conditions at the sea-surface.

On the basis of these remarks, it was decided to use a bimodal model to represent the austral winter aerosol at coastal sites, consisting of: (i) a fine water-soluble particle mode, and (ii) an accumulation particle mode composed mainly of sea-salt particles transported from remote ocean areas. Each mode of the three Antarctic bimodal size-distribution curves was assumed to have an analytical form given by Eq. (3) for the values of shape-parameters r_c and σ reported in Table 5, and to consist of the mass percentages defined in Table 5 for the four 6S (Vermote et al., 1997b) basic components.

Because of the predominant mass fractions of nss sulphate in the fine particle mode and of sea-salt in the accumulation/coarse mode, the three bimodal size-distributions of Antarctic particles considered above provided the unimodal average values of refractive index parts $n(0.55\ \mu m)$ and $k(0.55\ \mu m)$ given in Table 5. For these aerosol extinction models, values of $\omega(0.55\ \mu m)$ ranging from ~ 0.80 (for the coarse mode of coastal aerosols) to 0.99 (for the accumulation mode of austral winter aerosol) were obtained (see Table 5). These estimates of $\omega(0.55\ \mu m)$ agree very well with the

in-situ evaluations made by: (i) Virkkula et al. (2006a, 2006b) at Aboa, who obtained values of $\omega_o(0.55\ \mu m) > 0.95$ for about 93% of *in-situ* measurements, and < 0.90 for only 3.5% of cases, (ii) Weller and Lampert (2008) at Neumayer, who estimated that $\omega_o(0.55\ \mu m)$ varied from 0.97 to 1.00 in more than 95% of samples, and (iii) Tomasi et al. (2012), who found values of $\omega_o(0.55\ \mu m)$ mainly ranging from 0.95 to 0.98 for the particulate chemical composition measurements made by Hillamo et al. (1998) and Fattori et al. (2005) at Mario Zucchelli, and those conducted by Weller and Wagenbach (2007), Weller et al. (2008), and Weller and Lampert (2008) at Neumayer. These findings are in good agreement with the *in-situ* evaluations made by: (i) Bodhaine (1995), who obtained monthly mean values of $\omega_o(0.55\ \mu m)$ at South Pole, varying from 0.942 to 0.972 during the austral summer, and an annual mean value of $\omega_o(0.55\ \mu m) = 0.97$, (ii) Heintzenberg et al. (1997), who determined an annual average value of $\omega_o = 0.965$ in the visible at South Pole; and (iii) Tuncel et al. (1989) and Arimoto et al. (2004) at South Pole, and Piel et al. (2006) at Kohnen, who obtained values of $\omega_o(0.55\ \mu m)$ ranging from 0.95 to 0.98.

The daily mean values of $\tau(0.55\ \mu m)$ retrieved by Campbell et al. (2012) from the 2007 MODIS and MISR satellite observations recorded over Antarctica were all lower than 0.10 throughout the whole year. Reliable measurements of AOT were not retrieved by Winker et al. (2010) from the CALIOP lidar observations during the Antarctic "polar night", since they were lower than the lidar detection limit. This was confirmed by Winker et al. (2013), who showed that the CALIPSO mean cloud-free day-time and night-time values of $\tau(0.532\ \mu m)$ were all lower than 0.05 over the Antarctic continent and the peri-Antarctic regions during the long austral winter, from March to November. Therefore, the AOT contribution exhibited by fine particles is in general < 0.01 in the austral winter months, while that of sea-salt accumulation mode particles increases appreciably yielding daily values of $\tau(0.50\ \mu m)$ varying from 0.02 to 0.05 during the coldest season, and values of α mainly ranging from 0.50 to 0.70 over the peri-Antarctic regions (Winker et al., 2013).

1922 The angular diagrams of phase function $P(\Theta)$ obtained for the unimodal size-distribution curves
1923 defined in Table 5 for the three Antarctic aerosol types are presented on the right-hand side of Fig.
1924 26 as a function of scattering angle Θ. The most pronounced forward scattering lobe is given by the
1925 coarse particle mode of the austral summer coastal aerosol, while the austral summer coarse particle
1926 mode of the Antarctic Plateau size-distribution yields a slightly lower forward scattering lobe and
1927 the most marked backward and lateral (at $\Theta = 90°$) scattering intensities. As a result, four case
1928 studies of Antarctic aerosol were analysed to determine the corresponding best-fit linear
1929 combinations of fine and accumulation/coarse particle modes, for the following sets of $\tau(0.50\ \mu m)$
1930 and α: (i) the austral summer coastal aerosol case (e) obtained at Mario Zucchelli for the mean
1931 values of $\tau(0.50\ \mu m) = 0.030$ and $\alpha = 0.90$, (ii) the austral summer coastal aerosol case (f)
1932 determined at Neumayer for the mean values of $\tau(0.50\ \mu m) = 0.043$ and $\alpha = 0.68$, (iii) the austral
1933 summer Antarctic Plateau aerosol case (g) defined at South Pole for the mean values of $\tau(0.50\ \mu m)$
1934 $= 0.018$ and $\alpha = 1.49$, and (iv) the austral winter aerosol case (h) defined on the basis of *in-situ*
1935 aerosol measurements conducted during the austral winter months at Neumayer and evaluated to
1936 give the average seasonal values of $\tau(0.50\ \mu m) = 0.035 \pm 0.015$ and $\alpha = 0.65 \pm 0.10$. The bimodal
1937 size-distribution curves obtained by applying the best-fit procedure for the four values of α given
1938 above are shown on the right-hand side of Fig. 27, where the columnar number contents N_f and $N_{a/c}$
1939 are also given. The size-distribution curves obtained in cases (e), (f) and (g) by assuming the
1940 presence of a coarse mode are characterized by robust right-hand wings over the super-micron
1941 radius range. In fact, in the two coastal cases (e) and (f), the columnar number content $N_{a/c}$ is lower
1942 than N_f by more than 6 and 5 orders of magnitude, respectively. Figure 27 also shows that the
1943 relative contribution of sea-salt coarse mode particles is appreciably higher at Neumayer than at
1944 Mario Zucchelli, according to the results shown in Figs. 9 and 11, respectively. Considerably
1945 different values of N_f and $N_{a/c}$ by at least nine orders of magnitude were found in case (g) for the
1946 Antarctic Plateau aerosol, giving a measure of the large differences characterizing the atmospheric

concentrations of nss sulphate fine mode and sea-salt coarse mode particles. By contrast, the accumulation mode used in case (h) to represent the sea-salt particles during the austral winter seems to contribute more weakly (by only 4 orders of magnitude) to enhance $N_{a/c}$, with respect to N_f.

6.3. Evaluations of direct aerosol-induced radiative forcing effects in polar regions

Atmospheric aerosols are known to affect the radiation balance of the surface-atmosphere system (i) directly through interaction with solar (short-wave) radiation (Haywood and Boucher, 2000) and terrestrial (long-wave) radiation (Lubin et al., 2002), and (ii) indirectly, by acting as cloud condensation nuclei and modifying cloud albedo characteristics (Schwartz and Andreae, 1996). They can considerably modify the horizontal and vertical distribution of radiant energy passing through the atmosphere (Stone et al., 2008), generally causing more intense changes in the outgoing flux of solar radiation at TOA-level than those affecting the long-wave radiation, as clearly indicated by Mie (1908) theory. For this reason, the direct aerosol-induced radiative forcing (hereinafter referred to as DARF) is commonly evaluated by only considering variations induced by airborne aerosols on the short-wave radiation flux and by neglecting those affecting long-wave radiation. Instantaneous DARF effects can vary on a diurnal basis as a function of solar zenith angle θ_0, and closely depend on: (a) aerosol scattering and absorption characteristics (represented in terms of parameters $\tau(\lambda)$, α, $n(\lambda)$, $k(\lambda)$, $P(\Theta)$, $g(\lambda)$, and $\omega(\lambda)$ at solar wavelengths), and (b) the spectral and geometrical features of surface reflectance. Three different instantaneous DARF terms are usually considered in these calculations: (i) at the TOA-level, as the difference $\Delta F_{TOA}(t)$ estimated at a certain time t between the upward solar radiation fluxes emerging from the real atmosphere with aerosols and from the pristine atmosphere without aerosols (Hänel et al., 1999), (ii) at the bottom-of-atmosphere (BOA) level (i.e. at the surface), as the difference $\Delta F_{BOA}(t)$ estimated at a certain time t between the net short-wave fluxes determined at surface-level in the atmosphere with aerosols and in the same atmosphere assumed without aerosols (Satheesh and Ramanathan, 2000),

and (iii) within the atmosphere, as the difference $\Delta F_{ATM}(t)$ between terms $\Delta F_{TOA}(t)$ and $\Delta F_{\mathrm{BOA}}(t)$ (Ramanathan et al., 2001). To give an average measure of the daily DARF effects, the instantaneous terms $\Delta F_{TOA}(t)$, $\Delta F_{BOA}(t)$ and $\Delta F_{ATM}(t)$ are generally evaluated at pre-fixed hours of the day, and then integrated over the entire period from sunrise to sunset, and divided by the 24-hour period. The corresponding diurnally averaged DARF terms ΔF_{TOA}, ΔF_{BOA} and ΔF_{ATM} were calculated by following such a procedure, based on the Bush and Valero (2003) criteria. Negative values of ΔF_{TOA} indicate that aerosols cause an increase in the radiation budget of the surface-atmosphere system at TOA-level, producing direct cooling effects on the climate system, while positive values of ΔF_{TOA} indicate the occurrence of a warming effect during the day. Term ΔF_{BOA} at the surface gives a measure of the perturbation induced by airborne aerosols in the net flux reaching the surface, which may be positive (warming) or negative (cooling), while term $\Delta F_{ATM} = \Delta F_{TOA} - \Delta F_{BOA}$ defines the radiation surplus (or deficit) induced by aerosols within the atmosphere. In practice, ΔF_{ATM} is the amount of latent heat released in the atmosphere by aerosols and internally redistributed with the effects of modifying both temperature gradients and atmospheric circulation.

Calculations of ΔF_{TOA}, ΔF_{BOA} and ΔF_{ATM} have been made by Tomasi et al. (2014) using the radiative transfer 6S code of Vermote et al. (1997a) for the aerosol loads and composition, and optical characteristics defined in Table 6, pertaining to 11 Arctic aerosol types and 4 Antarctic background austral summer aerosol types. The calculation procedure consisted of the following seven steps:

(i) Determination of the columnar aerosol extinction parameters $\tau(\lambda)$ and α from the field sun-photometer measurements collected at Barrow, Ny-Ålesund, Summit, Sodankylä, Tiksi, Mario Zucchelli, Neumayer, Dome Concordia and South Pole, from which the average values of $\tau(0.50\ \mu m)$ and $\alpha(0.40\text{-}0.87\ \mu m)$ given in Table 6 were obtained.

(ii) Calculation of the spectral values of parameters $n(\lambda)$ and $k(\lambda)$ for the chemical composition data based on the OPAC mass percentages of fine and accumulation/coarse particles defined by Hess et al. (1998) for the six OPAC basic components reported in Table 6 at 50% relative humidity of air.

(iii) Definition of the multimodal linear combinations of the size-distribution curves for the 15 aerosol types considered in Table 6 to fit the values of $\alpha(0.40\text{-}0.87\ \mu m)$ given in Table 6.

(iv) Calculation of the aerosol single scattering albedo $\omega(0.55\ \mu m)$ reported in Table 6 for the 15 multimodal size-distribution curves defined at the previous step.

(v) Selection of the BRDF surface reflectance models of Tomasi et al. (2013) to represent the surface reflectance characteristics of the land surfaces described in terms of MODIS Level 3.0 MCD43C3 products around the principal sun-photometer stations, and those of Arctic and Antarctic oceanic surfaces. The analysis of such observational data suggested that the following models were suitable in the present calculations: (a) the BRDF ocean surface reflectance model OS1, defined for surface wind velocity V_w = 2 m s^{-1} and giving a value of broadband albedo $A_b(\theta_0=60°)$ = 0.193, (b) the BRDF surface reflectance model VS1, yielding a value of $A_b(\theta_0=60°)$ = 0.155, and used to represent a land area covered by tundra and conifer forests in the surroundings of Barrow, Sodankylä and Tiksi, (c) the BRDF land surface reflectance model PS1 for land surfaces covered by snow-fields and glaciers, giving a value of $A_b(\theta_0=60°)$ = 0.854, and used to represent the surface reflectance characteristics observed around Summit in the Arctic and Neumayer, Dome Concordia and South Pole in Antarctica for fresh snow conditions, (d) the BRDF surface albedo model PS2, yielding a value of $A_b(\theta_0=60°)$ = 0.775, which was adopted to represent the surface reflectance characteristics for land areas covered by slightly polluted snow (at Sodankylä) and not entirely snow-covered areas (Mario Zucchelli, Neumayer, and other coastal sites), (e) the BRDF model PS3, giving $A_b(\theta_0=60°)$ = 0.564, which was chosen to represent the surface albedo characteristics observed over Spitsbergen in late winter and early spring, and (f) the BRDF model PS4, yielding

2020 $A_b(\theta_0=60°)$ = 0.329, which realistically represents the mixed ice-covered and ice-free land areas
2021 around Ny-Ålesund in late spring and summer.
2022 (vi) Calculations of the daily time-patterns of instantaneous and diurnally averaged DARFs were
2023 made using the 6S (Vermote et al., 1997a) radiative transfer code for: (a) the values of $\tau(0.50\ \mu m)$
2024 and $\alpha(0.40\text{-}0.87\ \mu m)$ defined in Table 6 for the various aerosol types and assumed to be stable from
2025 sunrise to sunset, (b) the values of angle θ_0 calculated at the various hours of the day, for the above
2026 stations and seasonal periods, (c) the multimodal size-distribution curves determined at step (iii),
2027 (d) the spectral values of $\omega(\lambda)$ for each of the multimodal size-distribution curves determined at step
2028 (iv), and (e) the surface albedo models chosen at step (v) for the various Arctic and Antarctic sites.
2029 The time-patterns of $\Delta F_{TOA}(t)$, $\Delta F_{BOA}(t)$ and $\Delta F_{ATM}(t)$ were then integrated to calculate the daily
2030 values of ΔF_{TOA}, ΔF_{BOA} and ΔF_{ATM} given in Table 6 for the various aerosol types and BRDF surface
2031 albedo models.
2032 Examining the results given in Table 6, it can be seen that ΔF_{TOA} varies appreciably at Barrow as
2033 one passes from the OS1 to VS1 model in the Asian dust (AD) case, and from the OS1 to PS2
2034 model in the BFF smoke case, while only limited variations of ΔF_{TOA} from about -10 W m^{-2} to no
2035 more than +10 W m^{-2} were obtained for the background summer aerosol and Arctic haze cases
2036 considered at the 5 above-chosen Arctic sites. Similar features were also noted for ΔF_{BOA},
2037 illustrating larger variations in the AD and BFF aerosol cases monitored at Barrow, and mainly
2038 ranging from -5 to +5 W m^{-2} in all the background summer aerosol and Arctic haze cases.
2039 Correspondingly, rather large variations in ΔF_{ATM} were obtained not only for the Barrow AD and
2040 BFF cases but also for the Arctic haze cases observed at Barrow and Ny-Ålesund for $\tau(0.50\ \mu m) >$
2041 0.10. In particular, we have estimated an Asian dust value of $\Delta F_{TOA} \approx 9$ W m^{-2} for $\tau(0.50\ \mu m) =$
2042 0.20 measured at Barrow.
2043 The diurnally averaged DARF terms ΔF_{TOA}, ΔF_{BOA} and ΔF_{ATM} given in Table 6 for four Antarctic
2044 background austral summer aerosol cases indicate that larger variations have been estimated at

Mario Zucchelli and Neumayer, passing from the low surface reflectance oceanic model OS1 to the land surface albedo model PS2 characterised by highly reflecting and snow-covered surfaces. Conversely, very limited variations in the three DARF terms have been obtained at the four Antarctic sites, when passing from one PS land surface albedo model to another, since they all pertain to land surfaces covered by glaciers and snow fields that do not exhibit marked differences in their reflectance characteristics. Actually, it is important to mention that the above DARF evaluations may be affected by large uncertainties, associated with the numerous approximations made in the above calculations when: (a) assuming constant time-patterns of AOT and stable aerosol optical parameters throughout the day, (b) neglecting the occurrence of variations in the scattering, absorption and extinction properties of aerosol with height, and assuming that the vertical profiles of such optical parameters did not exhibit multi-layered features, (c) using simplified radiative transfer codes in a cloud-free atmosphere, which can lead to significant errors in estimating the DARF effects, as pointed out by Valero and Bush (1999), and (d) choosing inappropriate surface reflectance models to represent the surface albedo characteristics, as would especially be the case for the VS1 and OS1 models, which may differ considerably in some cases from the real surface conditions, as pointed out by Stone et al. (2008). With regard to this, calculations of the DARF effects made by Tomasi et al. (2014) using the sets of four oceanic surface (OS) and four vegetation-covered (VS) BRDF models indicate that changes varying from 10% to 50% may affect the calculations of ΔF_{TOA} and ΔF_{BOA}, and consequently even greater differences can be found in evaluating ΔF_{ATM}. Therefore, it is fair to highlight that the present evaluations of ΔF_{TOA}, ΔF_{BOA} and ΔF_{ATM} obtained using the OS1 calm-wind ocean model could differ appreciably from those occurring for stronger winds causing higher surface reflectance conditions in sea areas.

Calculations of the DARF efficiency parameters E_{TOA}, E_{BOA} and E_{ATM} were finally made by dividing the values of ΔF_{TOA}, ΔF_{BOA} and ΔF_{ATM} given in Table 6 for the various polar aerosol types by the corresponding mean values of $\tau(0.50\ \mu m)$. The evaluations of E_{TOA}, E_{BOA} and E_{ATM} are shown in

Fig. 28 as a function of the broadband albedo $A_b(\theta_0 = 60°)$ determined for the various BRDF surface reflectance models chosen above. The values of E_{ToA}, E_{BoA} and E_{Atm} obtained at the five Arctic sites for various aerosol types indicate that DARF efficiencies are subject to large variations when passing from the low surface albedo characteristics of the VS1 and OS1 models to the high reflectance surfaces of the PS models. The results shown in Fig. 28 indicate that:

(a) E_{TOA} increases from less than -100 W m^{-2} over the VS1 surface (for BG summer aerosol over sea, at Ny-Ålesund) to more than +100 W m^{-2} over the PS4 surface (for Arctic dense summer aerosol at Ny-Ålesund), and assumes slightly positive values as the broadband albedo increases from 0.56 to 0.85, ranging from about + 30 W m^{-2} (over the PS2 surface for Arctic haze at Sodankylä and for BG summer aerosol at Dome Concordia) to no more than + 92 W m^{-2} (over the PS2 surface, for Asian dust at Barrow). These estimates had relative standard deviations varying on average from 10% over the PS4 surface to 50% over the VS1 and OS1 surfaces (i.e from 6 to 26 W m^{-2}).

(b) E_{BOA} varies from less than -100 W m^{-2} over the VS1 surface (for BG summer aerosol at Tiksi) to around +80 W m^{-2} over the OS1 surface (for Arctic haze at Barrow). The estimates of E_{BOA} obtained for the high-reflectance PS surface reflectance models did not vary by much with the aerosol type, ranging from -57 W m^{-2} (for Arctic BG aerosol at Ny-Ålesund) to +20 W m^{-2} (for Antarctic BG summer aerosol at Dome Concordia).

(c) E_{ATM} varies from about -240 W m^{-2} over the OS1 surface (for Antarctic BG summer aerosol at Mario Zucchelli) to more than +150 W m^{-2} over the PS4 surface (for Arctic dense summer aerosol at Ny-Ålesund). Figure 28 shows that E_{ATM} exhibits a large range over the VS1 and OS1 surfaces, and then assumes stable and positive values over the PS surfaces, varying from +10 W m^{-2} (for Antarctic BG summer aerosol at Dome Concordia) to +151 W m^{-2} over the PS4 surface (for dense Arctic haze at Ny-Ålesund).

2095 The present DARF efficiency evaluations are affected by considerable uncertainties, since they
2096 were determined with relative standard deviations varying from about ±10% (over the PS4 surface)
2097 to around ±50% (over the VS1 and OS1 surfaces).
2098 The results shown in Fig. 28 have been obtained for various Arctic and Antarctic aerosol types with
2099 values of $\omega(0.55\ \mu m)$ ranging from about 0.76 (for BFF smoke at Barrow) to nearly 1.00 (for
2100 Antarctic background aerosol at Dome Concordia). The value of E_{TOA} for the BFF smoke load
2101 observed at Barrow was found to be of -68 ± 27 W m^{-2} over the tundra (VS1) surface, while Stone
2102 et al. (2008) estimated an average efficiency value of -20 W m^{-2} in summer 2004. The
2103 corresponding value of E_{BOA} was estimated by us at -95 ± 36 W m^{-2} , while Stone et al. (2008)
2104 estimated a lower average efficiency of about -40 W m^{-2}. Thus, we obtained a value of E_{ATM} equal
2105 to +27 ± 63 W m^{-2}, against an estimate of +20 W m^{-2} by Stone et al. (2008), resulting in an
2106 atmospheric warming rate of about 1 K per day.
2107
2108 **7. Conclusions**
2109 Monthly mean values of $\tau(0.50\ \mu m)$ and Ångström exponent α determined from multi-year sets of
2110 ground-based sun-photometer measurements at 21 polar sites, yielded a comprehensive picture of
2111 atmospheric turbidity conditions due to polar aerosols. The results are presented as a function of the
2112 winter-spring and summer periods over the whole Arctic region and include observations conducted
2113 in Alaska, Northern Canada, Greenland, Svalbard, Northern Scandinavia and Northern-Central
2114 Siberia. The analysis of the measurements acquired at the 12 Arctic sites listed in Table 1
2115 highlighted the seasonality of columnar aerosol extinction parameters, showing that α ranges
2116 mainly from 1.0 to 1.6 throughout the year at all stations, and $\tau(0.50\ \mu m)$ values were mainly lower
2117 than 0.08 in summer (for background aerosol) and appreciably higher during the winter-spring
2118 period. The latter phenomenon is associated with the occurrence of dense Arctic haze episodes that
2119 are often observed at remote Arctic sites as the result of the transport of anthropogenic polluted

2120 aerosols from the industrialized and most densely populated areas of mid-latitude North America,
2121 Europe and Asia.
2122 Sun-photometer measurements collected during the Antarctic summer were analysed for six coastal
2123 sites (Marambio, Neumayer, Novolazarevskaya, Mirny, Syowa, Mario Zucchelli), one mid-altitude
2124 station (Troll) and two high-altitude bases on the Antarctic Plateau (Dome Concordia and South
2125 Pole). Monthly mean $\tau(0.50\ \mu m)$ values usually ranged from less than 0.02 on the Antarctic Plateau
2126 to no more than 0.06 at the coastal stations, with α decreasing respectively from extremes of 1.8 (at
2127 South Pole and Dome Concordia, for aerosols dominated by nss sulphates), to around 0.6 at Mario
2128 Zucchelli, Neumayer and the other coastal sites (where aerosol light extinction is predominantly
2129 influenced by sea-salt particles).
2130 Ship-borne sun-photometer measurements were conducted during 14 spring and summer
2131 AERONET/MAN cruises across the Greenland Sea and Norwegian Sea, the West Siberian Sea and
2132 the North-American Arctic Ocean. The results yielded monthly mean estimates of $\tau(0.50\ \mu m)$ and α
2133 that were found to be comparable with results obtained from ground-based sun-photometer
2134 measurements taken at the stations located on the coasts of the same oceanic sectors during the
2135 March to September period, thus confirming the covariance features of $\tau(0.50\ \mu m)$ and α
2136 determined at the ground-based sun-photometer sites. The analysis of ship-borne sun-photometer
2137 measurements performed during the 18 AERONET/MAN cruises conducted in the coastal and off-
2138 shore Antarctic areas of the Indian, Pacific and Atlantic Oceans and along the Antarctic Peninsula
2139 coasts showed that the monthly mean values of $\tau(0.50\ \mu m)$ varied between the extremes of 0.02 and
2140 0.06 from December to April, while decreasing from 0.12 in October to 0.07 in November for
2141 measurements acquired around the Antarctic Peninsula. The large magnitude AOTs in the latter
2142 case were likely the result of stronger winds from the northern and western quadrants producing
2143 more sea-salt particles, which are transported toward the continent, while the rapidly decreasing
2144 trend results from a rapid decrease in the amplitude of these winds (a contention that is further
2145 supported by the corresponding increase in α values, between October and January, while $\tau(0.50$

2146 *μm)* systematically decreases). In more general terms we would argue that scattergrams of α versus
2147 *τ(0.50 μm)* for the ensemble of both land-based and ship-borne based sun-photometry showed a
2148 roughly inverse relationship of high α, small *τ(0.50 μm)* to low α, high *τ(0.50 μm)* that was
2149 representative of a progressive transformation from fine mode dominated nss sulphates above the
2150 Antarctic Plateau to sea-salt dominated aerosols for coastal sites.
2151 The vertical distribution of the aerosol extinction coefficient was investigated with ground-based
2152 lidars at Arctic and Antarctic sites. In particular, the monthly mean vertical profiles of backscatter
2153 coefficient, along with lidar ratio trends and depolarisation ratio covariance with backscattering
2154 coefficient were illustrated for tropospheric altitudes using data acquired at Ny-Ålesund by the AWI
2155 KARL lidar from 1 November, 2012, to 31 October, 2013. As part of this investigation, we
2156 illustrated the seasonal variations of integrated backscatter coefficient and lidar ratio, as influenced
2157 by Arctic haze episodes in late winter and spring, and the background aerosol in summer.
2158 Evaluations of AOT in the visible have been obtained using the operational algorithms applied to
2159 MODIS (Levy et al., 2013; Glantz et al., 2014), MISR (Diner et al., 2005b; Kahn et al., 2010) and
2160 AATSR (Holzer-Popp et al., 2013) satellite observations, which were found to substantially agree
2161 with the values of AOT obtained from the ground-based and ship-borne sun-photometer
2162 measurements conducted in the Arctic and Antarctic open-water regions. Reliable evaluations of
2163 *τ(0.55 μm)* have also been retrieved from the AATSR measurements recorded over the Arctic
2164 oceanic and land regions covered by sea ice, land ice and snow using observations taken in different
2165 spectral channels (Istomina et al., 2011), and by using the DVMS method (Mei et al., 2013b). These
2166 retrievals allow the aerosol spatial distribution (e.g., pollution events) to be analyzed on short term
2167 scales, but may contain an AOT offset due to many challenges connected to virtually unknown
2168 surface types and aerosol optical properties. The global application of these procedures is at present
2169 a challenging problem because of the very high sensitivity of the retrievals to unscreened thin
2170 clouds. In fact, these data are already affected by large uncertainties and need to be further
2171 validated, to overcome the errors that may arise from cloud contamination and the complex picture

of polar conditions (low values of AOT, various aerosol/cloud types, atmospheric inversions, variable features of snow- and ice-covered surface reflectance,….).

The main characteristics of multimodal particle size-distribution curves have been defined by: (i) taking into account the *in-situ* aerosol sampling measurements conducted at various Arctic sites (Barrow, Ny-Ålesund, Sodankylä) and Antarctic sites (Mario Zucchelli, Neumayer, Aboa, South Pole, Dome Concordia), and (ii) assuming that the overall size-distribution curves determined at the various sites consist in general of a fine particle mode and an accumulation or coarse particle mode, linearly combined to give a bimodal aerosol columnar load for each value of α obtained from the field measurements. Eight log-normal curves were defined for the Arctic stations on the basis of *in-situ* particle samples collected for Arctic haze, summer background aerosol, Asian dust and BFF smoke. They can be used for each spectral set of sun-photometer $\tau(\lambda)$ measurements to fit the derived value of α. The radiative parameters of the eight unimodal curves were defined by taking into account the complex refractive index and single scattering albedo derived from *in-situ* measurements conducted with nephelometers and aethalometers and/or using the simulations of the aerosol optical properties made with the aerosol extinction models given by the 6S code. Six log-normal curves were defined to represent the unimodal size-distribution curves of Antarctic fine, accumulation and coarse particles, using field data obtained from the aerosol collected at coastal and high-altitude sites. The optical properties of particulate matter were defined according to the data provided by the *in-situ* active remote sensing measurements, and used to determine the optical characteristics of six Antarctic log-normal size-distribution curves shown in Table 5.

Assumptions about the aerosol optical properties are totally based on the particulate chemical composition measured at the ground and, therefore, may differ appreciably from airborne particles suspended within the upper layers of the atmosphere in all cases of aerosol transport from remote areas (like Arctic haze, Asian dust, and BFF smoke), as shown for instance by the PAMARCMiP airborne measurements conducted in April 2009 (Stone et al., 2010). However, the best-fit procedure to combine the fine particle mode with the accumulation/coarse particle mode to fit the

2198 value of α will have probably allowed us to evaluate the average spectral features of the column
2199 loading consisting of larger particles.
2200 The bimodal size-distribution curves of Arctic and Antarctic aerosol obtained as linear
2201 combinations of the fine particle and accumulation/coarse particle modes have been defined by
2202 varying their columnar number contents until a best-fit value of α was obtained for each spectral
2203 series of $\tau(\lambda)$. All these bimodal models were assumed to exhibit the well-defined optical properties
2204 given in Table 5 and to represent the most relevant optical characteristics of Arctic and Antarctic
2205 columnar aerosol. Additional realistic multimodal extinction models of fine, accumulation and
2206 coarse particles have been defined as linear combinations of the OPAC components proposed by
2207 Hess et al. (1998), which fit the mean values of α determined for different columnar aerosol types.
2208 Using these multimodal aerosol extinction models, instantaneous and diurnally averaged DARF
2209 effects induced by atmospheric aerosol at the TOA- and BOA-levels, and within the atmosphere
2210 have been calculated over sea and land surfaces by using the sets of BRDF surface reflectance
2211 models determined by Tomasi et al. (2013) for vegetation-covered, oceanic, and polar snow-
2212 covered surfaces. The results indicate that the diurnally averaged DARF terms vary strongly as a
2213 function of $\tau(0.50\ \mu m)$, aerosol single scattering albedo and surface albedo. The corresponding
2214 efficiency at the TOA-level was found to increase appreciably as surface albedo over sea and land
2215 increases until higher and more stable values over the snow- and ice-covered surfaces are attained.
2216 Less variable values and a more limited dependence of the BOA-level DARF efficiency on surface
2217 albedo were found, so that the atmospheric DARF efficiency resulted in: (1) a stronger increase
2218 when passing from vegetation-covered and oceanic surfaces to surfaces covered only in part by
2219 snow, and (2) more stable positive values over the polar surfaces covered by fresh snow and clean
2220 glaciers in the Arctic and Antarctic regions.
2221
2222 **Acknowledgments.**

The present study was developed as a part of the CLIMSLIP (*Climate Impacts of Short-Lived Pollutants in the Polar Regions*) joint project, approved by the European Polar Consortium and coordinated by A. Stohl at NILU (Kjeller, Norway), and supported by the Italian Research Programme in Antarctica (PNRA). The authors gratefully acknowledge the Office of Antarctic Observation of the Japan Meteorological Agency (Tokyo, Japan), for supplying the data-set of EKO sun-photometer measurements carried out at Syowa (Antarctica) from 2000 to 2011. In general we acknowledge the support provided by the AERONET network in the Arctic and Antarctica and the AEROCAN / AERONET sub-network in the Canadian Arctic. The Cimel sun-photometer data at Barrow (Alaska) were collected by the U.S. Department of Energy as part of the Atmospheric Radiation Measurement Program Climate Research Facility (ARM) and processed by AERONET. James H. Butler (Global Monitoring Division, Earth System Research Laboratory (ERL), National Oceanic and Atmospheric Administration (NOAA), Boulder, Colorado, USA) is acknowledged for his effort in establishing and maintaining the activities at the AERONET South Pole Amundsen-Scott base. The colleagues D. G. Chernov, Yu. S. Turchinovich and Victor V. Polkin, (V. E. Zuev Institute of Atmospheric Optics (IAO), Siberian Branch, Russian Academy of Sciences, Tomsk, Russia) are also acknowledged for their participation to field measurements conducted at Barentsburg and in Antarctica. Author's acknowledgements are also due to the managerial and operational support given by M. Fily (LGGE, CNRS, Grenoble, France) at the AERONET Antarctic Dome Concordia station, and to the P.I.s of the AERONET/MAN cruises conducted in the Arctic and Antarctic Oceans, during which Microtops measurements of aerosol optical thickness were performed and examined in the present analysis: Patricia K. Quinn (NOAA Pacific Marine Environmental Laboratory, Seattle, Washington, USA), Andrey Proshutinsky (Woods Hole Oceanographic Institution, Woods Hole, Massachusetts, USA), Carlos Duarte (Instituto Mediterráneo de Estudios Avanzados, Esporles, Mallorca, Spain), Simon Bélanger (Université du Québec, Rimouski, Québec, Canada), Elizabeth A. Reid (Naval Research Laboratory, Monterey, California, USA), Gennadi Milinevsky (Space Physics Laboratory, Taras Shevchenko National

University of Kyiv, Kyiv, Ukraine), and Heitor Evangelista (Rio de Janeiro State University, Brazil). The analyses and visualizations used in this paper to obtain the sets of MODIS and MISR daily aerosol optical thickness Level-3 data over the Arctic and Antarctic regions were produced with the Giovanni online data system, developed and maintained by the NASA GES DISC.

2254 **References**

2255

2256 Aaltonen, V., Lihavainen, H., Kerminen, V.-M., Komppula, M., Hatakka, J., Eneroth, K., Kulmala,
2257 M., Viisanen, Y., 2006. Measurements of optical properties of atmospheric aerosols in
2258 Northern Finland. Atmospheric Chemistry and Physics 6, 1155-1164, doi:10.5194/acp-6-
2259 1155-2006.

2260 Ackermann, J., 1998. The extinction-to-backscatter ratio of tropospheric aerosol: A numerical
2261 study. Journal of Atmospheric and Oceanic Technology 15, 4, 1043-1050, doi:10.1175/1520-
2262 0426(1998)015<1043:TETBRO>2.0.CO;2.

2263 Ackerman, S. A., Strabala, K. I., Menzel, W. P., Frey, R. A., Moeller, C. C., Gumley, L. E., 1998.
2264 Discriminating clear sky from clouds with MODIS, Journal of Geophysical Research 103,
2265 D24, 32141-32157, doi:10.1029/1998JD200032.

2266 Ackerman, S. A., Frey, R., Strabala, K., Liu, Y., Gumley, L., Baum, B., Menzel, P., 2010.
2267 Discriminating Clear-Sky from Cloud with MODIS - Algorithm Theoretical Basis Document.
2268 Products: MOD35. ATBD Reference Number: ATBD-MOD-06 (http://modis-
2269 atmos.gsfc.nasa.gov/MOD35_L2/atbd.html).

2270 Allen, R. C. Jr., Durkee, P. A., Wash, C. H., 1990. Snow/cloud discrimination with multispectral
2271 satellite measurements. Journal of Applied Meteorology 29, 10, 994-1004, doi:10.1175/1520-
2272 0450(1990)029<0994:SDWMSM>2.0.CO;2.

2273 Ångström, A., 1964. The parameters of atmospheric turbidity. Tellus 16, 64-75, doi:10.1111/j.2153-
2274 3490.1964.tb00144.x.

2275 Anderson, T. L., Ogren, J. A., 1998. Determining aerosol radiative properties using the TSI 3563
2276 Integrating Nephelometer. Aerosol Science and Technology 29, 57-69,
2277 doi:10.1080/02786829808965551.

2278 Ansmann, A., Wandinger, U., Riebesell, M., Weitkamp, C., Michaelis, W., 1992. Independent
2279 measurement of extinction and backscatter profiles in cirrus clouds by using a combined

2280 Raman elastic-backscatter lidar. Applied Optics 31, 33, 7113-7131,
2281 doi:10.1364/AO.31.007113.
2282 Arimoto, R., Hogan, A., Grube, P., Davis, D., Webb, J., Schloesslin, C., Sage, S., Raccah, F., 2004.
2283 Major ions and radionuclides in aerosol particles from the South Pole during ISCAT-2000.
2284 Atmospheric Environment 38, 5473-5484, doi:10.1016/j.atmosenv.2004.01.049.
2285 Barrie, L. A., Hoff, R. M., Daggupaty, S. M., 1981. The influence of mid-latitudinal pollution
2286 sources on haze in the Canadian Arctic. Atmospheric Environment 15, 8, 1407-1419,
2287 doi:i:10.1016/0004-6981(81)90347-4.
2288 Bodhaine, B. A., 1995. Aerosol absorption measurements at Barrow, Mauna Loa and South Pole.
2289 Journal of Geophysical Research 100, 8967-8975, doi:10.1029/95JD00513.
2290 Bourassa, A. E., Degenstein, D. A., Elash, B. J., Llewellyn, E. J., 2010. Evolution of the
2291 stratospheric aerosol enhancement following the eruptions of Okmok and Kasatochi: Odin-
2292 OSIRIS measurements. Journal of Geophysical Research 115, D2, D00L03.
2293 doi:10.1029/2009JD013274.
2294 Brock, C. A., Cozic, J., Bahreini, R., Froyd, K. D., Middlebrook, A. M., McComiskey, A., Brioude,
2295 J., Cooper, O. R., Stohl, A., Aikin, K. C., de Gouw, J. A., Fahey, D. W., Ferrare, R. A., Gao,
2296 R.-S., Gore, W., Holloway, J. S., Huebler, G., Jefferson, A., Lack, D. A., Lance, S., Moore, R.
2297 H., Murphy, D. M., Nenes, A., Novelli, P. C., Nowak, J. B., Ogren, J. A., Peischl, J., Pierce,
2298 R. B., Pilewskie, P., Quinn, P. K., Ryerson, T. B., Schmidt, K. S., Schwarz, J. P., Sodemann,
2299 H., Spackman, J. R., Stark, H., Thomson, D. S., Thornberry, T., Veres, P., Watts, L. A.,
2300 Warneke, C., Wollny, A. G., 2011. Characteristics, sources, and transport of aerosols
2301 measured in spring 2008 during the Aerosol, Radiation, and Cloud Processes Affecting Arctic
2302 Climate (ARCPAC) project. Atmospheric Chemistry and Physics 11, 6, 2423-2453,
2303 doi:10.5194/acp-11-2423-2011.
2304 Bush, B. C., Valero, F. P. J., 2003. Surface aerosol radiative forcing at Gosan during the ACE-Asia
2305 campaign. Journal of Geophysical Research 108, D23, 8660, doi: 10.1029/2002JD003233.

2306 Campbell, J. R., Tackett, J. L., Reid, J. S., Zhang, J., Curtis, C. A., Hyer, E. J., Sessions, W. R.,
2307 Westphal, D. L., Prospero, J. M., Welton, E. J., Omar, A. H., Vaughan, M. A., Winker, D. M.,
2308 2012. Evaluating nighttime CALIOP 0.532 μm aerosol optical depth and extinction coefficient
2309 retrievals. Atmospheric Measurement Techniques 5, 9, 2143-2160, doi:10.5194/amt-5-2143-
2310 2012.
2311 Curier, L., de Leeuw, G., Kolmonen, P., Sundstrom, A.-M., Sogacheva, L., Bennouna, Y., 2009.
2312 Aerosol retrieval over land using the (A)ATSR dual-view algorithm. In "Satellite Aerosol
2313 Remote Sensing over Land" (A. A. Kokhanovsky and G. de Leeuw, eds.), Chichester (UK),
2314 Praxis Publishing, pp. 135-160.
2315 Damoah, R., Spichtinger, N., Forster, C., James, P., Mattis, I., Wandinger, U., Beirle, S., Wagner,
2316 T., Stohl, A., 2004. Around the world in 17 days - hemispheric-scale transport of forest fire
2317 smoke from Russia in May 2003. Atmospheric Chemistry and Physics 4, 1311-1321,
2318 doi:10.5194/acp-4-1311-2004.
2319 Delene, D. J., Ogren, J. A., 2002. Variability of aerosol optical properties at four North American
2320 surface monitoring sites. Journal of the Atmospheric Sciences 59, 1135-1150,
2321 doi:10.1175/1520-0469(2002)059<1135:VOAOPA>2.0.CO;2.
2322 Deuzé, J. L., Bréon, F. M., Devaux, C., Goloub, P., Herman, M., Lafrance, B., Maignan, F.,
2323 Marchand, A., Nadal, F., Perry, G., Tanré, D., 2001. Remote sensing of aerosol over land
2324 surfaces from POLDER-ADEOS-1 polarized measurements. Journal of Geophysical Research
2325 106, D5, 4913-4926, doi:10.1029/2000JD900364.
2326 Devasthale, A., Tjernströ, M., Omar, A. H., 2011. The vertical distribution of thin features over the
2327 Arctic analysed from CALIPSO observations. Part II: Aerosols. Tellus 63B, 1, 86-95,
2328 doi:10.1111/j.1600-0889.2010.00517.x.
2329 de Villiers, R. A., Ancellet, G., Pelon, J., Quennehen, B., Schwarzenboeck, A., Gayet, J. F., Law, K.
2330 S., 2010. Airborne measurements of aerosol optical properties related to early spring transport

of mid-latitude sources into the Arctic. Atmospheric Chemistry and Physics 10, 11, 5011-5030, doi:10.5194/acp-10-5011-2010.

Di Carmine, C., Campanelli, M., Nakajima, T., Tomasi, C., Vitale, V., 2005. Retrievals of Antarctic aerosol characteristics using a Sun-sky radiometer during the 2001-2002 austral summer campaign. Journal of Geophysical Research 110, D13202, doi:10.1029/2004JD005280.

Diner, D. J., Beckert, J. C., Reilly, T. H., Bruegge, C. J., Conel, J. E., Kahn, R. A., Martonchik, J. V., Ackerman, T. P., Davies, R., Gerstl, S. A.W., Gordon, H. R., Muller, J.-P., Myneni, R. B., Sellers, P. J., Pinty, B., Verstraete, M. M., 1998. Multi-angle Imaging SpectroRadiometer (MISR) instrument description and experiment overview. IEEE Transactions on Geoscience and Remote Sensing 36, 4, 1072-1087, doi: 10.1109/36.700992.

Diner, D. J., Martonchik, J. V., Kahn, R. A., Pinty, B., Gobron, N., Nelson, D. L., Holben, B. N., 2005a. Using angular and spectral shape similarity constraints to improve MISR aerosol and surface retrievals over land. Remote Sensing of Environment, 94, 2, 155-171, doi:10.1016j.rse.2004.09.009.

Diner, D. J., Braswell, B. H., Davies, R., Gobron, N., Hu, J., Jin, Y., Kahn, R. A., Knyazikhin, Y., Loeb, N., Muller, J.-P., Nolin, A. W., Pinty, B., Schaaf, C. B., Seiz, G., Stroeve, J., 2005b. The value of multiangle measurements for retrieving structurally and radiatively consistent properties of clouds, aerosols, and surfaces. Remote Sensing of Environment 97, 4, 495-518, doi:10.1016/j.rse.2005.06.006.

Di Pierro, M., Jaeglé, L., Anderson, T. L., 2011. Satellite observations of aerosol transport from East Asia to the Arctic: three case studies. Atmospheric Chemistry and Physics, 11, 2225-2243, doi:10.5194/acp-11-2225-2011.

Dong, X., Xi, B., Crosby, K., Long, C. N., Stone, R. S., Shupe, M. D., 2010. A 10 year climatology of Arctic cloud fraction and radiative forcing at Barrow, Alaska. Journal of Geophysical Research 115, D17212, doi:10.1029/2009JD013489.

2356 Dubovik, O., Herman, M., Holdak, A., Lapyonok, T., Tanré, D., Deuzé, J. L., Ducos, F., Sinyuk,
2357 A., and Lopatin, A., 2011. Statistically optimized inversion algorithm for enhanced retrieval
2358 of aerosol properties from spectral multi-angle polarimetric satellite observations.
2359 Atmospheric Measurement Techniques, 4, 975-1018, doi:10.5194/amt-4-975-2011.
2360 Eck, T. F., Holben, B. N., Reid, J. S., Dubovik, O., Smirnov, A., O'Neill, N. T., Slutsker, I., Kinne,
2361 S., 1999. Wavelength dependence of the optical depth of biomass burning, urban, and desert
2362 dust aerosols, Journal of Geophysical Research 104, D24, 31333-31349,
2363 doi:10.1029/1999JD900923.
2364 Eckhardt, S., Hermansen, O., Grythe, H., Fiebig, M., Stebel, K., Cassiani, M., Baecklund, A., Stohl,
2365 A., 2013. The influence of cruise ship emissions on air pollution in Svalbard - a harbinger of a
2366 more polluted Arctic?, Atmospheric Chemistry and Physics 13, 8401-8409, doi:10.5194/acp-
2367 13-8401-2013.
2368 Fattori, I., Becagli, S., Bellandi, S., Castellano, E., Innocenti, M., Mannini, A., Severi, M., Vitale,
2369 V., Udisti, R., 2005. Chemical composition and physical features of summer aerosol at Terra
2370 Nova Bay and Dome C, Antarctica. Journal of Environmental Monitoring 7, 1265-1274.
2371 Fiebig, M., Lunder, C. R., Stohl, A., 2009. Tracing biomass burning aerosol from South America to
2372 Troll Research Station, Antarctica. Geophysical Research Letters 36, L14815,
2373 doi:10.1029/2009GL038531.
2374 Garrett, T. J., Verzella, L.L., 2008. Looking back: An evolving history of Arctic aerosols. Bullettin
2375 of the American Meteorological Society 89, 299-302, doi: 10.1175/BAMS-89-3-299.
2376 Gesell, G., 1989. An algorithm for snow and ice detection using AVHRR data. An extension to the
2377 APOLLO software package, International Journal of Remote Sensing 10, 4-5, 897-905,
2378 doi:10.1080/01431168908903929.
2379 Glantz, P., Bourassa, A., Herber, A., Iversen, T., Karlsson, J., Kirkevåg, A., Maturilli, M., Seland,
2380 Ø., Stebel, K., Struthers, H., Tesche, M., Thomason, L., 2014. Remote sensing of aerosols in

the Arctic for an evaluation of global climate model simulations. Journal of Geophysical Research 119, 13, 8169-8188, doi:10.1002/2013JD021279.

Gobbi, G. P., Kaufman, Y. J., Koren, I., Eck, T. F., 2007. Classification of aerosol properties derived from AERONET direct sun data. Atmospheric Chemistry and Physics 7, 2, 453-458, doi:10.5194/acp-7-453-2007.

Gomez-Chova, L., Camps-Valls, G., Calpe-Maravilla, J., Guanter, L., Moreno, J., 2007. Cloud-Screening Algorithm for ENVISAT/MERIS Multispectral Images. IEEE Transactions on Geoscience and Remote Sensing 45, 12, 4105-4118, doi:10.1109/TGRS.2007.905312.

Govaerts, Y. M., Wagner, S., Lattanzio, A., Watts, P. , 2010. Joint retrieval of surface reflectance and aerosol optical depth from MSG/SEVIRI observations with an optimal estimation approach: 1. Theory. Journal of Geophysical Research 115, D2, doi:10.1029/2009JD011779.

Grey, W. M. F., North, P. R. J., 2009. Aerosol optical depth from dual-view (A)ATSR satellite observations. In *Satellite Aerosol Remote Sensing Over Land* (Kokhanovsky, A.A., and G. de Leeuw, eds.), Springer-Praxis (Berlin), 2009, ISBN 978-3-540-69396-3, 388 pp.

Hagler, G. S. W., Bergin, M. H., Smith, E. A., Town, M., Dibb, J. E., 2008. Local anthropogenic impact on particulate elemental carbon concentrations at Summit, Greenland. Atmospheric Chemistry and Physics 8, 2485-2491, doi:10.5194/acp-8-2485-2008.

Han, W., Stamnes, K., Lubin, D., 1999. Remote sensing of surface and cloud properties in the Arctic from AVHRR measurements. Journal of Applied Meteorology 38, 7, 989-1012, doi:10.1175/1520-0450(1999)038<0989:RSOSAC>2.0.CO;2.

Hänel, G., Adam, W., Bundke, U., Komguem, L., Leiterer, U., 1999. Optical properties of boundary layer particles, columnar absorption and direct radiative forcing by particles in the solar spectral region. Journal of Aerosol Science 30, Suppl. 1, S171-S172.

Hara, K., Osada, K., Kido, M., Hayashi, M., Matsunaga, K., Iwasaka, Y., Yamanouchi, T., Hashida, G., Fukatsu, T., 2004. Chemistry of sea-salt particles and inorganic halogen species in

2406 Antarctic regions: Compositional differences between coastal and inland stations. Journal of
2407 Geophysical Research 109, D20208, doi:10.1029/2004JD004713.
2408 Haywood, J., Boucher, O., 2000. Estimates of the direct and indirect radiative forcing due to
2409 tropospheric aerosols: A review. Reviews of Geophysics 38, 4, 513-543, doi:
2410 10.1029/1999RG000078.
2411 Heintzenberg, J., Charlson, R. J., Clarke, A. D., Liousse, C., Ramaswamy, V., Shine, K. P.,
2412 Wendisch, M., Helas, G., 1997. Measurements and modelling of aerosol single scattering
2413 albedo: progress, problems and prospects. Contribution to Atmospheric Physics 70, 249-263.
2414 Herber, A., Thomason, L. W., Gernandt, H., Leiterer, U., Nagel, D., Schulz, K., Kaptur, J.,
2415 Albrecht, T., Notholt, J., 2002. Continuous day and night aerosol optical depth observations in
2416 the Arctic between 1991 and 1999. Journal of Geophysical Research 107**,** D10, 4097,
2417 doi:10.1029/2001JD000536.
2418 Herber, A. B., Haas, C., Stone, R. S., Bottenheim, J. W., Liu, P., Li, S.-M., Staebler, R. M., Strapp,
2419 J. W., Dethloff, K., 2012. Regular airborne surveys of Arctic sea ice and atmosphere. EOS 93,
2420 4, 41-48, doi:10.1029/2012EO040001.
2421 Hess, M., Koepke, P., Schult, I., 1998. Optical properties of aerosols and clouds: The software
2422 package OPAC. Bulletin of the American Meteorological Society 79, 5, 831-844, doi:
2423 10.1175/1520-0477(1998)079<0831:OPOAAC>2.0.CO;2.
2424 Hillamo, R., Allegrini, I., Sparapani, R., Kerminen, V.-M., 1998. Mass size distributions and
2425 precursors gas concentrations of major inorganic ions in Antarctic aerosol. International
2426 Journal of Environmental Analytical Chemistry 71, 353-372,
2427 doi:10.1080/03067319808032638.
2428 Hirdman, D., Sodemann, H., Eckhardt, S., Burkhart, J. F., Jefferson, A., Mefford, T., Quinn, P. K.,
2429 Sharma, S., Ström, J., Stohl, A., 2010, Source identification of short-lived air pollutants in the
2430 Arctic using statistical analysis of measurement data and particle dispersion model output.
2431 Atmospheric Chemistry and Physics 10, 669-693, doi:10.5194/acp-10-669-2010.

2432 Hoffmann, A., Ritter, C., Stock, M., Shiobara, M., Lampert, A., Maturilli, M., Orgis, T., Neuber, R.,
2433 Herber, A., 2009. Ground-based lidar measurements from Ny-Ålesund during ASTAR 2007.
2434 Atmospheric Chemistry and Physics 9, 22, 9059-9081, doi:10.5194/acp-9-9059-2009.
2435 Hoffmann, A., Ritter, C., Stock, M., Maturilli, M., Eckhardt, S., Herber, A., Neuber, R., 2010. Lidar
2436 measurements of the Kasatochi aerosol plume in August and September 2008 in Ny-Ålesund,
2437 Spitsbergen. Journal of Geophysical Research 115**,** D00L12, doi:10.1029/2009JD013039.
2438 Hoffmann, A., Osterloh, L., Stone, R., Lampert, A., Ritter, C., Stock, M., Tunved, P., Hennig, T.,
2439 Bockmann, C., Li, S.-M., Eleftheriadis, K., Maturilli, M., Orgis, T., Herber, A., Neuber, R.,
2440 Dethloff, K., 2012. Remote sensing and in-situ measurements of tropospheric aerosol, a
2441 PAMARCMiP case study. Atmospheric Environment 52C, 56-66,
2442 doi:10.1016/j.atmosenv.2011.11.027.
2443 Holben, B. N., Eck, T. F., Slutsker, I., Tanré, D., Buis, J. P., Setzer, A., Vermote, E., Reagan, J. A.,
2444 Kaufman, Y. J., Nakajima, T., Lavenu, F., Jankowiak, I., Smirnov, A., 1998. AERONET - A
2445 federated instrument network and data archive for aerosol characterization. Remote Sensing of
2446 Environment 66, 1, 1-16, doi: S0034-4257(98)00031-5.
2447 Holzer-Popp, T., de Leeuw, G., Griesfeller, J., Martynenko, D., Klüser, L., Bevan, S., Davies, W.,
2448 Ducos, F., Deuzé, J. L., Graigner, R. G., Heckel, A., von Hoyningen-Hüne, W., Kolmonen, P.,
2449 Litvinov, P., North, P., Poulsen, C. A., Ramon, D., Siddans, R., Sogacheva, L., Tanré, D.,
2450 Thomas, G. E., Vountas, M., Descloitres, J., Griesfeller, J., Kinne, S., Schulz, M., Pinnock, S.,
2451 2013. Aerosol retrieval experiments in the ESA Aerosol_cci project. Atmospheric
2452 Measurement Techniques 6, 8, 1919-1957, doi:10.5194/amt-6-1919-2013.
2453 Hori, M., Aoki, T., Tanikawa, T., Motoyoshi, H., Hachikubo, A., Sugiura, K., Yasunari, T. J., Eide,
2454 H., Storvold, R., Nakajima, Y., Takahashi, F., 2006. In-situ measured spectral directional
2455 emissivity of snow and ice in the 8-14 μm atmospheric window. Remote Sensing of
2456 Environment 100, 4, 486-502, doi:10.1016/j.rse.2005.11.001.

2457 Hsu, N. C., Tsay, S. C., King, M. D., Herman, J. R., 2004. Aerosol properties over bright reflecting
2458 source regions. IEEE Transactions on Geoscience and Remote Sensing, 42, 3, 557-569, doi:
2459 10.1117/12.975846.
2460 Hsu, N. C., Jeong, M.-J., Bettenhausen, C., Sayer, A. M., Hansell, R., Seftor, C. S., Huang, J., Tsay,
2461 S.-C., 2013. Enhanced Deep Blue aerosol retrieval algorithm: The second generation. Journal
2462 of Geophysical Research (Atmospheres) 118, 16, 9296–9315, doi:10.1002/jgrd.50712.
2463 Intrieri, J. M., Shupe, M. D., 2004. Characteristics and radiative effects of diamond dust over the
2464 Western Arctic ocean region. Journal of Climate 17, 15, 2953-2960, doi:10.1175/1520-
2465 0442(2004)017<2953:CAREOD>2.0.CO;2.
2466 IPCC, 2013. Climate Change 2013: The Physical Science Basis, Fifth Assessment Report of the
2467 United Nations "Intergovernmental Panel on Climate Change (IPCC), Chapter 7, Clouds and
2468 Aerosols, Cambridge University Press, Cambridge (UK)
2469 (http://www.climatechange2013.org/images/report/WG1AR5_Chapter07_FINAL.pdf).
2470 Iqbal, M. (1983), An Introduction to Solar Radiation, Academic Press, Toronto, 390 pp (see Table
2471 1.2.1 at pages 4-5).
2472 Istomina, L.G., von Hoyningen-Huene, W., Kokhanovsky, A. A., Burrows, J. P., 2009. Retrieval of
2473 aerosol optical thickness in Arctic region using dual-view AATSR observations, Proceedings
2474 of ESA Atmospheric Science Conference, ESA SP-676, Barcelona (Spain), 7-11 September
2475 2009.
2476 Istomina, L. G., von Hoyningen-Huene, W., Kokhanovsky, A. A., Burrows, J. P., 2010. The
2477 detection of cloud-free snow-covered areas using AATSR measurements. Atmospheric
2478 Measurement Techniques 3, 1005-1017, doi:10.5194/amt-3-1005-2010.
2479 Istomina, L. G., von Hoyningen-Huene, W., Kokhanovsky, A. A., Schultz, E., Burrows, J. P., 2011.
2480 Remote sensing of aerosols over snow using infrared AATSR observations, Atmospheric
2481 Measurement Techniques 4, 1133-1145, doi:10.5194/amt-4-1133-2011.

2482 Justice, C. O., Vermote, E., Townshend, J. R. G., Defries, R., Roy, D. P., Hall, D. K., Salomonson,
2483 V. V., Privette, J. L., Riggs, G., Strahler, A., Lucht, W., Myneni, R. P., Knyazikhin, Y.,
2484 Running, S. W., Nemani, R. R., Wan, Z., Huete, A. R., van Leeuwen, W., Wolfe, R. E.,
2485 Giglio, L., Muller, J.-P., Lewis, P., Barnsley, M. J., 1998. The Moderate Resolution Imaging
2486 Spectroradiometer (MODIS): Land Remote Sensing for Global Change Research. IEEE
2487 Transactions on Geoscience and Remote Sensing 36, 4, 1228-1249, doi:10.1109/36.701075.
2488 Kahn, R. A., Li, W.-H., Martonchik**,** J. V., Bruegge**,** C. J., Diner**,** D. J., Gaitley**,** B. J., Abdou, W.,
2489 Dubovik**,** O., Holben**,** B., Smirnov, A., Jin, Z., Clark, D., 2005. MISR calibration and
2490 implications for low-light-level aerosol retrieval over dark water. Journal of the Atmospheric
2491 Sciences 62, 4, 1032-1052, doi:10.1175/JAS3390.1.
2492 Kahn, R. A., Gaitley, B. J., Garay, M. J., Diner, D. J., Eck, T. F., Smirnov, A., Holben, B. N., 2010.
2493 Multiangle Imaging SpectroRadiometer global aerosol product assessment by comparison
2494 with the Aerosol Robotic Network. Journal of Geophysical Research 115, D23209,
2495 doi:10.1029/2010JD014601.
2496 Kahn, R. A., Garay, M. J., Nelson, D. L., Levy, R. C., Bull, M. A., Diner, D. J., Martonchik, J. V.,
2497 Hansen, E. G., Remer, L. A., Tanré, D., 2011. Response to ‘‘Toward unified satellite
2498 climatology of aerosol properties. 3. MODIS versus MISR versus AERONET’’. Journal of
2499 Quantitative Spectroscopy and Radiative Transfer 112, 5, 901-909,
2500 doi:10.1016/j.jqsrt.2009.11.003.
2501 Kaufman, Y. J., Tanré, D., Remer, L., Vermote, E. F., Chu, A., Holben, B. N., 1997. Operational
2502 remote sensing of tropospheric aerosol over the land from EOS-MODIS. Journal of
2503 Geophysical Research 102, D14, 17051-17067, doi:10.1029/96JD03988.
2504 Kerminen, V.-M., Teinilä, K., Hillamo, R., 2000. Chemistry of sea-salt particles in the summer
2505 Antarctic atmosphere. Atmospheric Environment 34, 2817-2825, doi:10.1016/S1352-
2506 2310(00)00089-3.

2507 Key, J., Barry, R. G., 1989. Cloud cover analysis with Arctic AVHRR data. 1. Cloud detection.
2508 Journal of Geophysical Research 94, D15, 18521-18535, doi:10.1029/JD094iD15p18521.
2509 King, M. D., Dubovik, O., 2013. Determination of aerosol optical properties from inverse methods.
2510 In *Aerosol Remote Sensing* (J. Lenoble, L. Remer, and D. Tanré, Eds.), Springer-Verlag, pp.
2511 101-136.
2512 Koponen, I. K., Virkkula, A., Hillamo, R., Kerminen, V.-M. , Kulmala, M., 2003. Number size
2513 distributions and concentrations of the continental summer aerosols in Queen Maud Land,
2514 Antarctica. Journal of Geophysical Research 108, D18, 4587, doi:10.1029/2003JD003614.
2515 Knapp, K. R., Vonder Haar, T. H., Kaufman, Y. J., 2002. Aerosol optical depth retrieval from
2516 GOES-8: Uncertainty study and retrieval validation over South America, Journal of
2517 Geophysical Research (Atmospheres) 107, D7, AAC 2-1 – AAC 2-12,
2518 doi:10.1029/2001JD000505.
2519 Lambert, A., Ehrlich, A., Dörnbrack, A., Jourdan, O., Gayet, J.-F., Mioche, G., Shcherbakov, V.,
2520 Ritter, C., Wendisch, M., 2009. Microphysical and radiative characterization of a subvisible
2521 midlevel Arctic ice cloud by airborne observations a case study. Atmospheric Chemistry and
2522 Physics 9, 8, 2647-2661, doi:10.5194/acp-9-2647-2009.
2523 Lambert, A., Ritter, C., Hoffmann, A., Gayet, J.-F., Mioche, G., Ehrlich, A., Doernbrack, A.,
2524 Wendisch, M., Shiobara, M., 2010. Lidar characterization of the Arctic atmosphere during
2525 ASTAR 2007: four cases studies of boundary layer, mixed-phase and multi-layer clouds.
2526 Atmospheric Chemistry and Physics 10, 6, 2847-2866, doi: doi:10.5194/acp-10-2847-2010.
2527 Law, K. S., Stohl, A., Quinn, P. K., Brock, C., Burkhart, J., Paris, J.-D., Ancellet, G., Singh, H. B.,
2528 Roiger, A., Schlager, H., Dibb, J., Jacob, D. J., Arnold, S. R., Pelon, J., Thomas, J. L., 2014.
2529 Arctic air pollution: 1 New insights from POLARCAT-IPY. Bulletin of the American
2530 Meteorological Society, doi:10.1175/BAMS-D-13-00017.1. In press.
2531 Levy, R. C., Remer, L. A., Mattoo, S., Vermote, E. F., Kaufman, Y. J., 2007. Second-generation
2532 operational algorithm: Retrieval of aerosol properties over land from inversion of Moderate

2533 Resolution Imaging Spectroradiometer spectral reflectance. Journal of Geophysical Research
2534 112, D13211, doi:10.1029/2006JD007811.
2535 Levy, R. C., Remer, L. A., Kleidman, R. G., Mattoo, S., Ichoku, C., Kahn, R., Eck, T. F., 2010.
2536 Global evaluation of the Collection 5 MODIS dark-target aerosol products over land.
2537 Atmospheric Chemistry and Physics 10, 10399-10420, doi:10.5194/acp-10-10399-2010.
2538 Levy, R. C., Mattoo, S., Munchak, L. A., Remer, L. A., Sayer, A. M., Patadia, F., Hsu, N. C., 2013.
2539 The Collection 6 MODIS aerosol products over land and ocean. Atmospheric Measurement
2540 Techniques 6, 2989-3034, doi:10.5194/amt-6-2989-2013.
2541 Liu, Y., Key, J. R., Frey, R. A., Ackerman, S. A., Menzel, W. P., 2004. Nighttime polar cloud
2542 detection with MODIS, Remote Sensing of Environment 92, 2, 181-194,
2543 doi:10.1016/j.rse.2004.06.004.
2544 Lubin, D., Satheesh, S., McFarquar, G., Heymsfield, A., 2002. Longwave radiative forcing of
2545 Indian Ocean tropospheric aerosol. Journal of Geophysical Research 107, D19, 8004,
2546 doi:10.1029/2001JD001183.
2547 Macdonald, M., Anderson, P., Carrea, L., Dobke, B., Embury, O., Merchant, C., Bensi, P., 2014.
2548 Concepts for a geostationary-like polar missions. In: *Sensors, Systems and Next-Federation*
2549 *Satellites XVIII*. Proceedings of the SPIE 2014 (Meynart, R., Neeck, S. P., and Shimoda, H.,
2550 eds.), Vol. 9421, ISBN 9781628413045.
2551 Martonchik, J. V., Diner, D. J., Kahn, R. A., Ackerman, T. P., Verstraete, M. M., Pinty, B., Gordon,
2552 H. R., 1998a. Techniques fot the retrieval of aerosol properties over land and ocean using
2553 multi-angle imagery. IEEE Transactions on Geoscience and Remote Sensing 36, 4, 1212-
2554 1227, doi:10.1109/36.701027.
2555 Martonchik, J. V., Diner, D. J., Pinty, B., Verstraete, M. M., Myneni, R. B., Knyazikhin, Y.,
2556 Gordon, H. R., 1998b. Determination of land and ocean reflective, radiative, and biophysical
2557 properties using multiangle imaging. IEEE Transactions on Geoscience and Remote Sensing
2558 36, 4, 1266-1281, doi:10.1109/36.701077.

2559 Martonchik, J. V., Diner, D. J., Crean, K. A., Bull, M. A., 2002. Regional aerosol retrieval results
2560 from MISR. IEEE Transactions on Geoscience and Remote Sensing 40, 7, 1520-1531,
2561 doi:10.1109/TGRS.2002.801142.
2562 Mazzola, M., Stone, R. S., Herber, A., Tomasi, C., Lupi, A., Vitale, V., Lanconelli, C., Toledano,
2563 C., Cachorro, V. E., O'Neill, N.T., Shiobara, M., Aaltonen, V., Stebel, K., Zielinski, T.,
2564 Petelski, T., Ortiz de Galisteo, J. P., Torres, B., Berjon, A., Goloub, P., Li, Z., Blarel, L.,
2565 Abboud, I., Cuevas, E., Stock, M., Schulz, K.-H., Virkkula, A., 2012. Evaluation of sun
2566 photometer capabilities for retrievals of aerosol optical depth at high latitudes: The POLAR-
2567 AOD intercomparison campaigns, Atmospheric Environment 52C, 1-14,
2568 doi:10.1016/j.atmosenv.2011.07.042.
2569 Mei, L., Xue, Y., 2013. Aerosol optical thickness retrieval over snow-covered surface using
2570 AATSR data, *The 2013 IEEE International Geoscience and Remote Sensing Symposium*
2571 *(IGARSS),* Melbourne, Australia, 21-26 July 2013.
2572 Mei, L., Xue, Y., de Leeuw, G., Holzer-Popp, T., Guang, J., Li, Y., Yang, L., Xu, H., Xu, X., Li, C.,
2573 Wang, Y., Wu, C., Hou, T., He, X., Liu, J., Dong, J., Chen, Z., 2012. Retrieval of aerosol
2574 optical depth over land based on a time series technique using MSG/SEVIRI data.
2575 Atmospheric Chemistry and Physics 12, 9167-9185, doi:10.5194/acp-12-9167-2012.
2576 Mei, L., Xue, Y., de Leeuw, G., von Hoyningen-Huene, W., Kokhanovsky, A. A., Istomina, L.,
2577 Guang, J., Burrows, J. P., 2013a. Aerosol optical depth retrieval in the Arctic region using
2578 MODIS over snow. Remote Sensing of Environment 128, 234-245,
2579 doi:10.1016/j.rse.2012.10.009.
2580 Mei, L., Xue, Y., Kokhanovsky, A. A., von Hoyningen-Huene, W., Istomina, L., de Leeuw, G.,
2581 Burrows, J. P., Guang, J., Jing, Y., 2013b. Aerosol optical depth retrieval over snow using
2582 AATSR data, International Journal of Remote Sensing 34, 14, 5030-5041,
2583 doi:10.1080/01431161.2013.786197.

2584 Mei, L., Xue, Y., Kokhanovsky, A. A., von Hoyningen-Huene, W., de Leeuw, G., Burrows, J. P.,
2585 2014. Retrieval of aerosol optical depth over land surfaces from AVHRR data, Atmospheric
2586 Measurement Techniques, in press.
2587 Mie, G., 1908. Beiträge zur Optik trüber Medien, speziell kolloidaler Metallösungen. Annalen der
2588 Physik, Vierte Folge, 25, 3, 377-445.
2589 Mielonen, T., Levy, R. C., Aaltonen, Komppula, M., de Leeuw, G., Huttunen, J., Lihavainen, H.,
2590 Kolmonen, P., Lehtinen, K. E. J., Arola, A., 2011. Evaluating the assumptions of surface
2591 reflectance and aerosol type selection within the MODIS aerosol retrieval over land: the
2592 problem of dust type selection. Atmospheric Measurement Techniques 4, 201-214,
2593 doi:10.5194/amt-4-201-2011.
2594 Mielonen, T., Aaltonen, V., Lihavainen, H., Hyvärinen, A.-P., Arola, A., Komppula, M., Kivi, R.,
2595 2013. Biomass burning aerosols observed in Northern Finland during the 2010 wildfires in
2596 Russia. Atmosphere 4, 17-34, doi:10.3390/atmos4010017.
2597 Minikin, A., Legrand, M., Hall, J., Wagenbach, D., Kleefeld, C., Wolff, E., Pasteur, E. C., Ducroz,
2598 F., 1998. Sulfur-containing species (sulfate and MSA) in coastal Antarctic aerosol and
2599 precipitation. Journal of Geophysical Research 103, D9, 10975-10990,
2600 doi:10.1029/98JD00249.
2601 Mishchenko, M. I., Liu, L., Geogdzhayev, I. V., Travis, L. D., Cairns, B., Lacis, A. A., 2010.
2602 Toward unified satellite climatology of aerosol properties. 3. MODIS versus MISR versus
2603 AERONET. Journal of Quantitative Spectroscopy and Radiative Transfer 111, 4, 540-552,
2604 doi:10.1016/j.jqsrt.2009.11.003.
2605 Mitchell, J. M., 1957. Visual range in the polar regions with particular reference to the Alaskan
2606 Arctic. Journal of Atmospheric and Terrestrial Physics, Special Supplement, 195-211.
2607 Moore, C. W., Obrist, D., Steffen, A., Staebler, R. M., Douglas, T. A., Richter, A., Nghiem, S. V.,
2608 2014. Convective forcing of mercury and ozone in the Arctic boundary layer induced by leads
2609 in sea ice. Nature, 506, 7486, 81-84. doi:10.1038/nature12924.

2610 Nakajima, T., Yoon, S. C., Ramanathan, V., Shi, G. Y., Takemura, T., Higurashi, A., Takamura, T.,
2611 Aoki, K., Sohn, B. J., Kim, S. W., Tsuruta, H., Sugimoto, N., Shimizu, A., Tanimoto, H.,
2612 Sawa, Y., Lin, N. H., Lee, C. T., Goto, D., Schutgens, N., 2007. Overview of the Atmospheric
2613 Brown Cloud East Asian Regional Experiment 2005 and a study of the aerosol direct radiative
2614 forcing in east Asia. Journal of Geophysical Research 112, D24S91,
2615 doi:10.1029/2007JD009009.
2616 Negi, H. S., Singh, S. K., Kulkarni, A. V., Semwal, B. S., 2010. Field-based spectral reflectance
2617 measurements of seasonal snow cover in the Indian Himalaya. International Journal of
2618 Remote Sensing 31, 9, 2393-2417, doi:10.1080/01431160903002417.
2619 Nghiem, S. V., Rigor, I. G., Richter, A., Burrows, J. P., Shepson, P. B., Bottenheim, J., Barber, D.
2620 G., Steffen, A., Latonas, J., Wang, F., Stern, G., Clemente-Colón, P., Martin, S., Hall, D. K.,
2621 Kaleschke, L., Tackett, P., Neumann, G., Asplin, M. G., 2012. Field and satellite observations
2622 of the formation and distribution of Arctic atmospheric bromine above a rejuvenated sea ice
2623 cover. Journal of Geophysical Research 117, D17, doi:10.1029/2011JD016268.
2624 Nordenskiöld, A. E., 1883. Nordenskiöld on the inland ice of Greenland. Science 2, 732-739.
2625 Nott, G. J., Duck, T. J., 2011. Lidar studies of the polar troposphere. Meteorological Applications
2626 18, 3, 383–405, doi:10.1002/met.289.
2627 Nyeki, S., Halios, C. H., Baum, W., Eleftheriadis, K., Flentje, H., Gröbner, J., Vuilleumier, L.,
2628 Wehrli, C., 2012. Ground-based aerosol optical depth trends at three high-altitude sites in
2629 Switzerland and southern Germany from 1995 to 2010. Journal of Geophysical Research 117,
2630 D18202, doi:10.1029/2012JD017493.
2631 Ohno, T., 2005. Aerosol routine observation operated by the Japan Meteorological Agency. In
2632 ”WMO/GAW Experts Workshop on a Global Surface Based Network for Long Term
2633 Observations of Column Aerosol Optical Properties”, GAW Rep. 162, WMO TD 1287, pp.
2634 70-71, World Meteorological Organization, Geneva, Switzerland.

2635 O'Neill, N. T., Ignatov, A., Holben, B. N., Eck, T. F., 2000. The lognormal distribution as a
2636 reference for reporting aerosol optical depth statistics; Empirical tests using multi-year, multi-
2637 site AERONET Sunphotometer data. Geophysical Research Letters 27, 20, 3333-3336,
2638 doi:10.1029/2000GL011581.
2639 O'Neill, N. T., Dubovik, O., Eck, T. F., 2001a. Modified Ångström exponent for the
2640 characterization of submicrometer aerosol. Applied Optics 40, 15, 2368-2375,
2641 doi:10.1364/AO.40.002368.
2642 O'Neill, N. T., Eck, T. F., Holben, B. N., Smirnov, A., Dubovik, O., Royer, A., 2001b. Bimodal
2643 size distribution influences on the variation of Ångström derivatives in spectral and optical
2644 depth space. Journal of Geophysical Research 106, D9, 9787-9806,
2645 doi:10.1029/2000JD900245.
2646 O'Neill, N. T., Eck, T. F., Smirnov, A., Holben, B. N., Thulasiraman, S., 2003. Spectral
2647 discrimination of coarse and fine mode optical depth. Journal of Geophysical Research 108,
2648 D17, 4559, doi:10.1029/2002JD002975.
2649 O'Neill, N. T., Perro, C., Saha, A., Lesins, G., Duck, T. J., Eloranta, E. W., Nott, G. J., Hoffmann,
2650 A., Karumudi, M. L., Ritter, C., Bourassa, A., Abboud, I., Carn, S. A., Savastiouk, V., 2012.
2651 Properties of Sarychev sulphate aerosols over the Arctic. Journal of Geophysical Research
2652 117**,** D04203, doi:10.1029/2011JD016838.
2653 Piel, C., Weller, R., Huke, M., Wagenbach, D., 2006. Atmospheric methane sulfonate and non-sea-
2654 salt sulfate records at the European Project for Ice Coring in Antarctica (EPICA) deep-drilling
2655 site in Dronning Maud Land, Antarctica. Journal of Geophysical Research 111, D03304,
2656 doi:10.1029/2005JD006213.
2657 Polissar, A. V., Hopke, P. K., Paatero, P., Malm, W. C., Sisler, J. F., 1998. Atmospheric aerosol
2658 over Alaska. 2. Elemental composition and sources. Journal of Geophysical Research 103,
2659 D15, 19045-19057, doi:10.1029/98JD01212.

2660 Polissar, A.V., Hopke, P. K., Harris, J. M., 2001. Source regions for atmospheric aerosol measured
2661 at Barrow, Alaska. Environmental Science Technology 35, 4214-4226,
2662 doi:10.1021/es0107529.
2663 Posyniak, M., Markowicz, K., 2009. Measurement of aerosol optical thickness over the Atlantic
2664 Ocean and in West Antarctica, 2006-2007. Acta Geophysica 57, 2, 494-508,
2665 doi:10.2478/s11600-009-0002-0.
2666 Quinn, P. K., Miller, T. L., Bates, T. S., Ogren, J. A., Andrews, E., Shaw, G. E., 2002. A 3-year
2667 record of simultaneously measured aerosol chemical and optical properties at Barrow, Alaska.
2668 Journal of Geophysical Research 107, D11, AAC8-1–AAC8-15, doi:10.1029/2001JD001248.
2669 Quinn, P., Shaw, G., Andrews, E., Dutton, E. G., Ruoho-Airola, T., Gong, S. L., 2007. Arctic haze:
2670 current trends and knowledge gaps. Tellus 59B, 1, 99-114, doi: 10.1111/j.1600-
2671 0889.2006.00238.x.
2672 Radionov, V. F., 2005. Temporal variability of the aerosol optical characteristics of the atmosphere
2673 in the Russian Arctic (Historical review). In WMO/GAW Experts Workshop on a Global
2674 Surface Based Network for Long Term Observations of Column Aerosol Optical Properties,
2675 GAW Rep. 162, WMO TD 1287, pp. 82-85, World Meteorological Organization, Geneva,
2676 Switzerland.
2677 Radionov, V. F., Lamakin, M. V., Herber, A., 2002. Changes in the aerosol optical depth of the
2678 Antarctic atmosphere. Izvestia, Atmospheric and Oceanic Physics 38, 179-183.
2679 Rahn, K.A., Borys, R. D., Shaw, G. E., 1977. Asian source of Arctic haze bands. Nature 268, 713-
2680 715, doi: 10.1038/268713a0.
2681 Ramanathan, V., Crutzen, P. J., Kiehl, J. T., Rosenfeld, D., 2001. Aerosols, climate and the
2682 hydrological cycle. , Science 294, 2119-2124, doi: 10.1126/science.1064034.
2683 Remer, L. A., Kaufman, Y. J., Tanré, D., Mattoo, S., Chu, D. A., Martins, J. V., Li, R.-R., Ichoku,
2684 C., Levy, R. C., Kleidman, R. G., Eck T. F., Vermote, E., Holben, B. N., 2005. The MODIS

aerosol algorithm, products, and validation. Journal of the Atmospheric Sciences, 62, 4, 947-973, doi: 10.1175/JAS3385.1.

Remer, L. A., Mattoo, S., Levy, R. C., Munchak, L. A., 2013. MODIS 3 km aerosol product: algorithm and global perspective. Atmospheric Measurement Techniques 6, 1829-1844, doi:10.5194/amt-6-1829-2013.

Rogers, R. R., Hostetler, C. A., Hair, J. W., Ferrare, R. A., Liu, Z., Obland, M. D., Harper, D. B., Cook, A. L., Powell, K. A., Vaughan, M. A., Winker, D. M., 2011. Assessment of the CALIPSO Lidar 532 nm attenuated backscatter calibration using the NASA LaRC airborne High Spectral Resolution Lidar. Atmospheric Chemistry and Physics 11, 1295-1311, doi:10.5194/acp-11-1295-2011.

Rozwadowska, A., Zielinski, T., Petelski, T., Sobolewski, P., 2010. Cluster analysis of the impact of air back-traiectories on aerosol optical properties at Hornsund, Spitsbergen. Atmospheric Chemistry and Physics 10, 3, 877-893, doi:10.5194/acp-10-877-2010.

Rozwadowska, A., Sobolewski, P., 2010. Variability in aerosol optical properties at Hornsund, Spitsbergen. Oceanologia 52, 4, 599-620, doi:10.5697/oc.52-4.599.

Sakerin, S. M., Kabanov, D. M., Rostov, A. P., Turchinovich, S. A., 2009. Portative Solar Photometer. Pribory i Tekhnika Eksperimenta (Instruments and Experimental Techniques) 2, 181-182 (in Russian).

Sakerin, S. M., Chernov, D. G., Kabanov, D. M., Kozlov, V. S., Panchenko, M. V., Polkin, V. V., Radionov, V. F., 2012. Preliminary results of studying the aerosol characteristics of the atmosphere in the region of Barentsburg, Spitsbergen. Problems of the Arctic and Antarctica 1, 91, 20-31 (in Russian).

Sakerin, S. M., Andreev, S. Yu., Kabanov, D. M., Nikolashkin, S. V., Prakhov, A. N., Radionov, V. F., Turchinovich, Ju. S., Chernov, D. G., Holben, B. N., Smirnov, A., Sorokin, M. G., 2014. On results of studies of atmospheric aerosol optical depth in Arctic regions. Atmospheric and Oceanic Optics 27, No. 5. 413-423 (in Russian).

2711 Satheesh, S. K., Ramanathan, V., 2000. Large differences in tropical aerosol forcing at the top of
2712 the atmosphere and Earth's surface. Nature 405, 60-63, doi: 10.1038/35011039.
2713 Saunders, R. W., Kriebel, K. T., 1988. An improved method for detecting clear sky and cloudy
2714 radiances from AVHRR data. International Journal of Remote Sensing 9, 1, 123-150,
2715 doi:10.1080/01431168808954841.
2716 Sayer, A. M., Hsu, N. C., Bettenhausen, C., Jeong, M.-J., Holben, B. N., Zhang, J., 2012. Global
2717 and regional evaluation of over-land spectral aerosol optical depth retrievals from SeaWiFS,
2718 Atmospheric Measurement Techniques 5, 1761-1778, doi:10.5194/amt-5-1761-2012.
2719 Schlundt, C., Kokhanovsky, A. A., von Hoyningen-Huene, W., Dinter, T., Istomina, L., Burrows, J.
2720 P., 2011. Synergetic cloud fraction determination for SCIAMACHY using MERIS.
2721 Atmospheric Measurement Techniques 4, 2, 319-337, doi:10.5194/amt-4-319-2011.
2722 Schutgens, N. A. J., Nakata, M., Nakajima, T., 2013. Validation and empirical correction of
2723 MODIS AOT and AE over ocean. Atmospheric Measurement Techniques 6, 2455-2475,
2724 doi:10.5194/amt-6-2455-2013.
2725 Schwartz, S. E., Andreae, M. O., 1996. Uncertainty in climate change caused by aerosols. Science
2726 272, 5265, 1121-1122, doi:10.126/science.272.5265.1121.
2727 Sharma, S., Andrews, E., Barrie, L. A., Ogren, J. A., Lavoué, D., 2006. Variations and sources of
2728 equivalent black carbon in the high Arctic revealed by long-term observations at Alert and
2729 Barrow: 1989-2003. Journal of Geophysical Research 111, D14208,
2730 doi:10.1029/2005JD006581.
2731 Shaw, G. E., 1976. Error analysis of multi-wavelength sun photometry 114, 1, 1-14,
2732 doi:10.1007/BF00875487.
2733 Shaw, G. E., 1988. Antarctic aerosols: A review. Reviews of Geophysics 26, 1, 89-112, doi:
2734 10.1029/RG026i001p00089.
2735 Shaw, G. E., 1995. The arctic haze phenomenon. Bulletin of the American Meteorological Society
2736 76, 12, 2403-2413, doi: 10.1175/1520-0477(1995)076<2403:TAHP>2.0.CO;2.

2737 Shi, T., Yu, B., Braverman, A. J., 2002. MISR Cloud Detection over Ice/Snow Using Linear
2738 Correlation Matching.Technical Report 630, University of California, Department of
2739 Statistics, Berkeley, CA.
2740 Shi, T., Clothiaux, E. E., Yu, B., Braverman, A. J., Groff, D.N., 2007. Detection of daytime arctic
2741 clouds using MISR and MODIS data. Remote Sensing of Environment 107, 1-2, 172-184,
2742 doi:10.1016/j.rse.2006.10.015.
2743 Sinyuk, A., Holben, B. N., Smirnov, A., Eck, T. F., Slutsker, I., Schafer, J. S., Giles, D. M.,
2744 Sorokin, M., 2012. Assessment of error in aerosol optical depth measured by AERONET due
2745 to aerosol forward scattering. Geophysical Research Letters 39, L23806,
2746 doi:10.1029/2012GL053894.
2747 Six, D., Fily, M., Blarel, L., Goloub, P., 2005. First aerosol optical thickness measurements at
2748 Dome C (East Antarctica), summer season 2003–2004. Atmospheric Environment 39, 28,
2749 5041-5050, doi:10.1016/j.atmosenv.2005.05.010.
2750 Smirnov, A., Holben, B. N., Eck, T. F., Dubovik, O., Slutsker, I., 2000. Cloud-screening and quality
2751 control algorithms for the AERONET database. Remote Sensing of Environment 73, 3, 337-
2752 349, doi:10.1016/S0034-4257(00)00109-7.
2753 Smirnov, A., Holben, B. N., Slutsker, I., Giles, D. M., McClain, C. R., Eck, T. F., Sakerin, S. M.,
2754 Macke, A., Croot, P., Zibordi, G., Quinn, P. K., Sciare, J., Kinne, S., Harvey, M., Smyth, T. J.,
2755 Piketh, S., Zielinski, T., Proshutinsky, A., Goes, J. I., Nelson, N. B., Larouche, P., Radionov,
2756 V. F., Goloub, P., Moorthy, K. K., Matarrese, R., Robertson, E. J., Jourdin, F, 2009. Maritime
2757 Aerosol Network as a component of Aerosol Robotic Network. Journal of Geophysical
2758 Research, 114, D06204, doi:10.1029/2008JD011257.
2759 Smirnov, A., Holben, B. N. , Giles, D. M., Slutsker, I., O'Neill, N. T., Eck, F., Macke, A., Croot, P.,
2760 Courcoux, Y. , Sakerin, S. M., Smyth, T. J., Zielinski, T., Zibordi, G., Goes, J. I., Harvey, M.
2761 J., Quinn, P. K., Nelson, N. B., Radionov, V. F., Duarte, C. M., Losno, R., Sciare, J., Voss, K.
2762 J., Kinne, S., Nalli, N. R., Joseph, E., Krishna Moorthy, K., Covert, D. S., Gulev, S. K.,

2763 Milinevsky, G., Larouche, P., Belanger, S., Horne, E., Chin, M., Remer, L. A., Kahn, R. A.,
2764 Reid, J. S., Schulz, M., Heald, C. L., Zhang, J., Lapina, K., Kleidman, R. G., Griesfeller, J.,
2765 Gaitley, B. J., Tan, Q., Diehl, T. L., 2011. Maritime aerosol network as a component of
2766 AERONET - first results and comparison with global aerosol models and satellite retrievals.
2767 Atmospheric Measurement Techniques, 4, 583–597, doi:10.5194/amt-4-583-2011.
2768 Spangenberg, D. A., Chakrapani, V., Doelling, D. R., Minnis, P., Arduini, R. F., 2001.
2769 Development of an automated Arctic cloud mask using clear sky satellite observations taken
2770 over the SHEBA and ARM NSA sites. Proceedings of the AMS 6th Conference on Polar
2771 Meteorology and Oceanography, San Diego, CA, May 14-18, 2001, pp. 246-249.
2772 Stamnes, K., Li, W., Spurr, R., Eide, H. A., Stamnes, J. J., 2004. Simultaneous retrieval of aerosol
2773 and surface properties over bright targets including snow and ice using multi- and
2774 hyperspectral data. Proceedings SPIE 5569, 56-67, doi:10.1117/12.565453.
2775 Stock, M., Ritter, C., Herber, A., von Hoyningen-Huene, W., Baibakov, K., Gräser, J., Orgis, T.,
2776 Treffeisen, R., Zinoviev, N., Makshtas, A., Dethloff, K., 2012. Springtime Arctic aerosol:
2777 Smoke versus haze, a case study for March 2008. Atmospheric Environment 52C, 48-55,
2778 doi:10.1016/j.atmosenv.2011.06.051.
2779 Stohl, A., 2006. Characteristics of atmospheric transport into the Arctic troposphere. Journal of
2780 Geophysical Research 111, D11306, doi:10.1029/2005JD006888.
2781 Stohl, A., Andrews, E., Burkhart, J. F., Forster, C., Herber, A., Hoch, S. W., Kowal, D., Lunder, C.,
2782 Mefford, T., Ogren, J. A., Sharma, S., Spichtinger, N., Stebel, K., Stone, R., Ström, J.,
2783 Tørseth, K., Wehrli, C., Yttri, K.E., 2006. Pan-Arctic enhancements of light absorbing aerosol
2784 concentrations due to North American boreal forest fires during summer 2004. Journal of
2785 Geophysical Research 111, D22214, doi:10.1029/2006JD007216.
2786 Stohl, A., Sodemann, H., 2010. Characteristics of atmospheric transport into the Antarctic
2787 troposphere. Journal of Geophysical Research 115, D02305, doi:10.1029/2009JD012536.

2788 Stone, R. S., 2002. Monitoring aerosol optical depth at Barrow, Alaska, and South Pole; historical
2789 overview, recent results and future goals. SIF Conference Proceedings 80, 123-144.
2790 Stone, R. S., Key, J. R., Dutton, E. G., 1993. Properties and decay of stratospheric aerosols in the
2791 Arctic following the 1991 eruptions of Mount Pinatubo. Geophysical Research Letters 20, 21,
2792 2359-2362, doi:10.1029/93GL02684.
2793 Stone, R. S., Anderson, G. P., Andrews, E., Dutton, E. G., Shettle, E. P., Berk, A., 2007. Incursions
2794 and radiative impact of Asian dust in northern Alaska. Geophysical Research Letters 34,
2795 L14815. doi:10.1029/2007GL029878.
2796 Stone, R. S., Anderson, G. P., Shettle, E. P., Andrews, E., Loukachine, K., Dutton, E. G., Schaaf,
2797 C., Roman III, M. O., 2008. Radiative impact of boreal smoke in the Arctic: Observed and
2798 modeled. Journal of Geophysical Research 113, D14S16, doi:10.1029/2007JD009657.
2799 Stone, R. S., Herber, A., Vitale, V., Mazzola, M., Lupi, A., Schnell, R. C., Dutton, E. G., Liu, P. S.
2800 K., Li, S.-M., Dethloff, K., Lampert, A., Ritter, C., Stock, M., Neuber, R., Maturilli, M., 2010.
2801 A three-dimensional characterization of Arctic aerosols from airborne Sun photometer
2802 observations: PAM-ARCMIP, April 2009. Journal of Geophysical Research 115, D13203,
2803 doi:10.1029/2009JD013605.
2804 Stone, R. S., Sharma, S., Herber, A., Eleftheriadis, K., Nelson, D. W., 2014. A characterization of
2805 Arctic aerosols on the basis of aerosol optical depth and black carbon measurements.
2806 Elementa: Science of Anthropocene 2, 22 pp, doi:10.12952/journal.elementa.000027.
2807 Ström, J., Umegård, J., Tørseth, K., Tunved, P., Hansson, H.-C., Holmén, K., Wismann, V., Herber,
2808 A., König-Langlo, G., 2003. One year of particle size distribution and aerosol chemical
2809 composition measurements at the Zeppelin station, Svalbard, March 2000-March 2001.
2810 Physics and Chemistry of the Earth 28, 1181-1190, doi:10.1016/j.pce.2003.08.058.
2811 Strunin, M. A., Postnov, A. A., Mezrin, M. Y., 1997. Meteorological potential for contamination of
2812 Arctic troposphere: Boundary layer structure and turbulent diffusion characteristics.
2813 Atmospheric Research, 44, 37-51, doi:10.1016/S0169-8095(97)00008-2.

2814 Teinilä, K., Kerminen, V.-M., Hillamo, R., 2000. A study of size-segregated aerosol chemistry in
2815 the Antarctic atmosphere. Journal of Geophysical Research 105, D3, 3893-3904,
2816 doi:10.1029/1999JD901033.
2817 Tang, J., Xue, Y., Yu, T., Guan, Y., 2005. Aerosol optical thickness determination by exploiting the
2818 synergy of TERRA and AQUA MODIS. Remote Sensing of Environment, 94, 3, 327-334,
2819 doi:10.1016/j.rse.2004.09.013.
2820 Tanré, D., Kaufman, Y. J., Herman, M., Mattoo, S., 1997. Remote sensing of aerosol properties
2821 over oceans using the MODIS/EOS spectral radiances. Journal of Geophysical Research 102.
2822 D14, 16971-16988, doi:10.1029/96JD03437.
2823 Thomason, L. W., Herman, B. M., Reagan, J. A., 1983. The effect of atmospheric attenuators with
2824 structured vertical distributions on air mass determinations and Langley plot analyses. Journal
2825 of the Atmospheric Sciences 40, 7, 1851-1854, doi:10.1175/1520-
2826 0469(1983)040<1851:TEOAAW>2.0.CO;2.
2827 Thomason, L. W., Peter, T. (eds.), 2006. Assessment of stratospheric aerosol properties (ASAP).
2828 SPARC Report N°4 (Stratospheric Aerosol Properties and their Role in Climate), WCRP-124,
2829 WMO/TD-No. 1295.
2830 Thomason, L.W., Burton, S. P., Luo, B.-P., Peter, T., 2008. SAGE II measurements of stratospheric
2831 aerosol properties at non-volcanic levels. Atmospheric Chemistry and Physics 8, 4, 983-995,
2832 doi:10.5194/acp-8-983-2008.
2833 Toledano, C., Cachorro, V. E., Gausa, M., Stebel, K., Aaltonen, V., Berjón, A., Ortiz de Galisteo, J.
2834 P., De Frutos, A. M., Bennouna, Y., Blindheim, S., Myhre, C. L., Zibordi, G., Wehrli, C.,
2835 Kratzer, S., Hakansson, B., Carlund, T., de Leeuw, G., Herber, A., Torres, B., 2012. Overview
2836 of sun photometer measurements of aerosol properties in Scandinavia and Svalbard.
2837 Atmospheric Environment 52C, 18-28, doi:10.1016/j.atmosenv.2011.10.022.
2838 Tomasi, C., Vitale, V., Lupi, A., Di Carmine, C., Campanelli, M., Herber, A., Treffeisen, R., Stone,
2839 R. S., Andrews, E., Sharma, S., Radionov, V., von Hoyningen-Huene, W., Stebel, K., Hansen,

2840 G. H., Myhre, C.L., Wehrli, C., Aaltonen, V., Lihavainen, H., Virkkula, A., Hillamo, R.,
2841 Ström, J., Toledano, C., Cachorro, V. E., Ortiz, P., de Frutos, A. M., Blindheim, S., Frioud,
2842 M., Gausa, M., Zielinski, T., Petelski, T., Yamanouchi, T., 2007. Aerosols in polar regions: a
2843 historical overview based on optical depth and in situ observations. Journal of Geophysical
2844 Research 112, D16205, doi:10.1029/2007JD008432.
2845 Tomasi, C., Petkov, B. H., Stone, R. S., Benedetti, E., Vitale, V., Lupi, A., Mazzola, M.,
2846 Lanconelli, C., Herber, A., von Hoyningen-Huene, W., 2010. Characterizing polar
2847 atmospheres and their effect on Rayleigh-scattering optical depth. Journal of Geophysical
2848 Research 115, D02205, doi:10.1029/2009JD012852.
2849 Tomasi, C., Lupi, A., Mazzola, M., Stone, R. S., Dutton, E. G., Herber, A., Radionov, V. F.,
2850 Holben, B. N., Sorokin, M. G., Sakerin, S. M., Terpugova, S. A., Sobolewski, P. S.,
2851 Lanconelli, C., Petkov, B. H., Busetto, M., Vitale, V., 2012. An update on polar aerosol
2852 optical properties using POLAR-AOD and other measurements performed during the
2853 International Polar Year. Atmospheric Environment 52C, 29-47,
2854 doi:10.1016/j.atmosenv.2012.02.055.
2855 Tomasi, C., Lanconelli, C., Lupi, A., Mazzola, M., 2013. Dependence of direct aerosol radiative
2856 forcing on the optical properties of atmospheric aerosol and underlying surface. Light
2857 Scattering Reviews 8 (Kokhanovsky, A. A., ed.), Chapter 11, 505-626, Springer-Praxis Books
2858 in Environmental Sciences, Heidelberg, Germany.
2859 Tomasi, C., Petkov, B. H., 2014. Calculations of relative optical air masses for various aerosol types
2860 and minor gases in Arctic and Antarctic atmospheres. Journal of Geophysical Research:
2861 Atmospheres 119, 3, 1363-1385, doi:10.1002/2013JD020600.
2862 Tomasi, C., Lanconelli, C., Lupi, A., Mazzola, M., 2014. Diurnally averaged direct aerosol-induced
2863 radiative forcing from cloud-free field measurements performed during seven regional
2864 experiments. Light Scattering Reviews 9, (Kokhanovsky, A. A., ed.), Chapter 8, 297-425,

2865 Springer-Praxis Books in Environmental Sciences, Heidelberg, Germany, November 2014, in
2866 press.
2867 Treffeisen, R., Tunved, P., Ström, J., Herber, A., Bareiss, J., Helbig, A., Stone, R. S., von
2868 Hoyningen-Huene, W., Krejci, R., Stohl, A., Neuber, R., 2007. Arctic smoke - aerosol
2869 characteristics during a record smoke event in the European Arctic and its radiative impact.
2870 Atmospheric Chemistry and Physics 7, 3035-3053, doi:10.5194/acp-7-3035-2007.
2871 Trepte, Q., Arduini, R. F., Chen, Y., Sun-Mack, S., Minnis, P., Spangenberg, D. A., Doelling, D.
2872 R., 2001. Development of a daytime polar cloud mask using theoretical models of near -
2873 infrared bidirectional reflectance for ARM and CERES. Proceedings of the AMS 6th
2874 Conference on Polar Meteorology and Oceanography, San Diego, CA, May 14-18, 2001, pp.
2875 242-245.
2876 Tuncel, G., Aras, N. K., Zoller, W. H., 1989. Temporal variations and sources of elements in the
2877 South Pole atmosphere. 1. Non enriched and moderately enriched elements. Journal of
2878 Geophysical Research 94, D10, 13025-13038, doi:10.1029/JD094iD10p13025.
2879 Vermote, E. F., Tanré, D., Deuzé, J. L., Herman, M., Morcrette, J.-J., 1997a. Second simulation of
2880 the satellite signal in the solar spectrum (6S): An overview. IEEE Transactions on Geoscience and
2881 Remote Sensing 35, 3, 675-686, doi: 10.1109/36.581987.
2882 Vermote, E., Tanré, D., Deuzé, J. L., Herman, M., Morcrette, J. J., 1997b. Second Simulation of the
2883 Satellite Signal in the Solar Spectrum (6S), 6S User Guide Version 2, July 1997. Universitè de
2884 Lille, France, 218 pp.
2885 Virkkula, A., Teinilä, K., Hillamo, R., Kerminen, V.-M., Saarikoski, S., Aurela, M. , Koponen, I.
2886 K., Kulmala, M., 2006a. Chemical size distributions of boundary layer aerosol over the
2887 Atlantic Ocean and at an Antarctic site. Journal of Geophysical Research 111, D05306,
2888 doi:10.1029/2004JD004958.

2889 Virkkula, A., Koponen, I. K., Teinilä, K., Hillamo, R., Kerminen, V.-M., Kulmala, M., 2006b.
2890 Effective real refractive index of dry aerosols in the Antarctic boundary layer. Geophysical
2891 Research Letters 33, L06805, doi:10.1029/2005GL024602.
2892 von Hoyningen-Huene, W., Freitag, M., Burrows, J. P., 2003. Retrieval of aerosol optical thickness
2893 over land surface from top-of-atmosphere radiance, Journal of Geophysical Research 108, D9,
2894 doi:10.1029/2001JD002018.
2895 von Hoyningen-Huene, W., Yoon, J., Vountas, M., Istomina, L. G., Rohen, G., Dinter, T.,
2896 Kokhanovsky, A. A., Burrows, J. P., 2011. Retrieval of spectral aerosol optical thickness over
2897 land using ocean color sensors MERIS and SeaWiFS. Atmospheric Measurement Techniques
2898 4, 151-171, doi:10.5194/amt-4-151-2011.
2899 Wang, Y., Xue, Y., Li, Y., Guang, J., Mei, L., Xu, H.,Ai, J., 2012. Prior knowledge-supported
2900 aerosol optical depth retrieval over land surface at 500 m spatial resolution with MODIS data.
2901 International Journal of Remote Sensing, 33, 3, 674-691, doi:10.1080/01431161.2011.577832.
2902 Warneke, C., Froyd, K. D., Brioude, J., Bahreini, R., Brock, C. A., Cozic, J., de Gouw, J. A., Fahey,
2903 D. W., Ferrare, R., Holloway, J. S., Middlebrook, A. M., Miller, L., Montzka, S., Schwarz, J.
2904 P., Sodemann, H., Spackman, J. R., Stohl, A., 2010. An important contribution to springtime
2905 Arctic aerosol from biomass burning in Russia. Geophysical Research Letters 37, L01801,
2906 doi:10.1029/2009GL041816.
2907 Warren, S. G., Wiscombe, W. J., 1980. A model for the spectral albedo of snow. II: Snow
2908 containing atmospheric aerosols. Journal of the Atmospheric Sciences 37, 12, 2734-2745,
2909 doi:10.1175/1520-0469(1980)037<2734:AMFTSA>2.0.CO;2.
2910 Wehrli, C., 2000. Calibrations of filter radiometers for determination of atmospheric optical depths.
2911 Metrologia, 37, 419-422.
2912 Weitkamp, C. (Ed.), 2005. Lidar: Range-Resolved Optical Remote Sensing of the Atmosphere.
2913 Springer Series in Optical Sciences, Vol. 102, ISBN 978-0-387-40075-4, 455 pp.

2914 Weller, R., Wagenbach, D., 2007. Year-round chemical aerosol records in continental Antarctica
2915 obtained by automatic samplings. Tellus 59C, 755-765, doi:10.1111/j.1600-
2916 0889.2007.00293.x.
2917 Weller, R., Lampert, A., 2008. Optical properties and sulfate scattering efficiency of boundary layer
2918 aerosol at coastal Neumayer Station, Antarctica. Journal of Geophysical Research 113,
2919 D16208, doi:10.1029/2008JD009962.
2920 Weller, R., Wöltjen, J., Piel, C., Resenberg, R., Wagenbach, D., König-Langlo, G., Kriews, M.,
2921 2008. Seasonal variability of crustal and marine trace elements in the aerosol at Neumayer
2922 Station, Antarctica. Tellus 60B, 742-752, doi:10.1111/j.1600-0889.2008.00372.x.
2923 Whitt, D. B., Jacobson, M. Z., Wilerson, J. T., Naiman, A. D., Lele, S. K., 2011. Vertical mixing of
2924 commercial aviation emissions from cruise altitude to the surface. Journal of Geophysical
2925 Research 116, D14109, doi:10.1029/2010JD015532.
2926 Wilson, D. I., Piketh, S. J., Smirnov, A., Holben, B. N., Kuyper, B., 2010. Aerosol optical
2927 properties over the South Atlantic and Southern Ocean during the 140th cruise of the M/V S.A.
2928 Agulhas. Atmospheric Research 98, 2 – 4, 285-296, doi:10.1016/j.atmosres.2010.07.007.
2929 Winker, D. M., Vaughan, M. A., Omar, A., Hu, Y., Powell, K. A, 2009. Overview of the CALIPSO
2930 mission and CALIOP data processing algorithms. Journal of Atmospheric and Oceanic
2931 Technology 26, 11, 2310-23231, doi:10.1175/2009JTECHA1281.1.
2932 Winker, D. M., Pelon, J., Coakley, J. A. Jr., Ackerman, S. A., Charlson, R. J., Colarco, P. R.,
2933 Flamant, P., Fu, Q., Hoff, R. M., Kittaka, C., Kubar, T. L., Le Treut, H., McCormick, M. P.,
2934 Mégie, G., Poole, L., Powell, K., Trepte, C., Vaughan, M. A., Wielicki, B. A., 2010. The
2935 CALIPSO mission: A global 3D view of aerosols and clouds. Bulletin of the American
2936 Meteorological Society 91, 9, 1211-1229, doi:10.1175/2010BAMS3009.1.
2937 Winker, D. M., Tackett, J. L., Getzewich, B. J., Liu, Z., Vaughan, M. A., Rogers, R. R., 2013. The
2938 global 3-D distribution of tropospheric aerosols as characterized by CALIOP. Atmospheric
2939 Chemistry and Physics 13, 9, 3345-3361, doi:10.5194/acp-13-3345-2013.

Wolff, E. W., Cachier, H., 1998. Concentrations and seasonal cycle of black carbon in aerosol at a coastal Antarctic station. Journal of Geophysical Research 103, D9, 11033-11041, doi:10.1029/97JD01363.

Xue, Y., Cracknell, A. P., 1995. Operational bi-angle approach to retrieve the Earth surface albedo from AVHRR data in the visible band. International Journal of Remote Sensing 16, 3, 417-429, doi:10.1080/01431169508954410.

Xue, Y., He, X., Xu, H., Guang, J., Guo, J., Mei, L., 2014. China Collection 2.0: The aerosol optical depth dataset from the synergetic retrieval of aerosol properties algorithm. Atmospheric Environment 95, 45-58, doi:10.1016/j.atmosenv.2014.06.019.

Yamanouchi, T., Treffeisen, R. , Herber, A., Shiobara, M., Yamagata, S., Hara, K., Sato, K., Yabuki, M., Tomikawa, Y., Rinke, A., Neuber, R., Schumachter, R., Kriews, M., Ström, J., Schrems, O., Gernandt, H., 2005. Arctic Study of Tropospheric Aerosol and Radiation (ASTAR) 2000: Arctic haze case study. Tellus B 57, 2, 141-152, doi:10.1111/j.1600-0889.2005.00140.x.

Yoon, J., von Hoyningen-Huene, W., Kokhanovsky, A. A., Vountas, M., Burrows, J. P., 2012. Trend analysis of aerosol optical thickness and Ångström exponent derived from the global AERONET spectral observations. Atmospheric Measurement Techniques 5, 6, 1271-1299, doi:10.5194/amt-5-1271-2012.

2960

2961 **Figure legends**

2962

2963 Figure 1. Schematic of the main transport pathways of aerosols into the Arctic, as described by Law
2964 et al. (2014) [used with permission of the American Meteorological Society].

2965

2966 Figure 2. Part (a): Map of the Arctic with the geographical positions of the ground-based sun-
2967 photometer stations (solid stars), labelled with the following numbered circles: (1) Barrow, (2)
2968 Resolute Bay, (3) Eureka-0PAL, (4) Alert, (5) Thule, (6) Summit, (7) Ittoqqortoormiit, (8) Ny-
2969 Ålesund, (9) Barentsburg, (10) Hornsund, (11) Sodankylä, (12) Tiksi, (13) Andenes/ALOMAR, and
2970 (14) Kiruna. Grey symbols indicate the geographical positions of ship-borne sun-photometer
2971 measurements made on clear-sky days during the AERONET/MAN cruises in three different
2972 sectors: (i) Northern Greenland-Norwegian Sea (GNS), between 20° W and 30° E (squares), (ii)
2973 Barents Sea and West Siberian Sea (BWS), between 30° E and 130° E (diamonds), and (iii) Eastern
2974 Chuckci Sea, Beaufort Sea and Amundsen Gulf (NAA), between 170° W and 110° W (triangles).
2975 Part (b): as in the upper part, for the Antarctic ground-based sun-photometer and/or lidar stations
2976 (crosses), labelled with the following numbered circles: (1) Marambio, (2) Neumayer, (3) Troll, (4)
2977 Novolazarevskaya, (5) Mirny, (6) Syowa, (7) Mario Zucchelli, (8) Dome Concordia, (9) South Pole,
2978 (10) McMurdo, and (11) Dumont d'Urville. Grey symbols indicate the geographical positions of the
2979 ship-borne sun-photometer measurement days during the AERONET/MAN cruises, subdivided into
2980 the four following oceanic sectors: (i) Southern Indian Ocean (IND), between 20° E and 150° E
2981 (squares), (ii) Southern Pacific Ocean (PAC), between 150° E and 75° W (upward triangles), (iii)
2982 Southern Atlantic Ocean (ATL), between 50° W and 20° E (diamonds), and (iv) Antarctic
2983 Peninsula (APE), between 75° and 50° W (downward triangles).

2984

2985 Figure 3.- Left-hand side: Time-patterns of the monthly mean values and standard deviations
2986 (defined by the grey shaded areas) of aerosol optical thickness $\tau(0.50\ \mu m)$ (open squares) and
2987 Ångström wavelength exponent α (solid circles) obtained from both series of multi-year sun-
2988 photometer measurements conducted at Barrow (Alaska) by (a) GMD/NOAA (Boulder, Colorado,
2989 USA) over the period from March 2000 to September 2012, using the Carter Scott sun-photometers
2990 listed in Table 1, and (b) NASA/GSFC (USA) (in cooperation with the Brookhaven National
2991 Laboratory (Upton, NY, USA)) over the period from March 2002 to September 2013, using the
2992 AERONET Cimel CE-318 sun-photometer having the spectral characteristics given in Table 1.
2993 Right-hand side: Relative frequency histograms of $\tau(0.50\ \mu m)$ and exponent α obtained separately
2994 for the winter-spring (Arctic haze) period from December to May (black colour) and the summer-
2995 autumn (background aerosol) period from June to October (grey colour). The seasonal mean values
2996 and 25th, 50th, and 75th percentiles of $\tau(0.50\ \mu m)$ and α are reported in the boxes inserted into the
2997 graphs, as obtained by examining the daily mean values of both optical parameters measured at this
2998 coastal site of the Arctic Ocean in the winter-spring (black italics) and summer-autumn (grey
2999 italics) periods.
3000
3001 Figure 4.- As in Figure 3, for the multi-year sun-photometer measurements of aerosol optical
3002 thickness $\tau(0.50\ \mu m)$ and exponent α conducted at: (a) Resolute Bay by Environment Canada
3003 (Ontario, Canada) over the period from July 2004 to October 2012, using the
3004 AERONET/AEROCAN Cimel CE-318 sun-photometer having the spectral characteristics given in
3005 Table 1; (b) Eureka-0PAL by CARTEL (Sherbrooke University, Canada) from April 2007 to
3006 September 2011, using the AERONET/AEROCAN Cimel CE-318 sun-photometer having the
3007 spectral characteristics given in Table 1; and (c) Alert by GMD/NOAA (Boulder, Colorado, USA)
3008 from August 2004 to September 2012, using the Carter Scott SP02 sun-photometer, with the
3009 characteristics given in Table 1.
3010

3011 Figure 5.- As in Figure 3, for the for the multi-year sun-photometer measurements of aerosol optical
3012 thickness $\tau(0.50\ \mu m)$ and exponent α conducted at: (a) Thule (North-western Greenland) by
3013 NASA/GSFC (USA) over the period from March 2007 to September 2012, using an AERONET
3014 Cimel CE-318 sun-photometer having the spectral characteristics reported in Table 1; (b) Summit
3015 (Central Greenland) by PMOD/WRC (Switzerland) from January 2001 to October 2011, using a
3016 PFR (No. N34) sun-photometer of the GAW-PFR network, having the spectral characteristics given
3017 in Table 1; and (c) Ittoqqortoormiit (Eastern Greenland) by NASA/GSFC (USA) over the period
3018 from May 2010 to October 2013, using an AERONET Cimel CE-318 sun-photometer having the
3019 spectral characteristics reported in Table 1.
3020
3021 Figure 6.- As in Figure 3, for the sun-photometer measurements of aerosol optical thickness $\tau(0.50$
3022 $\mu m)$ and exponent α conducted on Spitsbergen Island (Svalbard, Norway) at: (a) Ny-Ålesund by
3023 AWI (Bremerhaven, Germany) from April 2000 to September 2013, using the sun- and star-
3024 photometers listed in Table 1; (b) Ny-Ålesund by NILU (Kjeller, Norway) from April 2002 to
3025 September 2004 and from March 2006 to September 2013, using a PFR (No. N18) sun-photometer
3026 of the GAW network; (c) Barentsburg by IAO-SB-RAS (Tomsk, Russia) in the April-August
3027 months of 2011 and 2012, using the SPM portable sun-photometer having the characteristics
3028 reported in Table 1, and (d) Hornsund by NASA/GSFC (USA) in cooperation with the Warsaw
3029 University (PAS, Poland from April 2005 to August 2013, using an AERONET Cimel CE-318 sun-
3030 photometer having the characteristics reported in Table 1.
3031
3032 Figure 7.- As in Figure 3, for the sun-photometer measurements of aerosol optical thickness $\tau(0.50$
3033 $\mu m)$ and exponent α conducted at: (a) Sodankylä (Northern Finland) by FMI (Helsinki, Finland) in
3034 the winter-spring and summer-autumn periods from late May 2004 to March 2013, using a PFR
3035 (No. N32) sun-photometer having the characteristics reported in Table 1, (b) Sodankylä by
3036 NASA/GSFC (USA) in cooperation with FMI (Helsinki, Finland) from February 2007 to November

3037 2013, using an AERONET Cimel CE-318 sun-photometer having the characteristics reported in
3038 Table 1; and (c) Tiksi (North-central Siberia, Russia) by NASA/GSFC (USA) in the summer-
3039 autumn months (June-October) of 2010, 2011 and 2012, using an AERONET Cimel CE-318 sun-
3040 photometer having the characteristics given in Table 1. In the first graphs, the time-patterns of the
3041 monthly mean values of $\tau(0.50\ \mu m)$ and α (solid and open diamonds, respectively) estimated by
3042 Toledano et al. (2012) at Kiruna from PFR measurements conducted over the 2007-2010 period are
3043 shown with their standard deviations (vertical bars) for comparison with the FMI results found at
3044 Sodankylä. The time-patterns of the monthly mean values of $\tau(0.50\ \mu m)$ and α (solid and open
3045 triangles, respectively) estimated by Toledano et al. (2012) at Kiruna from the Cimel CE-318
3046 measurements conducted from 2002 to 2007 are shown in the seconda graph for comparison with
3047 those derived from the AERONET measurements carried out at Sodankylä.
3048
3049 Figure 8.- Upper part (a): Scatter plot of the seasonal median values of the Ångström exponent α
3050 versus the corresponding seasonal median values of aerosol optical thickness $\tau(0.50\ \mu m)$
3051 determined from the sun-photometer measurements listed in Table 1. Acronym key: Barrow (BRW-
3052 NOAA for the GMD/NOAA measurements, and BRW-AER for the NASA/GSFC AERONET
3053 measurements), Resolute Bay (RES), Eureka-0PAL (E0P), Alert (ALE) Thule (THU), Summit
3054 (SUM), Ittoqqortoormiit (ITT), Ny-Ålesund (NYA-AWI and NYA-NILU, for the AWI and NILU
3055 measurements, respectively), Barentsburg (BAR), Hornsund (HOR), Sodankylä (SOD-PFR and
3056 SOD-AER, for the PFR and AERONET measurements, respectively) and Tiksi (TIK). The median
3057 values are represented using grey-solid and grey-and-white open symbols to represent the summer-
3058 autumn results (as shown in the legend) and solid or black-and-white open symbols to represent the
3059 winter-spring results, showing the background aerosol and Arctic haze optical characteristics,
3060 respectively. The 25^{th} and 75^{th} percentiles are used to define the limits of the vertical and horizontal
3061 dashed bars. Part (b), as in the upper part (a), for the winter-spring (grey symbols) and summer-
3062 autumn (open symbols) median values of α plotted versus the corresponding median values of

3063 $\tau(0.50\ \mu m)$, as obtained from the seasonal sets of ship-borne sun-photometer measurements
3064 collected over the Arctic Ocean sectors: (i) GNS (Greenland Sea and Norwegian Sea) (diamonds),
3065 (ii) BWS (Barents Sea and West Siberian Sea) (circles), and (iii) NAA (North-American Arctic
3066 ocean, including the East Chukchi Sea, the Bering Strait, the Beaufort Sea and the Amundsen Gulf)
3067 (squares).
3068
3069 Figure 9.- As in Figure 3, for sun-photometer measurements of aerosol optical thickness $\tau(0.50\ \mu m)$
3070 and exponent α conducted during the September-April period at: (a) Marambio in the Seymour-
3071 Marambio Island (Antarctic Peninsula) by FMI (Helsinki, Finland), using a PFR (No. N29) sun-
3072 photometer from August 2011 to March 2013; (b) Neumayer on the Akta Bay (Weddel Sea coast)
3073 by AWI (Bremerhaven, Germany), using the sun-photometers SP1A and SP2H, and the star-
3074 photometer STAR01 listed in Table 2 from September 2000 to April 2007; and (c) Troll located at
3075 Jutulsessen (in the Queen Maud Land, 235 km from the coast, at 1309 m a.m.s.l.) by NILU (Kjeller,
3076 Norway), alternately using two PFR (Nos. N40 and N42) sun-photometers from January 2007 to
3077 April 2013
3078
3079 Figure 10.- As in Figure 3, for sun-photometer measurements of aerosol optical thickness $\tau(0.50$
3080 $\mu m)$ and exponent α conducted at the Antarctic sites of: (a) Novolazarevskaya in the Schirmaker
3081 Oasis (Quenn Maud Land), 75 km from the coast, by AARI (St. Petersburg, Russia), using a hand-
3082 held Microtops calibrated at GSFC (USA) over the periods from December 2008 to February 2009
3083 and from November 2009 to February 2010, and obtaining Level 1.5 cloud-screened data; and (b)
3084 Mirny on the Davis Sea coast by AARI (St. Petersburg, Russia), using the AARI, SPM and
3085 Microtops sun-photometers, having the spectral characteristics given in Table 2, over the period
3086 from March 2000 to October 2013.
3087

Figure 11. As in Figure 3, for sun-photometer measurements of aerosol optical thickness $\tau(0.50\,\mu m)$ and exponent α conducted at the Antarctic sites of: (a) Syowa (East Ongul Island, Lützow-Holm Bay) over the period from January 2000 to December 2011 by the Office of Antarctic Observation (Japan Meteorological Agency, Tokyo, Japan), using the EKO MS-110 sun-photometer, having the spectral characteristics given in Table 2; and (b) Mario Zucchelli on the Terra Nova Bay (Ross Sea, Victoria Land) during the austral summer periods of 2001/2002 and 2005/2006 by ISAC-CNR (Bologna, Italy), using the PREDE POM-01L and the ASP-15WL sun-photometers, having the spectral characteristics given in Table 2.

Figure 12. Upper part: as in Figure 3, for sun-photometer measurements of aerosol optical thickness $\tau(0.50\,\mu m)$ and exponent α conducted at: (a) the high-altitude site of Dome Concordia (DomeC), on the Eastern Antarctic Plateau, over the period from September to April, by (i) GMD/NOAA (Boulder, Colorado, USA) from January to November 2010, using a Carter Scott SP02 sun-photometer (squares); (ii) NASA/GSFC (USA) in cooperation with LGGE/CNRS (Grenoble, France) in January and December of 2003, and in January 2004, using an AERONET Cimel CE-318 sun-photometer having the spectral characteristics reported in Table 2 (circles); and (iii) OPAR Institute (University of Réunion, St. Denis, France) in January of 2010, 2011 and 2012, using an hand-held Microtops II sun-photometer calibrated at GSFC (USA), obtaining Level 1.5 cloud-screened data (triangles). Lower part: as in Figure 3, for sun-photometer measurements of aerosol optical thickness $\tau(0.50\,\mu m)$ and exponent α conducted at the high-altitude site of South Pole (SPO) by (i) GMD/NOAA (Boulder, Colorado, USA), using a Carter Scott SP02 sun-photometer in the September-March period from November 2001 to March 2012; and (ii) NASA/GSFC (USA) in cooperation with GMD/NOAA (Boulder, Colorado, USA) using an AERONET Cimel CE-318 sun-photometer having the spectral characteristics reported in Table 2 in the November-February period from November 2007 to December 2012.

3114 Figure 13.- Part (a): as in Figure 8, but for the sun-photometer measurements listed in Table 2.
3115 Acronym key: Marambio (MAR), Neumayer (NEU), Troll (TRO), Novolazarevskaya (NOV),
3116 Mirny (MIR), Syowa (SYO), Mario Zucchelli (MZS), Dome Concordia (DMC-NOAA, DMC-
3117 AER, and DMC-OPAR, for the measurement sets collected by GMD/NOAA, AERONET and
3118 OPAR groups, respectively (see Table 4)) and South Pole (SPO-NOAA and SPO-AER, for the
3119 measurement sets collected by GMD/NOAA and AERONET groups, respectively). Part (b): as in
3120 part (a), for the Microtops sun-photometer measurements performed in Antarctic coastal (open
3121 symbols) and off-shore areas (solid symbols) during the cruises conducted in the four following
3122 oceanic sectors: (i) IND (Southern Indian Ocean, squares), (ii) PAC (Southern Pacific Ocean,
3123 upward triangles), (iii) ATL (Southern Atlantic Ocean, diamonds), and (iv) APE (Antarctic
3124 Peninsula, downward triangles).
3125
3126 Figure 14. Part (a): as in Figure 3, for Microtops sun-photometer measurements of aerosol optical
3127 thickness $\tau(0.50\ \mu m)$ and exponent α performed during the cruises conducted from 2003 to 2012 in
3128 the GNS (Greenland Sea and Norwegian Sea) sector (solid circles), from 2006 to 2012 in the BWS
3129 (Barents Sea and West Siberian Sea) sector (solid squares), and from 2008 to 2011 in the NAA
3130 (Eastern Chuckci Sea, Beaufort Sea and Amundsen Gulf) sector (open triangles) (see also Table 3).
3131 Part (b): relative frequency histograms of the daily mean values of aerosol optical thickness $\tau(0.50$
3132 $\mu m)$ and exponent α determined from the Microtops measurements conducted from March to
3133 September over the GNS (Greenland Sea and Norwegian Sea) sector, and the NAA (North
3134 American Arctic Ocean) sector, including the Eastern Chuckci Sea, Beaufort Sea and Amundsen
3135 Gulf.
3136
3137 Figure 15. Part (a): as in Figure 3, for Microtops sun-photometer measurements of $\tau(0.50\ \mu m)$ and
3138 α performed during the cruises conducted from late 2005 to spring 2013 in the frame of the
3139 Maritime Aerosol Network (MAN) activities listed in Table 4. The data refer to coastal (open

symbols) and off-shore (solid symbols) measurements, carried out in the IND sector (Southern Indian Ocean, circles), PAC sector (Southern Pacific Ocean, upward triangles), ATL sector (Southern Atlantic Ocean, squares), and APE sector (Antarctic Peninsula, downward triangles). Part (b): Relative frequency histograms of $\tau(0.50\ \mu m)$ and α obtained for the coastal data-sets collected (i) on 226 measurement days from November to February over the Southern Indian Ocean (IND) sector; (ii) 63 measurement days from December to April over the Southern Atlantic Ocean (ATL) sector; and (iii) on 49 measurement days from October to April over the coastal area surrounding the Antarctic Peninsula (APE sector).

Figure 16. Monthly and bi-monthly averaged vertical profiles of aerosol volume backscatter coefficient $\beta_{bs}(0.532\ \mu m)$ obtained from the KARL lidar measurements conducted at Ny-Ålesund (AWIPEV station) from 1 November, 2012, to 31 October, 2013.

Figure 17. Time-patterns of the monthly average values of the aerosol volume backscatter coefficient $\beta_{bs}(0.532\ \mu m)$ integrated over the different altitude ranges reported in the legend, as obtained from the KARL lidar measurements performed at Ny-Ålesund (AWIPEV station) from 1 November, 2012, to 31 October, 2013.

Figure 18. Time-patterns of the monthly average values of the lidar ratio $S_a(0{,}532\ \mu m) = \beta_{ext}(0.532\ \mu m)/\beta_{bs}(0.532\ \mu m)$ calculated over the whole altitude range (triangles) and the altitude sub-ranges $z < 3.5$ km (squares) and $z > 3.5$ km (+), as obtained from the KARL lidar measurements conducted at Ny-Ålesund (AWIPEV station) from 1 November, 2012, to 31 October, 2013.

Figure 19. Scatter plots of the monthly and bi-monthly averaged values of the depolarisation ratio (%) versus the aerosol backscatter coefficient $\beta_{bs}(0.532\ \mu m)$, as obtained from the KARL lidar

3165 measurements conducted at Ny-Ålesund (AWIPEV station) from 1 November, 2012, to 31 October,
3166 2013.
3167
3168 Figure 20. Arctic maps of the seasonal average Level-3 aerosol optical thickness $\tau(0.55\ \mu m)$ derived
3169 from MODIS/Aqua (upper part) and MODIS/Terra (lower part) satellite data recorded from 2005 to
3170 2012 during the spring (left-hand side) and summer (right-hand side) 3-month periods.
3171
3172 Figure 21. Antarctic maps of the austral summer Level-3 aerosol optical thickness $\tau(0.55\ \mu m)$
3173 derived from the MODIS/Terra (left-hand side) and MODIS/Aqua (right-hand side) satellite data
3174 recorded over the 2005-2012 period.
3175
3176 Figure 22. Maps of aerosol optical thickness $\tau(0.55\ \mu m)$ derived over the Arctic region from the
3177 MODIS/Aqua observations made on 29 March, 2006 (left-hand side) and 3 May, 2006 (right-hand
3178 side) using the method of Mei et al. (2013a).
3179
3180 Figure 23. Upper part: Arctic maps of the seasonal average Level-3 aerosol optical thickness $\tau(0.55$
3181 $\mu m)$ derived from the MISR satellite data recorded from 2005 to 2012 during the spring (left-hand
3182 side) and summer (right-hand side) 3-month periods. Lower part: As in the upper part, for the
3183 austral summer average Level-3 aerosol optical thickness $\tau(0.55\ \mu m)$ derived from MISR satellite
3184 data recorded from 2005 to 2012 over oceans and land areas not covered by snow and ice.
3185
3186 Figure 24. Time sequence of aerosol optical thickness $\tau(0.55\ \mu m)$ retrieved using AATSR data over
3187 sea-ice and snow-covered land surfaces with the algorithm described by Istomina et al. (2011). Left
3188 panel refers to orbit No. 31673 on 21 March, 2008; middle panel to orbit No. 31687 on 22 March,
3189 2008; and right panel to orbit No. 31773 on 28 March, 2008. The increase in $\tau(0.55\ \mu m)$ might be

3190 connected to ozone depletion/bromine explosions observed during March 2008 in the region
3191 (Nghiem et al., 2012; Moore et al., 2014).
3192
3193 Figure 25. Maps of aerosol optical thickness $\tau(0.55\ \mu m)$ retrieved from AATSR data taken with 1
3194 km × 1 km resolution on 9, 15, 18, and 21 April, 2009, over snow-covered surfaces in west
3195 Greenland using the method of Mei et al. (2013b).
3196
3197 Figure 26. Angular distribution curves of phase function $P(\Theta)$ as a function of the scattering angle
3198 Θ for the 8 unimodal Arctic aerosol extinction models (left) and the 6 unimodal Antarctic aerosol
3199 extinction models defined in Table 5.
3200
3201 Figure 27. Left-hand side: examples of bimodal particle size-distribution curves obtained as best-fit
3202 linear combinations of aerosol unimodal models for fine and accumulation/coarse particles defined
3203 in Table 3 in the following four case studies: (a) the average winter-spring aerosol case determined
3204 at Eureka (Nunavut, Northern Canada) for the mean values $\tau(0.50\ \mu m) = 0.12$ and $\alpha = 1.48$; (b) the
3205 summer background aerosol case determined at Tiksi (Russia) in North-central Siberia for the mean
3206 values $\tau(0.50\ \mu m) = 0.08$ and $\alpha = 1.60$; (c) the Asian dust episode observed at Barrow on 16 April,
3207 2002, giving the mean daily values $\tau(0.50\ \mu m) = 0.22$ and $\alpha = 0.26$; and (d) the BFF smoke episode
3208 observed by Stock et al. (2012) at Ny-Ålesund on 23 March, 2008, for the daily mean values $\tau(0.50$
3209 $\mu m) = 0.22$ and $\alpha = 1.50$. Right-hand side: as on the left, for the following four case studies: (e) the
3210 austral summer coastal aerosol case determined at Mario Zucchelli (MZS) for the mean values
3211 $\tau(0.50\ \mu m) = 0.03$ and $\alpha = 0.90$; (f) the austral summer coastal aerosol case determined at
3212 Neumayer (NEU) for the mean values of $\tau(0.50\ \mu m) = 0.045$ and $\alpha = 0.78$; (g) the austral summer
3213 Antarctic Plateau aerosol case determined at South Pole for the mean values $\tau(0.50\ \mu m) = 0.018$ and

α = 1.49; and (h) the austral winter aerosol case assumed at Neumayer for the seasonal average values $\tau(0.50\,\mu m) = 0.035$ and $\alpha = 0.65$.

Figure 28. Scatter plots of the daily mean values of DARF efficiencies E_{TOA} at the TOA-level (upper part), E_{BOA} at the BOA-level (middle part), and E_{ATM} in the atmosphere (lower part) shown versus the broadband albedo calculated by Tomasi et al. (2014) at solar zenith angle $\theta_o = 60°$, for the BRDF oceanic surface (OS1), vegetation-covered surface (VS1) and snow-covered polar surface (PS1, PS2, PS3 and PS4) models, and for the 15 polar aerosol types defined in Table 6 and represented using different symbols.

3225 **FIGURES**

3226

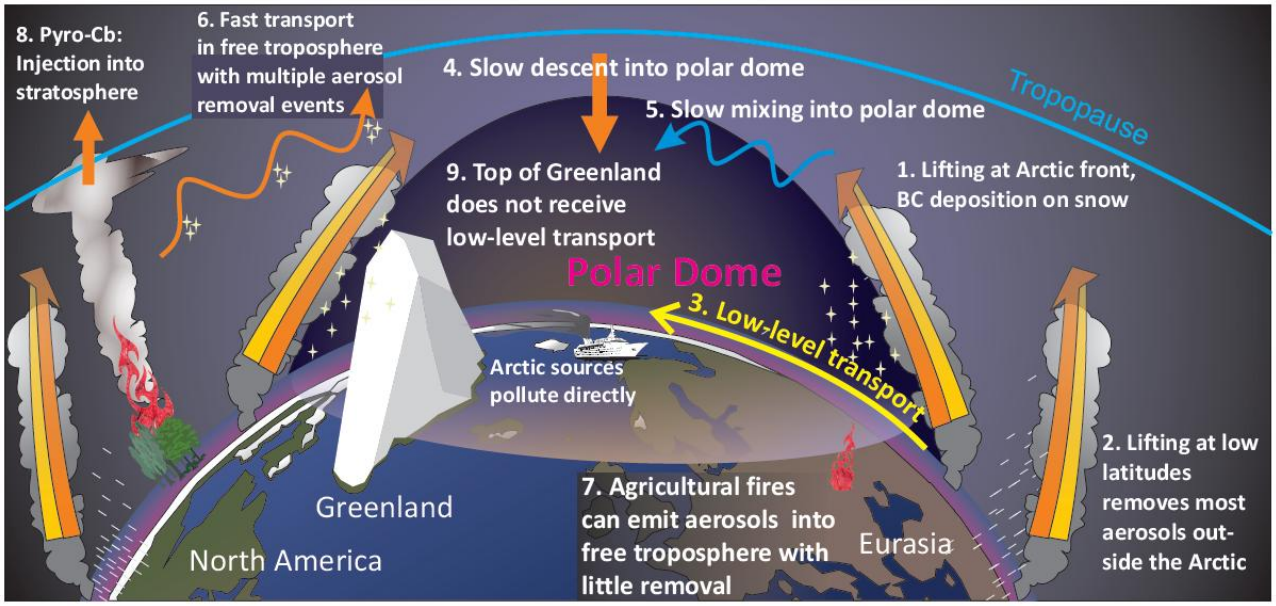

3227

3228 Figure 1. Schematic of the main transport pathways of aerosols into the Arctic, as described by Law

3229 et al. (2014) [used with permission of the American Meteorological Society].

3230

3231

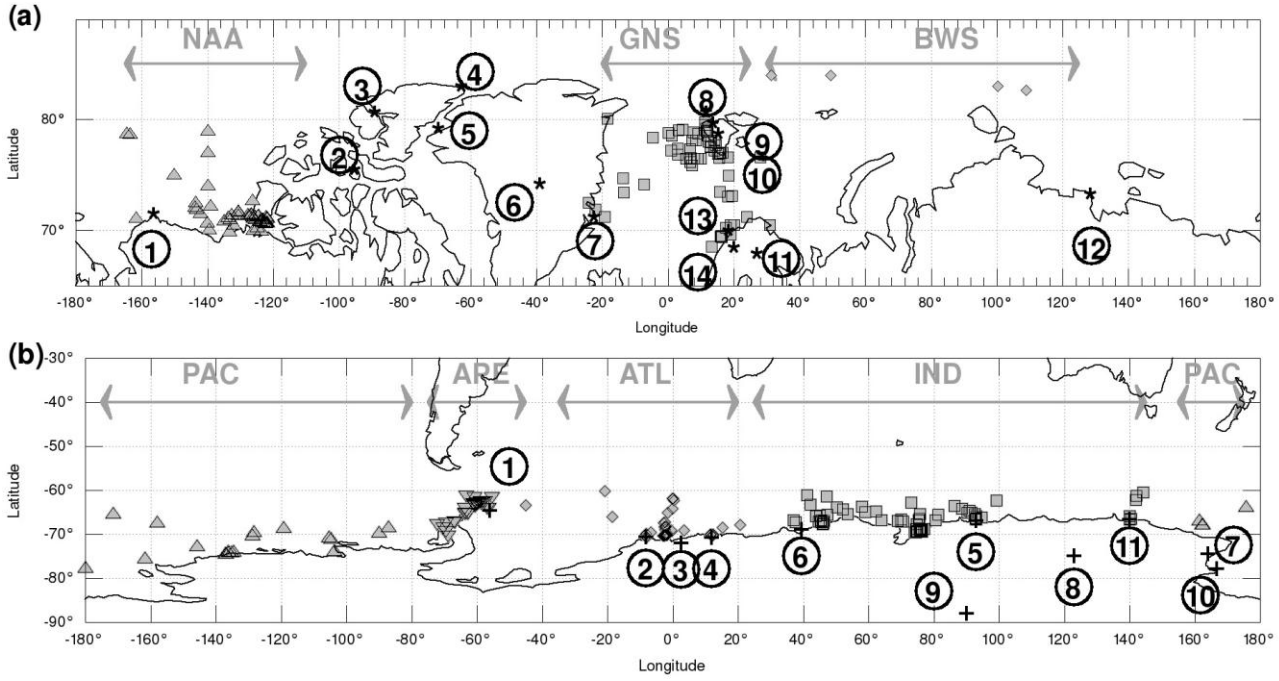

Figure 2. Part (a): Map of the Arctic with the geographical positions of the ground-based sun-photometer stations (solid stars), labelled with the following numbered circles: (1) Barrow, (2) Resolute Bay, (3) Eureka-0PAL, (4) Alert, (5) Thule, (6) Summit, (7) Ittoqqortoormiit, (8) Ny-Ålesund, (9) Barentsburg, (10) Hornsund, (11) Sodankylä, (12) Tiksi, (13) Andenes/ALOMAR, and (14) Kiruna. Grey symbols indicate the geographical positions of ship-borne sun-photometer measurements made on clear-sky days during the AERONET/MAN cruises in three different sectors: (i) Northern Greenland-Norwegian Sea (GNS), between 20° W and 30° E (squares), (ii) Barents Sea and West Siberian Sea (BWS), between 30° E and 130° E (diamonds), and (iii) Eastern Chuckci Sea, Beaufort Sea and Amundsen Gulf (NAA), between 170° W and 110° W (triangles). Part (b): as in the upper part, for the Antarctic ground-based sun-photometer and/or lidar stations (crosses), labelled with the following numbered circles: (1) Marambio, (2) Neumayer, (3) Troll, (4) Novolazarevskaya, (5) Mirny, (6) Syowa, (7) Mario Zucchelli, (8) Dome Concordia, (9) South Pole, (10) McMurdo, and (11) Dumont d'Urville. Grey symbols indicate the geographical positions of the ship-borne sun-photometer measurement days during the AERONET/MAN cruises, subdivided into the four following oceanic sectors: (i) Southern Indian Ocean (IND), between 20° E and 150° E (squares), (ii) Southern Pacific Ocean (PAC), between 150° E and 75° W (upward triangles), (iii) Southern Atlantic Ocean (ATL), between 50° W and 20° E (diamonds), and (iv) Antarctic Peninsula (APE), between 75° and 50° W (downward triangles).

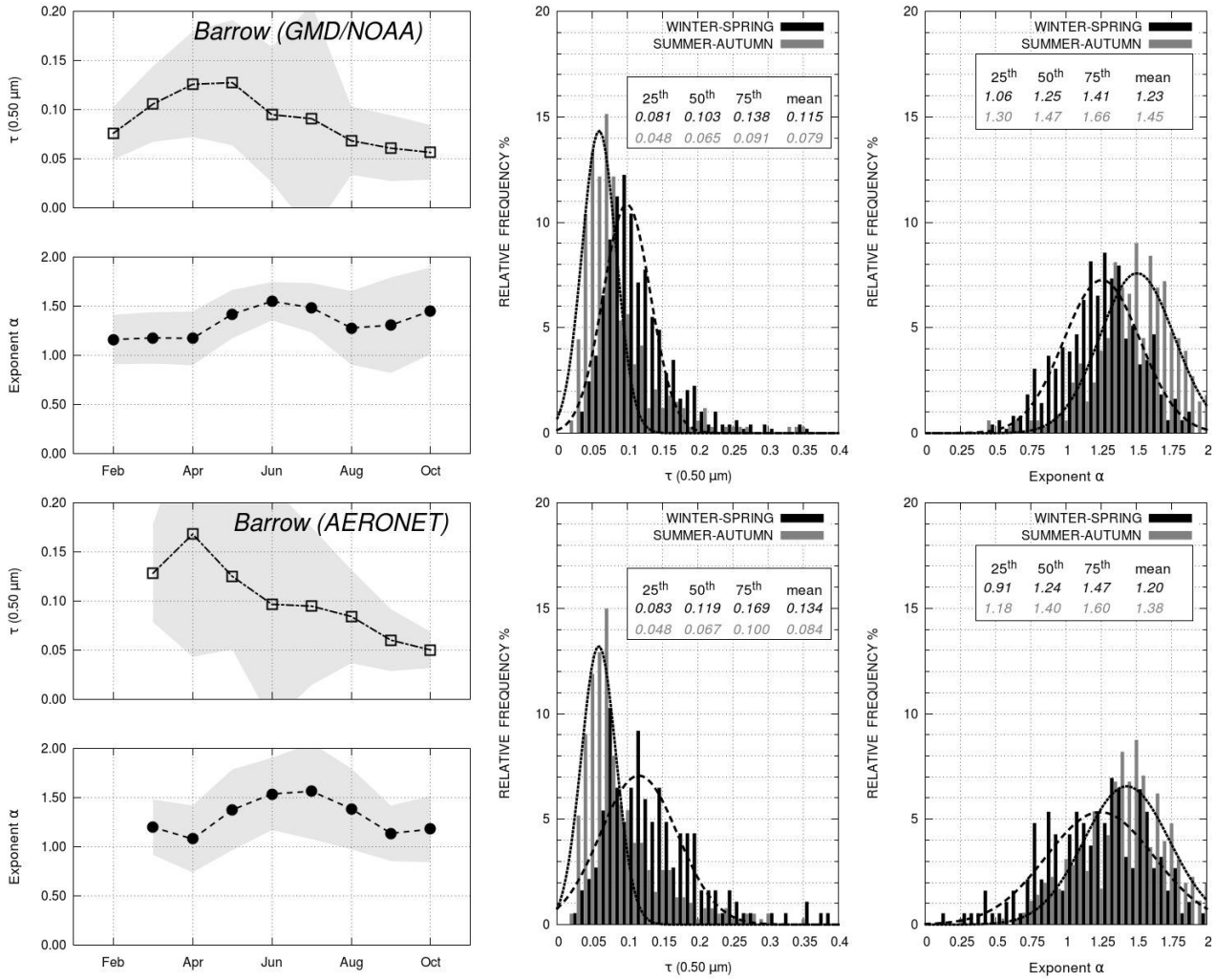

Figure 3.- Left-hand side: Time-patterns of the monthly mean values and standard deviations (defined by the grey shaded areas) of aerosol optical thickness $\tau(0.50\ \mu m)$ (open squares) and Ångström wavelength exponent α (solid circles) obtained from both series of multi-year sun-photometer measurements conducted at Barrow (Alaska) by (a) GMD/NOAA (Boulder, Colorado, USA) over the period from March 2000 to September 2012, using the Carter Scott sun-photometers listed in Table 1, and (b) NASA/GSFC (USA) (in cooperation with the Brookhaven National Laboratory (Upton, NY, USA)) over the period from March 2002 to September 2013, using the AERONET Cimel CE-318 sun-photometer having the spectral characteristics given in Table 1. Right-hand side: Relative frequency histograms of $\tau(0.50\ \mu m)$ and exponent α obtained separately for the winter-spring (Arctic haze) period from December to May (black colour) and the summer-autumn (background aerosol) period from June to October (grey colour). The seasonal mean values and 25th, 50th, and 75th percentiles of $\tau(0.50\ \mu m)$ and α are reported in the boxes inserted into the graphs, as obtained by examining the daily mean values of both optical parameters measured at this coastal site of the Arctic Ocean in the winter-spring (black italics) and summer-autumn (grey italics) periods.

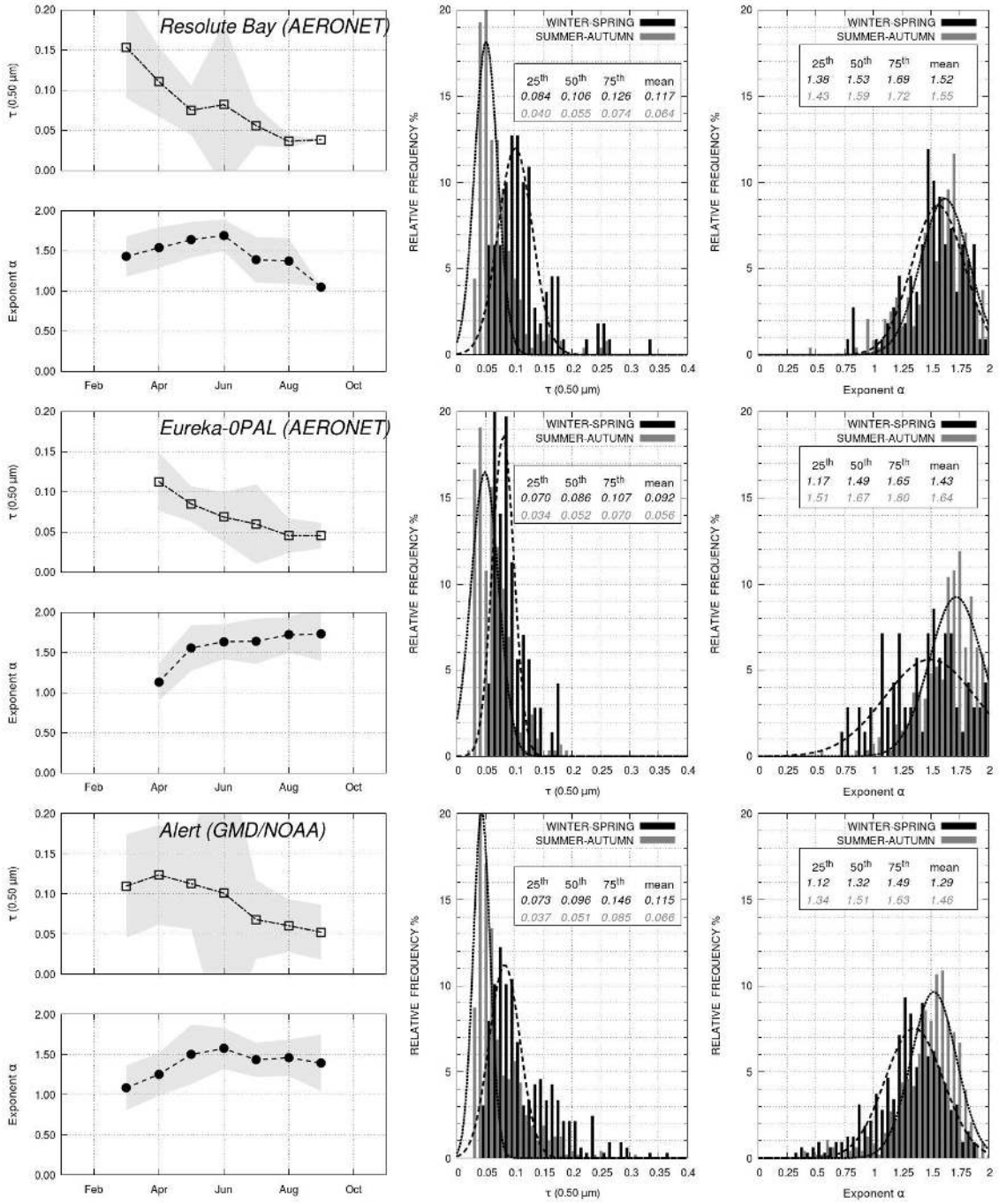

Figure 4.- As in Figure 3, for the multi-year sun-photometer measurements of aerosol optical thickness $\tau(0.50\ \mu m)$ and exponent α conducted at: (a) Resolute Bay by Environment Canada (Ontario, Canada) over the period from July 2004 to October 2012, using the AERONET/AEROCAN Cimel CE-318 sun-photometer having the spectral characteristics given in Table 1; (b) Eureka-0PAL by CARTEL (Sherbrooke University, Canada) from April 2007 to September 2011, using the AERONET/AEROCAN Cimel CE-318 sun-photometer having the spectral characteristics given in Table 1; and (c) Alert by GMD/NOAA (Boulder, Colorado, USA) from August 2004 to September 2012, using the Carter Scott SP02 sun-photometer, with the characteristics given in Table 1.

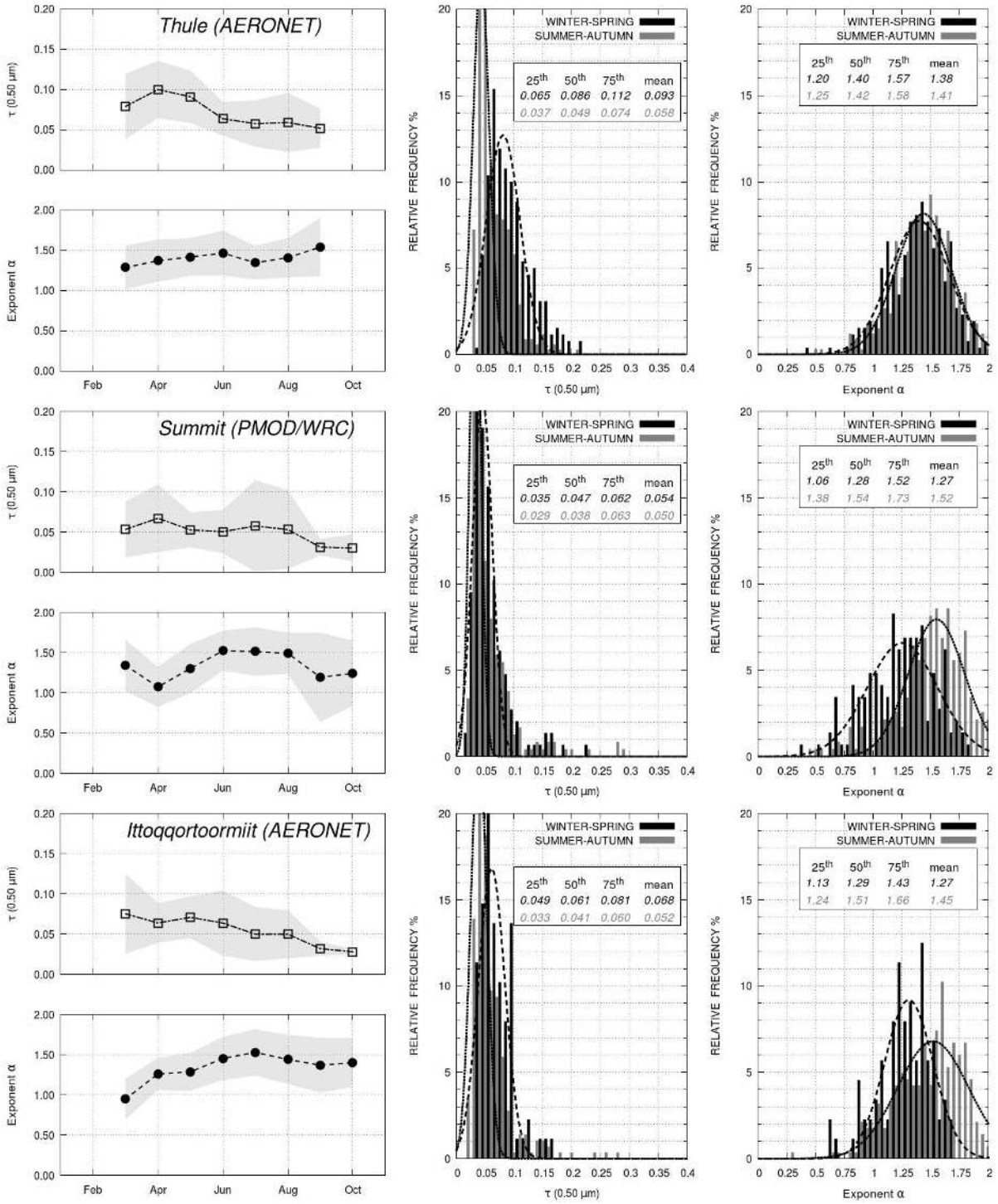

Figure 5.- As in Figure 3, for the for the multi-year sun-photometer measurements of aerosol optical thickness $\tau(0.50\ \mu m)$ and exponent α conducted at: (a) Thule (North-western Greenland) by NASA/GSFC (USA) over the period from March 2007 to September 2012, using an AERONET Cimel CE-318 sun-photometer having the spectral characteristics reported in Table 1; (b) Summit (Central Greenland) by PMOD/WRC (Switzerland) from January 2001 to October 2011, using a PFR (No. N34) sun-photometer of the GAW-PFR network, having the spectral characteristics given in Table 1; and (c) Ittoqqortoormiit (Eastern Greenland) by NASA/GSFC (USA) over the period from May 2010 to October 2013, using an AERONET Cimel CE-318 sun-photometer having the spectral characteristics reported in Table 1.

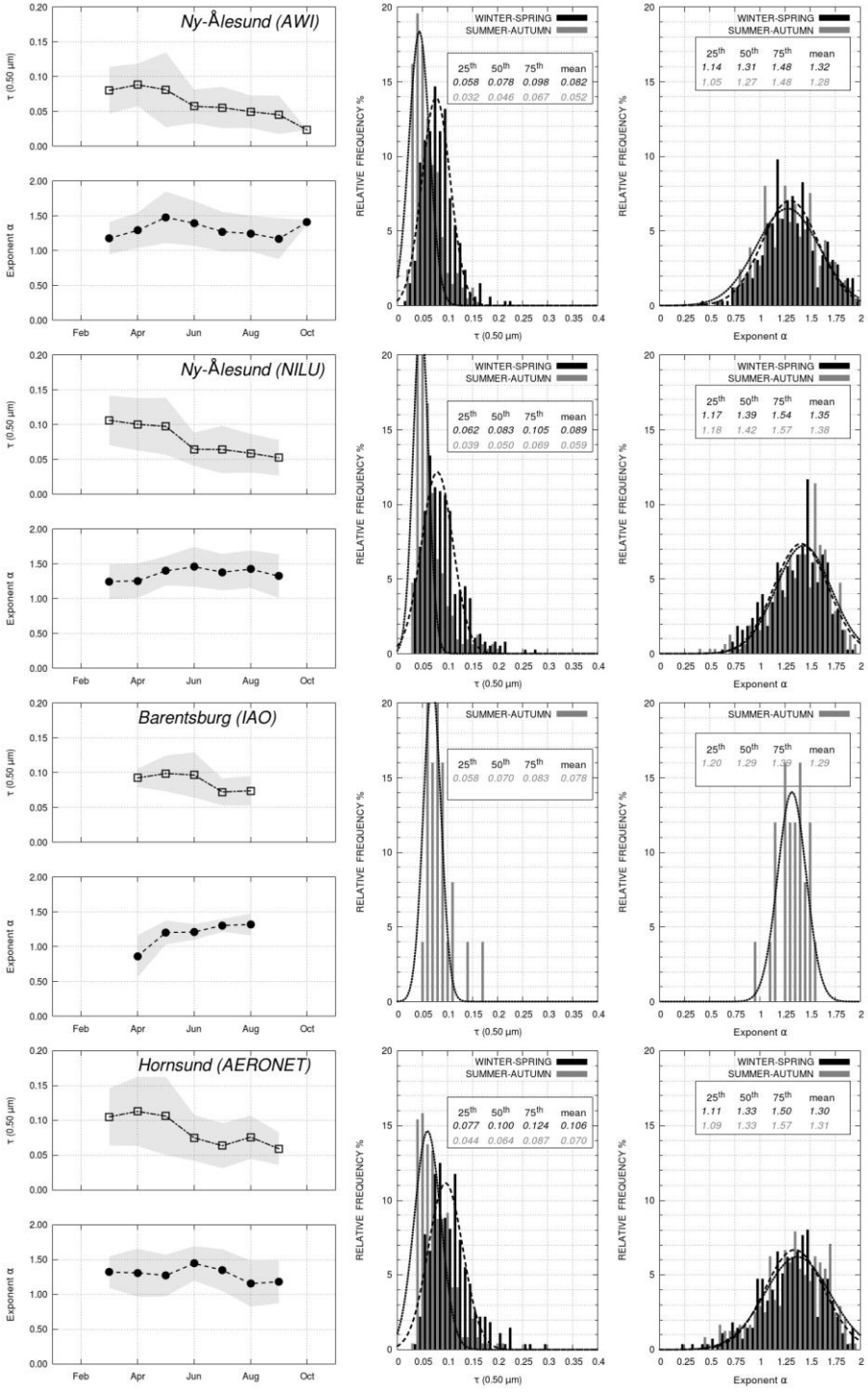

Figure 6.- As in Figure 3, for the sun-photometer measurements of aerosol optical thickness *τ(0.50 μm)* and exponent α conducted on Spitsbergen Island (Svalbard, Norway) at: (a) Ny-Ålesund by AWI (Bremerhaven, Germany) from April 2000 to September 2013, using the sun- and star-photometers listed in Table 1; (b) Ny-Ålesund by NILU (Kjeller, Norway) from April 2002 to September 2004 and from March 2006 to September 2013, using a PFR (No. N18) sun-photometer of the GAW network; (c) Barentsburg by IAO-SB-RAS (Tomsk, Russia) in the April-August months of 2011 and 2012, using the SPM portable sun-photometer having the characteristics reported in Table 1, and (d) Hornsund by NASA/GSFC (USA) in cooperation with the Warsaw University (PAS, Poland from April 2005 to August 2013, using an AERONET Cimel CE-318 sun-photometer having the characteristics reported in Table 1.

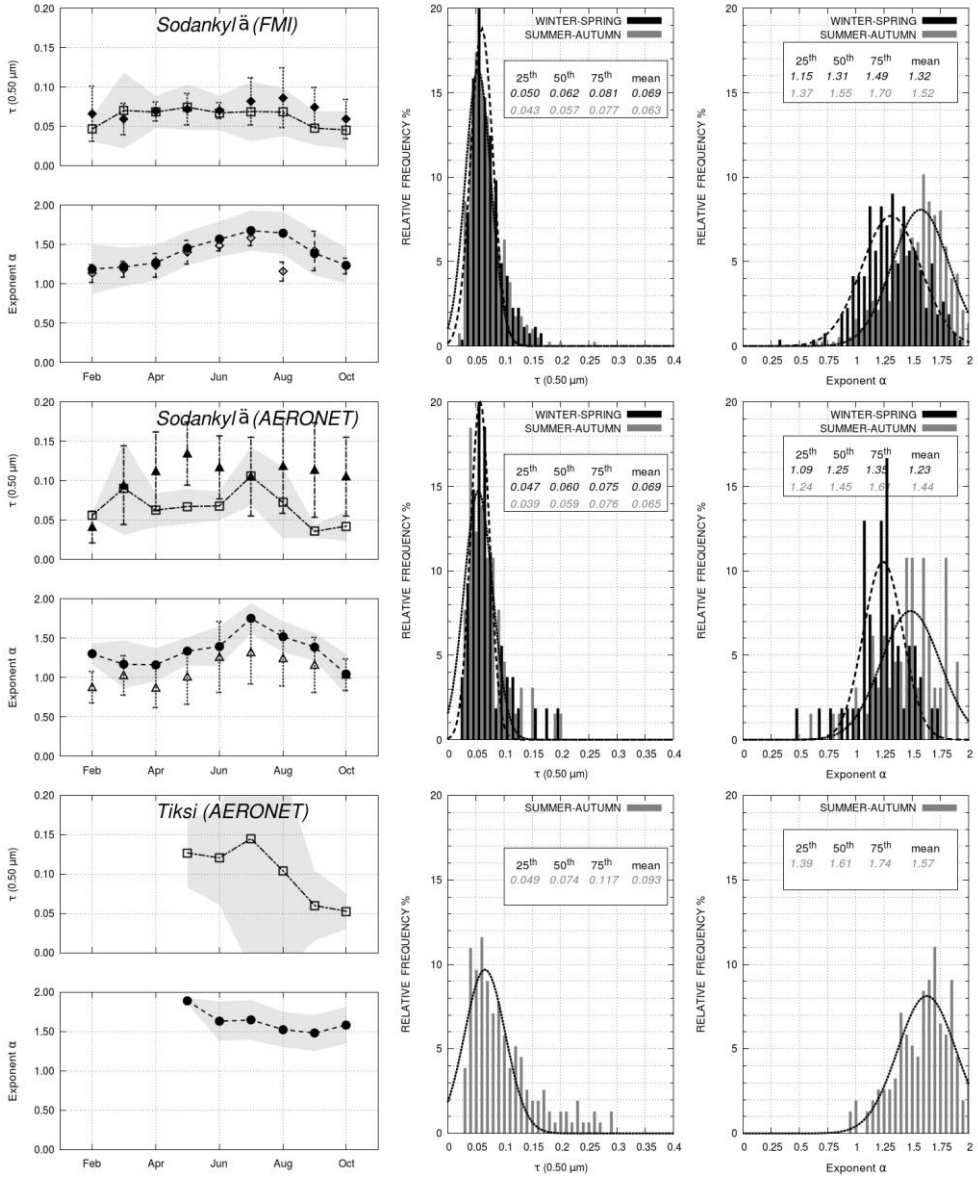

Figure 7.- As in Figure 3, for the sun-photometer measurements of aerosol optical thickness $\tau(0.50\ \mu m)$ and exponent α conducted at: (a) Sodankylä (Northern Finland) by FMI (Helsinki, Finland) in the winter-spring and summer-autumn periods from late May 2004 to March 2013, using a PFR (No. N32) sun-photometer having the characteristics reported in Table 1, (b) Sodankylä by NASA/GSFC (USA) in cooperation with FMI (Helsinki, Finland) from February 2007 to November 2013, using an AERONET Cimel CE-318 sun-photometer having the characteristics reported in Table 1; and (c) Tiksi (North-central Siberia, Russia) by NASA/GSFC (USA) in the summer-autumn months (June-October) of 2010, 2011 and 2012, using an AERONET Cimel CE-318 sun-photometer having the characteristics given in Table 1. In the first graphs, the time-patterns of the monthly mean values of $\tau(0.50\ \mu m)$ and α (solid and open diamonds, respectively) estimated by Toledano et al. (2012) at Kiruna from PFR measurements conducted over the 2007-2010 period are shown with their standard deviations (vertical bars) for comparison with the FMI results found at Sodankylä. The time-patterns of the monthly mean values of $\tau(0.50\ \mu m)$ and α (solid and open triangles, respectively) estimated by Toledano et al. (2012) at Kiruna from the Cimel CE-318 measurements conducted from 2002 to 2007 are shown in the seconda graph for comparison with those derived from the AERONET measurements carried out at Sodankylä.

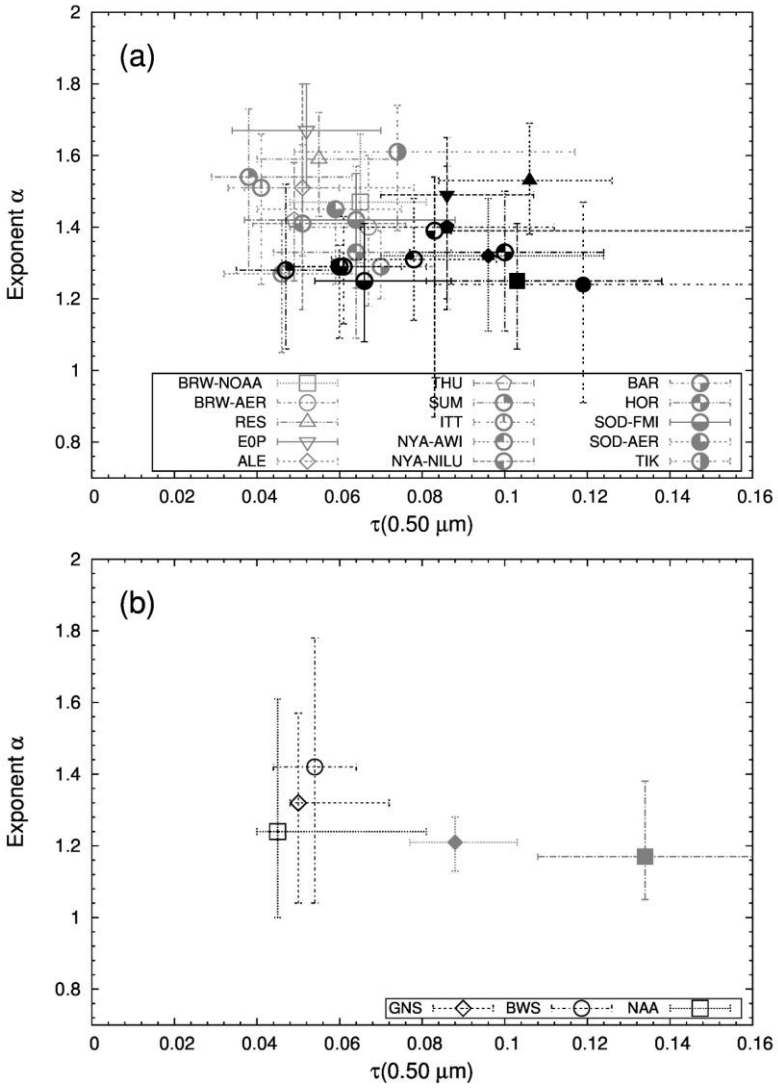

Figure 8.- Upper part (a): Scatter plot of the seasonal median values of the Ångström exponent α versus the corresponding seasonal median values of aerosol optical thickness $\tau(0.50\ \mu m)$ determined from the sun-photometer measurements listed in Table 1. Acronym key: Barrow (BRW-NOAA for the GMD/NOAA measurements, and BRW-AER for the NASA/GSFC AERONET measurements), Resolute Bay (RES), Eureka-0PAL (E0P), Alert (ALE) Thule (THU), Summit (SUM), Ittoqqortoormiit (ITT), Ny-Ålesund (NYA-AWI and NYA-NILU, for the AWI and NILU measurements, respectively), Barentsburg (BAR), Hornsund (HOR), Sodankylä (SOD-PFR and SOD-AER, for the PFR and AERONET measurements, respectively) and Tiksi (TIK). The median values are represented using grey-solid and grey-and-white open symbols to represent the summer-autumn results (as shown in the legend) and solid or black-and-white open symbols to represent the winter-spring results, showing the background aerosol and Arctic haze optical characteristics, respectively. The 25th and 75th percentiles are used to define the limits of the vertical and horizontal dashed bars. Part (b), as in the upper part (a), for the winter-spring (grey symbols) and summer-autumn (open symbols) median values of α plotted versus the corresponding median values of $\tau(0.50\ \mu m)$, as obtained from the seasonal sets of ship-borne sun-photometer measurements collected over the Arctic Ocean sectors: (i) GNS (Greenland Sea and Norwegian Sea) (diamonds), (ii) BWS (Barents Sea and West Siberian Sea) (circles), and (iii) NAA (North-American Arctic ocean, including the East Chukchi Sea, the Bering Strait, the Beaufort Sea and the Amundsen Gulf) (squares).

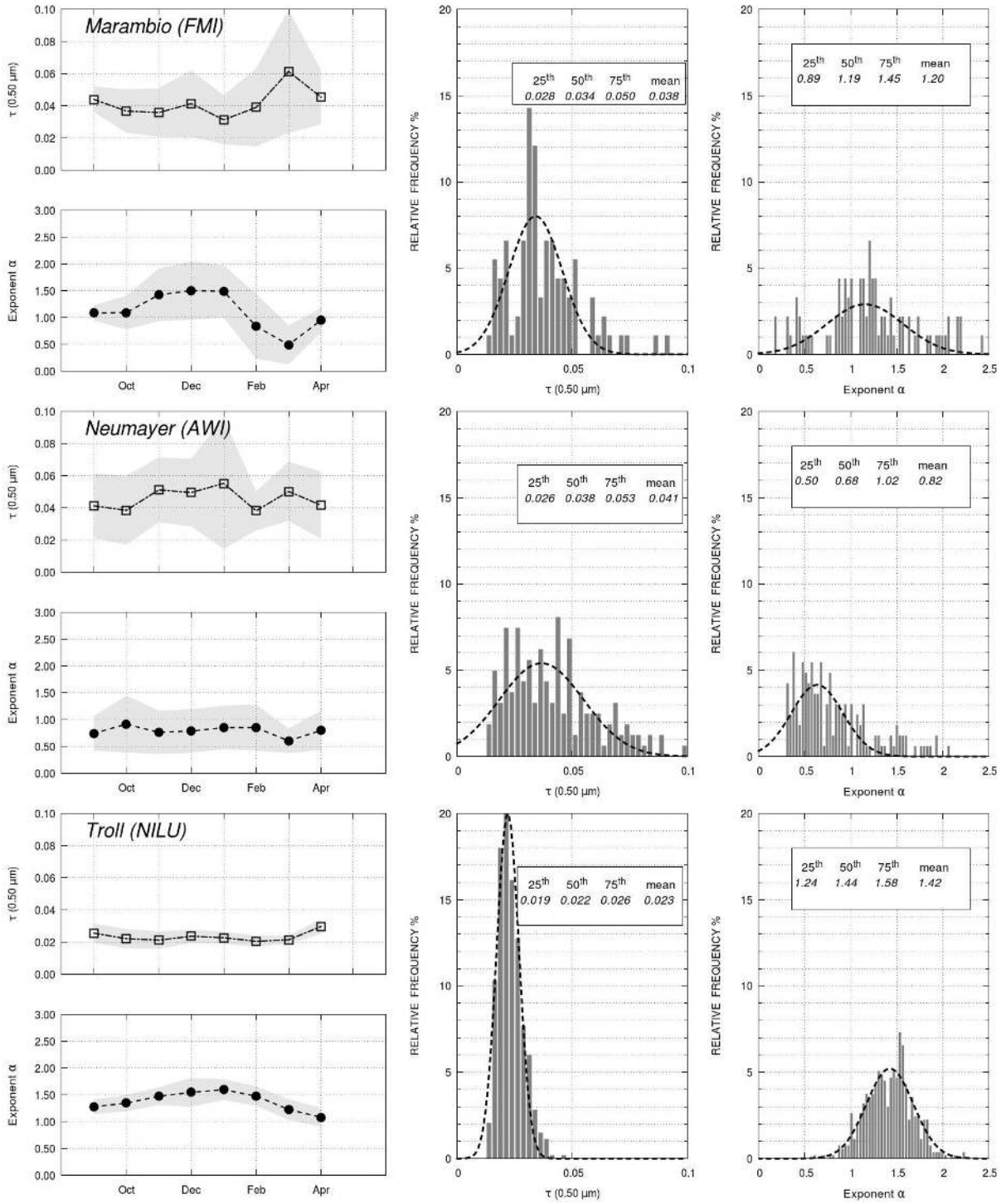

Figure 9.- As in Figure 3, for sun-photometer measurements of aerosol optical thickness $\tau(0.50\ \mu m)$ and exponent α conducted during the September-April period at: (a) Marambio in the Seymour-Marambio Island (Antarctic Peninsula) by FMI (Helsinki, Finland), using a PFR (No. N29) sun-photometer from August 2011 to March 2013; (b) Neumayer on the Akta Bay (Weddel Sea coast) by AWI (Bremerhaven, Germany), using the sun-photometers SP1A and SP2H, and the star-photometer STAR01 listed in Table 2 from September 2000 to April 2007; and (c) Troll located at Jutulsessen (in the Queen Maud Land, 235 km from the coast, at 1309 m a.m.s.l.) by NILU (Kjeller, Norway), alternately using two PFR (Nos. N40 and N42) sun-photometers from January 2007 to April 2013

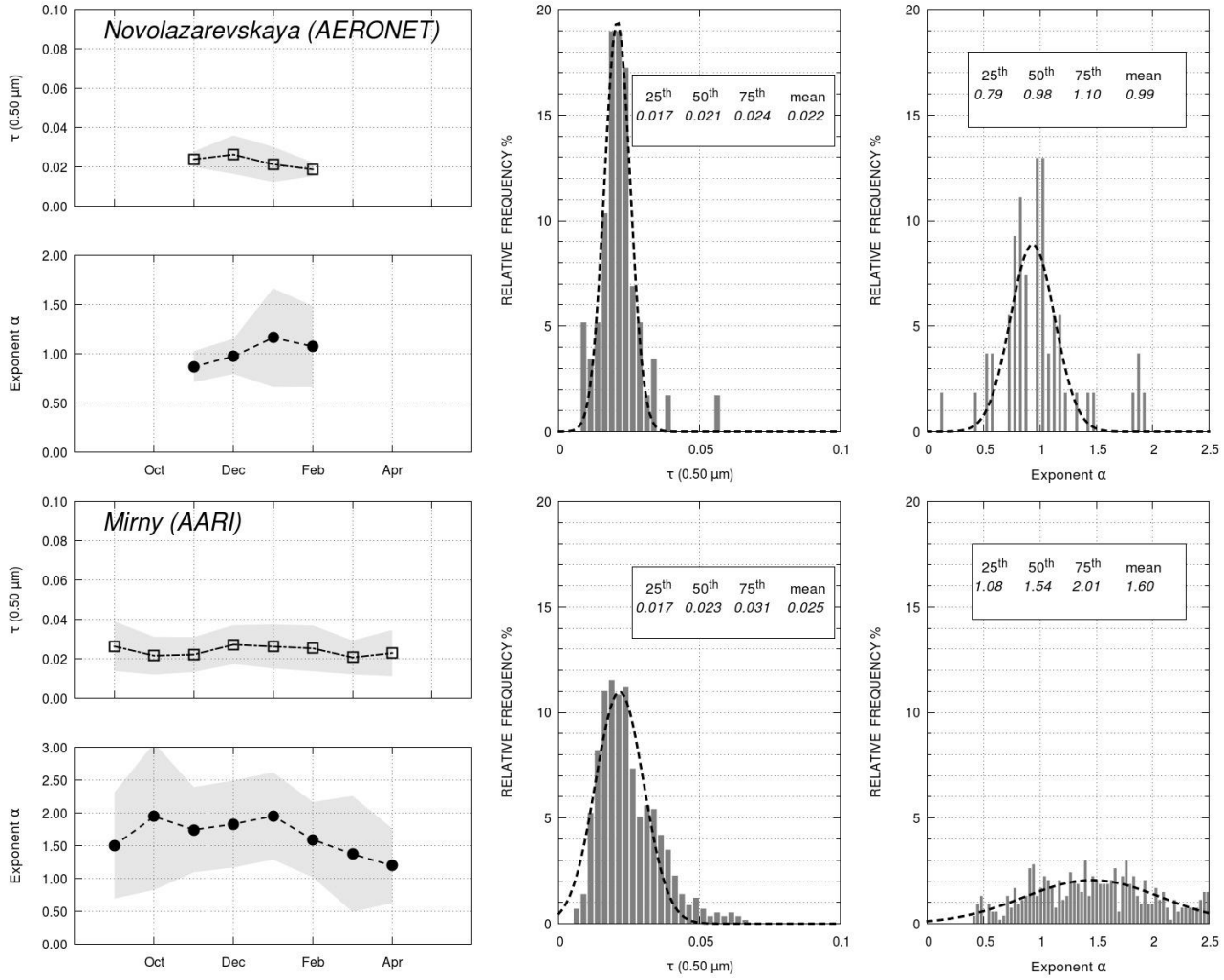

Figure 10.- As in Figure 3, for sun-photometer measurements of aerosol optical thickness $\tau(0.50\ \mu m)$ and exponent α conducted at the Antarctic sites of: (a) Novolazarevskaya in the Schirmaker Oasis (Quenn Maud Land), 75 km from the coast, by AARI (St. Petersburg, Russia), using a hand-held Microtops calibrated at GSFC (USA) over the periods from December 2008 to February 2009 and from November 2009 to February 2010, and obtaining Level 1.5 cloud-screened data; and (b) Mirny on the Davis Sea coast by AARI (St. Petersburg, Russia), using the AARI, SPM and Microtops sun-photometers, having the spectral characteristics given in Table 2, over the period from March 2000 to October 2013.

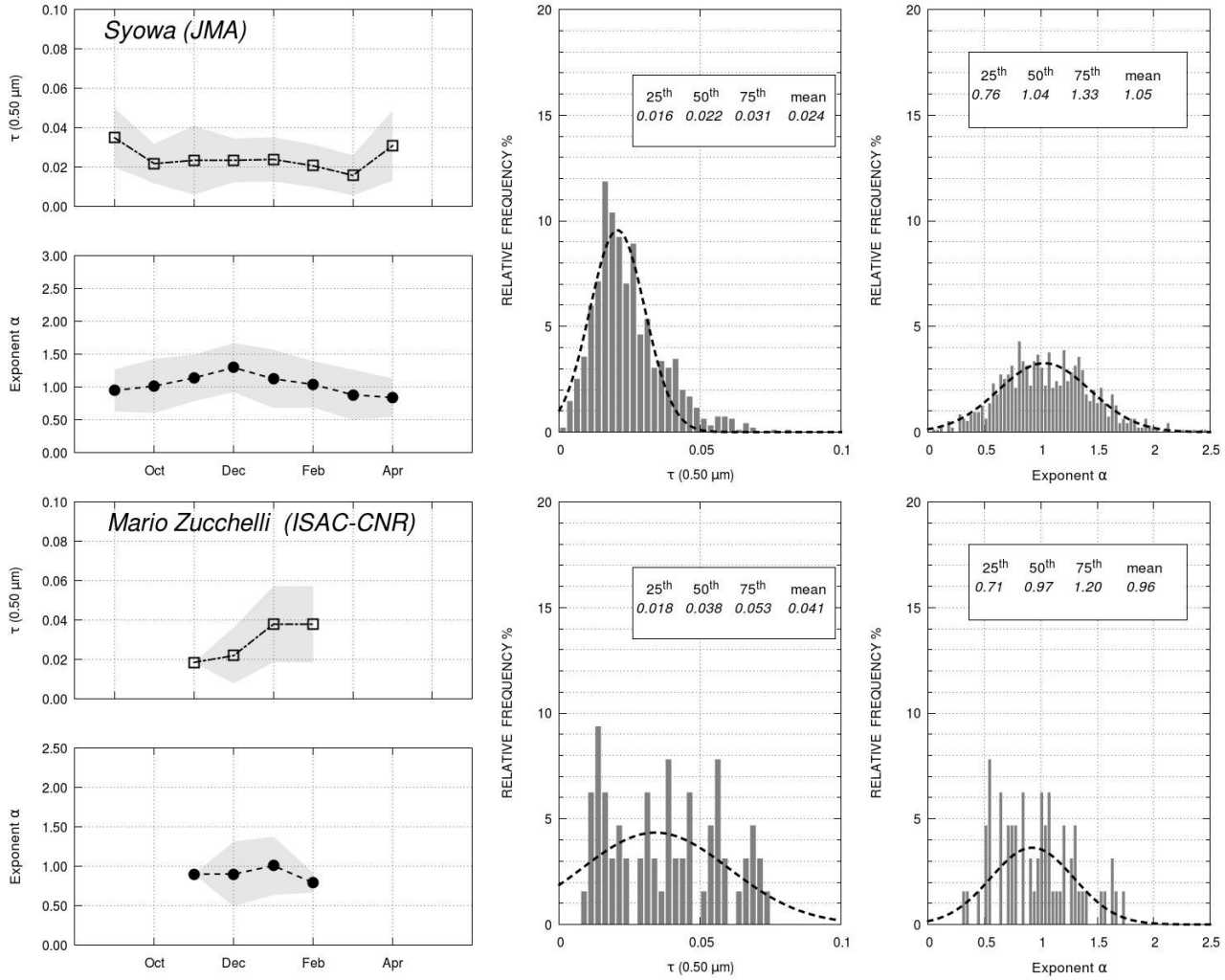

Figure 11. As in Figure 3, for sun-photometer measurements of aerosol optical thickness $\tau(0.50\,\mu m)$ and exponent α conducted at the Antarctic sites of: (a) Syowa (East Ongul Island, Lützow-Holm Bay) over the period from January 2000 to December 2011 by the Office of Antarctic Observation (Japan Meteorological Agency, Tokyo, Japan), using the EKO MS-110 sun-photometer, having the spectral characteristics given in Table 2; and (b) Mario Zucchelli on the Terra Nova Bay (Ross Sea, Victoria Land) during the austral summer periods of 2001/2002 and 2005/2006 by ISAC-CNR (Bologna, Italy), using the PREDE POM-01L and the ASP-15WL sun-photometers, having the spectral characteristics given in Table 2.

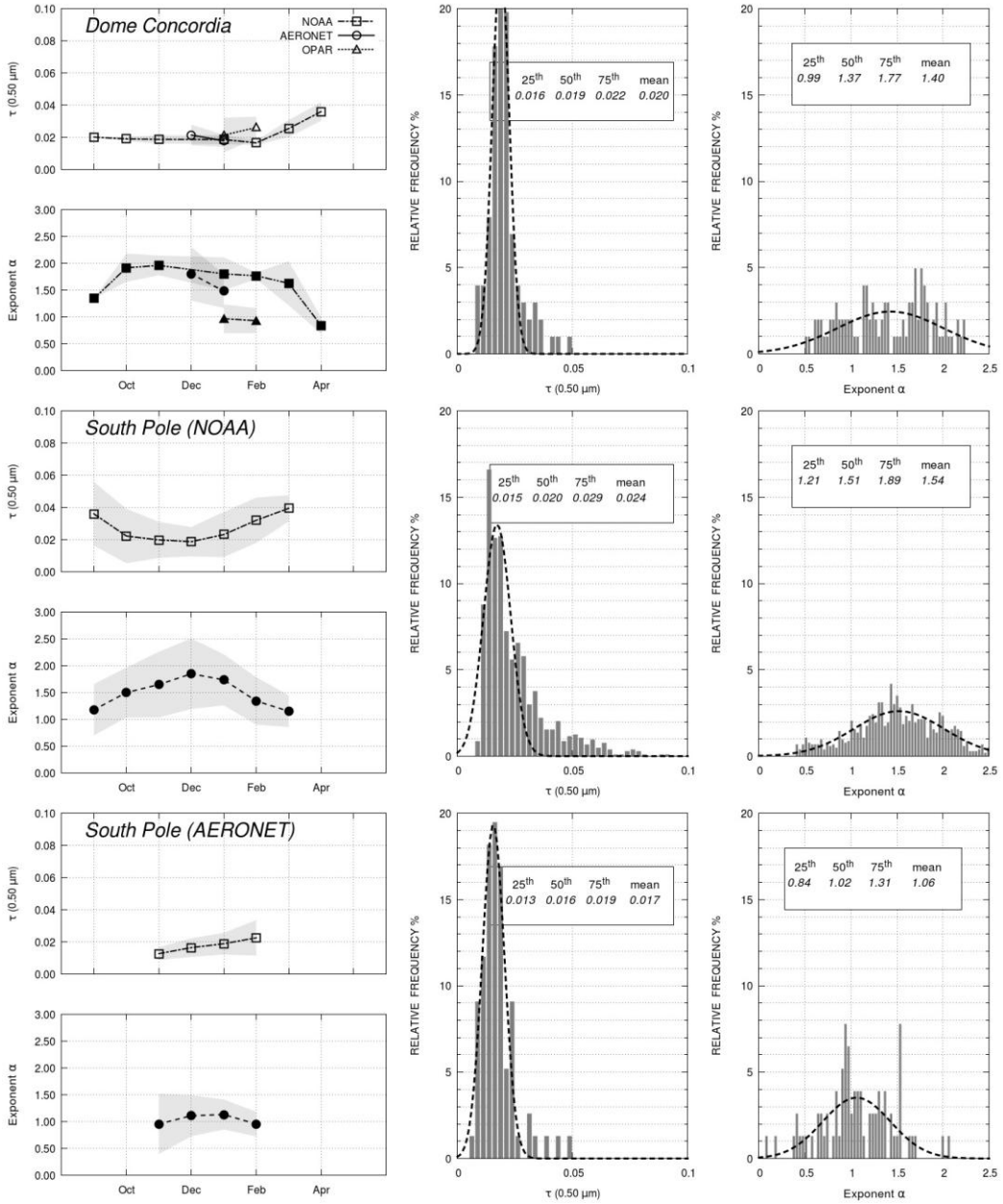

Figure 12. Upper part: as in Figure 3, for sun-photometer measurements of aerosol optical thickness $\tau(0.50\,\mu m)$ and exponent α conducted at: (a) the high-altitude site of Dome Concordia (DomeC), on the Eastern Antarctic Plateau, over the period from September to April, by (i) GMD/NOAA (Boulder, Colorado, USA) from January to November 2010, using a Carter Scott SP02 sun-photometer (squares); (ii) NASA/GSFC (USA) in cooperation with LGGE/CNRS (Grenoble, France) in January and December of 2003, and in January 2004, using an AERONET Cimel CE-318 sun-photometer having the spectral characteristics reported in Table 2 (circles); and (iii) OPAR Institute (University of Réunion, St. Denis, France) in January of 2010, 2011 and 2012, using an hand-held Microtops II sun-photometer calibrated at GSFC (USA), obtaining Level 1.5 cloud-screened data (triangles). Lower part: as in Figure 3, for sun-photometer measurements of aerosol optical thickness $\tau(0.50\,\mu m)$ and exponent α conducted at the high-altitude site of South Pole (SPO) by (i) GMD/NOAA (Boulder, Colorado, USA), using a Carter Scott SP02 sun-photometer in the September-March period from November 2001 to March 2012; and (ii) NASA/GSFC (USA) in cooperation with GMD/NOAA (Boulder, Colorado, USA) using an AERONET Cimel CE-318 sun-photometer having the spectral characteristics reported in Table 2 in the November-February period from November 2007 to December 2012.

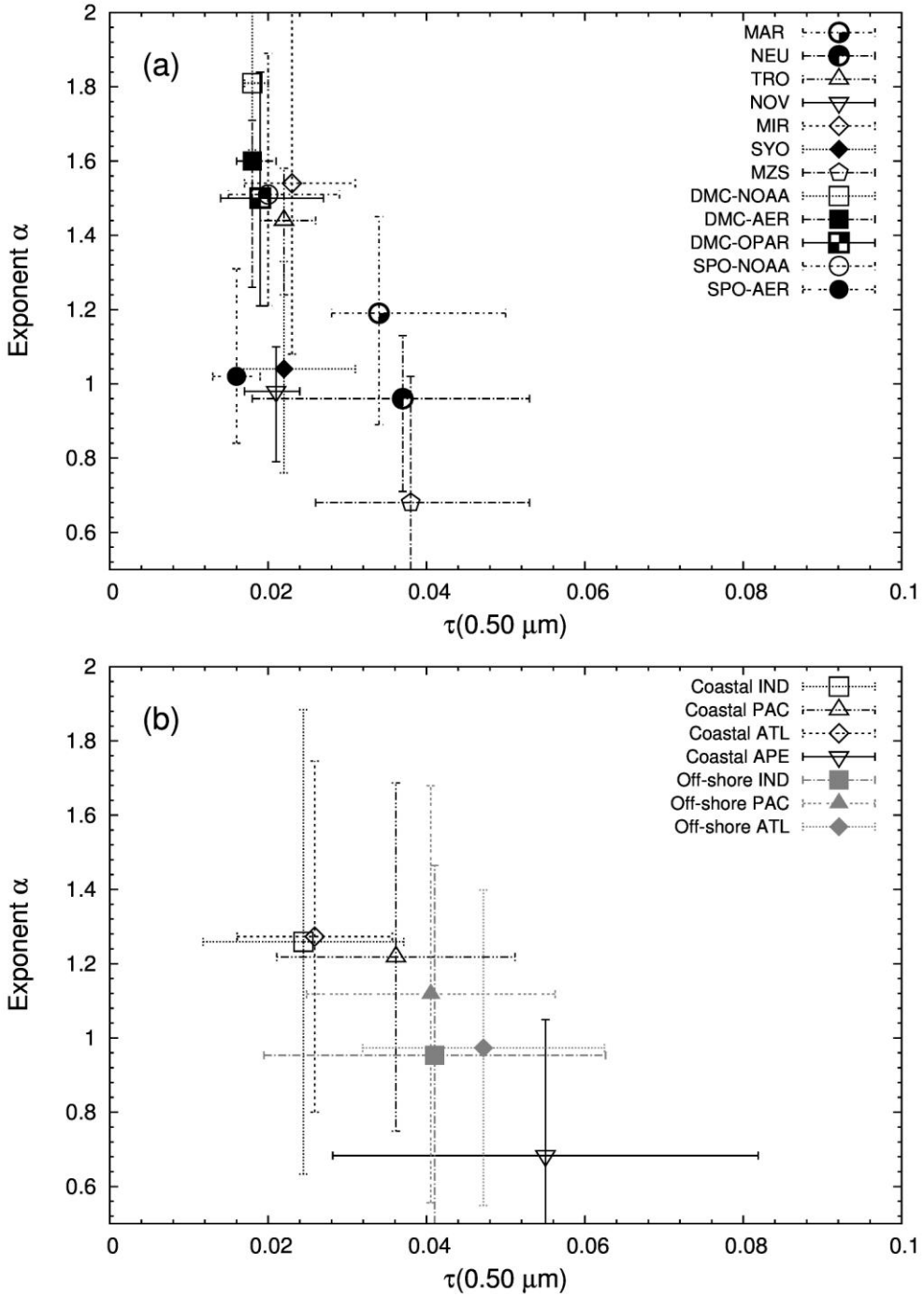

Figure 13.- Part (a): as in Figure 8, but for the sun-photometer measurements listed in Table 2. Acronym key: Marambio (MAR), Neumayer (NEU), Troll (TRO), Novolazarevskaya (NOV), Mirny (MIR), Syowa (SYO), Mario Zucchelli (MZS), Dome Concordia (DMC-NOAA, DMC-AER, and DMC-OPAR, for the measurement sets collected by GMD/NOAA, AERONET and OPAR groups, respectively (see Table 4)) and South Pole (SPO-NOAA and SPO-AER, for the measurement sets collected by GMD/NOAA and AERONET groups, respectively). Part (b): as in part (a), for the Microtops sun-photometer measurements performed in Antarctic coastal (open symbols) and off-shore areas (solid symbols) during the cruises conducted in the four following oceanic sectors: (i) IND (Southern Indian Ocean, squares), (ii) PAC (Southern Pacific Ocean, upward triangles), (iii) ATL (Southern Atlantic Ocean, diamonds), and (iv) APE (Antarctic Peninsula, downward triangles).

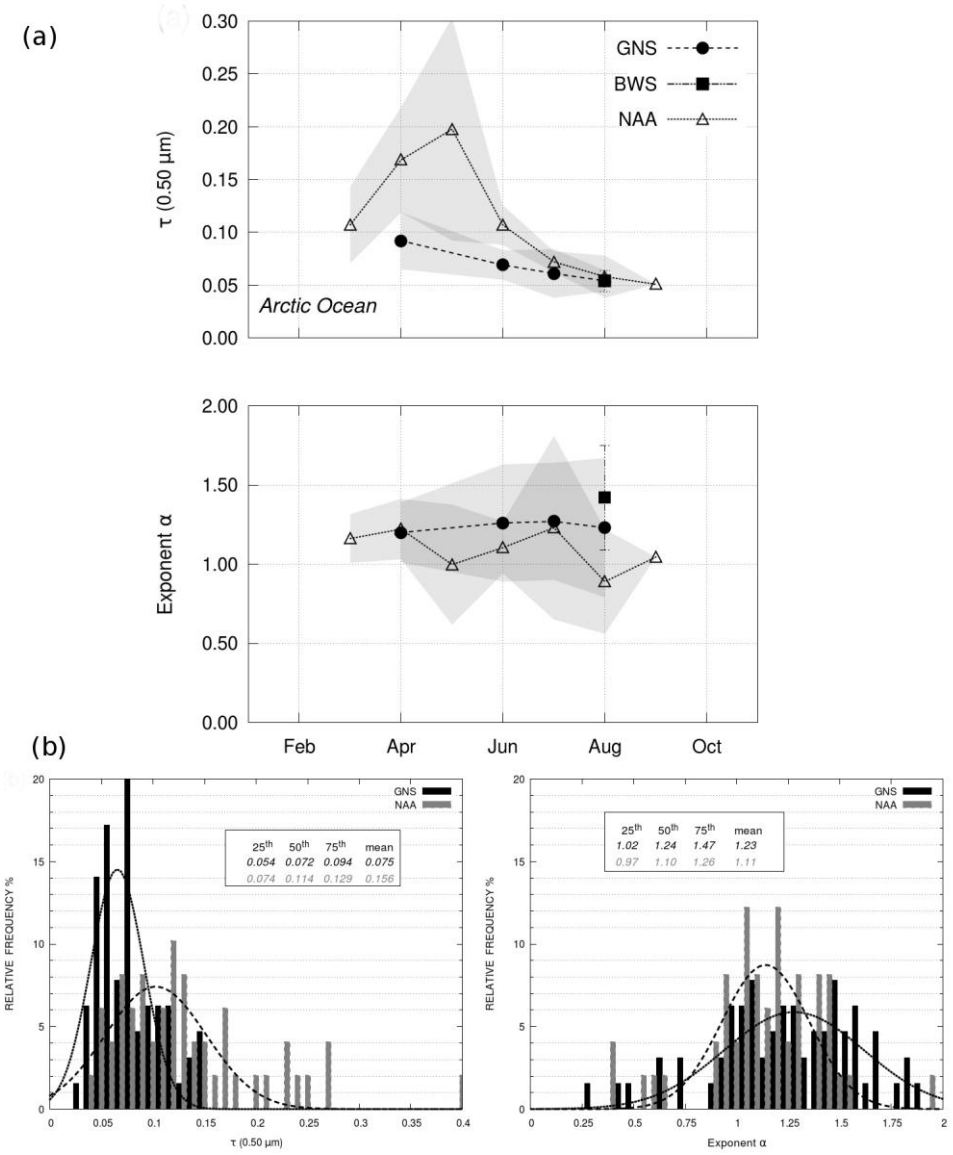

Figure 14. Part (a): as in Figure 3, for Microtops sun-photometer measurements of aerosol optical thickness $\tau(0.50\ \mu m)$ and exponent α performed during the cruises conducted from 2003 to 2012 in the GNS (Greenland Sea and Norwegian Sea) sector (solid circles), from 2006 to 2012 in the BWS (Barents Sea and West Siberian Sea) sector (solid squares), and from 2008 to 2011 in the NAA (Eastern Chuckci Sea, Beaufort Sea and Amundsen Gulf) sector (open triangles) (see also Table 3). Part (b): relative frequency histograms of the daily mean values of aerosol optical thickness $\tau(0.50\ \mu m)$ and exponent α determined from the Microtops measurements conducted from March to September over the GNS (Greenland Sea and Norwegian Sea) sector, and the NAA (North American Arctic Ocean) sector, including the Eastern Chuckci Sea, Beaufort Sea and Amundsen Gulf.

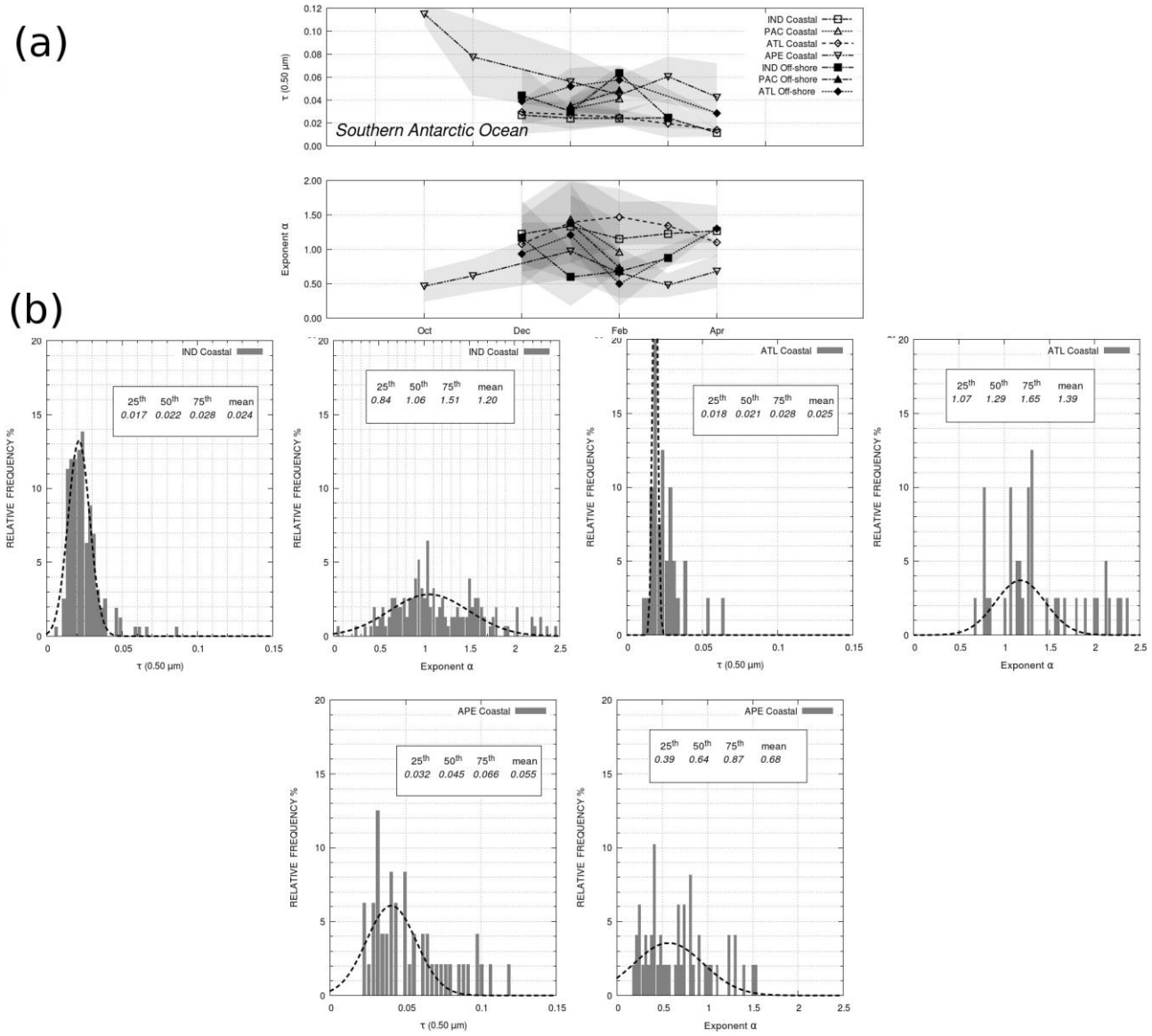

Figure 15. Part (a): as in Figure 3, for Microtops sun-photometer measurements of $\tau(0.50\ \mu m)$ and α performed during the cruises conducted from late 2005 to spring 2013 in the frame of the Maritime Aerosol Network (MAN) activities listed in Table 4. The data refer to coastal (open symbols) and off-shore (solid symbols) measurements, carried out in the IND sector (Southern Indian Ocean, circles), PAC sector (Southern Pacific Ocean, upward triangles), ATL sector (Southern Atlantic Ocean, squares), and APE sector (Antarctic Peninsula, downward triangles). Part (b): Relative frequency histograms of $\tau(0.50\ \mu m)$ and α obtained for the coastal data-sets collected (i) on 226 measurement days from November to February over the Southern Indian Ocean (IND) sector; (ii) 63 measurement days from December to April over the Southern Atlantic Ocean (ATL) sector; and (iii) on 49 measurement days from October to April over the coastal area surrounding the Antarctic Peninsula (APE sector).

3444

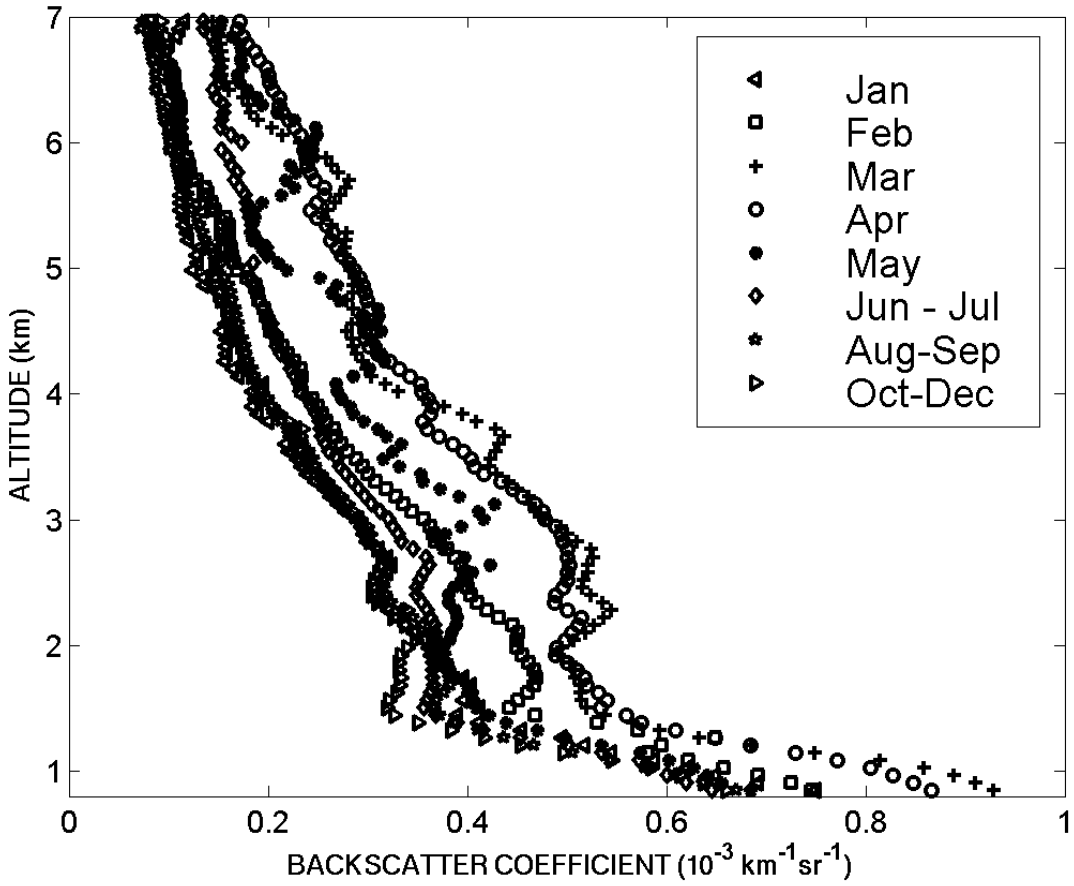

3445

3446 Figure 16. Monthly and bi-monthly averaged vertical profiles of aerosol volume backscatter
3447 coefficient $\beta_{bs}(0.532\ \mu m)$ obtained from the KARL lidar measurements conducted at Ny-Ålesund
3448 (AWIPEV station) from 1 November, 2012, to 31 October, 2013.
3449

3450

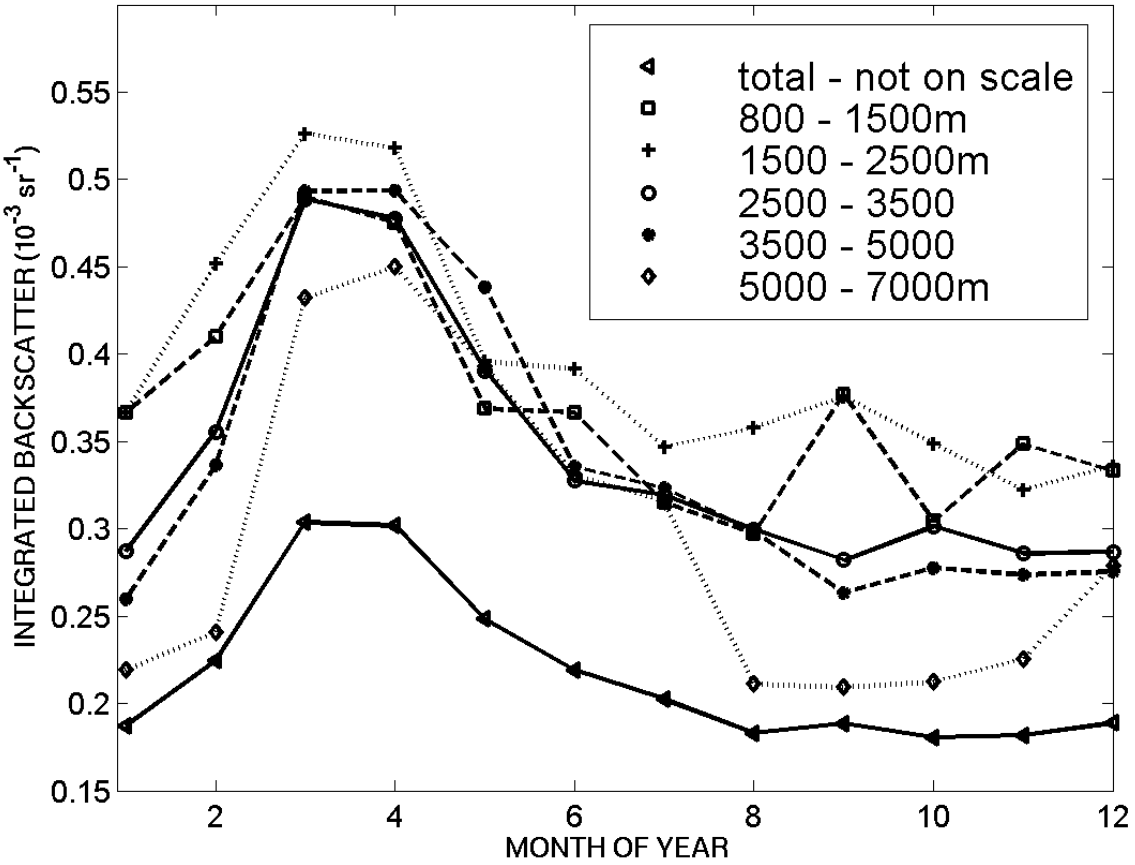

3451

3452 Figure 17. Time-patterns of the monthly average values of the aerosol volume backscatter
3453 coefficient $\beta_{bs}(0.532\ \mu m)$ integrated over the different altitude ranges reported in the legend, as
3454 obtained from the KARL lidar measurements performed at Ny-Ålesund (AWIPEV station) from 1
3455 November, 2012, to 31 October, 2013.
3456

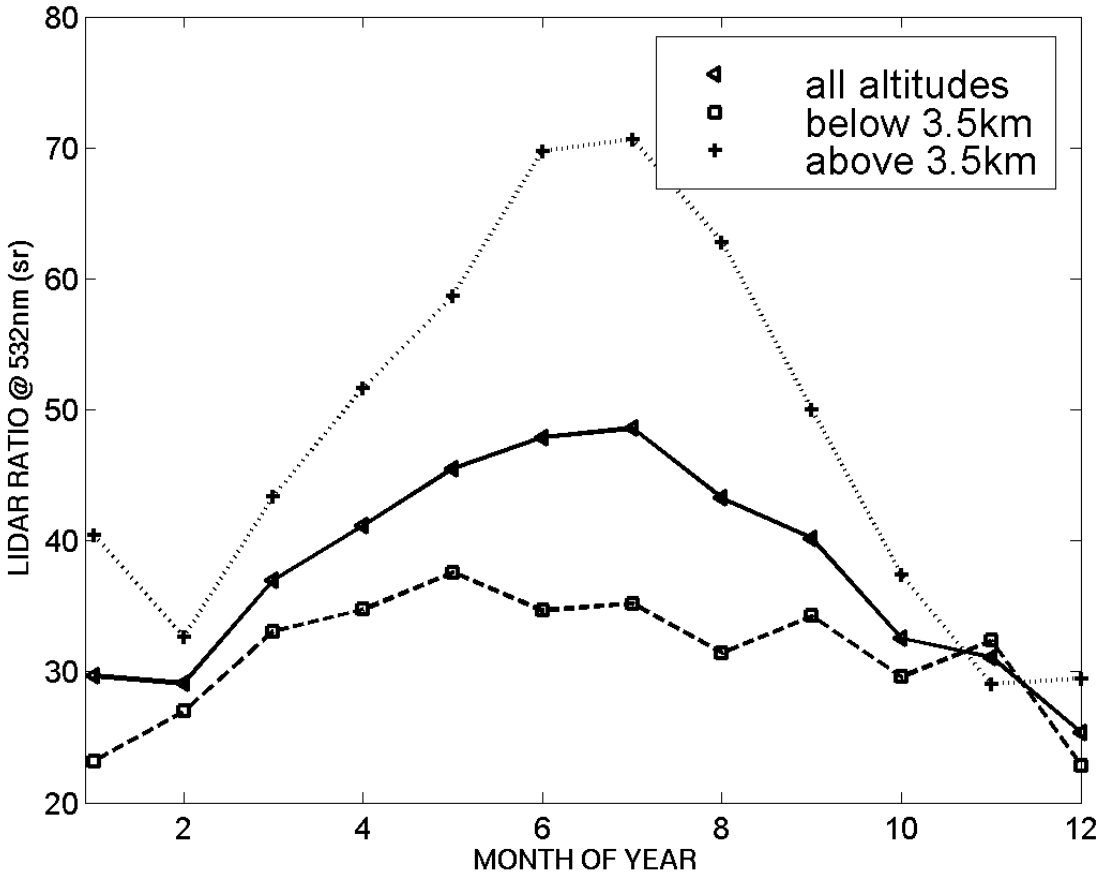

Figure 18. Time-patterns of the monthly average values of the lidar ratio $S_a(0{,}532\ \mu m) = \beta_{ext}(0.532\ \mu m)/\beta_{bs}(0.532\ \mu m)$ calculated over the whole altitude range (triangles) and the altitude sub-ranges $z < 3.5$ km (squares) and $z > 3.5$ km (+), as obtained from the KARL lidar measurements conducted at Ny-Ålesund (AWIPEV station) from 1 November, 2012, to 31 October, 2013.

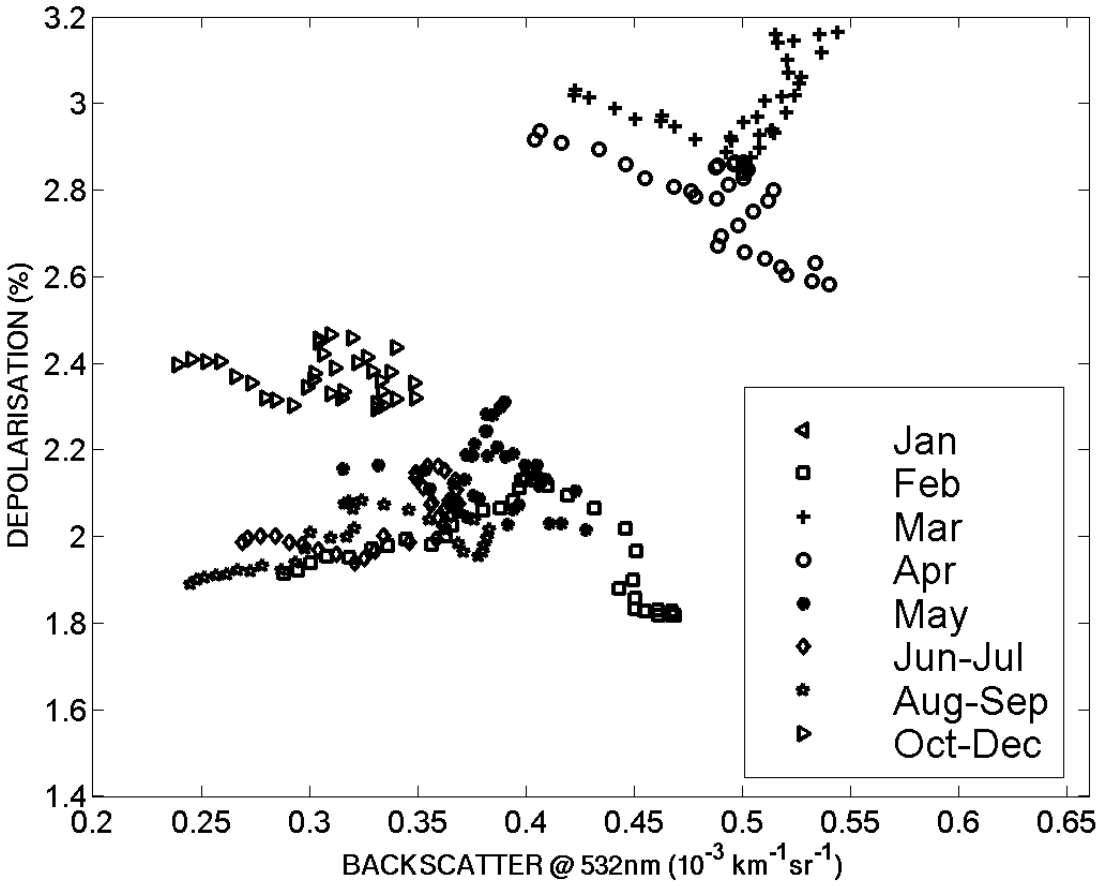

Figure 19. Scatter plots of the monthly and bi-monthly averaged values of the depolarisation ratio (%) versus the aerosol backscatter coefficient $\beta_{bs}(0.532\ \mu m)$, as obtained from the KARL lidar measurements conducted at Ny-Ålesund (AWIPEV station) from 1 November, 2012, to 31 October, 2013.

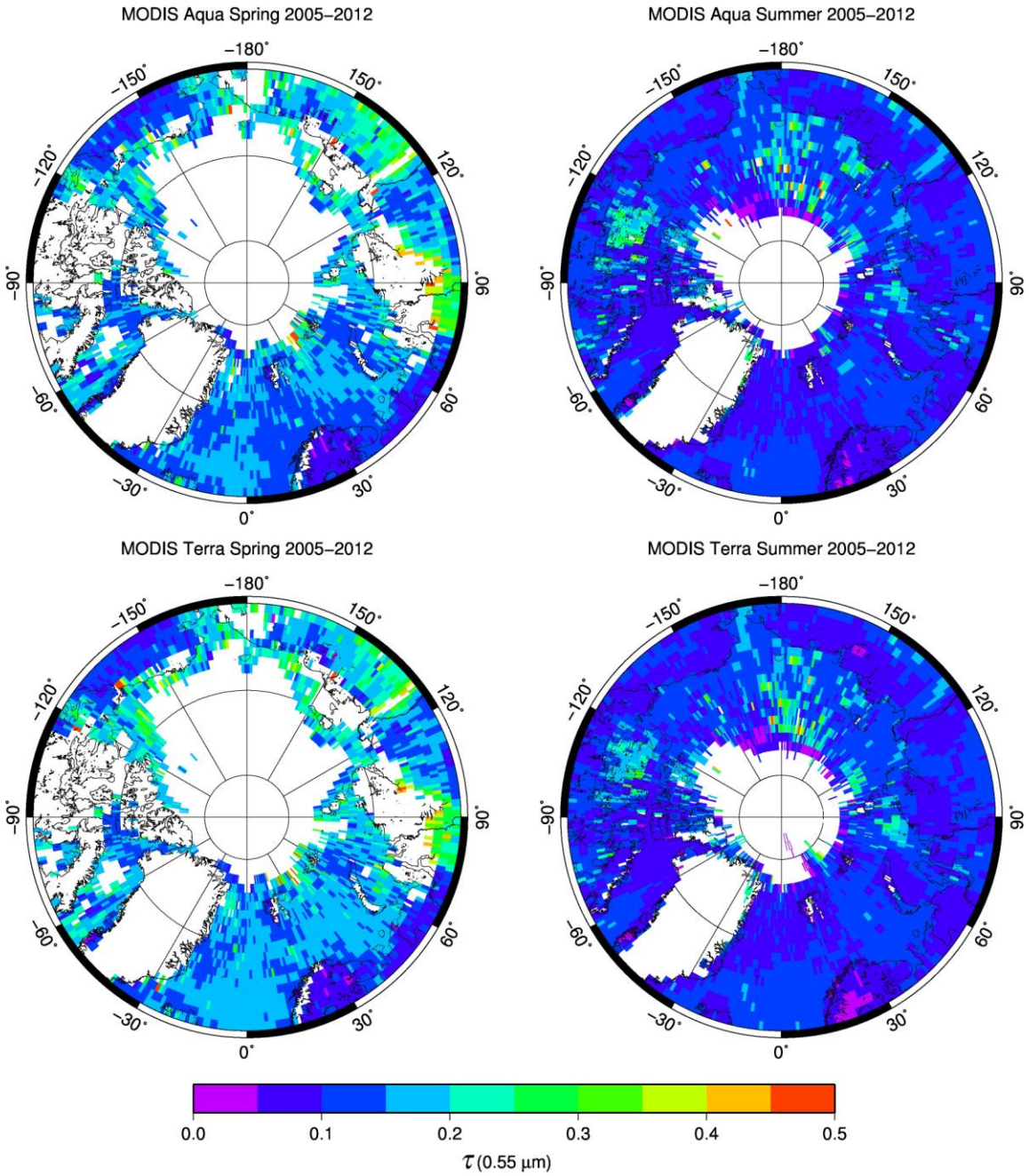

Figure 20. Arctic maps of the seasonal average Level-3 aerosol optical thickness $\tau(0.55\,\mu m)$ derived from MODIS/Aqua (upper part) and MODIS/Terra (lower part) satellite data recorded from 2005 to 2012 during the spring (left-hand side) and summer (right-hand side) 3-month periods.

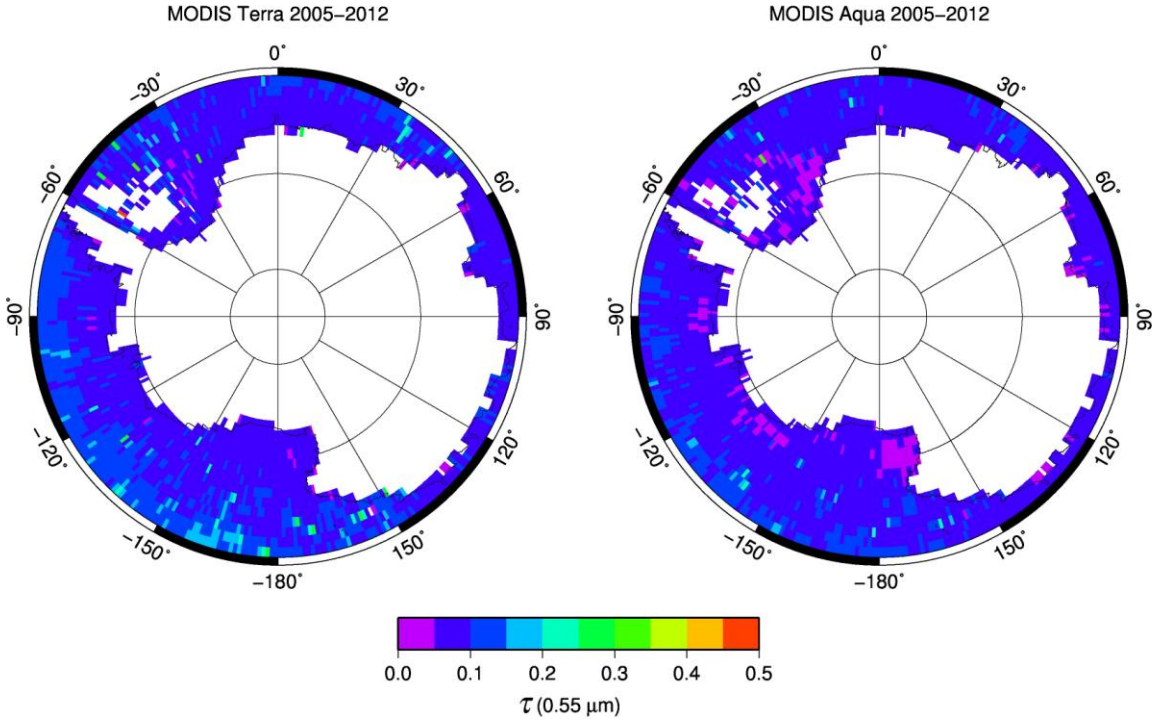

Figure 21. Antarctic maps of the austral summer Level-3 aerosol optical thickness *τ(0.55 µm)* derived from the MODIS/Terra (left-hand side) and MODIS/Aqua (right-hand side) satellite data recorded over the 2005-2012 period.

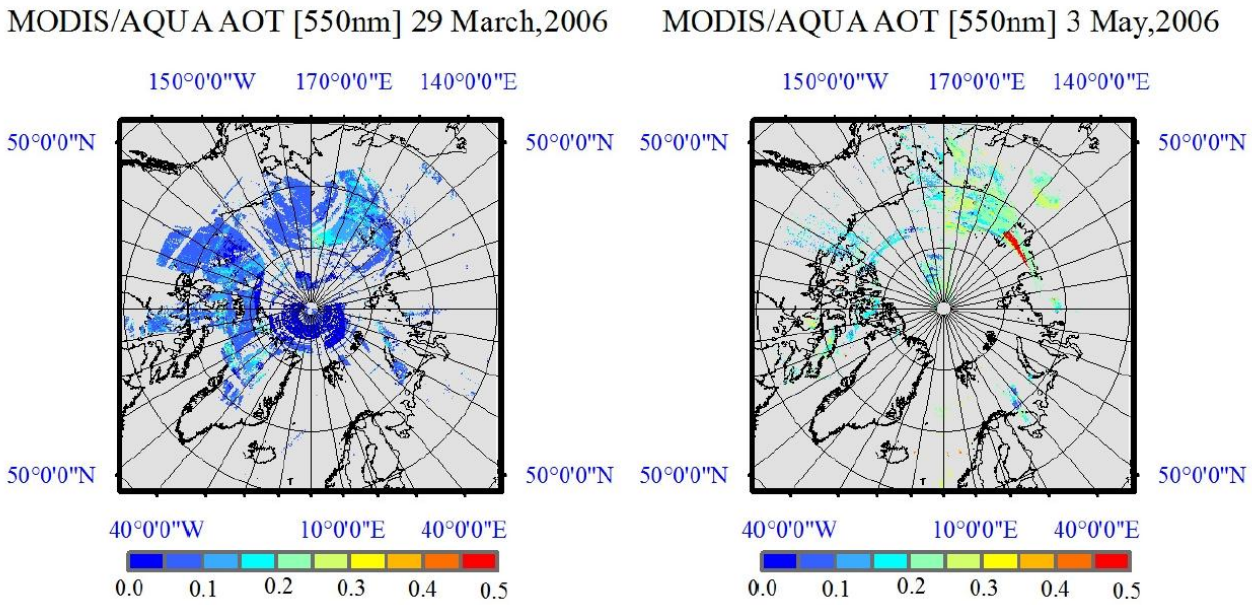

Figure 22. Maps of aerosol optical thickness $\tau(0.55\ \mu m)$ derived over the Arctic region from the MODIS/Aqua observations made on 29 March, 2006 (left-hand side) and 3 May, 2006 (right-hand side) using the method of Mei et al. (2013a).

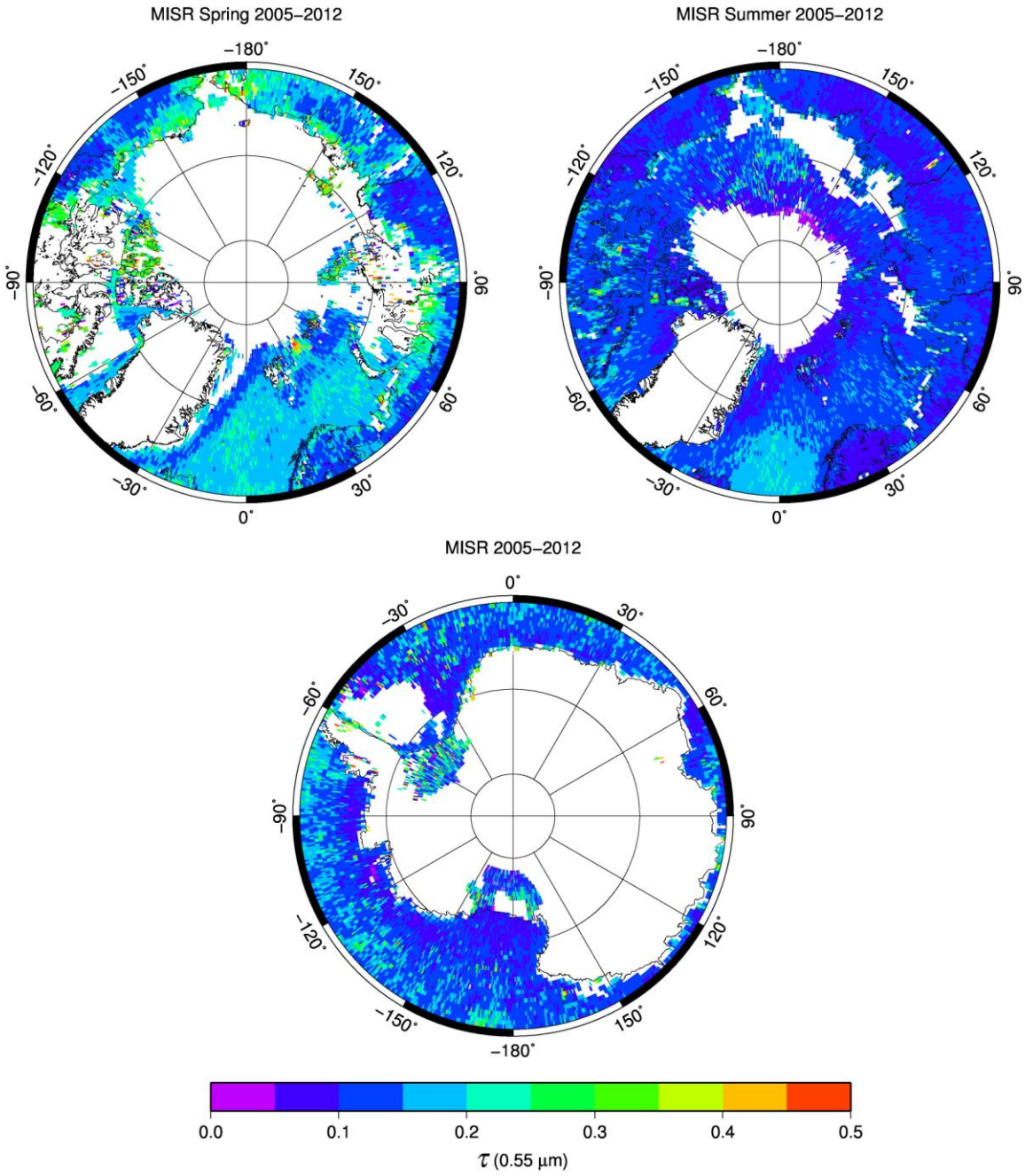

Figure 23. Upper part: Arctic maps of the seasonal average Level-3 aerosol optical thickness *τ(0.55 µm)* derived from the MISR satellite data recorded from 2005 to 2012 during the spring (left-hand side) and summer (right-hand side) 3-month periods. Lower part: As in the upper part, for the austral summer average Level-3 aerosol optical thickness *τ(0.55 µm)* derived from MISR satellite data recorded from 2005 to 2012 over oceans and land areas not covered by snow and ice.

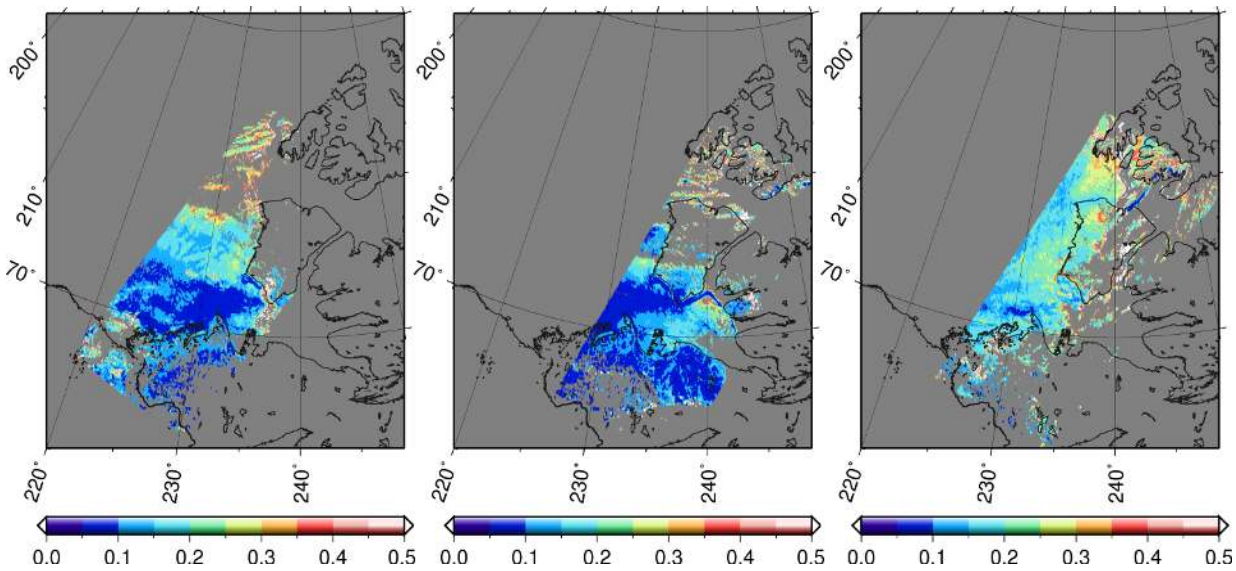

Figure 24. Time sequence of aerosol optical thickness $\tau(0.55\ \mu m)$ retrieved using AATSR data over sea-ice and snow-covered land surfaces with the algorithm described by Istomina et al. (2011). Left panel refers to orbit No. 31673 on 21 March, 2008; middle panel to orbit No. 31687 on 22 March, 2008; and right panel to orbit No. 31773 on 28 March, 2008. The increase in $\tau(0.55\ \mu m)$ might be connected to ozone depletion/bromine explosions observed during March 2008 in the region (Nghiem et al., 2012; Moore et al., 2014).

3507

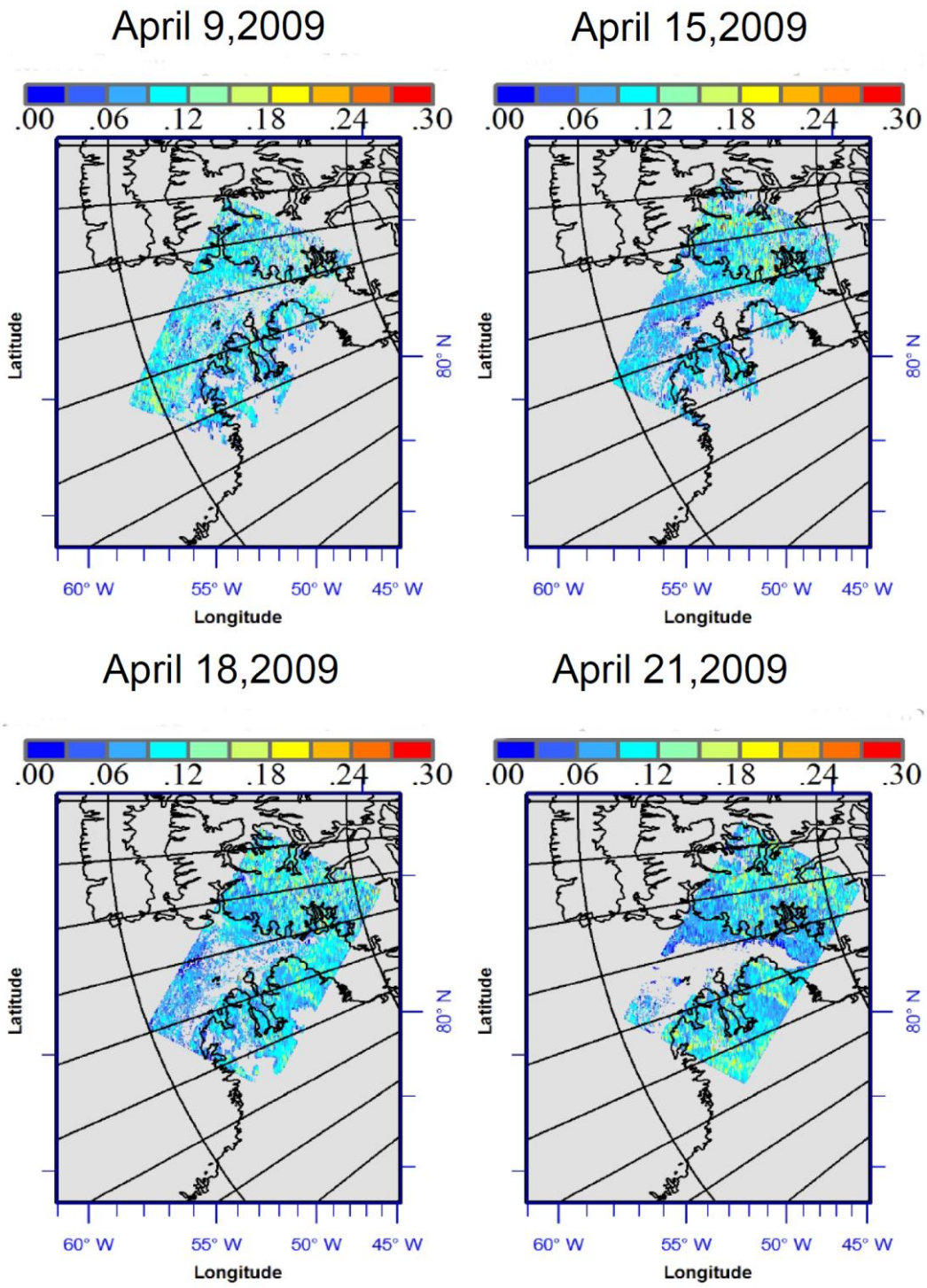

3508

3509 Figure 25. Maps of aerosol optical thickness $\tau(0.55\ \mu m)$ retrieved from AATSR data taken with 1
3510 km × 1 km resolution on 9, 15, 18, and 21 April, 2009, over snow-covered surfaces in west
3511 Greenland using the method of Mei et al. (2013b).
3512

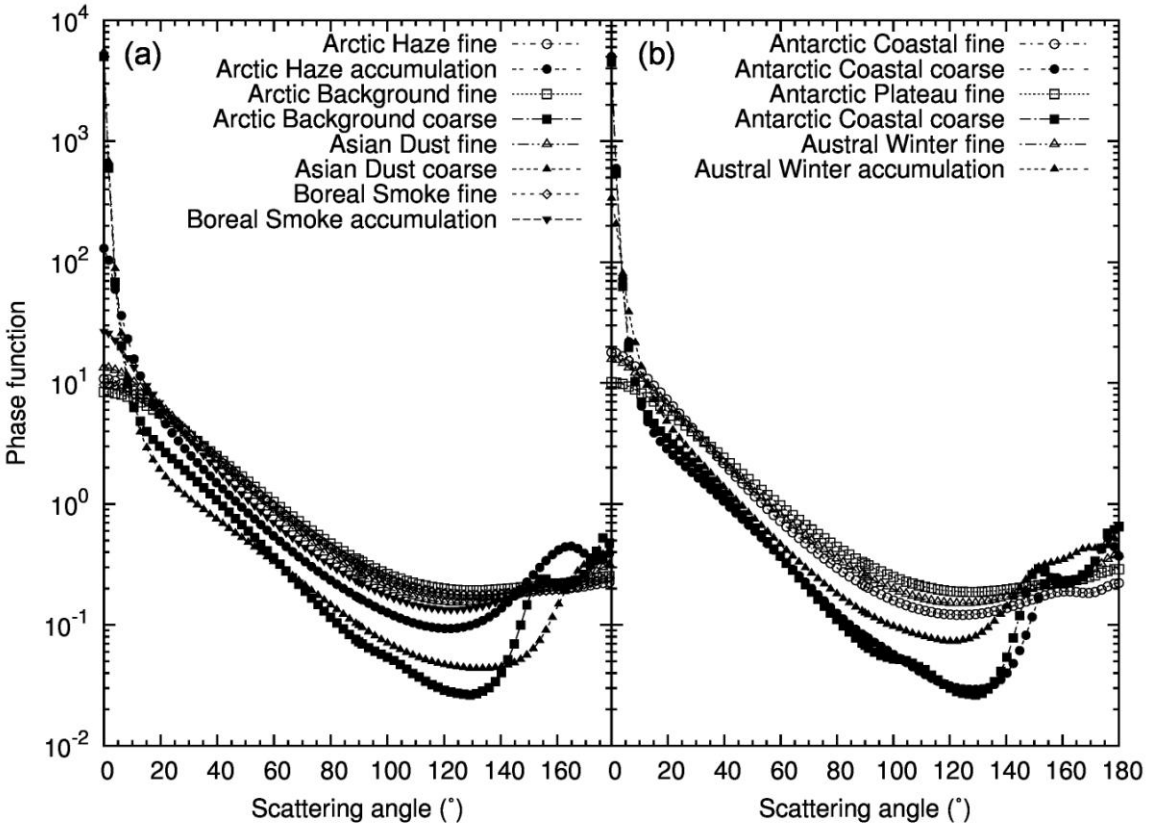

Figure 26. Angular distribution curves of phase function $P(\Theta)$ as a function of the scattering angle Θ for the 8 unimodal Arctic aerosol extinction models (left) and the 6 unimodal Antarctic aerosol extinction models defined in Table 5.

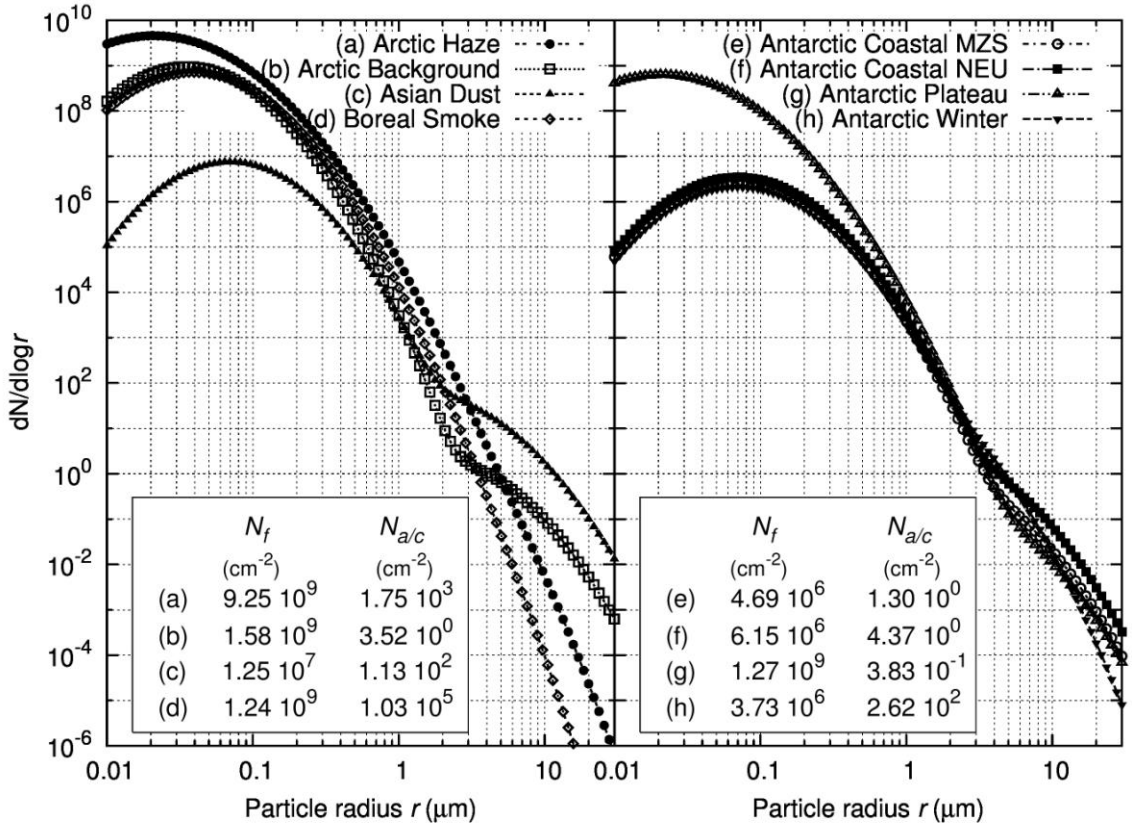

Figure 27. Left-hand side: examples of bimodal particle size-distribution curves obtained as best-fit linear combinations of aerosol unimodal models for fine and accumulation/coarse particles defined in Table 3 in the following four case studies: (a) the average winter-spring aerosol case determined at Eureka (Nunavut, Northern Canada) for the mean values $\tau(0.50\ \mu m) = 0.12$ and $\alpha = 1.48$; (b) the summer background aerosol case determined at Tiksi (Russia) in North-central Siberia for the mean values $\tau(0.50\ \mu m) = 0.08$ and $\alpha = 1.60$; (c) the Asian dust episode observed at Barrow on 16 April, 2002, giving the daily mean values $\tau(0.50\ \mu m) = 0.22$ and $\alpha = 0.26$; and (d) the BFF smoke episode observed by Stock et al. (2012) at Ny-Ålesund on 23 March, 2008, for the daily mean values $\tau(0.50\ \mu m) = 0.22$ and $\alpha = 1.50$. Right-hand side: as on the left, for the following four case studies: (e) the austral summer coastal aerosol case determined at Mario Zucchelli (MZS) for the mean values $\tau(0.50\ \mu m) = 0.03$ and $\alpha = 0.90$; (f) the austral summer coastal aerosol case determined at Neumayer (NEU) for the mean values of $\tau(0.50\ \mu m) = 0.045$ and $\alpha = 0.78$; (g) the austral summer Antarctic Plateau aerosol case determined at South Pole for the mean values $\tau(0.50\ \mu m) = 0.018$ and $\alpha = 1.49$; and (h) the austral winter aerosol case assumed at Neumayer for the seasonal average values $\tau(0.50\ \mu m) = 0.035$ and $\alpha = 0.65$.

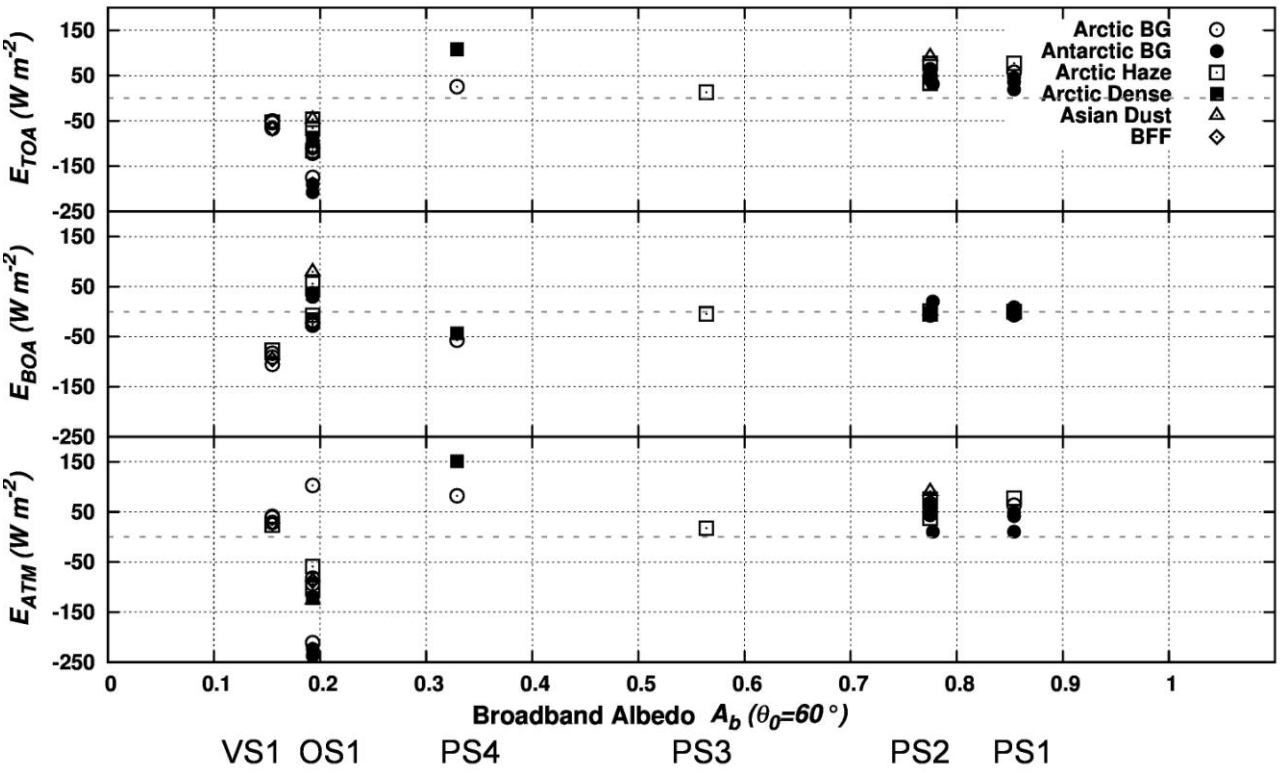

Figure 28. Scatter plots of the daily mean values of DARF efficiencies E_{TOA} at the TOA-level (upper part), E_{BOA} at the BOA-level (middle part), and E_{ATM} in the atmosphere (lower part) shown versus the broadband albedo calculated by Tomasi et al. (2014) at solar zenith angle $\theta_o = 60°$, for the BRDF oceanic surface (OS1), vegetation-covered surface (VS1) and snow-covered polar surface (PS1, PS2, PS3 and PS4) models, and for the 15 polar aerosol types defined in Table 6 and represented using different symbols.

TABLES

Table 1. List of the Arctic stations, where regular ground-based sun-photometer measurements have been conducted over the past decades, using different instrument models equipped with a variable number of narrow-band interference filters to determine the spectral values of aerosol optical thickness $\tau(\lambda)$ and Ångström wavelength exponent α in the visible and near-infrared wavelength range.

Sun-photometer stations	Managing institutions	Geographical coordinates and altitude	Overall number of measurement days	Measurement period	Sun-photometer model	Peak wavelengths (nm) of the spectral channels	Spectral interval (nm) of α	References
Barrow, Alaska (USA)	GMD/NOAA, Boulder, Colorado, USA	71° 19' N, 156° 36' W, 8 m a.m.s.l.	832 (cloud-screened by GMD/NOAA)	March 2000-September 2012	Carter Scott SP02	412, 500, 675, 862	412-862	Stone (2002)
					Carter Scott SP01-A	367, 610, 778, 1050	367-778	
					Carter Scott SP022	368, 610, 778, 1050	368-778	
Barrow, Alaska (USA)	AERONET, NASA/GSFC, (Greenbelt, Maryland, USA); U.S. DoE Atmospheric Radiation Measurement Program, USA	71° 19' N, 156° 40' W, 0 m a.m.s.l.	579 (Level 2.0)	March 2002-September 2013	Cimel CE-318	340, 380, 440, 500, 675, 870, 1020, 1640	440-870	Holben et al. (1998)
Resolute Bay, Nunavut (Canada)	AERONET/ AEROCAN, Environment Canada, Downsview, Ontario, Canada	74° 44' N, 94° 54' W, 40 m a.m.s.l.	361 (Level 2.0)	July 2004-October 2012	Cimel CE-318	340, 380, 440, 500, 675, 870, 1020, 1640	440-870	
Eureka-0PAL,	AERONET/	79° 59' N,	360 (Level	April 2007-	Cimel CE-318	340, 380, 440, 500,	440-870	

Nunavut (Canada)	AEROCAN, CARTEL, University of Sherbrooke, Canada	85° 56’ W, 0 m a.m.s.l.	2.0)	September 2011		675, 870, 1020, 1640		
Alert, Ellesmere Island, Nunavut (Canada)	GMD/NOAA, Boulder, Colorado, USA	82° 28' N, 62° 30' W, 210 m a.m.s.l.	810 (cloud-screened by GMD/NOAA)	August 2004-September 2012	Carter Scott SP02	412, 500, 675, 862, or 368, 610, 778, 1050	412-862 or 368-778	Stone (2002)
Thule, NW Greenland	AERONET, NASA/GSFC, Greenbelt, Maryland, USA	76° 31' N, 68° 46' W, 225 m a.m.s.l.	605 (Level 2.0)	March 2007-September 2012	Cimel CE-318	380, 440, 500, 675, 870, 1020	440-870	Holben at al. (1998)
Summit, Central Greenland	PMOD/WRC, Davos, Switzerland	72° 35' N, 38° 28' W, 3250 m a.m.s.l.	391 (cloud-screened by PMOD/WRC)	January 2001-October 2011	PFR#34	368, 412, 500, 862	412-862	Wehrli (2000)
Ittoqqortoormiit, Eastern Greenland	AERONET, NASA/GSFC, Greenbelt, Maryland, USA	70° 29' N, 21° 57' W, 68 m a.m.s.l.	307 (Level 2.0)	May 2010-October 2013	Cimel CE-318	340, 380, 440, 500, 675, 870, 1020	440-870	Holben at al. (1998)
Ny-Ålesund, Spitsbergen (Svalbard, Norway)	AWI, Bremerhaven, Germany	78° 54' N, 11° 53' E, 5 m a.m.s.l.	749 (cloud-screened by AWI)	April 2000-September 2013	SP1A	371, 380, 416, 443, 500, 532, 609, 675, 778, 864, 1025, 1046, 1062	443-864	Herber et al. (2002)
					SP2H	367, 380, 413, 441, 501, 531, 605, 673, 776, 862, 1023, 1045	441-862	
					STAR01	390, 441, 501, 531, 605, 673, 776, 862	441-862	
Ny-Ålesund, Spitsbergen (Svalbard, Norway)	NILU, Kjeller, Norway	78° 54' N, 11° 53' E, 5 m a.m.s.l.	693 (cloud-screened by NILU)	March 2002-September 2004, and March 2006-	PFR#18	367.7, 411.9, 500.6, 862.5	411.9-862.5	Wehrli (2000)

				September 2013				
Barentsburg, Spitsbergen (Svalbard, Norway)	IAO-SB-RAS, Tomsk, Russia	78° 04' N, 14° 13' E, 20 m a.m.s.l.	56 (cloud-screened by IAO)	April-August of 2011 and 2012	New portable SPM	339, 380, 442, 500, 547, 675, 871, 1020, 1240, 1553, 2134	442-871	Sakerin et al. (2009, 2012, 2014)
Hornsund, Spitsbergen (Svalbard, Norway)	AERONET, NASA/GSFC, Greenbelt, Maryland, USA; Warsaw University, PAS, Poland)	77° 00' N, 15° 34' E, 10 m a.m.s.l.	514 (Level 2.0)	April 2005-August 2013	Cimel CE-318	380, 440, 500, 675, 870, 1020	440-870	Holben et al. (1998)
Sodankylä, Northern Finland	FMI, Helsinki, Finland	67° 22' N, 26° 38' E, 184 m a.m.s.l.	312 (cloud-screened by FMI)	May 2004-September 2013	PFR#32	367.6, 411.4, 500.5, 861.6	411.4-861.6	Wehrli (2000)
Sodankylä, Northern Finland	AERONET, NASA/GSFC, Greenbelt, Maryland, USA; FMI, Helsinki, Finland	67° 22' N, 26° 38’ E, 184 m a.m.s.l.	119 (Level 2.0)	February 2007-November 2013	Cimel CE-318	340, 380, 440, 500, 675, 870, 1020, 1640	440-870	Holben et al. (1998)
Tiksi, Northern-Central Siberia (Russia)	AERONET, NASA/GSFC, Greenbelt, Maryland, USA	71° 35' N, 128° 55' E, 0 m a.m.s.l.	162 (Level 2.0)	June - October of 2010, 2011 and 2012	Cimel CE-318	340, 380, 440, 500, 675, 870, 1020	440-870	Holben et al. (1998)

Table 2. List of the coastal and high-altitude Antarctic stations, where regular ground-based sun-photometer measurements have been conducted over the two past decades, using different instrument models equipped with a variable number of narrow-band interference filters to determine the spectral values of background aerosol optical thickness $\tau(\lambda)$ and Ångström wavelength exponent α in the visible and near-infrared wavelength range.

Sun-photometer stations	Managing institutions	Geographical coordinates and altitude	Overall number of measurement days	Measurement period	Sun-photometer model	Peak wavelengths (nm) of the aerosol spectral channels	Spectral interval (nm) of α	References
Marambio, Seymour-Marambio Island	FMI, Heksinki, Finland	64° 14' S, 56° 37' W, 205 m a.m.s.l.	139 (cloud-screened by FMI)	August 2011-March 2013	PFR #29	367.6, 411.4, 500.5, 861.6	367.6-861.6	Wehrli (2000)
Neumayer, Weddell Sea coast	AWI, Bremerhaven, Germany	70° 39' S, 8° 15' W, 40 m a.m.s.l.	234 (cloud-screened by AWI)	September 2000-April 2007	SP1A	371, 380, 416, 443, 500, 532, 609, 675, 778, 864, 1025, 1046, 1062	443-864	Herber et al. (2002)
					SP2H	367, 380, 413, 441, 501, 531, 605, 673, 776, 862, 1023, 1045	441-862	
					STAR01	390, 441, 501, 531, 605, 673, 776, 862	441-862	
Troll, Queen Maud Land	NILU, Kjeller, Norway	72° 01' S, 2° 32' E, 1309 m a.m.s.l.	547 (cloud-screened by NILU)	January 2007-April 2013	PFR#40 PFR#42	368.7, 411.9, 500.6, 862.5 368.9, 412.1, 499.7, 862.2	411.9-862.5 412.1-862.2	Wehrli (2000)
Novolazarevskaya, Queen Maud Land	AARI, San Petersburg, Russia; AERONET, NASA/GSFC, Greenbelt, Maryland,	70° 46' S, 11° 50’ E, 119 m a.m.s.l.	83 (Level 1.5, cloud-screened by NASA/GSFC	December 2008-February 2009; November 2009-February 2010	Hand-held Microtops, calibrated at GSFC	440, 500, 675, 870	440-870	Smirnov et al. (2009)

	USA.							
Mirny, Davis Sea coast	AARI, St. Petersburg, Russia	66° 33' S, 93° 01' E, 40 m a.m.s.l.	725 (ABAS and SPM data cloud-screened by AARI; Microtops data cloud-screened using the Smirnov et al. (2009) procedure)	March 2000-October 2013	ABAS	395, 408, 479, 581, 651, 789, 873, 1041	408-873	Radionov et al. (2002), Radionov (2005)
					SPM	340, 379, 443, 499, 548, 676, 871, 1019, 1244, 1555, 2134	443-871	Sakerin et al. (2009, 2012) Tomasi et al. (2012)
					Microtops	440, 500, 675, 870	440-870	Smirnov et al. (2009)
Syowa, East Ongul Island, Lützow-Holm Bay	Japan Meteorological Agency (JMA), Tokyo, Japan	69° 00' S, 39° 35' E, 21 m a.m.s.l.	987 (cloud-screened by JMA)	January 2000-December 2011	EKO MS-110 model (with 2.5° field-of-view diameter)	368, 500, 675, 778, 862	368-862	Ohno (2005)
Mario Zucchelli, Terra Nova Bay, Ross Sea coast, Victoria Land	ISAC-CNR, Bologna, Italy	74° 42' S, 164° 07' E, 15 m a.m.s.l.	87 (cloud-screened by ISAC-CNR)	November 2001-February 2002	Prede POM-01L	400, 500, 675, 870, 1020	400-870	Di Carmine et al. (2005)
				December 2005-February 2006	ASP-15WL	381, 412, 451, 500, 551, 610, 673, 775, 861, 1026	412-861	Tomasi et al, (2007)
Dome Concordia, East Antarctic Plateau	AERONET , NASA/GSFC, Greenbelt, Maryland, USA	75° 05' S, 123° 18' E, 3260 m a.m.s.l.	44 (Level 1.5 data, cloud-screened by NASA/GSFC)	January and December 2003; January 2004	Cimel CE-318	440, 675, 870, 1020	440-870	Holben et al. (1998), Six et al. (2005)
	GMD/NOAA, Boulder, Colorado, USA	75° 06' S, 123° 21' E, 3233 m a.m.s.l.	65 (cloud-screened by GMD/NOAA)	January 2006-November 2010	Carter Scott SP02	412, 500, 675, 862	412-862	Stone (2002)
	OPAR	75° 05' E,	39 (Level 1.5	January, 2010,	Hand-held	379, 441, 674, 868	441-868	Smirnov et al.

	Institute, (Univ. de la Réunion - CNRS, Saint Denis de la Réunion, France), and NASA/GSFC, (Greenbelt, Maryland, USA)	123° 18' E, 3260 m a.m.s.l.	data, cloud-screened by NASA/GSFC)	2011, and 2012	Microtops calibrated at the NASA/ GSFC Facility			(2011)
South Pole, Antarctic Plateau	GMD/NOAA, Boulder, Colorado, USA	90° 00' S, 00° 00’ E, 2835 m a.m.s.l.	1279 (cloud-screened by GMD/NOAA)	November 2001-March 2012	Carter Scott SP02	412, 500, 675, 862	412-862	Stone (2002)
	AERONET, NASA/GSFC, Greenbelt, Maryland, USA; GMD/NOAA, Boulder, Colorado, USA	89° 59' S, 70° 18’ E, 2850 m a.m.s.l.	147 (Level 2.0 data, cloud-screened by NASA/GSFC)	November 2007-December 2012	Cimel CE-318	340, 380, 440, 500, 675, 870, 1020	440-870	Holben et al. (1998)

Table 3. List of the 14 cruises undertaken in the Arctic oceanic regions by various managing institutions in different geographical areas (at latitudes > 67 °N), where the ship-borne Level 2.0 sun-photometer measurements of the Maritime Aerosol Network (MAN) programme were conducted from 2003 to 2012, using hand-held Microtops sun-photometers calibrated at the NASA/GSFC calibration facility (Smirnov et al., 2009, 2011). The peak-wavelengths of the narrow-band interference filters mounted on the instruments are given, together with the names of the sun-photometer measurement P.I.s.

Cruises and sun-photometer managing institutions	Geographical area	Overall number of measurement days	Measurement period	Peak wavelengths (nm) of the spectral channels used to measure aerosol optical thickness $\tau(\lambda)$	Principal Investigator and references
RV Oceania 2003 (IOPAS, Sopot, Poland)	Norwegian Sea, west Spitsbergen 69°-79° N, 2°-14° E	5	June-July 2003	440, 500, 675, 870	T. Zielinsky (Tomasi et al., 2007)
RV Oceania 2006 (IOPAS, Sopot, Poland)	Greenland Sea and Norwegian Sea, 69°-79° N, 15° W-14° E	6	June-July 2006	440, 500, 675, 870	T. Zielinsky (Tomasi et al., 2007)
RV Oceania 2007 (IOPAS, Sopot, Poland)	Norwegian Sea, 69°-78° N, 1°-16° E	6	July 15-August 11, 2007	440, 500, 675, 870	T. Zielinsky
CCGS Louis St. Laurent 2007 (Wood Hole Oceanographic Institution, Woods Hole, Massachusetts, USA)	Beaufort Sea, 70°-79° N, 125°-150° W	9	July 28-August 25, 2007	440, 500, 675, 870	A. Proshutinsky
RV Knorr 2008 (PMEL, NOAA, Seattle, Washington, USA)	Norwegian Sea, 70°-71° N, 19°-31° E	4	April 6-10, 2008	440, 500, 675, 870	P. K. Quinn
CCGS Amundsen 2008 (Institut Maurice-Lamontagne, Mont-Joli, Quebec, Canada)	Beaufort Sea, 70°-73° N, 121°-131° W	43	March 16-August 2, 2008	440, 500, 675, 870	P. Larouche
RV Jan Mayen 2009 (IMEDEA, Esporles, Mallorca, Spain)	Norwegian Sea, 76°-80° N, 11°-28° E	4	June 18-22, 2009	440, 500, 675, 870	C. Duarte
RV Oceania 2009 (IOPAS, Sopot, Poland)	Norwegian Sea, 73°-79° N, 3°-16° E	11	June 23-July 13, 2009	440, 500, 675, 870	T. Zielinsky

CCGS Amundsen 2009 (Université du Québec, Rimouski, Québec, Canada)	Beaufort Sea, 70°-72° N, 127°-135° W	9	July 31-August 25, 2009	440, 500, 675, 870	S. Bélanger
RV Oceania 2010 (IOPAS, Sopot, Poland)	Norwegian Sea, 68°-80° N, 0°-13° E	9	July 6-August 17, 2010	380, 440, 500, 675, 870	T. Zielinsky
RV Oceania 2011 (IOPAS, Sopot, Poland)	Norwegian Sea, 69°-79° N, 3°-19° E	10	June 17-August 13, 2011	440, 500, 675, 870	T. Zielinsky
USCGC Healy 2011 (Naval Research Laboratory, Monterey, California, USA)	Eastern Chukci Sea, Beufort Sea and Arctic Canadian Ocean, 71°-79° N, 142°-165° W	6	August 18-September 24, 2011	440, 500, 675, 870	E. A. Reid
RV Oceania 2012 (IOPAS, Sopot, Poland)	Norwegian Sea, 73°-78° N, 10°-20° E	7	June 27-July 31, 2012	440, 500, 675, 870	T. Zielinsky
RV Polarstern 2012 (Institute of Environmental Physics, University of Bremen, Bremen, Germany)	Norwegian Sea, Barents Sea and West Siberian Sea, 70°-84° N, 18°-109° E	5	August 2-22, 2012	440, 500, 675, 870	L. Istomina

Table 4. List of the 18 cruises undertaken in the Antarctic oceanic regions by various managing institutions in different geographical areas (at latitudes > 62 °S), where the ship-borne sun-photometer measurements of the Maritime Aerosol Network (MAN) programme were conducted from 2005/2006 to 2012/2013 in the austral summer months, using hand-held Microtops sun-photometers calibrated at the NASA/GSFC calibration facility (Smirnov et al., 2009, 2011). The peak-wavelengths of the narrow-band interference filters mounted on the instruments are given, together with the names of the sun-photometer measurement P.I.s.

Cruises and sun-photometer managing institution	Geographical area	Overall number of measurement days	Measurement period	Peak wavelengths (nm) of the spectral channels used for measuring aerosol optical thickness $\tau(\lambda)$	Principal Investigator
RV Akademik Fedorov 2005/2006 (IAO-SB-RAS, Tomsk, Russia)	Southern Indian Ocean 65°-70° S, 44°-93° E	20	December 20, 2005-January 26, 2006	340, 440, 500, 675, 870	S. M. Sakerin
RV Akademik Fedorov 2006/2007 (IAO-SB-RAS, Tomsk, Russia)	Southern Indian Ocean 65°-69° S, 46°-93° E	40	December 13, 2006-March 4, 2007	340, 440, 500, 675, 870	S. M. Sakerin
MV SA Agulhas 2007/2008 (Climatology Research Group, University of Witwatersrand, Johannesburg, South Africa)	Southern Atlantic Ocean, 68°-70° S, 2° W-4° E	15	December 18, 2007-January 10, 2008	440, 500, 675, 870	S. Piketh (Wilson et al., 2010)
RV Akademik Fedorov 2007/2008 (IAO-SB-RAS, Tomsk, Russia)	Southern Indian Ocean, 66°-69° S, 45° E-95° E	18	December 14, 2007-January 4, 2008	440, 500, 675, 870	S. M. Sakerin
	Southern Pacific Ocean, 68°-72° S, 90°-163° W	14	January 24-February 17, 2008		
	Antarctic Peninsula, 63°-65° S, 60°-45° W	3	February 20-24, 2008		
	Southern Atlantic Ocean, 65°-70° S, 50°W-15° E	13	March 25-April 22, 2008		
RV Akademik Fedorov 2008/2009 (IAO-SB-RAS, Tomsk, Russia)	Southern Indian Ocean, 66°-69° S, 76° - 93° E	11	December 22, 2008-January 6, 2009; January 25-March 23, 2009	440, 500, 675, 870	S. M. Sakerin

	Southern Pacific Ocean, 67° S, 161° E	1	January 17, 2009		
Vessel RV Astrolabe 2009/2010 (OPAR, Univ. de Reunion, Reunion, France)	Southern Indian Ocean 66°-67° S, 140°-141° E	5	January 5-23, 2010	440, 500, 675, 870	Y. Courcoux
RV Akademik Fedorov 2009/2010 (IAO-SB-RAS, Tomsk, Russia)	Southern Indian Ocean, 65°-70° S, 70°-100° E	12	December 15, 2009-January 4, 2010; March 30-April 6, 2010	440, 500, 675, 870	S. M. Sakerin
	Southern Pacific Ocean 65°-75° S, 87°-172° W	7	January 19-28, 2010		
	Antarctic Peninsula, 62° S, 59° W	1	February 6, 2010		
Prince Albert II 2010 (Space Physics Laboratory, University of Kyiv, Kyiv, Ukraine)	Antarctic Peninsula 62°-67° S, 58°-67° W	11	January 9-February 17, 2010	440, 500, 675, 870	G. Milinevsky
NP Almirante Maximiano 2010/2011 (Rio de Janeiro State University, Rio de Janeiro, Brazil)	Antarctic Peninsula 62°-64° S, 56°-61° W	7	January 7-March 21, 2011	440, 500, 675, 870	H. Evangelista
RV Akademik Fedorov 2010/2011 (AARI, St. Petersburg, Russia)	Southern Indian Ocean 65°-69° S, 45°-93° E	18	December 18, 2010-February 2, 2011	440, 500, 675, 870	V. F. Radionov
RV Astrolabe 2011 (OPAR Institute, Univ. de la Réunion, Saint Denis de la Réunion, France)	Southern Indian Ocean 67° S, 140° E	24	January 5-March 1, 2011	340, 440, 500, 675, 870	Y. Courcoux
MV SA Agulhas 2011/2012 (Climatology Research Group, University of Witwatersrand, Johannesburg, South Africa)	Southern Atlantic Ocean 67°-71° S, 0°-9° W	17	December 19, 2011-February 13, 2012	340, 440, 500, 675, 870	S. Broccardo

NP Almirante Maximiano 2011/2012 (Rio de Janeiro State University, Rio de Janeiro, Brazil)	Antarctic Peninsula, 61°-62° S, 55°-59° W	6	October 24, 2011-November 14, 2011	440, 500, 675, 870	H. Evangelista
RV Akademik Fedorov 2011/2012 (AARI, St. Petersburg, Russia)	Southern Indian Ocean 66°-69° S, 37°-93° E	19	December 12, 2011-March 21, 2012	440, 500, 675, 870	V. F. Radionov
	Southern Atlantic Ocean 62°-70° S, 18° W-20° E	8	March 22-April 7, 2012		
	Antarctic Peninsula 62.2° S, 58.9° W	2	April 21 and 22, 2012		
RV Astrolabe 2012 (OPAR Institute, Univ. de la Réunion, Saint Denis de la Réunion, France)	Southern Indian Ocean 66° 40' S, 140° E	14	February 20-March 2, 2012	380, 440, 500, 675, 870	Y. Courcoux
RV SA Agulhas II 2012/2013 (Climatology Research Group, University of Witwatersrand, Johannesburg, South Africa)	Southern Atlantic Ocean 70° - 71° S, 1°-8° W	11	December 19, 2012-February 5, 2013	380, 440, 500, 675, 870	S. Broccardo
RV Akademik Fedorov 2012/2013 (AARI, St. Petersburg, Russia)	Southern Indian Ocean 66°-70° S, 46°-93° E	24	December 13, 2012-March 15, 2013	440, 500, 675, 870	V. F. Radionov
	Southern Atlantic Ocean 67°-70° S, 10°-12° E	3	March 22-24, 2013		
RV Akademik Treshnikov 2012/2013 (AARI, St. Petersburg, Russia)	Antarctic Peninsula, 64°-70° S, 57°-72° W	13	February 11-March 5, 2013	440, 500, 675, 870	V. F. Radionov

Table 5. Values of shape-parameters σ and r_c of the log-normal curves adopted to represent the fine, accumulation and coarse particle modes determined at Arctic and Antarctic sites, all normalized to give the value of overall particle number concentration N_o = 1000 cm^{-3}. They are given together with the spectral values of real part n and imaginary part k of the complex refractive index at the 0.55 μm wavelength, single-scattering albedo $\omega(0.55\ \mu m)$, asymmetry factor $g(0.55\ \mu m)$, volume extinction coefficient $\beta_{ext}(0.55\ \mu m)$ and Ångström's exponent α calculated over the 0.40 - 0.87 μm wavelength range for the spectral evaluations of $\beta_{ext}(\lambda)$ made using the 6S radiative transfer code of Vermote et al. (1997a). The 6S aerosol components are labelled according to Vermote et al. (1997 b): oceanic (OC), water-soluble (WS), dust-like (DL) and soot (SO).

Aerosol type	Log-normal mode	Mass percentages of the basic 6S dry-air components				Geometric standard deviation σ	Mode radius r_c (μm)	Particulate matter refractive index parts		$\omega(0.55\ \mu m)$	$g(0.55\ \mu m)$	$\beta_{ext}(0.55\ \mu m)$ (km^{-1})	Expo-nent α
		OC	WS	DL	SO			$n(0.55\ \mu m)$	$k(0.55\ \mu m)$				
Winter-spring (Arctic haze) aerosol	Fine	35	39	22	4	2.24	$2.1\ 10^{-2}$	1.487	$2.17\ 10^{-2}$	0.864	0.637	$1.221\ 10^{-8}$	1.581
	Accum.	58	4	38	-	2.03	$3.0\ 10^{-1}$	1.444	$3.28\ 10^{-3}$	0.937	0.745	$4.088\ 10^{-3}$	- 0.117
Arctic summer background aerosol	Fine	18	35	45.8	1.2	1.95	$3.5\ 10^{-2}$	1.506	$1.10\ 10^{-2}$	0.930	0.605	$4.353\ 10^{-8}$	1.871
	Coarse	71	1	28	-	2.03	1.75	1.424	$2.30\ 10^{-3}$	0.813	0.846	3.200	- 0.054
Asian dust	Fine	-	24	76	-	1.95	$7.0\ 10^{-2}$	1.530	$7.52\ 10^{-3}$	0.956	0.666	$5.094\ 10^{-6}$	1.039
	Coarse	4	6	90	-	2.15	1.30	1.552	$7.56\ 10^{-3}$	0.673	0.860	1.385	- 0.058
Boreal forest fire smoke	Fine	-	-	97.9	2.1	2.00	$3.9\ 10^{-2}$	1.535	$1.71\ 10^{-2}$	0.906	0.627	$1.698\ 10^{-7}$	1.556
	Accum.	-	-	98.4	1.6	2.00	$1.2\ 10^{-1}$	1.534	$1.49\ 10^{-2}$	0.892	0.700	$9.878\ 10^{-5}$	0.345
Antarctic austral summer coastal aerosol	Fine	52	40	7.5	0.5	2.03	$7.0\ 10^{-2}$	1.454	$6.30\ 10^{-3}$	0.958	0.712	$5.811\ 10^{-6}$	0.997
	Coarse	61	16.5	22.5	-	2.10	1.50	1.439	$2.79\ 10^{-3}$	0.795	0.844	2.117	- 0.058
Austral summer Antarctic Plateau aerosol	Fine	11.2	86.4	2.2	0.2	2.24	$2.1\ 10^{-2}$	1.514	$6.24\ 10^{-3}$	0.959	0.620	$1.320\ 10^{-8}$	1.603
	Coarse	86	6	8	-	2.03	1.75	1.402	$1.00\ 10^{-3}$	0.900	0.831	3.204	- 0.056
Antarctic austral winter aerosol (*)	Fine	-	90	10	-	2.03	$7.0\ 10^{-2}$	1.530	$6.20\ 10^{-3}$	0.960	0.671	$7.477\ 10^{-6}$	0.857
	Accum.	95	-	5	-	2.03	$5.0\ 10^{-1}$	1.388	$4.00\ 10^{-4}$	0.986	0.774	$2.724\ 10^{-2}$	- 0.157

(*) for its use at both Antarctic coastal and high-altitude sites.

Table 6. Multimodal aerosol extinction models based on the OPAC (Hess et al., 1998) components used to represent 4 Arctic and 4 Antarctic columnar contents of polar aerosol, with (i) the mass percentages of the OPAC components of fine and accumulation/coarse particle modes in the atmospheric column; (ii) the values of real part n and imaginary part k of complex refractive index at the 0.55 μm wavelength, (iii) the values of aerosol optical thickness $\tau(0.50\ \mu m)$ and Ångström's exponent α calculated over the 0.40-0.87 μm wavelength range, and (iv) the values of columnar aerosol single scattering albedo $\omega(0.55\ \mu m)$. The last three columns provide the values of diurnal average aerosol radiative forcing terms at the TOA-level (ΔF_{TOA}), at the surface (ΔF_{BOA}) and within the atmosphere (ΔF_{ATM}), estimated for the BRDF surface reflectance models OS1 (oceanic), VS1 (vegetation-covered) and PS1, PS2, PS3 and PS4 (polar ice- and snow-covered) determined by Tomasi et al. (2014). The acronym BG stands for "background". The OPAC aerosol components are indicated by the acronyms WASO (water-soluble), SSAM (sea-salt accumulation mode), SSCM (sea-salt coarse mode), INSO (insoluble), SOOT (soot), and MITR (mineral-transported).

Aerosol type	Mass percentages of the basic OPAC components calculated for relative humidity = 50% to give form to the fine and accumulation/coarse particle modes						Particulate matter refractive index parts		Aerosol optical thickness $\tau(0.50\ \mu m)$	Exponent α	$\omega(0.55\ \mu m)$	BRDF surface reflectance model	Diurnal average aerosol radiative forcing (W m^{-2})		
	Fine particle modes		Accumulation/coarse particle modes												
	WASO	SOOT	SSAM	SSCM	INSO	MITR	$n(0.50\ \mu m)$	$k(0.50\ \mu m)$					ΔF_{TOA}	ΔF_{BOA}	ΔF_{ATM}
Winter-spring Arctic haze (Barrow)	95.8	4.2	22.9	37.7	39.4	-	1.399	$3.3\ 10^{-3}$	0.116	1.28	0.840	OS1 PS1 PS2	-5.5 +9.0 +8.8	+6.5 +0.0 +0.1	-12.0 +8.9 +8.7
Winter-spring Arctic haze (Ny-Ålesund)	98.0	2.0	-	90.9	9.1	-	1.424	$7.3\ 10^{-3}$	0.080	1.29	0.949	OS1 PS3	-5.3 +1.0	-0.6 -0.4	-4.7 +1.4
Winter-spring Arctic haze (Sodankylä)	95.3	4.7	94.8	5.2	-	-	1.399	$3.9\ 10^{-3}$	0.066	1.25	0.840	OS1 VS1 PS2	-7.7 -3.5 +2.2	-1.1 -5.3 -0.3	-6.6 +1.8 +2.5
Background summer aerosol (Barrow)	96.8	3.2	11.0	43.6	45.4	-	1.444	$9.2\ 10^{-3}$	0.078	1.40	0.978	OS1 VS1	-9.2 -4.2	-1.9 -6.5	-7.3 +2.3
Background summer aerosol (Ny-Ålesund)	98.0	2.0	-	50.0	50.0	-	1,461	$7.9\ 10^{-3}$	0.041	1.20	0.966	OS1 PS4	-7.2 +1.0	+1.5 -2.3	-8.6 +3.4
Arctic dense summer aerosol (Ny-Ålesund)	97.6	2.4	6.3	59.7	34.0	-	1.437	$3.7\ 10^{-3}$	0,120	1.00	0.852	OS1 PS4	-10.4 +13.0	+4.2 -5.2	-14.6 +18.2
Background summer aerosol (Summit)	98.0	2.0	-	50.0	50.0	-	1.449	$8.8\ 10^{-3}$	0.039	1.48	0.969	PS1	+2.2	-0.2	+2.5
Background summer aerosol (Sodankylä)	98.0	2.0	-	50.0	50.0	-	1.452	$8.6\ 10^{-3}$	0.060	1.42	0.965	OS1 VS1	-6.5 -3.0	-1.6 -5.5	-4.9 +2.4

												PS2	+3.0	-0.4	+3.4
Background summer aerosol (Tiksi)	98.0	2.0	-	50.0	50.0	-	1.444	$9.2\ 10^{-3}$	0.085	1.60	0.977	OS1 VS1	-10.3 -5.6	-1.6 -9.0	-8.7 +3.3
Asian dust (Barrow)	100.0	-	5.8	2.4	56.5	35.3	1.527	$6.3\ 10^{-3}$	0.200	0.80	0.858	OS1 PS2	-9.3 +18.5	+16.0 +0.3	-25.3 +18.2
Boreal forest fire smoke (Barrow)	95.5	4.5	21.7	26.1	52.2	-	1.469	$2.5\ 10^{-3}$	0.300	1.20	0.758	OS1 VS1	-32.9 -20.2	-6.7 -28.6	-26.2 +8.3
Background austral summer aerosol (Mario Zucchelli)	99.5	0.5	-	73.9	26.1	-	1.468	$2.3\ 10^{-3}$	0.030	0.90	0.964	OS1 PS2	-6.2 +2.0	+0.9 -0.1	-7.1 +2.1
Background austral summer aerosol (Neumayer)	99.7	0.3	-	85.6	14.4	-	1.457	$1.3\ 10^{-3}$	0.043	0.68	0.975	OS1 PS1 PS2	-8.2 +1.9 +2.1	+1.4 -0.2 +0.0	-9.6 +2.1 +2.1
Background austral summer aerosol (Dome Concordia)	100.0	-	4.5	-	-	95.5	1.441	$2.0\ 10^{-3}$	0.019	1.77	0.999	PS1 PS2	+0.4 +0.6	+0.2 +0.4	+0.2 +0.2
Background austral summer aerosol (South Pole)	99.6	0.4	-	83.6	16.4	-	1.445	$3.2\ 10^{-3}$	0.018	1.49	0.988	PS1 PS2	+0.6 +0.7	-0.1 -0.1	+0.7 +0.8